Fall 12-18-2015

# Photooxidation Reactions of Small-Chain Methyl Esters, Aerosol Photoelectron Spectroscopy, and the Photodissociation of Ethylenediamine

Giel Muller

*University of San Francisco*, gielmuller@protonmail.com

# Photooxidation Reactions of Small-Chain Methyl Esters, Aerosol Photoelectron Spectroscopy, and the Photodissociation of Ethylenediamine

A Thesis Presented to the Faculty

of the Department of Chemistry

at the University of San Francisco

in partial fulfillment of the requirements for the Degree of

Master of Science in Chemistry

Written by

Giel Muller

Master of Science in Chemistry

University of South Carolina

12/8/2015

# Photooxidation Reactions of Small-Chain Methyl Esters, Aerosol Photoelectron Spectroscopy, and the Photodissociation of Ethylenediamine

Thesis written by Giel Muller

This thesis is written under the guidance of the Faculty Advisory Committee, and approved by all its members, has been accepted in partial fulfillment of the requirements for the degree of

**Master of Science**

**in Chemistry**

**at**

**the University of San Francisco**

Thesis Committee

Giovanni Meloni, Ph.D.

Research Advisor

William Melaugh, Ph.D.

Professor

Ryan West, Ph.D.

Assistant Professor

Marcelo Camperi, Ph.D.

Dean, College of Arts and Sciences

# Acknowledgments

My experience has taught me to find meaning in what I do, and not simply follow expectation and protocol for the sake of convention. I extend tremendous gratitude to Dr. Giovanni Meloni for the opportunity to conduct meaningful research within his physical chemistry group at the University of San Francisco, and for his encouragement to think creatively and explore new frontiers in science by *trying new things*. In my experience alone, Dr. Meloni has provided and fostered a wide array of relevant research opportunities that aim to significantly contribute to the scientific community, including theoretical investigations of novel superalkali clusters, experimental photooxidation reactions, FTIR studies of aerosols (and their reactions with ozone), aerosol photoelectron spectroscopy, negative ion photoelectron spectroscopy, and the TPEPICO study of ethylenediamine. His expertise, coupled with his grand sense of possibility and out-of-the-box creativity, has been invaluable to me as a growing scientist.

The USF chemistry faculty has been exceptional, as well. In addition to all of the professors in the department, I am grateful for Deidre Shymanski who has made the graduate program in chemistry at USF seamless from start to finish.

Additional thanks to Adam Scheer and Krisztina Voronova. It was truly a pleasure to work with each of you directly over an extended period of time — this thesis, again, would not be possible without your expertise and patience. Krisztián G. Torma, thank you for your support with TPEPICO time-of-flight spectra deconvolution and for your moral support and friendship.

# Table of Contents

# 4. Low Temperature Chlorine-Initiated Oxidation of Small-Chain Methyl Esters: Quantification of Chain-Terminating HO$_2$-Elimination Channels

# 5. Aerosol Photoelectron Spectroscopy

# 6. Rotamers and Migration: Investigating the Photodissociative Dynamics of the Ethylenediamine Ion

# Chapter 1: Introduction

## 1.1 A Bigger Picture: Atmospheric Pollution

The composition of Earth's atmosphere has biological and physical implications. Air pollution, specifically, has been a focus of interest in the areas of toxicology and epidemiology. The Environmental Protection Agency (EPA) has identified six common air pollutants: ozone, particulate matter, carbon monoxide, nitrogen oxides, sulfur dioxide, and lead.[1] Though air pollution is a mixture of several different types of gases, it is necessary to understand the independent role of each component on the health and well-being of humans, animals, and the environment. As it pertains to the current investigation, it is imperative to research new ways in which the production of these pollutants can be reduced and, in turn, the detrimental health effects mitigated.

### 1.1.1 Climate Change: Ozone, Its Precursors, and Particulate Matter

Though chlorofluorocarbons (CFCs) and other halogenated hydrocarbons were the main source of stratospheric $O_3$ depletion and have been significantly restricted since the Montreal Protocol in 1987,[2] global warming continues to be a threat much closer to the surface. As ozone in the stratosphere absorbs a significant portion of the intense cosmic and UV radiation that would otherwise harm life on the planet, it falls to reason that tropospheric (ground-level) ozone also possesses significant global warming potential. Long-term exposure to ground-level pollutants, such as ozone ($O_3$) and particulate matter (PM), is known to lead to increased rates of asthma and respiratory morbidity, even in ambient concentrations.[3-10]

It is important to recognize ground-level ozone precursors, such as nitric oxide (NO) and nitrogen dioxide ($NO_2$). These are the primary nitrogen oxide ($NO_x$) species involved in air pollution and they are related in a cycle with ozone ($O_3$). Nitrogen is able to unite with oxygen to form NO at elevated temperatures. In addition, a significant source of $NO_x$ includes the burning of fossil fuels in internal combustion engines.[3] Though studies have not been able to show a direct correlation between $NO_2$ exposure and human health conditions in the absence of $O_3$ and PM, lung function has been shown to be lower in communities where $NO_2$ concentration is higher.[11-13]

In one relatively beneficial aspect, NO is able to deplete ground-level ozone and oxidize to form $NO_2$, thereby reducing the effects of ground-level ozone (1.1.1a). This reaction typically takes place during the night, while during the day the sunlight breaks down $NO_2$ to reform NO and O·, the latter of which reacts with abundant $O_2$ to regenerate ground-level ozone (1.1.1b).

$$NO + O_3 \rightarrow NO_2 + O_2 \tag{1.1.1a}$$

$$NO_2 + O_2 + sunlight \rightarrow NO + O_3 \tag{1.1.1b}$$

This is a naturally occurring cycle that has existed throughout history and has not been of major concern until other elements, such as volatile organic compounds (VOCs), were added to the atmosphere in greater concentrations.

VOCs usually take form as hydrocarbon compounds that are released to the air in various ways including agriculture, forestry, and burning of fossil fuels. As such, an increase in VOC emissions is correlated with increased industrial activity. The VOCs provide an additional pathway to oxidize NO, where ground-level ozone depletion is not necessary in the formation of $NO_2$. With exposure to sunlight,

additional $O_3$ is generated from $NO_2$ to toxic levels known as photochemical smog. Thus, the addition of NO and VOCs to the atmosphere generates greater amounts of $NO_2$ that are available to form ground-level ozone. The concentration of tropospheric ozone is now at least 34 ppt, substantially higher than pre-industrial (prior to approx. 1750) levels of 25 ppt, and raises a major concern with respect to the future of the climate.[14]

While VOCs are a major contributor to increased $NO_x$ levels, the related greenhouse gas nitrous oxide ($N_2O$) is another contributing source. $N_2O$ forms NO upon reaction with oxygen. Human-related sources of $N_2O$ account for 38% of the total emissions, of which 10% is generated from fossil fuels combustion and other related processes.[15] Figure 1.1.1 shows the contribution of $N_2O$ to the total amount of greenhouse gases released in 2007. $N_2O$ is calculated to have between 265-310 times more global warming impact than carbon dioxide, which is the representative molecule in discussions centered around climate change, due to its prevalence in the environment.[16, 17]

In addition to VOC, $NO_x$, and $N_2O$ molecules as ground-level ozone precursor species, the influence of particulate matter (PM) upon the environment is also of scientific interest. Although they are small particles, PM are highly absorbing at IR and visible wavelengths and are able to scatter solar and thermal radiation to effect Earth's climate. Specifically, studies have focused on the refractive index of soot particles and other PM to gain insight to their radiative properties.[18-22] In terms of health and well-being, PM has been found to cause respiratory problems and are carcinogenic.[23, 24]

PM is produced by a wide range of sources and comes in many forms. Airborne soot and soot-containing aerosols (carbonaceous smokes) comprise a portion of the PM in the atmosphere and are produced from aircraft, rocket, and automobile engines, as well as industrial flames.[25, 26]

They can be classified into two distinct categories by diameter size: coarse particles (>2.5 μm) and fine particles (<2.5 μm). An additional category, ultrafine particles (<100 nm), often termed "aerosols", are suspended in gas and are the most abundant category of PM in the atmosphere. Under some circumstances, these can be converted from particle to gas and vice-versa.[27]
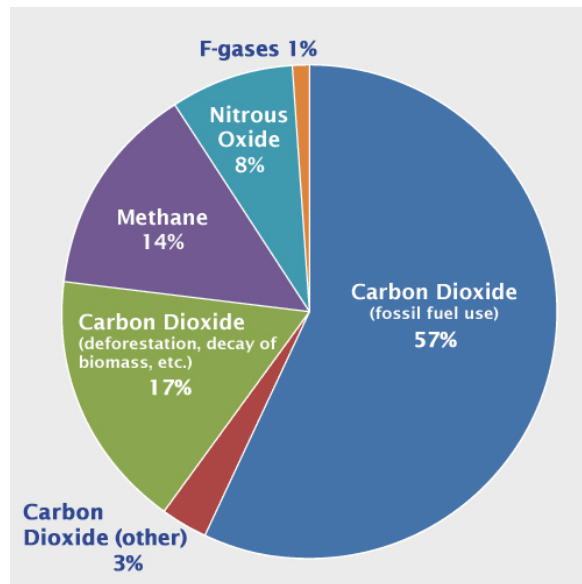


**Figure 1.1.1:** Global emissions of greenhouse gases as of 2007.[28]

## 1.2 Sustainable Energy: The Preservation of Health and Climate

$NO_x$, VOCs, $N_2O$, $CO_2$, and soot are all released by the combustion of fossil fuels, which include natural gas, petroleum, coal, shale oil, and bitumen. The

dependence on fossil fuels for energy spans centuries, and the combustion for transportation has been growing since the Industrial Revolution (Figure 1.2a). Approximately 13% of the fossil fuels used in 2007 was for transportation (Figure 1.2b), and the International Energy Agency (IEA) reported that 23% of global $CO_2$ emissions in 2009 were due to transportation, the largest contributor being motor vehicles.[29]

Environmentally "clean" sources of energy, such as wind and solar, have seen a mild increase in popularity as they can meet some home and office energy needs. However, these methods may have limited potential within the realm of transportation and supply-chain logistics. The energy demand for long-distance and daily transport of large volume of goods for trade are not so easily met by these alternative energy sources, and therefore focus has also been given to researching more efficient combustion methods that burn more efficiently with fewer emissions.
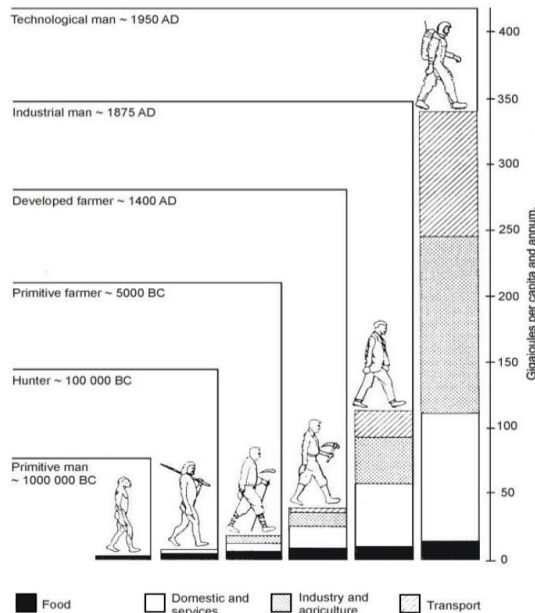


**Figure 1.2a:** The changes in the amount of fossil fuel used for various purposes over time.[30]
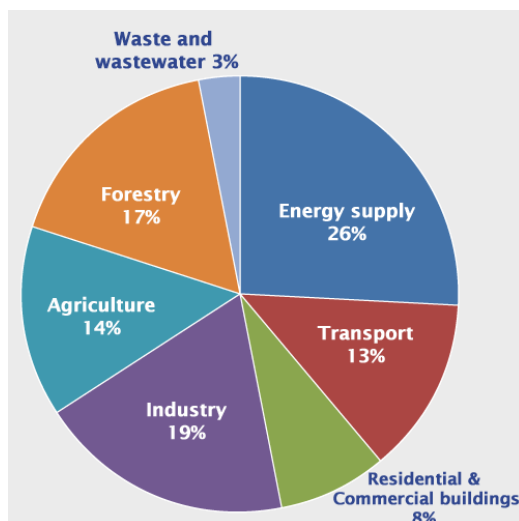
**Figure 1.2b:** The relative consumption of fossil fuels by use in 2007.[28]

## 1.3 Combustion Basics

Early on, the knowledge and necessary tools to understand the adverse effects of combustion on the environment were not available. Indeed, the first internal combustion engines were developed without much understanding of the complex chemical processes.[31] The general equation that has governed combustion processes is idealistic in that it is only accurate for complete combustion of very simple molecules, and therefore does not reflect the intermediates and byproducts that are now known to result:

$$\text{Fuel} + O_2 \rightarrow H_2O + CO_2 + \text{heat} \tag{1.3}$$

Figure 1.3 highlights the complexity of the oxidation of methane, the smallest hydrocarbon. Numerous intermediates, byproducts, and polycyclic aromatic hydrocarbons (PAH) are formed and can be released into the environment due to incomplete combustion, which can attribute to pollution levels.

The reaction mechanisms and the formation of potential pollutants vary greatly depending upon the fuel itself, as well as the engine in which the fuel is combusted.
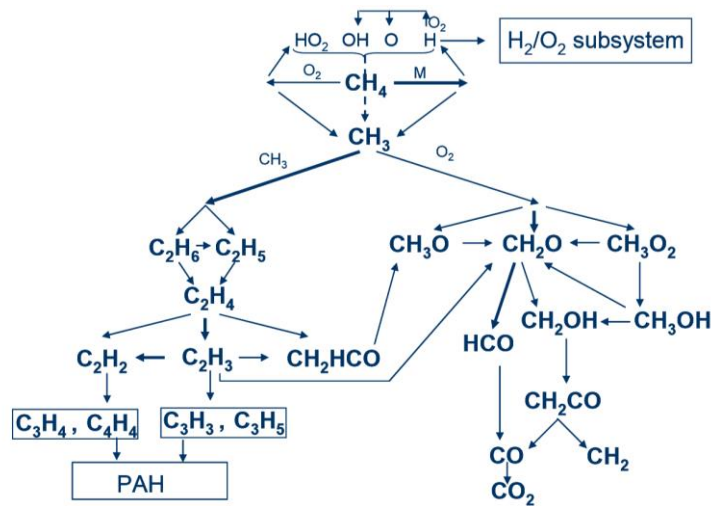
**Figure 1.3**: A simplified scheme showing the main reaction paths of methane oxidation.[32]

## 1.4 Engine Technology

Most of the energy for transportation is provided using internal combustion engines, specifically the spark ignition (SI) and the compression ignition (CI) engines. The SI engine is relatively simple and is therefore quite attractive in its lower initial cost. This engine relies upon gasoline or other fuel and requires a spark plug as an external ignition source. As such, there is only one point of ignition, which leads to engine knocking and lower thermodynamic efficiency. Engine knocking occurs when combustion takes place at a time or location other than that intended by the spark and generally happens when the compression ratio (the volume of the combustion

chamber when the piston is at the top vs. the volume of the combustion chamber when the piston is at the bottom)[33] is high. Theoretically, thermal efficiency is expected to increase with higher compression ratios, however limitations are usually experimentally determined and set to avoid knocking. The CI engine is much more efficient, although it releases substantially greater amounts of $NO_x$ and PM. Newer combustion engines aim to reduce $NO_x$ and soot emissions, knock sensitivity, and other undesirable aspects of conventional SI and CI engines.

The homogeneous charge compression ignition (HCCI) engine is a low-temperature combustion engine that can be run on a wide-array of fuels and lean fuel blends so long as the compression ratio and inlet temperature can be controlled. In an HCCI engine, a homogenous composition of pre-mixed fuel and air is compressed until autoignition takes place across the combustion chamber. As the combustion process occurs at lower temperatures than those in SI engines, there is a notable reduction in $NO_x$ and PM emissions. Yang et al.[34] reported better fuel consumption using HCCI engines relative to SI engines. Figure 1.4a displays the fundamental differences between SI, compression ignition (CI), and HCCI engines.

It has been described that HCCI engines are governed by three temperatures: the autoignition temperature, a good combustion efficiency temperature (~1400 K), and the limit of 1800 K to prevent a substantial increase in NO formation.[35] The temperature should be controlled so that the autoignition temperature of the fuel is reached at the end of the compression stroke to ensure ignition. The combustion efficiency temperature is somewhat dependent upon the mixture of the fuel. A rich mixture will increase the burn rate and lead to pressure increase and $NO_x$ formation at

higher temperatures. Analogously, if the composition is too lean the temperature increase from the combustion is low, resulting in incomplete combustion.
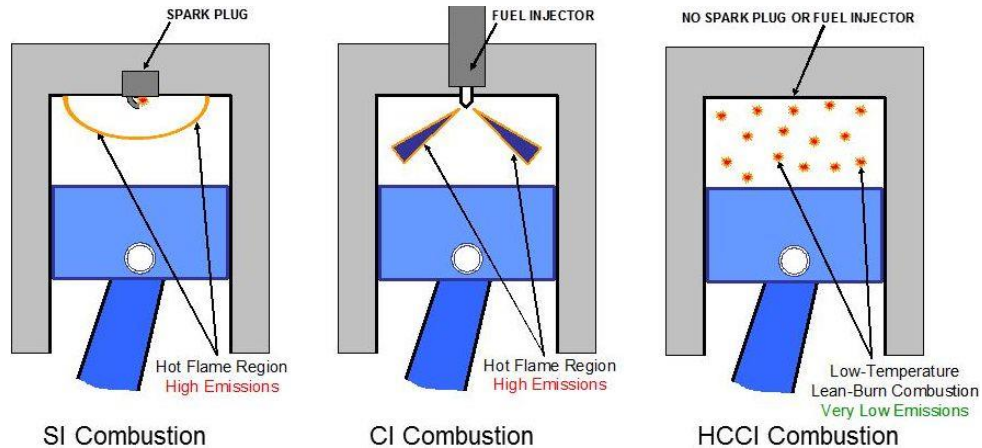


**Figure 1.4a:** A diagram illustrating the fundamental differences between SI, CI, and HCCI engine. The SI and CI engines have single point ignitions while the HCCI has multiple ignition points.[36]

In contrast to SI engines where the reaction time is signified by the spark ignition, the kinetics of the autoignition processes in HCCI engines are more complicated and need to be modeled accordingly. Specifically, $H_2O_2$ plays an integral role in autoignition, as it thermally decomposes into hydroxyl radicals ($\cdot$OH) that react with the air-fuel blend, effectively becoming the "igniter" for HCCI engines.[31] These radical-chain reactions consist of several steps: initiation, propagation, branching, and termination. Chain branching reactions do not always occur, however they lead to the formation of additional radicals. The reactions that take place between the radicals and the air-fuel blend are contingent upon the temperatures and the fuel components. Figure 1.4b shows the general radical-chain reactions that occur in each step.

$$RH + \dot{O}H \longrightarrow \dot{R} + H_2O$$

$$\dot{R} \xrightarrow[\text{rearrangement}]{\text{fragmentation}} \dot{R}_X$$

(initiation)

$$\dot{R} + O_2 \longrightarrow olefin + H\dot{O}_2$$

$$\dot{R} + O_2 \longrightarrow R\dot{O}_2$$

$$R\dot{O}_2 + RH \longrightarrow ROOH + \dot{R}$$

(propagation)

$$ROOH \longrightarrow R\dot{O} + \dot{O}H$$

$$2ROOH \longrightarrow R\dot{O}_2 + R\dot{O} + H_2O$$

$$R\dot{O} + RH \longrightarrow ROH + \dot{R}$$

$$\dot{O}H + RH \longrightarrow \dot{R} + H_2O$$

(chain branching)

$$2R\dot{O}_2 \longrightarrow inert\ products$$

$$R\dot{O}_2 + \dot{R} \longrightarrow ROOR$$

$$2\dot{R} \longrightarrow R\text{-}R$$

(termination)
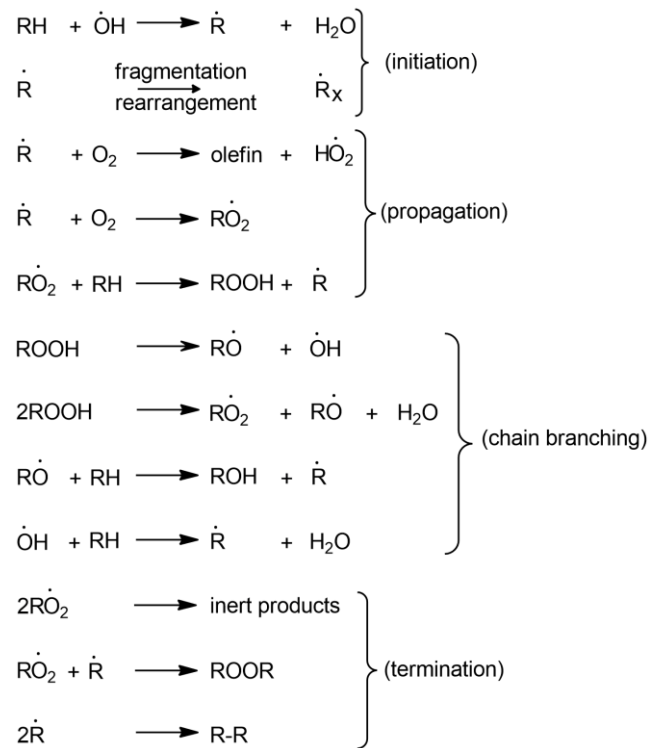
**Figure 1.4b**: Basic Autooxidation Scheme (BAS)[37] and generic reaction mechanisms of hydrocarbon autooxidation.[38]

## 1.5 Biofuels: Pitfalls and Promises

While one important aspect of reducing $NO_x$ emissions involves the engine mechanics, another important facet is the chemistry of the fuel blends themselves. Fossil fuels are currently the leading source of energy globally. As the dependence is high, the supply of fossil fuel reserves is a growing concern. It is difficult to predict how many years of fossil fuels are left for energy consumption, as new discoveries can be made and consumption is not constant. Colin Campbell,[39] a petroleum geologist, predicted that the production of conventional fuel would increase while new

discoveries of sources would decrease. This underlines the importance of finding alternative sources to meet energy needs (Figure 1.5a).

To offset the demand for fossil fuels, as well as the $NO_x$ emissions, attempts to improve the fuel itself have already been incorporated. Additives are often mixed with the fuel with the intention to mitigate some of the undesirable effects of fuels, namely those which arise from ignition delay. Specifically for diesel fuels, the combustion speed of the fuel blend is related to the engine performance and pollutant emissions. The longer the ignition delay, the greater the detrimental effects on the engine and environment. The speed of combustion of diesel fuels is represented by its cetane number (CN), where a higher number would correspond to a faster ignition of the engine after fuel injection.
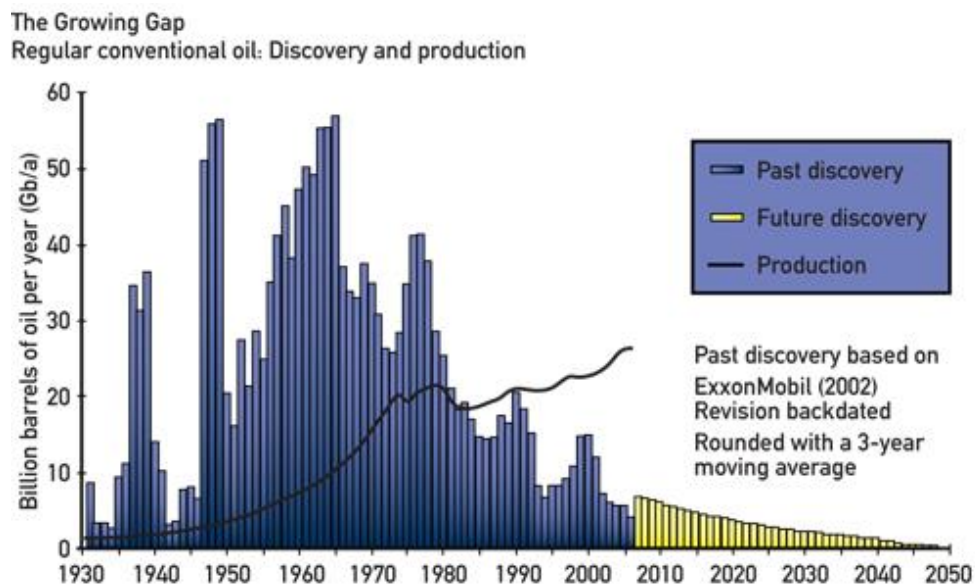


**Figure 1.5a**: It is expected that new discoveries of fossil fuel reserves will continue to decrease while demand remains high.[39]

Diesel fuels derived from biological sources are referred to as biofuels. Biofuel combustion is an environmentally-attractive, carbon-neutral alternative that would help reduce the global dependence on fossil fuels for energy. Many similar chemical components found in oil-based fuels can also be generated from plant-based sources, which include sugar cane, corn, wheat, rape seed, palm oil, wood, as well as from industrial wastes. The process by which biofuels are created from oils and fats is known as transesterification and is an important mechanism in biofuel generation as shown in Figure 1.5b.
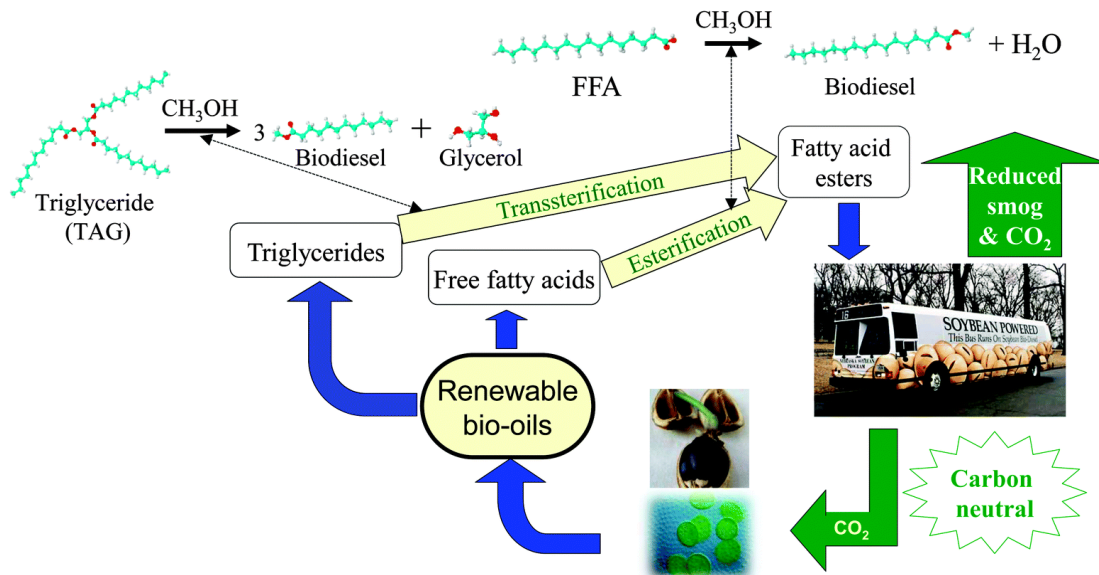


**Figure 1.5b:** The biofuel cycle, where the production and combustion processes are considered to be carbon-neutral.[40]

The concerns regarding biofuel production on a larger scale includes the realization that biofuel production from agricultural sources would cut into the food supply and increase prices as a result. In the early 2000s, for example, it was found that corn-derived ethanol contributed to 14-43% of US corn price increases.[41] In many

12

regions, the supply of water may also not be adequate to support the agricultural biofuel production that is necessary to meet demand.

These issues can somewhat be alleviated by diversification. Using various types of biofuels from various sources can reduce the strain on the production of food. Lignocellulosic biomass, for example, is derived from paper waste or non-edible plant matter and can be as an alternative to liquid fuels.[42-44] In addition, research has been underway to find cost-effective methods of biofuel production, including genetic modification of plants for biofuel production.[45, 46]

## 1.6 Purpose of this Work

Using the homogeneous compression ignition engine (HCCI) as the model engine for combustion, the autoignition mechanisms of various representative potential biofuels have been studied[47-50] and many more are relatively unknown. In this work, the $HO_2$- and OH-elimination pathways of small-chain methyl esters (methyl propanoate, methyl butanoate, and methyl valerate) are investigated to provide greater insight to the influence of the functional group on the combustion properties.

In addition to the bimolecular combustion reactions, such as those between methyl ester radicals and oxygen described above, the study of unimolecular reactions are important in that they reveal bonding characteristics that can influence their combustion behavior. As such, the photodissociation of ethylenediamine (a fuel additive) was also examined *via* TPEPICO (threshold photoelectron photoion coincidence spectroscopy) to observe the dissociation dynamics.

Finally, the relatively unexplored field of aerosols in combustion was studied in Taiwan, where isoprene and gamma-valerolactone were atomized and photoionized in both neutral and acidic environments to determine any changes in electronic structure. While data was not compelling, it paves the way for future research endeavors at USF in aerosol investigations.

## 1.7 References

1. Agency, E.P. *What Are the Six Common Air Pollutants?* 2015  [cited 2015 November 9, 2015]; Available from: http://www3.epa.gov/airquality/urbanair/.
2. *The Montreal Protocol*, E. Commission, Editor. 2007, European Communities: Luxembourg: Office for Official Publications of the European Communities.
3. Organization, W.H., *Health Aspects of Air Pollution with Particulate Matter, Ozone and Nitrogen Dioxide*. 2003, WHO: Geneva.
4. Organization, W.H., *World Health Report 2002. Reducing Risks, Promoting Healthy Life.* 2002, WHO: Geneva.
5. Seagrave, J., J.L. Mauderly, and S.K. Seilkop, *In Vitro Relative Toxicity Screening of Combined Particulate and Semivolatile Organic Fractions of Gasoline and Diesel Engine Emissions.* J. Toxicol. Env. Heal. A., 2003. **66**: p. 1113-1132.
6. Seagrave, J., et al., *Mutagenicity and In Vivo Toxicity of Combined Particulate and Semivolatile Organic Fractions of Gasoline and Diesel Engine Emissions.* Toxicol. Sci., 2002. **70**: p. 212-226.
7. Walsh, M.P., *Vehicle Emissions and Health in Developing Countries*, in *Air Pollution & Health in Rapidly Developing Countries*, G. McGranahan and F. Murray, Editors. 2003, Earthscan Publications: Sterling, VA. p. 146-175.
8. Oberdorster, G., et al., *Association of Particulate Air Pollution and Acute Mortality: Involvement of Ultrafine Particles?* Inhalation Taxicology, 1995. **7**(1): p. 111-124.
9. Elder, A., et al., *Pulmonary inflammatory response to inhaled ultrafine particles is modified by age, ozone exposure, and bacterial toxin.* Inhalation Taxicology, 2000. **12**(Supple): p. 4:227-246.
10. Madden, M.C., et al., *Effect of Ozone on Diesel Exhaust Particle Toxicity in Rat Lung.* Toxicology and Applied Pharmacology, 2000. **168**(2): p. 140-148.
11. Ackermann-Liebrich, U., et al., *Lung function and long term exposure to air pollutants in Switzerland. Study on Air Pollution and Lung Diseases in Adults (SAPALDIA) Team.* American Journal of Respiratory and Critical Care Medicine, 1997. **155**(1): p. 122-129.
12. Peters, J.M., et al., *A study of twelve Southern California communities with differing levels and types of air pollution. II. Effects on pulmonary function.* American Journal of Respiratory and Critical Care Medicine, 1999. **159**(3): p. 768-775.
13. Schlindler, C., et al., *Associations between Lung Function and Estimated Average Exposure to NO2 in Eight Areas of Switzerland.* Epidemiology, 1998. **9**(4).
14. IPCC. *Contribution of Working Group I (WG1) to the Third Assessment Report (TAR) of the Intergovernmental Panel on Climate Change (IPCC)*. Climate Change 2001: The Scientific Basis 2001.
15. Denman, K.L., et al., *Couplings Between Changes in the Climate System and Biogeochemistry. *, in *Climate Change 2007: The Physical Science Basis. Contribution of Working Group 1 to the Fourth Assessment Report of the Intergovernmental Panel on Climate Change*, S. Solomon, et al., Editors. 2007, Cambridge University Press: Cambridge, United Kingdom and New York, NY, USA.
16. *Overview of Greenhouse Gases -- Nitrous Oxide.* 2014.
17. *U. S. Greenhouse Gas Inventory Report: 1990-2013.* 2015.

18. Shaddix, C.R., et al., *Soot graphitic order in laminar diffusion flames and a large-scale JP-8 pool fire.* International Journal of Heat and Mass Transfer, 2005. **48**: p. 3604-3614.

19. Smyth, K.C. and C.R. Shaddix, *Brief Communication The Elusive History of m = 1.57 - 0.56i for the Refractive Index of Soot.* Combustion and Flame, 1996. **107**: p. 314-320.

20. Henriksen, T., et al., *Determination of Soot Refractive Index as a Function of Height in an Inverse Diffusion Flame*, in *5th US Combustion Meeting*. 2007, Western United States Section of the Combustion Institute: University of California at San Diego. p. 1795-1803.

21. Chylek, P., et al., *Optical properties and mass concentration of carbonaceous smokes.* Applied Optics, 1981. **20**(17): p. 2980-2985.

22. Bhardwaja, P.S., J. Herbert, and R.J. Charlson, *Refractive Index of Atmospheric Particulate Matter: an in situ Method for Determination.* Applied Optics, 1973. **13**(4): p. 731-734.

23. Cancer, I.A.f.R.o., *IARC: Outdoor air pollution a leading environmental cause of cancer dealths*. 2013, World Health Organization Lyon/Geneva. p. 1-4.

24. Enomoto, M., W.J. Tierney, and K. Nozaki, *Risk of human health by particulate matter as a source of air pollution--comparison with tobacco smoking.* J. toxicol. Sci., 2008. **33**(3): p. 251-267.

25. Gelencser and Varga, *Evaluation of the atmospheric significance of multiphase reactions in atmospheric secondary organic aerosol formation.* Atmospheric Chemistry and Physics, 2005. **5**: p. 2823-2831.

26. Manoj, B., et al., *Characterization of Diesel Soot from the Combustion in Engine by X-ray and Spectroscopic techniques.* International Journal of Electrochemical Science, 2012. **7**: p. 3215-3221.

27. Baek, B.-H., J.A. Koziel, and V.P. Aneja, *A preliminary review of gas-to-particle conversion monitoring and modelling efforts in the USA.* Int. J. Global Environmental Issues, 2006. **6**: p. 204-230.

28. IPCC, *Contribution of Working Group III to the Fourth Assessment Report of the Intergovernmental Panel on Climate Change*, B. Metz, et al., Editors. 2007, Intergovernmental Panel on Climate Change: Cambridge, United Kingdom and New York, NY, USA.

29. Agency, I.E., *CO2 Emissions From Fuel Combustion Highlights*. 2011, International Energy Agency.

30. Chmielewski, A.G., *Environmental Effects of Fossil Fuel Consumption*. 1999, Institute of Nuclear Chemistry and Technology: Warsaw, Poland.

31. Warnatz, J., U. Maas, and R.W. Dibble, *Combustion*. Vol. 4th Edition. 2006, New York: Springer.

32. Slavinskaya, N.A. and O.J. Haidn, *Kinetic Mechanism For Low Pressure Oxygen / Methane Ignition and Combustion*, in *49th AIAA Aerospace Sciences Meeting including the New Horizons Forum and Aerospace Exposition*. 2011, American Institute of Aeroneutics and Astronautics, Inc.: Orlando, Florida.

33. T., A., F.C. O., and P.G. Y., *Influence of compression ratio on the performance characteristics of a spark ignition engine.* Advances in Applied Science Research, 2012. **3**(4): p. 1915-1922.

34. Yang, J., T. Culo, and T. Kenney, *Development of a Gasoline Engine System Using HCCI Technology - The Concept and the Test Results*, in *SAE Powertrain and Fluid Systems Conference & Exhibition*. 2002, SAE.

35. Johansson, B., *Homogenous Charge Compression Ignition - the future of IC engines?* International Journal of Vehicle Design, 2007. **44**(1-2): p. 1-19.

36. Charalambides, A.G., *Homogenous Charge Compression Ignition (HCCI) Engines*, in *Advances in Internal Combustion Engines and Fuel Technologies*, H.K. Ng, Editor. 2013, InTech.

37. Gryn'ova, G., J.L. Hodgson, and M.L. Coote, *Revising the mechanism of polymer autooxidation.* Org. Biomol. Chem., 2011. **9**: p. 480-490.

38. Yetter, R.A. and I. Glassman, *Combustion, 4th ed.* 2008, San Diego, CA: Academic Press.

39. Campbell, C.J., *Oil Depletion - The Heart of the Matter*. 2003, The Association for the Study of Peak Oil and Gas. p. 1-13.

40. Lee, A.F., et al., *Heterogeneous Catalysis for Sustainable Biodiesel Production via Esterification and Transesterification.* Chem. Soc. Rev., 2014. **43**: p. 7887-7916.

41. Persson, U.M., *The impact of biofuel demand on agricultural commodity prices: a systematic review.* Wiley Interdisciplinary Reviews: Energy and Environment, 2014. **4**(5): p. 410-428.

42. Ragauskas, A.J., et al., *The Path Forward for Biofuels and Biomaterials.* Science, 2006. **311**(5760): p. 474-489.

43. Hill, J., et al. *Environmental, economic, and energetic costs and benefits of biodiesel and ethanol biofuels*. in *Proceedings of the National Academy of Sciences*. 2006. Proceedings of the National Academy of Sciences.

44. Carroll, A. and C. Somerville, *Cellulosic Biofuels.* Annual Review of Plant Biology, 2009. **60**: p. 165-182.

45. Sticklen, M.B., *Plant genetic engineering for biofuel production: towards affordable cellulosic ethanol.* Nature Reviews Genetics, 2008. **9**: p. 433-443.

46. Hisano, H., R. Nandakumar, and Z.-Y. Wang, *Genetic Modification of Lignin Biosynthesis for Improved Biofuel Production.* In Vitro Cellular & Developmental Biology. Plant, 2009. **45**(3): p. 306-313.

47. Ng, M.Y., et al., *Synchrotron Photoionization Study of Mesitylene Oxidation Initiated by Reaction with Cl(2P) or O(3P) Radicals.* Journal of Physical Chemistry, 2014. **118**(21): p. 3735-3748.

48. Welz, O., et al., *Low-temperature combustion chemistry of biofuels: pathways in the initial low-temperature (550 K - 750 K) oxidation chemistry of isopentanol.* Physical Chemistry Chemical Physics, 2012. **14**: p. 3112-3127.

49. Scheer, A., et al., *Low-temperature combustion chemistry of novel biofuels: resonance-stabilized QOOH in the oxidation of diethyl ketone.* Physical Chemistry Chemical Physics, 2014. **16**(26): p. 13027-13040.

50. Scheer, A.M., et al., *Low Temperature (550-700 K) Oxidation Pathways of Cyclic Ketones: Dominance of HO2-Elimination Channels Yielding Conjugated Cyclic Coproducts.* Physical Chemistry Chemical Physics, 2015. **17**: p. 12124-12134.

# Chapter 2: Important Concepts

## 2.1 The Potential Energy Surface

A potential energy surface is a mathematical function where the geometry of the molecule corresponds to a specific single point energy, derived by computational methodologies. Computational approaches are described in a later section, however a brief overview of potential energy surfaces (PES) is provided here as they are widely used to help explain molecular behavior.

Molecular mechanics has often compared molecules to balls held together by springs.[1] When the bond lengths are stretched or angles distorted, the potential energy of the molecule increases. With additional energy, they can access higher vibrational levels and bonds can lengthen and angles can change. In quantum-mechanics, only discrete energy values are possible and they are equally spaced as shown in Figure 2.1a. Molecules always possess some sort of energy as they constantly vibrate about an equilibrium conformation. The energy corresponding to vibrational quantum number of 0 is termed the zero-point energy.[2] Therefore, while the equilibrium configuration is the lowest-energy point in the potential energy surface (often referred to as a minimum), molecules do not actually take on this exact structure. The molecule is in the ground vibrational state ($\Psi'_0$) when it occupies the lowest possible vibrational level.

The ground vibrational state on a PES is known as the global minimum. The potential energy surface for water along two coordinates is shown in Figure 2.1b. As the O-H bond stretches along one axis and the H-O-H bond angle is distorted along

the other, the potential energy increases in any direction and the local minimum is observed. The O-H bond stretching on the PES in Figure 2.1b seems to be simply "uphill" as there is no barrier to dissociation. In which case, a one-dimensional slice along the O-H bond length coordinate would look quite similar to the 1D PES provided in Figure 2.1a, where the amount of energy required to break the bond is known as the bond dissociation energy (BDE).
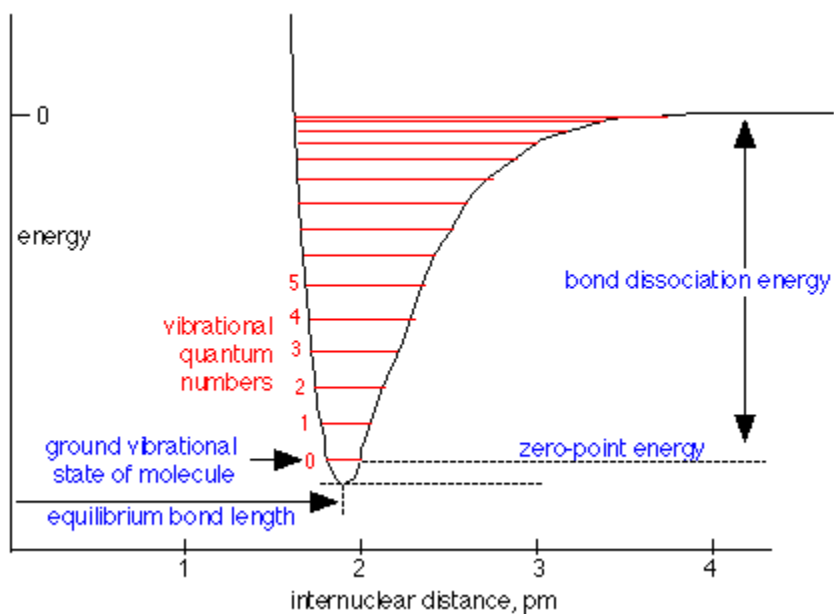


**Figure 2.1a:** A 1D general schematic of a potential energy surface of molecule with a barrierless ("uphill") dissociation pathway.[3]

However, a single molecule can possess more than one local minimum. This is exemplified in Figure 2.1c, where the blue areas in the top image represent two conformations of the same molecule (i.e., cis vs. trans) and are both local minima on the molecule's conformational PES. If all of the conformational surface (no bonds broken) of the molecule is well-explored, then a global minimum can be determined

as the deepest energy well. In Figure 2.1c this corresponds to the darkest blue area

in the top image. The global minimum on the PES is the lowest-energy conformation

and theoretically the most energetically preferable configuration. Thus, this geometry

can be expected to be of greatest abundance in low-energy conditions.
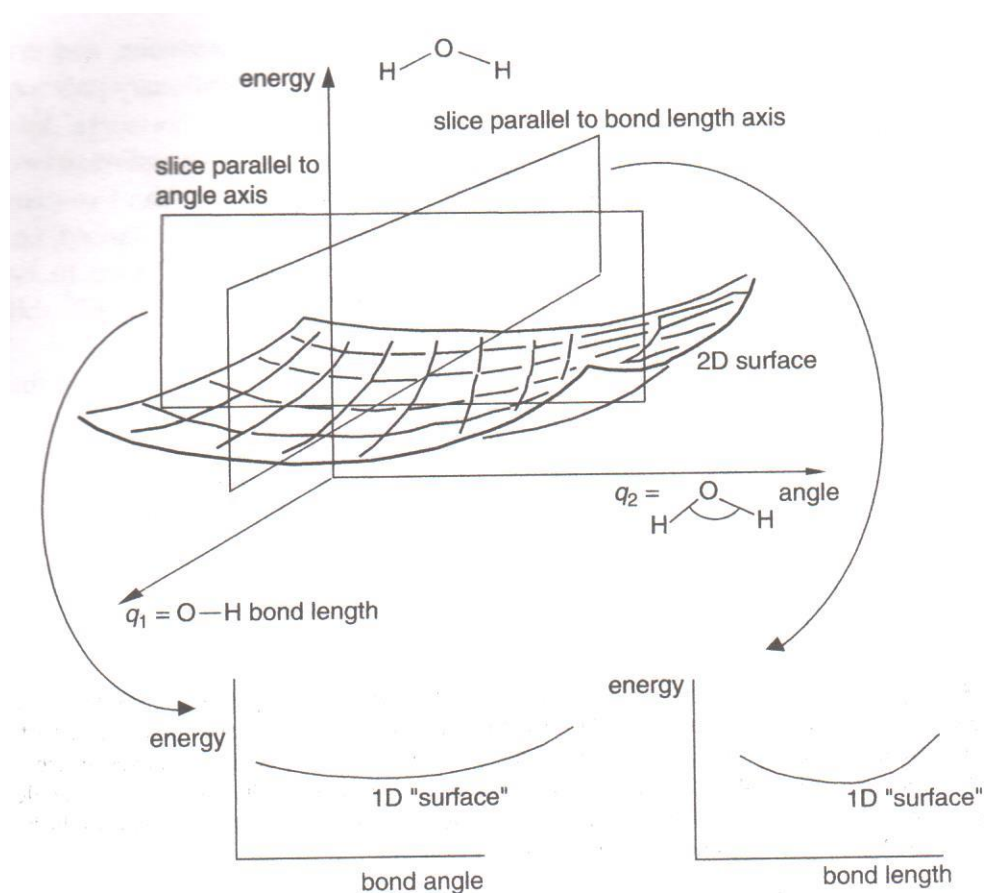


**Figure 2.1b:** The 2D potential energy surface of the water molecule and the two 1D
potential energy surfaces specific to each conformation coordinate.[1]

The top of Figure 2.1c shows a simple 2D potential energy surface along

conformational and reaction (i.e., isomerization and bond breaking) coordinates, and

the bottom shows the nomenclature of the associated counterparts. The higher

points on the PES are the saddle points, commonly referred to as transition states and activation barriers/complexes. Saddle points are also occasionally termed interconversion barriers in the case of isomerization processes. These points on the PES designate the minimum energy required for a molecule to transition from one molecular configuration (minimum) to another on the PES.
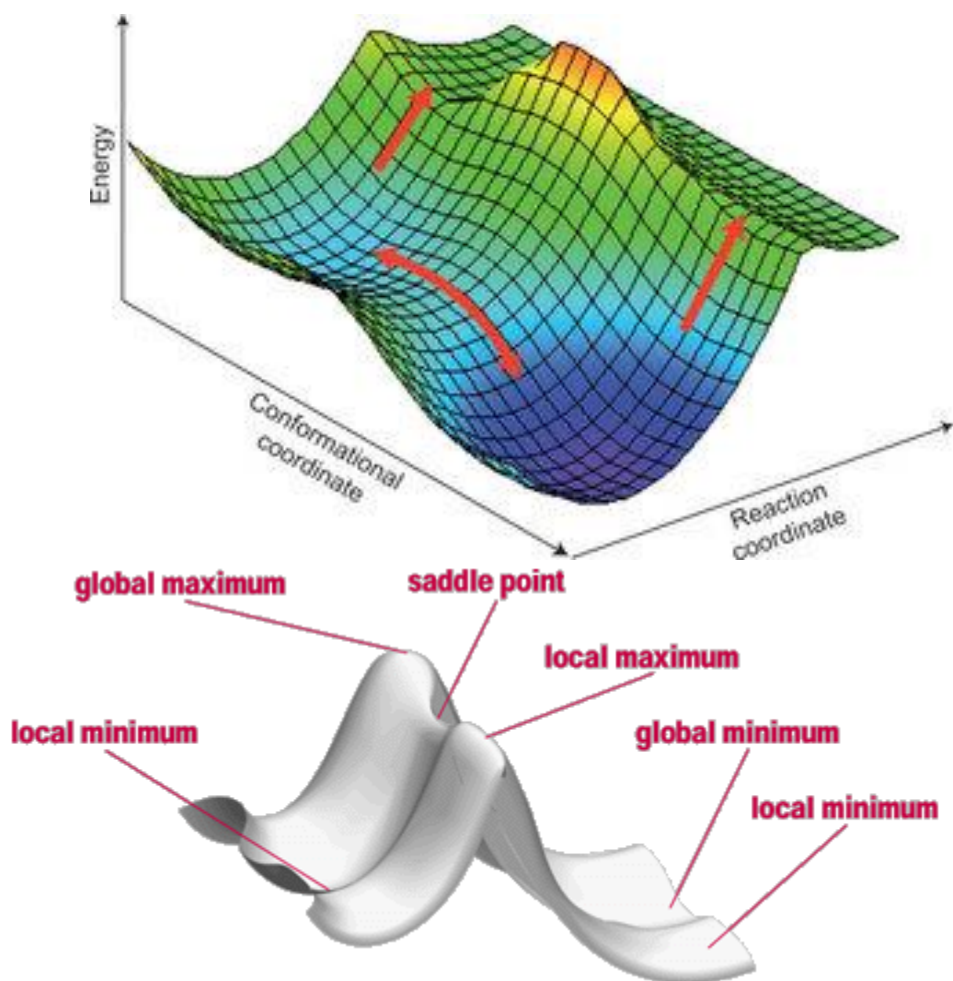


**Figure 2.1c:** Top: A sample 2D potential energy surface, showing potential energy as a function of conformational change and isomerization or dissociation.[4] Bottom image: The labeled pieces of a PES containing more than one local minimum.[5]
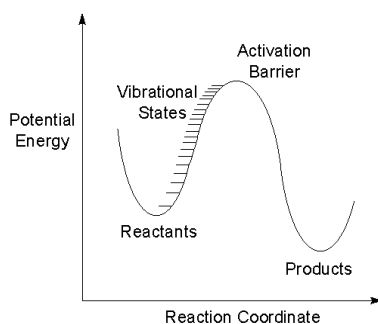
**Figure 2.1d:** A 1D PES displaying the potential energy necessary for vibrational excitation and crossing of a saddle point on a specific reaction coordinate to generate products.[6]

In the event that there is a barrier to dissociation, Figure 2.1a can instead be represented by Figure 2.1d. In this case, the products are fragments resulting from dissociation. The bond dissociation energy (BDE) is equal to the energy, or the "height", of the activation barrier. Note that the reaction coordinate as shown in Figure 2.1d is not limited to dissociation. Figure 2.1e shows a typical PES representative of conformational changes and isomerization that can result with an increase in energy.
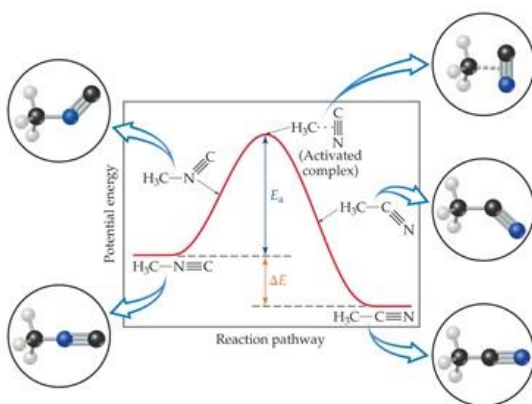


**Figure 2.1e:** Energy profile for methyl isonitrile isomerization.[7]

22

Here, methyl isonitrile isomerizes to acetonitrile over a specific saddle point, where the structure and energy are determined via computational analysis of the PES.

## 2.2 Ionization

Mass spectrometry is useful for studying ions in the gas phase. Mass spectra obtained relate ion signals to the mass-to-charge ratio (*m/z*).[1] These spectra enable the analysis of ion-neutral relationships and fragmentation pathways of ions, that continues to be valuable in environmental analysis, clinical applications, forensics, and more.[8]

The sample is typically diluted into a gas phase mixture and then ionized using one of a variety of methods. The ions are then separated by mass-to-charge ratio. Dependent upon the resolution capabilities and settings, each *m/z* in the spectra can be distinguished.

For ionization to occur, the neutral molecule in its ground state must absorb energy equal to, or in excess of, the amount required for electron removal. This is known as the ionization energy (IE).[9] This concept is quite clear atomically, as the trends on the Periodic Table of Elements are well-known and described by the influences of effective nuclear charge and the number of electrons in outermost orbital. Ionization energies are more complex for molecules in that specific bonds possess different electronic characteristics. Sigma bonds, for example, are less favorable locations for electron ejection than pi bonds. For this reason, the ionization energies for diatomic molecules are higher than for molecules which can stabilize the

charge more easily.[10] Molecules possessing a lone pair of electrons typically exhibit lower ionization energies than those without, as these sites are good locations for electron removal.

The methods of ionization can vary from bombarding molecules with a beam of electrons (electron ionization) or, alternatively, photons (photoionization).

## 2.2.1 Electron Ionization

Electron ionization (EI) involves bombarding the gaseous neutral molecules with high-energy electrons, which transfers some energy to the neutral.[11] If the transferred energy is sufficient, the neutral (M) will ionize to form a molecular positive radical ion ($M^{+\cdot}$):

$$M + e^- \rightarrow M^{+\cdot} + 2e^- \tag{2.2.1}$$

The particles ($M^{+\cdot}$) are then accelerated into a magnetic field where their trajectories are bent. The degree to which they are bent is dependent upon the inertia of the molecular ion, which is directly contingent upon its mass (Figure 2.2.1a).

EI are most frequently obtained between 60 – 80 eV because ionization cross section vs. electron energy spectra typically plateau around 70 eV (Figure 2.2.1b). The ionization cross section describes the probability of ionization and is elaborated in section 2.2.3.

In the case of methane, results are most agreeable around 60 eV. The variations of the cross sections do not change substantially within this energy range or 60 – 80 eV.
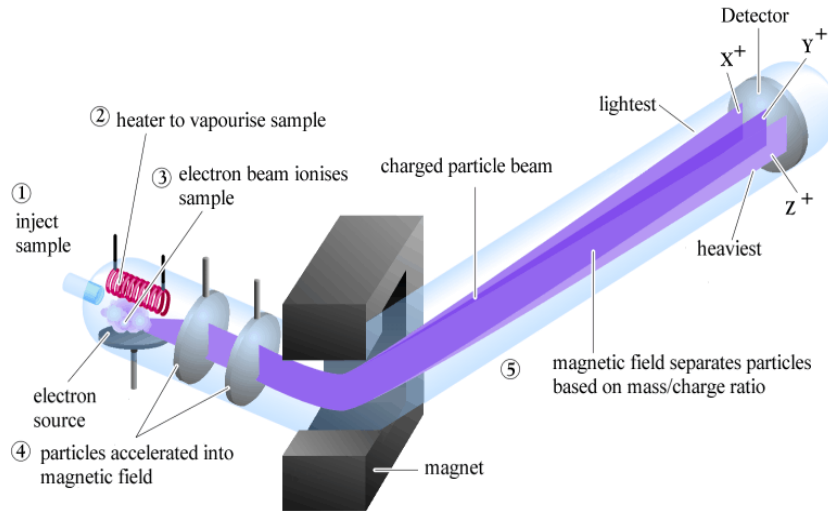


**Figure 2.2.1a:** The general schematic of an electron impact apparatus.[12]
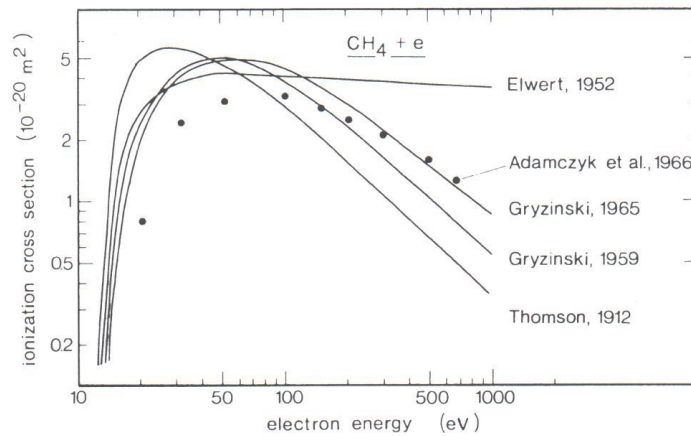


**Figure 2.2.1b:** The ionization cross sections of methane collected from electron impact (EI) experiments. Ionization cross sections are least affected by changes in electron energy within the range of 60 – 80 eV.[1]

## 2.2.2 Photoionization

The absorption of a photon can also eject an electron in a process known as photoionization:

$$M + hv \rightarrow M^{+\cdot} + e^-$$ (2.2.2a)

In equation 2.2.2a, M is again the neutral species in a dilute gaseous mixture and $M^{+\cdot}$ is the molecular cationic radical that results. Planck's constant is represented by $h$ and $v$ is the frequency of the light. The Planck-Einstein relationship of equation 2.2.2b simplifies $hv$ as the energy, E, of the photon used for ionization:

$$E = hv$$ (2.2.2b)

If the energy of the photons is equal to the IE of the molecule, in theory ionization should take place as shown in equation 2.2.2a. However, at energies very close to the ionization energy of the molecule, the probability of ionization is low. This probability is described as the ionization cross section.

## 2.2.3 Photoionization Cross Sections

An electron is released by the absorption of one photon, in which case the probability that the electron will be ejected is directly proportional to the number of photons, which come into contact with the molecule. Equation 2.2.3a relates number of photons absorbed per unit time (power) to the incident flux from states i to j:

$$\sigma = \frac{P}{I} = \frac{\pi^2 c^2}{n_\omega \omega_{ij}^2} T_{ij}$$ (2.2.3a)

where σ is the photoionization cross section, P is the power, I is the intensity, c is the speed of light, $n_\omega$ is the average number of photons in the beam, and ω describes the frequency interval.[13, 14] The transition probability, $T_{if}$, can be determined using Fermi's Golden Rule as:

$$T_{ij} = \frac{4\pi^2}{h} \left| M_{ij} \right|^2 \rho_j \qquad (2.2.3b)$$

and $\rho_j$ is the density of final states, while $M_{ij}$ is the Matrix element of the electric dipole momentum. The Matrix element for continuous wave functions, Ψ, is represented by:

$$\left| M_{ij} \right|^2 = \Sigma_i \Sigma_j \left| \int \Psi^*_j \Sigma_\mu \Psi^*_i dv \right|^2 \qquad (2.2.3c)$$

The photoionization cross section as a function of the frequency, v, of the photon beam can be rewritten as

$$\sigma_v = \frac{8\pi e^2}{3 c g_i h v'} \left| M_{ij} \right|^2 \qquad (2.2.3d)$$

where hv' represents the energy of photons above the ionization energy of the molecule, and $g_i$ is the statistical weight factor of the initial state.[13, 15] Thus, the photoionization cross section is commonly referred to as the probability in which the molecule will ionize when in contact with a photon beam of particular frequency.

However, at energies close to the ionization energy of the molecule, the efficiency of the ionization is close to zero and very few neutral molecules are ionized at the ionization threshold. Wigner's[16] threshold law suggests that attractive Coulomb potentials create a "zone" just above the ionization threshold where the local

27

wavelength of the wavefunction's oscillations is not dependent on hv', and the Coulomb potential dominates over the kinetic energy of the electron.[17] For electron impact ionization experiments where an electron is added to the system, Wannier's[18] classical theory uses the attraction and repulsion of ions and electrons to explain that the electrons must depart in opposite directions from equal distances from the ion and with the same speeds.[15]

Once the kinetic energy is enough to surpass the Coulombic zone, the ionization efficiency increases as energy is added in excess of the IE of the molecule. Each molecule behaves differently with respect to increasing photon energy, and thus the photoionization efficiencies are unique from compound to compound. If data is taken over a range of photon energies, then a spectrum of the detected ion intensity as a function of increasing energy can be generated to give the molecule's unique photoionization efficiency curve (PIE). These curves are described in greater depth in section 2.2.5. The increasing efficiency of ionization is directly related to the area through which the electron must travel to interact with the neutral species, known as the photoionization cross section of the molecule.[1]

The cross sections cannot easily be predicted accurately using *ab initio* or other computational techniques, though there are many studies that use different approximations to arrive at values for different molecules.[19-22] Alternatively, many scientists are able to determine absolute photoionization cross sections experimentally. This requires the use of a standard where the photoionization cross sections are well-known and published, as shown in equation 2.2.3e:

$$\sigma_T(\mathrm{E}) = \frac{S_T(E)\sigma_s(E)\delta_s C_s}{S_s(E)\delta_T C_T} \qquad\qquad (2.2.3e)$$

In the above equation, at each specific photon energy the signal of the standard $S_T$ and its known cross section $\sigma_T$ can be used along with the signal of the sample $S_S$, the mass discrimination factors ($\delta_T$ and $\delta_S$), and the concentration of samples $C_T$ and $C_S$) to arrive at the photoionization cross section for the sample $\sigma_T$. Photoionization cross sections are reported in units of $10^{-18}$ $cm^2$, more commonly referred to as megabarns (Mb).

The values for the photoionization cross sections of propene are available in literature[23] and studies have utilized these values in the determination of cross sections of various molecules.[24, 25] For those molecules where the ionization energy is lower than that for propene (approximately 9.7 eV[26]) and the photoionization cross-sections are not available for use, an average scaling factor[27] can be used, which can be found as the ratio of a known photoionization cross-section of propene to the experimental signal at a particular energy, $\sigma_s(E)/S_s(E)$. These scaling factors can be taken across a range of energies and then averaged to be used in equation 2.2.3e. Typically, research done in Professor Meloni's group at USF utilizes a calibration gas ("calgas") mixture of ethane, propene, and butene when obtaining absolute photoionization spectra.

## 2.2.4 Adiabatic vs. Vertical Ionizations

Of course, the structure of the molecule greatly influences the photoionization process. When a molecule is exposed to electromagnetic waves (visible light, for

example), oscillations can occur. The probability that these frequency-induced oscillations lead to a transition from one eigenstate Ψ' to another eigenstate Ψ" is given by equation 2.2.3c, where $M_{ij}$ is the electric dipole moment operator:

$$M_{ij} = \int \Psi_i\, \mu\, \Psi_j d\tau \tag{2.2.4a}$$

Throughout the transition, the Born-Oppenheimer approximation suggests that the nucleus and electrons possess equal momentum.[28, 29] Since momentum is contingent upon both the mass and velocity of the object, the approximation uses the large mass of the nucleus to justify its inertia and negligible velocity. Alternatively, the velocity of the electron is very fast. Thus, the factorization of the wavefunction into electronic and nuclear (vibrational and rotational) components enables them to be solved independently:

$$\Psi_{molecule} = \Psi_{electron}\, x\, \Psi_{nuclei} \tag{2.2.4b}$$

The Franck-Condon principle expands on the vibrational transition of the molecule from eigenstates $\Psi'_0$ to $\Psi''_v$, where $\Psi'_0$ refers to the neutral molecule in its vibrational ground state and $\Psi''_v$ denotes the molecular radical cation in vibrational state v. The Franck-Condon principle makes the assumption that the nucleus remains stationary, as the electronic transitions occur much faster than nuclear movement. In this case, the bond lengths and angles within the molecule are sustained throughout the ionization process, and the vibrational transition from the neutral ground state $\Psi'_0$ to cationic state $\Psi''_v$ is commonly described to be vertical (Figure 2.2.4a). If the nucleus is considered to be static, then the combination of

equations 2.2.4a and 2.2.4b leads to the transition moment integral with the electronic (first integral) and vibrational overlap (second integral) components:

$$M_{ij} = \int {\Psi''}^{*}_{el}\, \mu_{el}\, \Psi'_{el}\, d\tau_{el} \int \frac{S''^{*}_{vib} S'_{vib}}{R^2} R^2\, dR \qquad (2.2.4c)$$

where $S''_{vib}$ and $S'_{vib}$ are the vibrational wave functions for the cation and neutral electronic states.[15, 30]

The probability that a molecule will transition from the neutral ground state $\Psi'_0$ to a vibrational level of the ion $\Psi''_v$ is defined as its Franck-Condon factor, which takes into account the vibrational overlap between the eigenstates, and is represented in equation 2.2.4b.[1]

$$\text{Franck-Condon Factor} = \left| \int \Psi'_v \Psi''_v\, dR \right|^2 \qquad (2.2.4d)$$

The FC factor is also the square of the vibrational overlap integral of equation 2.2.4c.

Vertical ionization is accompanied by vibrational excitation as the geometry of the neutral is not a local minimum on the cationic potential energy surface (PES). The geometric variation between the local minimum on the cationic PES and the corresponding global minimum on the neutral PES is evident in the displacement of the nuclei, r. The greater the internuclear distance, $r_0$ to $r_1$, the poorer is the vibrational overlap between states, as shown in Figure 2.1.4a.

In order for the vibrational transition to have a large contribution to the transition moment in equation 2.2.4c, the overlap of the orbitals must be very strong (i.e., the stabilized geometry of the cation must be similar to the geometry of the neutral). The stronger the overlap, the closer the molecule's vertical ionization is to

an adiabatic ionization, which is defined as the energy difference between the cation and neutral where both are in their vibrational ground states (Figure 2.2.4b).
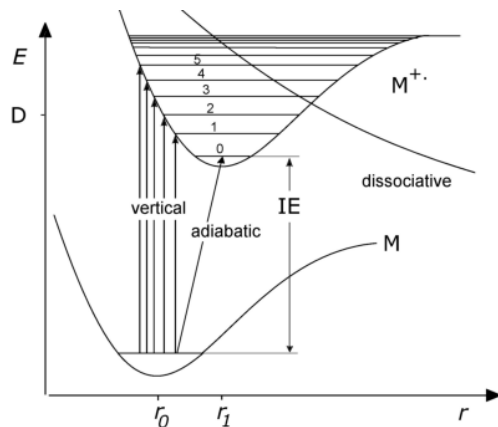


**Figure 2.1.4a:** A general representation of the vertical and adiabatic ionizations as they relate to internuclear distance between the neutral ($r_0$) and cationic ($r_1$) nuclei.[1]

The $\Psi'_0$ to $\Psi''_0$ transition is commonly denoted as $0 \leftarrow 0$ and the equation for the adiabatic ionization energy is shown in 2.2.4c:

$$AIE = E(\Psi''_0) - E(\Psi'_0) \qquad (2.2.4c)$$

When a neutral sample is ionized by a source of light, the electrons can be detected and separated by their kinetic energy (eKE) using velocity map imaging (VMI), and the eKE is directly related to the binding energy (BE) of the electron ($hv$ is the energy of the photons):

$$eKE = hv - BE \qquad (2.2.4d)$$

The intensity of electrons detected as a function of their kinetic energy can be represented in a photoelectron spectrum (PE spectrum), as shown in the inset of Figure 2.2.4b. The vertical ionization of the hydrogen molecule ($H_2$) is a $2 \leftarrow 0$

32

transition, and as a result the most intense band in the PE spectrum corresponds to the electronic kinetic energy of the $\Psi''_2$ vibronic state. The initial onset of the PE spectrum represents the $0 \leftarrow 0$ transition, equal to the AIE, if the overlap of states (Franck-Condon Factor) is decent enough to witness the band experimentally.
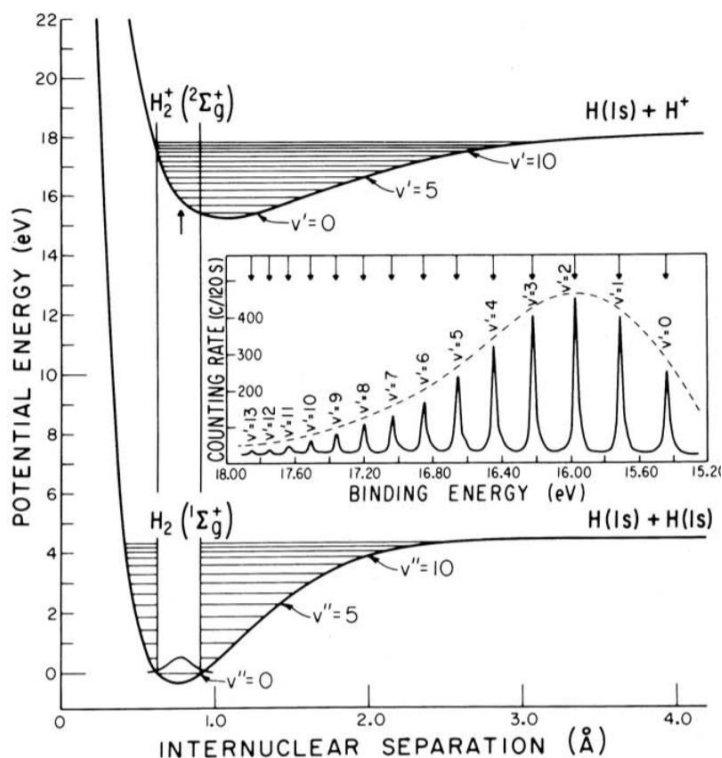


**Figure 2.2.4b:** Diagram showing the relationship between the Franck-Condon factor of $H_2$ and its photoelectron spectrum (inset). The overlap of orbitals in cationic and neutral states are good enough to witness the peak corresponding to the adiabatic ionization energy (AIE) at $\Psi''_0$. The most intense peak corresponds to the vertical $2 \leftarrow 0$ transition.[31]

Thus, quite an extensive amount of information can be provided on the structure and bonding of the material studied, and several investigations have been conducted using photoelectron spectroscopy as a means to determine these

characteristics.[32, 33] Negative ion spectroscopy uses the similar theory, but involves the ejection of the electrons from anionic species to generate neutrals. It has proven to be valuable in obtaining structural and bonding information of neutral species.[34, 35]

## 2.2.5 Photoionization Efficiency Curves (PIEs)

The number of ions is dependent upon the molecule's photoionization cross section at each particular energy (section 2.2.3). The intensity of the ions detected at each photon energy can be plotted as the molecule's photoionization efficiency (PIE) curve. Thus, PIE curves are directly related to the photoionization cross sections.

The PIE curve of a molecule is also related to its PE spectrum. Because a molecule's PE spectrum shows the relative intensity of electrons detected at particular kinetic energies, and since the relation of photon energy to eKE is known (equation 2.2.4b), the PIE curve can be easily obtained from the PE spectrum through integration.

Just as the photoelectron spectrum for each particular molecule is unique in that it accounts for Franck-Condon factors and adiabatic ionization energy, it falls to reason that PIE curves are also unique from one molecule to another. Figure 2.2.5a shows the absolute PIE curve (blue) obtained by Ng et al.[36] used as a standard to match a suspected product of mesitylene phootoxidation (red circles) of $m/z$ = 134. The onset (AIE) of both spectra matches agreeably, as well as the shape of the curve. Thus, it was proposed that the observed product was indeed 3,5-dimethylbenzaldehyde (the pathway to formation was also shown to be energetically favorable in their investigation).
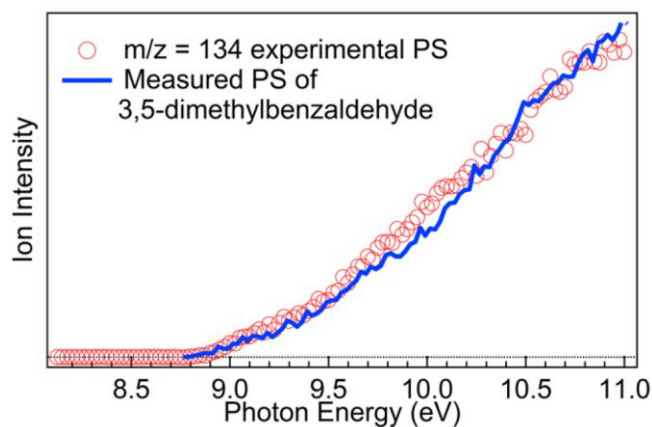
**Figure 2.2.5a:** The measured PIE curve of unknown product at *m/z* = 134 resulting from a photooxidation experiment (red circles) compared to the measured PIE curve of a 3,5-dimethylbenzaldehyde standard.[36]

While the case in Figure 2.2.5a seems simple, often times there may be isomers present with a particular *m/z*, as was found in the photooxidation reaction of *tert*-amyl methyl ether at *m/z* = 58 (Figure 2.2.5b).[37]

In this scenario, the total signal of photoionization is due to the contribution of both isomers. Since the PIE curve for each isomer is directly related to its respective photoionization cross sections, then the fractional abundance (A) of each can be found if the photoionization cross sections are known.[38] The following equations show the relationship:

$$A_1 + A_2 + A_3... = 1 \tag{2.2.5a}$$

$$\sigma_{Total} = A_1\sigma_1 + A_2\sigma_2 + A_3\sigma_3... \tag{2.2.5b}$$

In these types of photooxidation reactions presented, it is typically rare to have three or more isomers. However, Figures 2.1.5a and 2.1.5b underscore the ability to identify ions detected from reactions based on their PIE curves.
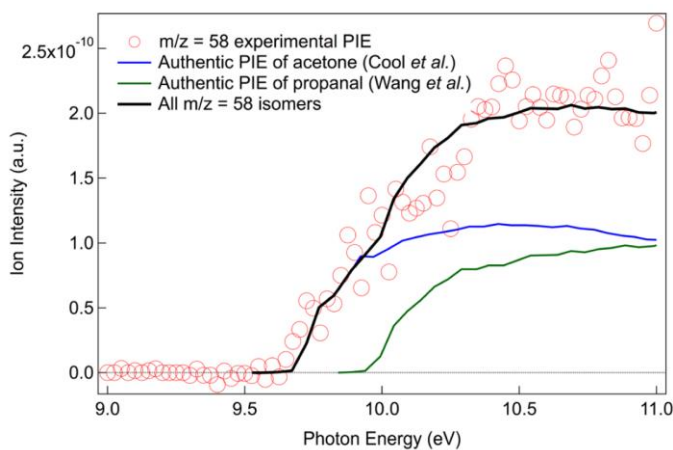


**Figure 2.2.5b:** Experimental PIE (red circles) of *m/z* = 58 product from *tert*-amyl methyl ether photooxidation[37] matched with literature PIE from Cool et al.[38] and Wang et al.[39]

## 2.3 The Cationic Potential Energy Surface

2.3.1 Isomerization and Unimolecular Dissociation Basics

As described in section 2.2.4, when a molecule is excited by an electromagnetic wave, oscillations can be induced. If the frequency of the electromagnetic wave is greater than the energy required to remove an electron from the neutral, the molecule will be ionized and will exist in the cationic state as a radical if the cationic state is bound. Some species do not have a bound cationic ground state and dissociatively ionize at the threshold.

36

To expand on Figure 2.2.4a further, the geometry of the neutral plays a large role in the immediate structure of the cation close to the ionization threshold since the ionization process is very fast with respect to any nuclear or bond shifting. When a vertical transition occurs, the resultant cation can exist on the PES in a specific vibronic state that has a geometry very similar to the neutral. The associated local minimum may not necessarily be the global minimum on the cationic PES. On the cationic PES there may be rotational and isomerization barriers that are accessible with vibrational excitations as a result of increasing photon energy.

In Figure 2.3.1a, for example, the PES shows the isomerization pathways of both cis and gauche conformations of cationic propanal, where the filled circles represent the Franck-Condon points with the respective neutral conformations.[40] There is a small interconversion barrier between gauche and cis forms in the charged state, and propanal is able to restructure from one to another if the appropriate amount of excess energy is available. Interestingly, when enough energy is available for dissociation, Kim et al.[40] have reported that the ultrafast dynamics of propanal in the excited state occur in the isolated regions on the potential energy surface, and thus the interconversion is not competitive with the dissociation process and conformer-specific products are formed as a result. At these higher energies, propanal is also able to isomerize prior to unimolecular dissociation, as shown in Figure 2.3.1b. Isomers have been reported as intermediates in various *ab initio* and experimental photodissociation studies.[41-43]
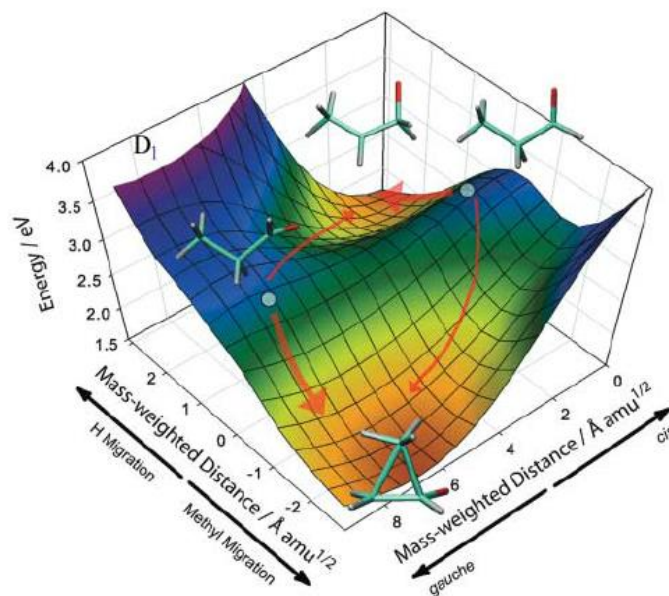
**Figure 2.3.1a:** Two-dimensional diagram of the propanal cation pathways from the Franck-Condon point (solid circle for the cis and gauche conformer).[40]
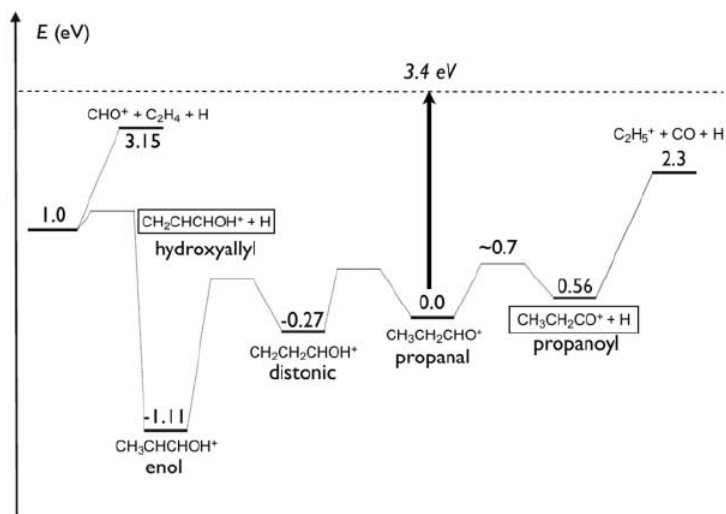


**Figure 2.3.1b:** Energy-level diagram for isomers and products of propanal cation dissociation (relative energy, E, to the cation ground state).[40]

Regardless, if photon energy increases and the ions possess sufficient internal energy, they can fragment in a process known as photodissociation.[44]

$$AB + h\nu \rightarrow AB^{+\cdot} \rightarrow A^+ + B^\cdot \qquad (2.3.1a)$$

$$AB + h\nu \rightarrow AB^{+\cdot} \rightarrow A^{+\cdot} + B \qquad (2.3.1b)$$

The first step of equation 2.3.1a and 2.3.1b is identical to the ionization equation 2.2.2a, where the neutral molecule M is replaced with AB here for simplicity. The molecular radical ion $AB^{+\cdot}$ is commonly referred to as the parent ion, while the detected cationic fragment $A^+$ is known as the daughter ion. Note that the dissociation of a molecular cation radical will lead to one cationic fragment and one neutral. Either a neutral radical fragment (equation 2.1.6a) or a neutral molecular fragment (equation 2.3.1b) is released, depending on the dissociation dynamics. As mass spectrometers are only able to detect ionic species, the neutral fragment is never detected in mass spectroscopy.

If there is no barrier to dissociation, as shown in Figure 2.3.1b, the energy required to form the fragment products is known as the bond dissociation energy (BDE) and can be calculated using the following relationship:

$$BDE = E_{fragments} - E_{parent} \qquad (2.3.1c)$$

In this case, the pathway is "uphill" and the energy at which the first detection of daughter ions occurs is simply equal to the BDE above the molecule's AIE:

$$AE = BDE + AIE \qquad (2.3.1d)$$

AE is the appearance energy of the cationic fragment, also often denoted as $E_0$.[44, 45]
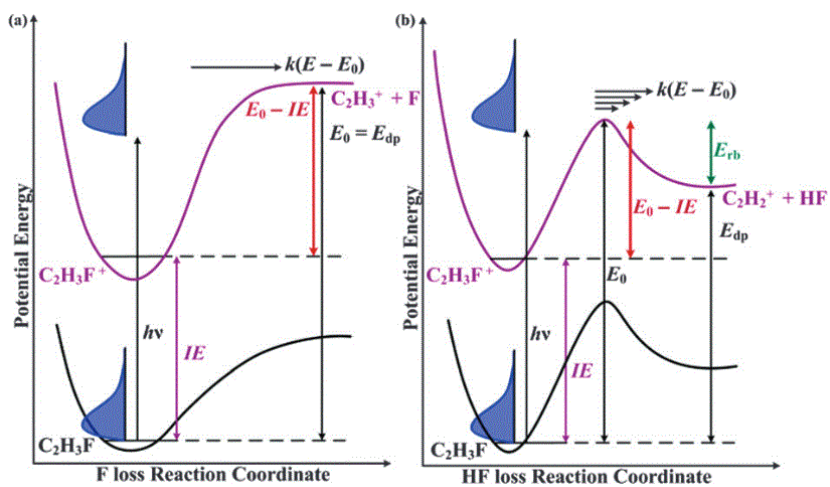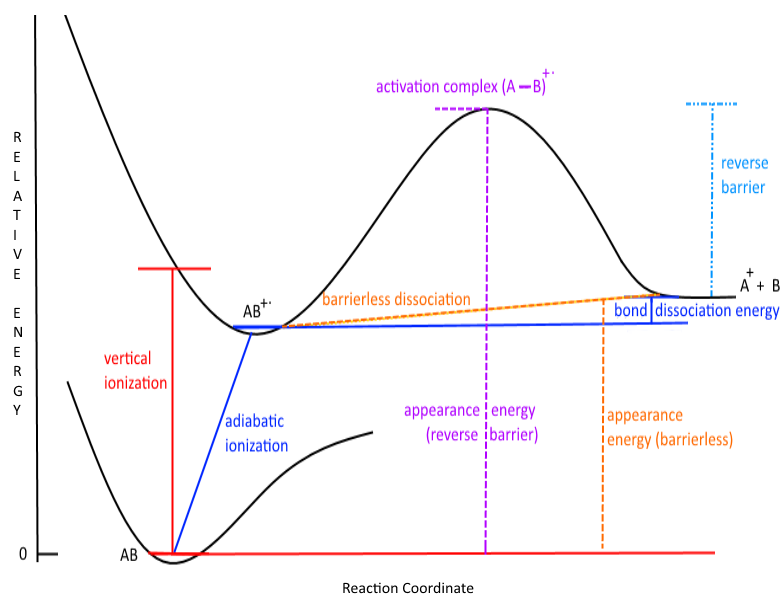
**Figure 2.3.1b:** Top: Diagram showing appearance energy determination with and without reverse barriers using terms described in this thesis. The figure was recreated based on information compiled from various sources.[1, 44-46] Bottom: Energy diagram for F-loss from $C_2H_3F^{+.}$ without reverse barrier (left) and HF-loss from $C_2H_3F^{+.}$ *with* a reverse barrier (right).[45] $E_0$ is 0 K appearance energy and $E_{rb}$ represents the energy of the reverse barrier.

## 2.3.2 Photodissociation and Thermodynamics

Thermodynamics can be coupled with the experimentally-derived AEs to provide useful thermochemical information regarding either of the fragments or the neutral molecule itself.[47, 48] The total enthalpy of the dissociation reaction is effectively equal to the AE and can be represented by:

$$\Delta H_{0K} = \Delta_f H^{\circ}_{0K}(A^+) + \Delta_f H^{\circ}_{0K}(B^{\cdot}) - \Delta_f H^{\circ}_{0K}(AB) \qquad (2.3.2a)$$

If heats of formation of two of the three species involved in photodissociation are well-known, the third can be determined as a result.[47] Equation 2.3.2b represents the relationship between the appearance energy (effectively the heat of the reaction) and heats of formation of species involved when there is no barrier to dissociation:

$$\Delta_f H^{\circ}_{0K}(A^+) = AE - \Delta_f H^{\circ}_{0K}(B^{\cdot}) + \Delta_f H^{\circ}_{0K}(AB) \qquad (2.3.2b)$$

Many vacuum ultraviolet photoelectron spectroscopy (VUVPES) experiments and photoelectron photoionization coincidence spectroscopy (PEPICO) experiments measure appearance energies at 0 K, while literature values are typically reported at 298 K. Thus, the conversion between 0 K and 298 K enthalpies is necessary:

$$\Delta_f H^{\circ}_{0K} = \Delta_f H^{\circ}_{298K} + \Sigma(H^{\circ}_{298K} - H^{\circ}_{0K})_{elements} - (H^{\circ}_{298K} - H^{\circ}_{0K})_{molecule} \qquad (2.3.2c)$$

In equation 2.3.2c, the $H^{\circ}_{298K} - H^{\circ}_{0K}$ values are known for the elements[49] and the heat content functions corresponding to small molecules can be calculated theoretically using statistical thermodynamic expressions. The calculations are elaborated in-depth in a following section.

If the dissociation channel possesses a barrier, then the AE of the cation is determined by:

$$AE = BDE + AIE + \text{reverse barrier} \qquad\qquad (2.3.2d)$$

The reverse barrier is effectively the energy difference between the sum of the product fragments and the transition state (TS) that leads to dissociation. More formally, the reverse barrier is described as the activation energy of the reverse reaction.[1] The AE can be simplified in equation 2.3.2e where $E(A \text{--} B)^{+\cdot\ddagger}$ is the energy of the activation complex and $E(AB)$ is that of the neutral species. This results in the relative energy, or height, of the dissociation barrier to the neutral species, which is the total energy necessary in order for the fragment to form (or, experimentally "appear").

$$AE = E(A - B)^{+\cdot\,\ddagger} - E(AB) \qquad\qquad (2.3.2e)$$

## 2.3.3 Detecting and Visualizing Fragments

In photoionization mass spectrometry, the fragment ion intensities are detected as a function of photon energy. The PIE curve of the parent ion is measured and the adiabatic ionization energy, as well as the appearance energy of each daughter ion, can be determined using an exponential function $1\text{-}e^{bE}$ as described by Ruscic and Berkowitz.[50] The relative difference between the AIE of the parent molecule and the AE of the daughter ion provides insight to the energy required for photodissociation, as described in the previous section by equation 2.3.2d. Depending upon the calculated energies of the fragments, it is possible to predict if a dissociation channel possesses a barrier or not.
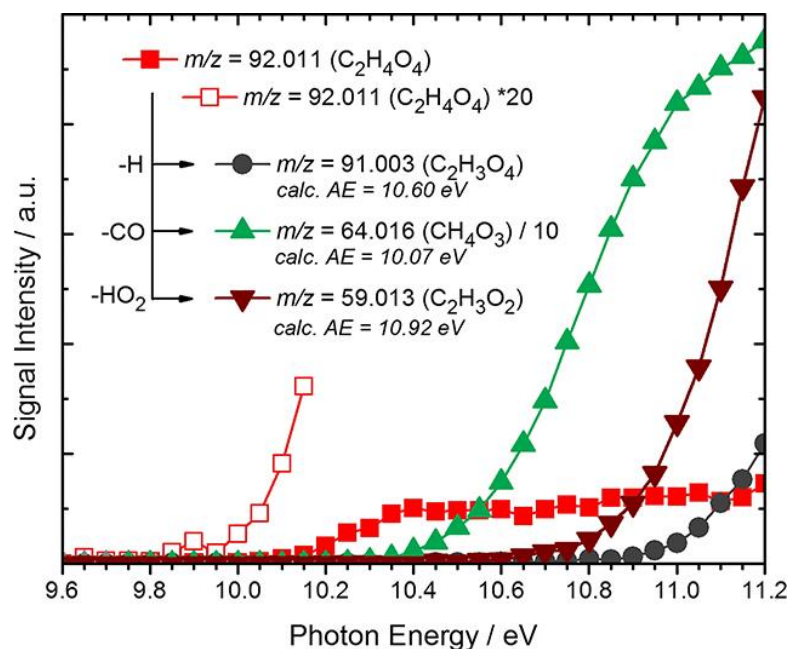
**Figure 2.3.3a:** The parent ion, $C_2H_4O_4^{+\cdot}$, and the three daughter ions that result from photodissociation via H-loss, CO-loss, and HO2-loss channels.[51]

Studies have used synchrotron photoionization mass spectrometry as a method to observe and identify fragments, as well as report possible mechanisms for molecular photodissociation.[24, 52] Figure 2.3.3a is a representation of the photoionization of dimethyl ether (red boxes) and the three daughter ions that are detected.[51] The approximate AEs were determined and fragments were assigned.

Breakdown diagrams are considered to be more useful, and are therefore more prevalent in the analysis of photodissociation processes. These diagrams, much like one shown in Figure 2.3.3b, are plots of the fractional abundance of each ion detected as a function of photon energy. Theoretically, these can be generated by photoionization mass spectrometry, but it is much more powerful in PEPICO (photoelectron photoion coincidence) spectroscopy experiments. In these

43

experiments, both the ions and the ejected photoelectrons are detected in coincidence. The electron and ion signals serve as the "start" and "stop" parameters for the ion time-of-flight distributions, which provide useful kinetic information.
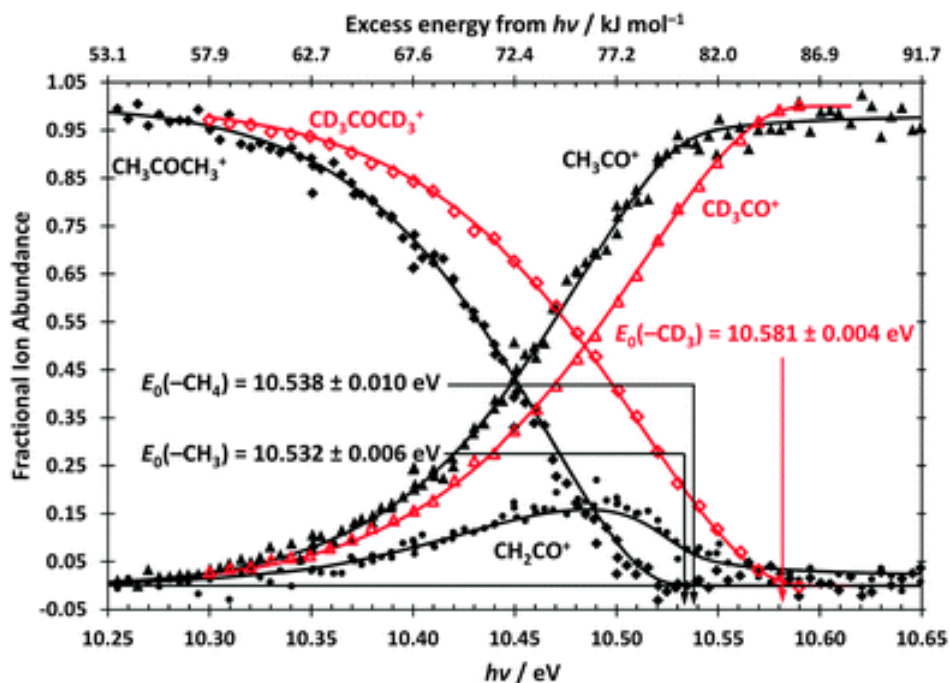


**Figure 2.3.3b:** Breakdown diagrams generated from PEPICO experiments of $CH_2COCH_3^{+\cdot}$ (black) and $CD_2COCD_3^{+\cdot}$ (red) photodissociation.[53]

Sophisticated computational software, such as MiniPEPICO,[54] calculate necessary density and number of states functions, as well as internal energy distributions to yield a breakdown diagram that can be modeled with the experimental data.
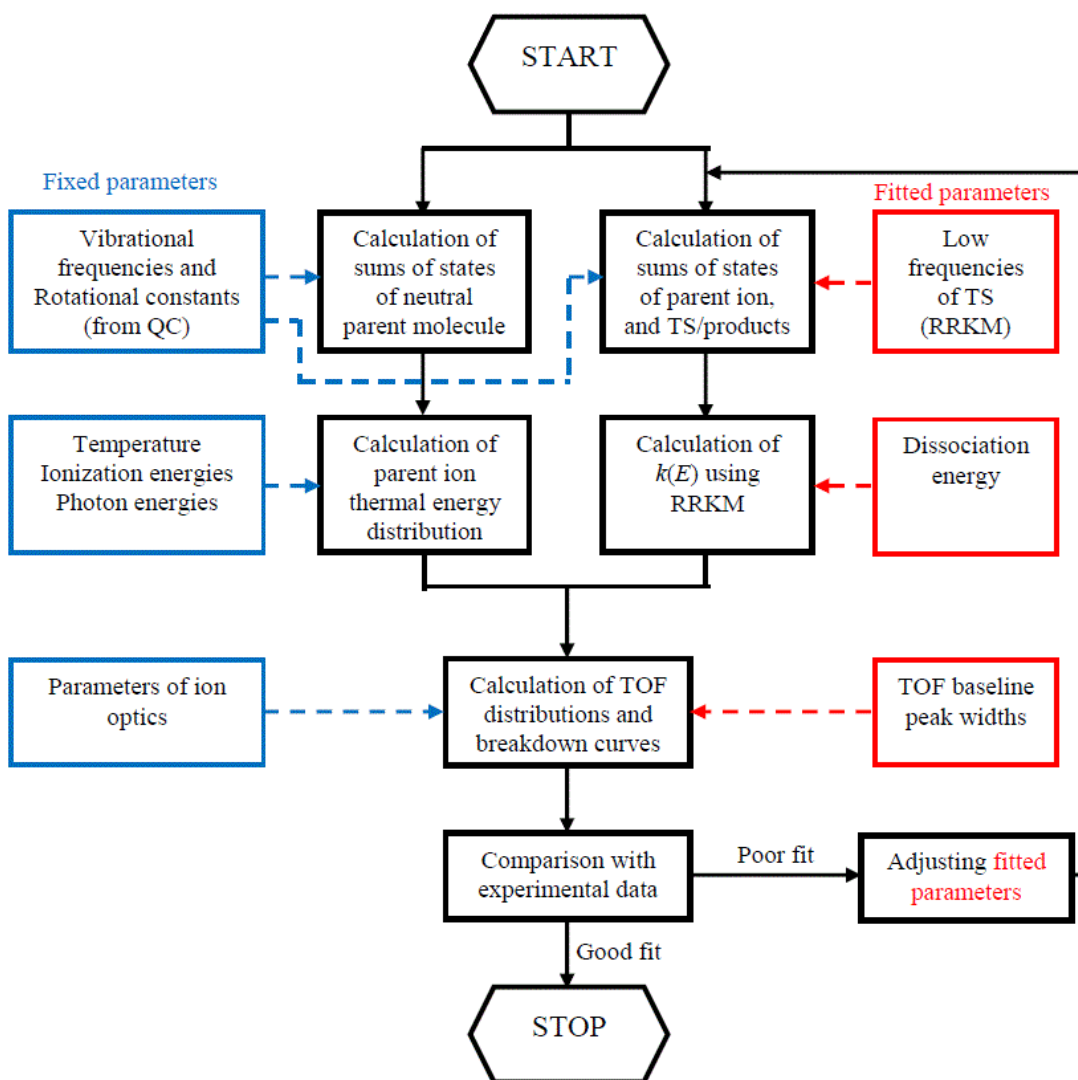
**Figure 2.3.3c:** A block diagram showing the parameters taken into account to model unimolecular reactions.[55]

The process by which MiniPEPICO obtains accurate bond dissociation energies is shown in Figure 2.3.3c. MiniPEPICO enables the experimental dissociation rates to be extracted using Rice, Ramsperger, Kassel, and Marcus's RRKM theory[56-58], as well as the variational transition state theory (VST),[59] and

simplified statistical adiabatic channel model (SSACM).[60] The RRKM rate constant as a function of internal energy (E) is given by

$$k(E) = \frac{\sigma N^{\ddagger}(E - E_{\mathrm{o}})}{h \rho(E)} \qquad (2.3.3)$$

where $N^{\ddagger}(E - E_0)$ is the number of states of the TS at excess energy above the dissociation barrier $E_0$, $\rho(E)$ is the density of states of the molecule, $h$ is Planck's constant and σ corresponds to the reaction degeneracy.[55] The statistical approach to this theory has been described in great detail.[60, 61]

## 2.4 Computational Approaches and Applications

The potential energy surfaces (PES) described in section 2.1 describe changes in energy as a result of molecular orientation. The Born-Oppenheimer approximation suggests that the electronically adiabatic energy (E) is determined by

$$E = T_R + V_{NR}(R) + E_\gamma^{(el)}(R) \qquad (2.4a)$$

where R is the 3N − 6 independent coordinate set, $T_R$ is the nuclear kinetic energy, and $V_{NR}(R)$ and $E_\gamma^{(el)}(R)$ are the nuclear Coulombic repulsion energy and electronic energy.[62] When the molecule is in the electronic ground state, the quantum number (γ) is equal to 1. In this case, the potential energy for nuclear motion is:

$$V(R) = V_{NR}(R) + E_1^{el}(R) \qquad (2.4b)$$

Since $E_\gamma^{(el)}$ is an eigenvalue of the electronic Hamiltonian, the PES can be obtained by theoretical electronic structure calculations.[62]

When computations terminate successfully, the input structures are "optimized" to fall to a local minimum on the PES. It should be noted that all minimization algorithms are able to find local minima based on input geometry, however there is never a guarantee a specific optimized structure is the global minimum. This is especially true for larger molecules, which possess substantially more degrees of freedom.

There are many computational approaches available to solve the Schrodinger equation and find minima on the PES. *Ab initio* calculations, for example, are solely based on theoretical principles and exclude any experimental influence.[62] Hartree-Fock (HF) theory is a well-known *ab initio* method, but is considered to be inaccurate in that it neglects electronic correlation. Zador et al.[63] explains simply that the "best strategy to increase the accuracy of electronic structure calculations is to balance the level of electron correlation and basis set" as described in Figure 2.4.
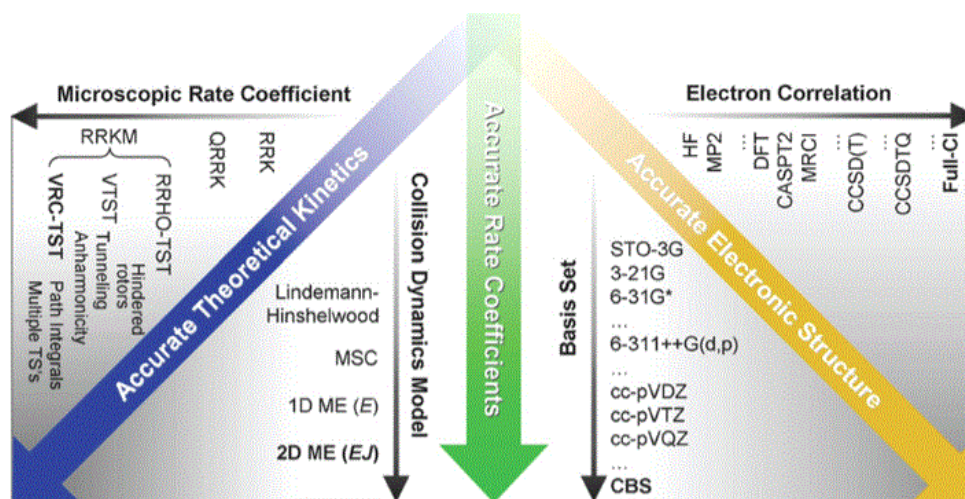


**Figure 2.4:** Diagram explaining the best computational approaches for determining accurate electronic structure calculations (right) and theoretical kinetics (left).[63]

Molecular geometries of all structures involved in the work presented in this thesis are completed using the CBS-QB3 composite method[64-66] in the Gaussian 09 software suite.[67] These energy calculations are computationally inexpensive and have quite high accuracy with a mean absolute deviation (MAD) of 1 kcal mol$^{-1}$ (or 0.05 eV).[68, 69] CBS methods are able to obtain highly accurate geometries and energies in that they extrapolate an infinitely large basis set by using a linear combination of atomic orbitals (LCAO-MO) approximations. CBS-QB3 calculations have been used to determine low-energy structures of novel superalkali monomers and clusters, for example, which may pave way for future use in an extensive number of real-world applications.[70, 71]

Although it is never known if a structure is the global minimum, it is possible to scan the PES for other local minima in search for lower-energy conformations. If another minimum is observed on the PES with a lower total energy, the original conformation is certainly not that of the global minimum. Throughout the work presented in this thesis, pertinent PES were scanned as functions of bond lengths and bond angles at the B3LYP/6-31G(d) level/basis set — both to verify as best as possible that the lowest-energy conformation was used, as well as to determine the dynamics of unimolecular or bimolecular reaction pathways.

With respect to transition state calculations, the non-real (negative) frequency corresponds to the motion over the saddle point on the potential energy surface. The approximate barriers can be found by scanning the PES along a reaction coordinate, or by using the Synchronous Transit-Guided Quasi-Newton (STQN) method

involving either QST2 or QST3 inputs.[72] [73] The energetic determination of the structure can be calculated in a similar way for maxima as they can for minima using CBS-QB3, however using the keyword opt=TS in the Gaussian input script. The imaginary frequency can be inspected using GaussView[74] and intrinsic reaction coordinate (IRC) calculations to verify direct relationships between reactant and product(s).[75, 76]

As computations are able to optimize structures in the neutral state, as well as charged states, the overlap of eigenstates can be witnessed. In which case, the optimized geometries resulting from calculations of the anion and neutral can be compared to experimental results from negative ion photoelectron spectroscopy. Analogously, the optimized structures of the neutral and cationic species can be used to simulate a photoelectron spectrum, where the Franck-Condon factor can be roughly assessed. The simulated PE spectrum can be superimposed onto an experimental spectrum to validate the identity of a species if there is a match. This is also true for photoionization efficiency curves, which can be obtained as the integration of the photoelectron spectrum (total ion signal as a function of energy), or directly from experimentation. Figure 2.4 shows an experimentally-obtained PIE curve with multiple photoelectron spectrum simulations superimposed onto the image to help determine its identity. The $CH_2OO$ (Criegee) intermediate, highly important in combustion processes, was verified via the computational PE spectrum simulation in that the onsets and shapes of the curves were very agreeable.
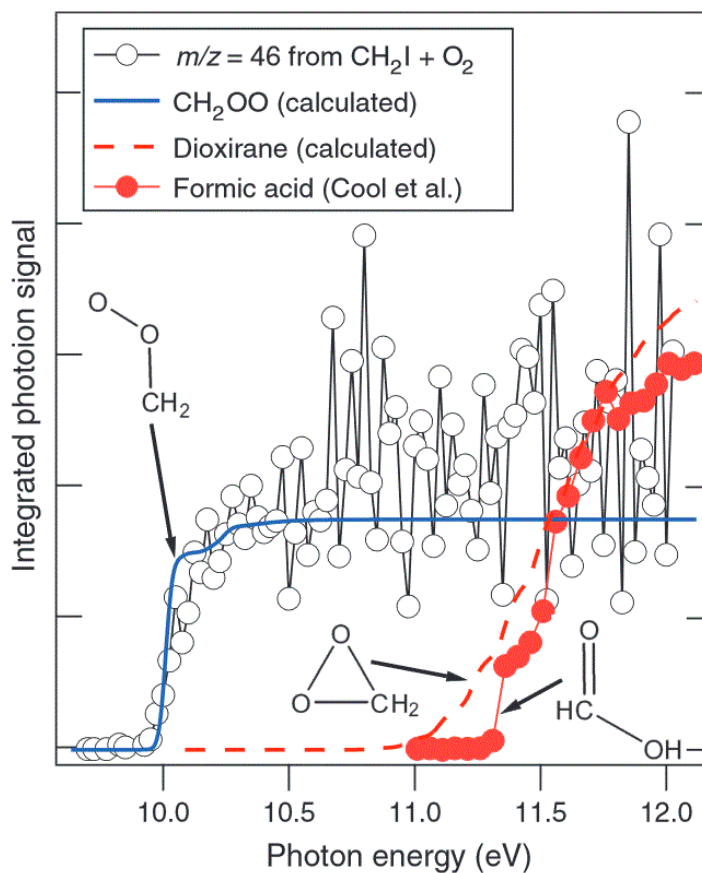
**Figure 2.4:** The experimental photoionization efficiency spectrum of the *m/z* = 46 product of $CH_2I$ with $O_2$ (black lines with open circles) compared to simulated spectra of $CH_2OO$, dioxirane, and formic acid (solid blue line, dashed red line, and red circles, respectively).[77] The calculated spectra were generated using CCSD(T)/CBS calculations.

Thermochemical calculations are especially useful in the analysis of unimolecular photodissociation reactions without reverser barriers. As described in sections 2.3.2 and 2.3.3, PEPICO experiments provide precise appearance energies of fragments resulting from photodissociation. Most PEPICO experiments are conducted at 0 K, and thus the AE is effectively the enthalpy of the reaction at 0 K

(equation 2.3.2b). Using equation 2.3.2c to convert to 298 K for comparison with literature values or to report new experimental findings, the heat content functions can be calculated for small molecules:

$$H^{\circ}_{298K} - H^{\circ}_{0K} = H_{corr} - \varepsilon_{ZPE} \tag{2.4c}$$

In the above equation, the enthalpy correction for the molecule (aka heat content function) is the difference between the thermal correction to enthalpy and the zero point energy, both of which are provided in the output file of the successfully terminated computation. Since the CBS-QB3 (0K) energy is ZPE-corrected, and the CBS-QB3 enthalpy includes the $H_{corr}$ value, these two numbers can also be used and the result is comparable to equation 2.4c.[78] This is useful in that the 0 K appearance energy can be used to determine an unknown heat of formation if the heats of formation of two of the three species in equation 2.3.2b are well-known.

However, if the heats of formation are unknown, computational analysis provides a powerful alternative. The CBS-QB3 enthalpy = X line in the Gaussian output file corresponds to a relative energy used in the determination of a heat of a reaction at 298 K:

$$\Delta H_{298K}^{(calc.)} = \Delta_f H^{\circ}_{298K}(A^+)^{(calc.)} + \Delta_f H^{\circ}_{298K}(B^{\cdot})^{(calc.)} - \Delta_f H^{\circ}_{298K}(AB)^{(calc.)} \tag{2.4d}$$

Since the calculated enthalpy of reaction can be directly compared to literature using reported heats of formations of all species involved, it is also possible to combine both literature heats of formations and calculated heat of reaction to solve for an unknown value, labeled accordingly above each term:

$$\Delta H_{298K}{}^{(\text{calc.})} = \Delta_f H^{\circ}{}_{298K}(A^+)^{(\text{unknown})} + \Delta_f H^{\circ}{}_{298K}(B^{\cdot})^{(\text{lit.})} - \Delta_f H^{\circ}{}_{298K}(AB)^{(\text{lit.})} \qquad (2.4e)$$

In this hypothetical case, the $\Delta_f H^{\circ}{}_{298K}(A^+)$ is not well-known in literature and is of interest to determine.

It is notable that this is only possible when the number and types of bonds are equal on both sides of the equation. It is best when a network of reactions is used to determine an average heat of formation for the species of interest. These types of calculations are known as isodesmic reaction calculations. A number of studies have been completed using isodesmic reaction networks, either to predict or validate experimentally measured heats of formations.[79, 80]

## 2.5 References

1. Gross, J.H., *Mass Spectrometry, 2nd ed.* 2011, Berlin Heidelberg: Springer.
2. Griffiths, D.J., *Introduction to Quantum Mechanics, 2nd ed.* 2004: Prentice Hall. 480.
3. Lower, S., *Chem1 General Chemistry Virtual Textbook*. Simon Fraser University: Barnaby/Vancouver, Canada.
4. Glowacki, D.R., J.N. Harvey, and A.J. Mulholland, *Taking Ockham's razor to enzyme dynamics and catalysis.* Nature Chemistry, 2012. **4**: p. 169-176.
5. Vasilyev, V. *Studying Chemical Reactions with Gaussian*. [cited 2015 December 4, 2015]; Available from: http://sf.anu.edu.au/~vvv900/gaussian/ts/.
6. Ommen, J.R.v. and W.F. Polik. *The Polyad Model Applied to Formaldehyde Vibrational States*. [cited 2015 December 4, 2015].
7. Brown, et al., *Chapter 12: Chemical Kinetics*, in *Chemistry The Central Science: A Broad Perspective 1st Ed.* 2003, Pearson Education Australia: New South Wales, Australia.
8. *About Mass Spectrometry*. 2012 [cited 2015 December 30, 2015]; Available from: http://www.asms.org/about/about-mass-spectrometry.
9. Oxtoby, D., H. Gillis, and A. Campion, *Principles of Modern Chemistry ed. 6*. 2007: Cengage Learning. 1104.
10. Lohninger, H., *Ionization Energies of Diatomic Molecule*, in *General Chemistry*. 2011, Epina eBook Team.
11. Peterkops, R., *Theory of Ionization of Atoms by Electron Impact*. 1977, Boulder, Colorado: Colorado Associated University Press.
12. Carey, F.A. and R.M. Giuliano, *Organic Chemistry, 9th ed.* 2013: McGraw-Hill Education. 1232.
13. Pradham, A.K. and S.N. Nahar, *6.2 Photoionization Cross Section*, in *Atomic Astrophysics and Spectroscopy*. 2011, Cambridge University Press: Cambridge, UK.
14. Demtroder, W., *7.6. Continuous Absorption and Emission Spectra*, in *Atoms, Molecules and Photons. An Introduction to Atomic-, Molecular- and Quantum Mechanics 2nd Ed.* 2006, Springer-Verlag: Berlin, Germany.
15. Ray, A., *Characterization of Ethene + OH Products and Cyclohexene Ring-Opening Mechanism Elucidation Via Synchrotron Photoionization Mass Spectrometry*, in *Chemistry*. 2010, University of San Francisco: San Francisco.
16. Wigner, E.P., *On the Behavior of Cross Sections Near Thresholds.* Phys. Rev., 1948. **73**(9): p. 1002-1009.
17. Sadeghpour, H.R., et al., *Collisions Near Threshold in Atomic and Molecular Physics.* J. Phys. B: At. Mol. Opt. Phys., 2000. **33**: p. R93-R140.
18. Wannier, G.H., *The Threshold Law for Single Ionization of Atoms or Ions by Electrons.* Phys. Rev., 1953. **90**(5): p. 817-825.
19. Dewar, M.J.S., A. Komornicki, and W. Thiel, *Calculation of photoionization cross sections using ab-initio wavefunctions and the plane wave approximation.* Chemical Physics Letters, 1975. **31**(2): p. 286-290.

20. Gokhberg, K., et al. *Molecular Photoionization Cross-Sections by Application of Stieltjes Imaging to Lanczos Pseudospectra*. in *AIP Conf. Proc.* 2007. Corfu: American Institute of Physics.

21. Samson, J.A.R., Y. Shefer, and G.C. Angel, *A critical test of many-body theory: the photoionization cross section of Cl as an Example of an Open-Shell Atom.* Physical Review Letters, 1986. **56**(19): p. 2020-2023.

22. Gozem, S., et al., *Photoelectron Wave Function in Photoionization: Plane Wave or Coulomb Wave?* J. Phys. Chem. Lett., 2015. **6**(22): p. 4532-4540.

23. Person, J.C. and P.P. Nicole, *Isotope effects in the photoionization yields and the absorption cross sections for acetylene, propyne, and propene.* J. Chem. Phys., 1970. **53**: p. 1167-1774.

24. Smith, A.R., *Absolute photoionization cross sections of furanic fuels: 2-ethylfuran, 2-acetylfuran and furfural.* Journal of Mass Spectrometry, 2015. **50**: p. 1206-1213.

25. Czekner, J., et al., *Absolute photoionization cross-sections of selected furanic and lactonic potential biofuels.* International Journal of Mass Spectrometry, 2013. **348**: p. 39-46.

26. Trager, J.C., *A study of the allyl cation thermochemistry by photoionization mass spectrometry.* International Journal of Mass Spectrometry, 1984. **58**: p. 259-271.

27. Savee, J.D., et al., *Absolute photoionization cross-section of the propargyl radical.* J. Chem. Phys., 2012. **136**(13): p. 134307/1-134307/10.

28. Que, L.J., *Physical Methods in Bioinorganic Chemistry*. 2000, Sausalito: University Science Books.

29. McQuarrie, D.A., *Physical Chemistry: A Molecular Approach*. 1997, Sausalito: University Science Books.

30. McQuarrie, D.A., *Quantum Chemistry*. 1983, Sausalito, CA: University Science Books.

31. Byers, L.R., *A teaching aid for the conceptualization of the Franck-Condon Factor.* J. Chem. Educ., 1975. **52**(12): p. 790.

32. Nagy-Felsobuki, E., J.B. Peel, and G.D. Willett, *The photoelectron spectrum of bromamine.* Journal of Electron Spectroscopy and Related Phenomena, 1978. **13**(1): p. 17-25.

33. Eland, J.H.D. and C.J. Danby, *Photoelectron spectra and ionic structure of carbon dioxide, carbon disulphide and sulphur dioxide.* International Journal of Mass Spectrometry and Ion Physics, 1968. **1**(2): p. 111-119.

34. Mabbs, R., E. Surber, and A. Sanov, *Photoelectron imaging of negative ions: atomic anions to molecular clusters.* Analyst, 2003. **128**: p. 765-772.

35. Zhang, X., et al., *Photoelectron spectroscopy of the aluminum hydride anions: AlH2-, AlH3-, Al2H6-, Al3H9-, and Al4H12-.* J. Chem. Phys., 2013. **138**: p. 124303-1 - 124303-4.

36. Ng, M.Y., et al., *Synchrotron Photoionization Syudy of Mesitylene Oxidation Initiated by Reaction with Cl ($^2$P) or O($^3$P) Radicals.* J. Phys. Chem. A., 2014. **118**: p. 3735-3748.

37. Ng, M.Y., et al., *Study of tert-Amyl Methyl Ether Low Temperature Oxidation Using Synchrotron Photoionization Mass Spectrometry.* J. Phys. Chem. A., 2015. **119**: p. 8667-8682.

38. Cool, T.A., et al., *Selective Detection of Isomers with Photoionization Mass Spectrometry for Studies of Hydrocarbon Flame Chemistry.* J. Chem. Phys., 2003. **119**: p. 8356-8365.

39. Wang, J., et al., *Near-Threshold Absolute Photoionization Cross-Sections of Some Reaction Intermediates in Combustion.* International Journal of Mass Spectrometry, 2008. **269**: p. 210-220.

40. Kim, M.H., et al., *Conformationally Controlled Chemistry: Excited-State Dynamics Dictate Ground-State Reaction.* Science, 2007. **315**: p. 1561-1565.

41. Dyakov, Y.A., et al., *Ab initio and RRKM study of photodissociation of azulene cation.* Physical Chemistry Chemical Physics, 2006. **8**: p. 1404-1415.

42. Hause, M.L., et al., *Roaming-mediated isomerization in the photodissociation of nitrobenzene.* Nature Chemistry, 2011. **3**: p. 932-937.

43. Mishima, K., M. Hayashi, and S.H. Lin, *Ab initio study of the isomerization and photodissociation of the C3H6O+ cation radicals.* International Journal of Mass Spectrometry, 2004. **238**(1): p. 1-15.

44. Baer, T., A. Bodi, and B. Sztaray, *Photoelectron-Photoion Coincidence Methods in Mass Spectrometry (PEPICO)*, in *Elsevier Reference Module in Chemistry, Molecular Sciences and Chemical Engineering*, J. Reedijk, Editor. 2014, Elseview: Waltham, MA.

45. Harvey, J., et al., *Dissociation dynamics of fluorinated ethene cations: from time bombs on a molecular level to double-regime dissociators.* Phys. Chem. Chem. Phys., 2012. **14**: p. 3935-3948.

46. Gengelicski, Z., S.N. Borkar, and B. Sztaray, *Dissociation of Energy-Selected 1,1-Dimethylhydrazine Ions.* J. Phys. Chem. A, 2010. **114**: p. 6103-6110.

47. Borkar, S. and B. Sztaray, *Self-Consistent Heats of Formation for the Ethyl Cation, Ethyl Bromide, and Ethyl Iodide from Threshold Photoelectron Photoion Coincidence Spectroscopy.* J. Phys. Chem. A, 2010. **114**(20): p. 6117-6123.

48. Shuman, N., et al., *Heat of formation of the allyl ion by TPEPICO spectroscopy.* J. Phys. Chem. A, 2009. **113**(40): p. 10710-10716.

49. Chase, M.W., Jr., *NIST-JANAF Thermochemical Tables, Fourth Edition.* Journal of Physical Chemistry, 1998. **Ref. Data**(Monograph 9): p. 1-1951.

50. Ruscic, B. and J. Berkowitz, *Heat of formation of CH₂OH and D₀(H-CH₂OH).* J. Phys. Chem., 1993. **97**: p. 11451-11455.

51. Moshammer, K., et al., *Detection and Identification of the Keto-Hydroperoxide (HOOCH₂OCHO) and Other Intermediates during Low-Temperature Oxidation of Dimethyl Ether.* J. Phys. Chem. A., 2015. **119**(28): p. 7361-7374.

52. Wei, L., Yang, B., Wang, J., Huang, C., Sheng, L., Zhang, Y., Qi, F., Lam, C., Li, W., *Vacuum Ultraviolet Photoionization Mass Spectrometric Study of Ethylenediamine.* Journal of Physical Chemistry, 2006. **110**: p. 9089-9098.

53. Bodi, A., et al., *Controlling tunnelling in methane loss from acetone by deuteration.* Phys. Chem. Chem. Phys., 2015. **17**: p. 28505-28509.

54. Sztaray, B., Bodi, A., Baer, T., *Modeling unimolecular reactions in photoelectron photoion coincidence experiments.* Journal of Mass Spectrometry, 2010. **45**: p. 1233-1245.

55

55. Borkar, S.N., *Very Accurate Gas-Phase Thermochemistry Through Photoelectron Photoion Coincidence (PEPICO) Spectroscopy*, in *Chemistry*. 2013, University of the Pacific: Stockton, California.

56. Marcus, R.A. and O.K. Rice, *The kinetics of the recombination of methyl radicals and iodine atoms.* J. Phys. Colloid Chem., 1951. **55**: p. 894.

57. Rice, O.K. and H.C. Ramsperger, *Theories of unimolecular reactions at low pressures.* J. Am. Chem. Soc., 1927. **49**: p. 1617.

58. Rice, O.K. and H.C. Ramsperger, *Theories of unimolecular reactions at low pressures II.* J. Am. Chem. Soc., 1928. **50**: p. 617.

59. Hase, W.L., *Variational unimolecular rate theory.* Acc. Chem. res., 1983. **16**: p. 258.

60. Baer, T. and W.L. Hase, *Unimolecular Reaction Dynamics: Theory and Experiments*. 1996, New York: Oxford University Press.

61. Beynon, J.H. and J.R. Gilbert, *Application of transition state theory to unimolecular reactions: An Introduction*. 1984, Chichester: Wiley Interscience.

62. Fernandez-Ramos, A., *Modeling the Kinetics of Biomolecular Reactions.* Chemical Reviews, 2006. **106**(11): p. 4523-4531.

63. Zador, J., C.A. Taatjes, and R.X. Fernandes, *Kinetics of elementary reactions in low-temperature autoignition chemistry.* Progress in Energy and Combustion Science, 2011. **37**: p. 371-421.

64. Montgomery, J.A., et al., *A complete basis set model chemistry. VI. Use of density functional geometries and frequencies.* J. Chem. Phys., 1999. **110**: p. 2822-2827.

65. Montgomery, J.A., et al., *A complete basis set model chemistry. VII. Use of the minimum population localization method. .* J. Chem. Phys., 2000. **112**: p. 6532-6542.

66. Ochterski, J.W., G.A. Petersson, and J.A. Montgomery, *A complete basis set model chemistry. V. Extensions to six or more heavy atoms.* J. Chem. Phys., 1996. **104**: p. 2598-2619.

67. Frisch, M.J., et al., *Gaussian 09*. 2009, Gaussian, Inc.: Wallingford, CT.

68. Ramakrishna, V. and B.J. Duke, *Extension of complete basis set model chemistries to molecules containing third row atoms Ga-Kr.* Journal of Chemical Physics, 2003. **118**(14): p. 6137-6143.

69. Sirjean, B., et al., *Extension of the composite CBS-QB3 method to singlet diradical calculations.* Chemical Physics Letters, 2007. **435**: p. 152-156.

70. Cochran, E., G. Muller, and G. Meloni, *Stability and bonding of new superalkali phosphide species.* Dalton Transactions, 2015. **44**: p. 14753-14762.

71. Cochran, E. and G. Meloni, *Hypervalence in monoxides and dioxides of superalkali clusters.* Journal of Chemical Physics, 2014. **140**: p. 204319-1/204319-13.

72. Peng, C. and H.B. Schlegel, *Combining Sychronous Transit and Quasi-Newton Methods to Find Transition States.* Israel J. of Chem., 1993. **33**(449): p. 449-454.

73. Peng, C., et al., *Using redundant internal coordinates to optimize equilibrium geometries and transition states.* Journal of Computational Chemistry, 1998. **17**(1): p. 49-56.

74. Dennington, R., T. Keith, and J. Millam, *GaussView*. 2009, SemiChem Inc.: Shawnee Mission, KS.

75.     Fukui, K., *The path of chemical reactions - the IRC approach.* Acc. Chem. Res., 1981. **14**(12): p. 363-368.

76.     Hratchian, H.P. and H.B. Schlegel, *Finding minima, transition states, and following reaction pathways on ab initio potential energy surfaces*, in *Theory and Applications of Computational Chemistry: The First 40 Years*, C.E. Dykstra, et al., Editors. 2005, Elsevier: Amsterdam. p. 195-249.

77.     Qelz, O., et al., *Direct Kinetic Measurements of Criegee Intermediate (CH2OO) Formed by Reaction of CH2I with O2.* Science, 2012. **335**: p. 204-207.

78.     Ochterski, J.W. *Thermochemistry in Gaussian*. 2000   [cited 2015 December 16, 2015]; Available from: http://www.gaussian.com/g_whitepap/thermo.htm.

79.     Bodi, A., et al., *Photoion Photoelectron Coincidence Spectroscopy of Primary Amines RCH2NH2 (R = H, CH3, C2H5, C3H7, i-C3H7): Alylamine and Alkyl Radical Heats of Formation by Isodesmic Reaction Networks.* J. Phys. Chem. A, 2006. **110**: p. 13425-13433.

80.     Sivaramakrishnan, R., R. Tranter, and K. Brezinsky, *Ring Conserved Isodesmic Reactions: A New Method for Estimating the Heats of Formations of Aromatics and PAHs.* Journal of Physical Chemistry A, 2005. **109**(8): p. 1621-1628.

# Chapter 3: Experimentation

## 3.1 Photooxidation Reactions at Lawrence Berkeley National Lab

Cl-initiated photooxidation experiments of small-chain methyl esters presented in Chapter 4 of this thesis were carried out at the Chemical Dynamics Beamline 9.0.2 using a multiplexed photoionization mass spectrometer (MPIMS) at the Lawrence Berkeley National Lab (LBNL). The intent behind these experiments was to characterize autoignition combustion behavior of methyl esters as a function of the length of the main aliphatic chain. As described in section 1.4 of this thesis, the autoignition characteristics of particular biofuels and biofuel blends can greatly influence the performance of homogenous charge compression ignition (HCCI) engines, which can have a profound impact on redirecting the current ecological and atmospheric climate crisis.

### 3.1.1 Excimer Laser and Cl· Production

In actual HCCI engines, $H_2O_2$ thermally decomposes to provide the OH radical "igniters" for the reaction — previously presented as the initiation step of Figure 1.4b in the autoignition scheme. Either ·OH or Cl· can be used in the initiation step to abstract a hydrogen from the hydrocarbon (RH) to generate the initial radicals (R·) that will react with $O_2$. In the investigation of methyl esters presented in Chapter 4 of this thesis, Cl· were used to initiate the reaction.

The chlorine radicals can be generated via photolysis of $Cl_2$ using an unfocused excimer laser. In general, many excimer lasers generate ultraviolet light

by supplying electric current through a mixture containing a noble and a halogen gas, although some simply use a pure noble gas. Common noble gases used include Kr, Ar, and Xe, and their mixtures are made using $F_2$, $Br_2$, or $Cl_2$. While noble gas molecules are unbound in the ground state, the appropriate combination of electric current and pressure generates excited dimers, or "excimers". This term has now been generalized to include all molecular ions that are bound in the excited state, while unbound in their ground state. Due to the instability of these excimers, their lifetime lasts on the order of nanoseconds as they quickly decay. Photons are released in the form of ultraviolet light upon relaxation to the ground state.[1] Because the ground state is highly unstable and not bound, it dissociates on the order of picoseconds.

The wavelength of UV light produced is dependent upon the mixture that is excited and the laser band gap between states, as shown in Figure 3.1.1.
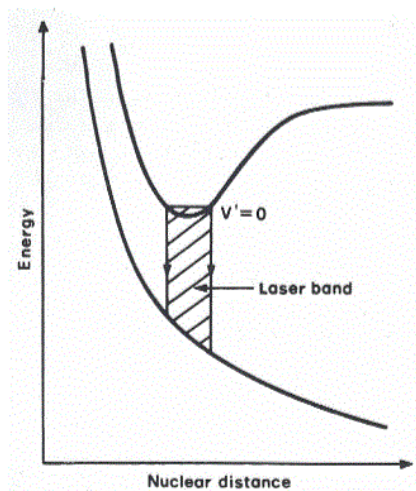


**Figure 3.1.1a:** Potential energy diagram of the ground (unbound) and excited (bound) state of either KrF or XeF to yield a laser band with wavelength of 248 nm or 351 nm, respectively.[2, 3]

For example, the relaxation of excited and unbound xenon fluoride ions produces photons at wavelength of 351 nm. This mixture is often used at the ALS, as it is sufficient for the photolysis of molecular chlorine to form the respective radicals.

A general schematic of an excimer laser and its parts is shown in Figure 3.1.1b. The laser cavity consists of the gas mixture used (such as Xe and $F_2$), as well as any additional buffer gas, such as He or Ne. An electric current from one electrode to another passes through the gas, enabling the electrons to excite the molecules. If the energy is sufficient, the noble gas and halogen molecules are ionized and rearranged into bound excimer species. The release of photons as these excimers decay is shown as output in Figure 3.1.1b, the energy of which can be determined by a wavelength meter.
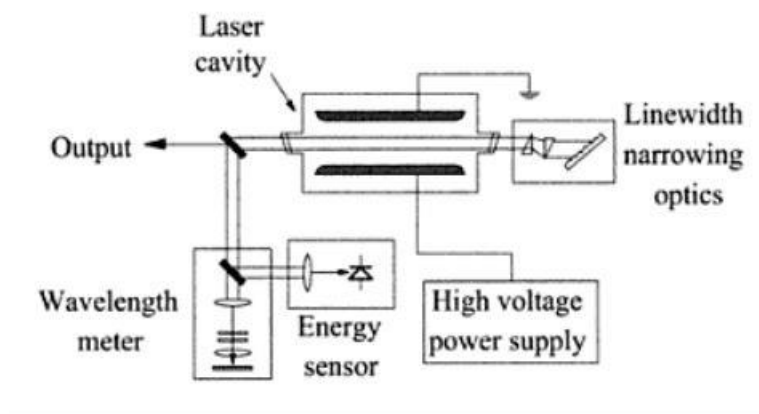


**Figure 3.1.1b:** A general schematic of an excimer laser.[4]

Excimer molecules can relax to the ground state via two different processes, spontaneous emission or stimulated emission. In spontaneous emission, the bound excimer molecules automatically decay through photon loss as described above.

However, it is possible that a photon emitted from the relaxation of one excimer can interact with another excimer and induce relaxation. In this case, the two photons travel in the same direction with the same energy and the photon beam will be amplified. In addition, if stimulated emission is substantial, it is possible that more of the gas molecules will exist in the excited state as opposed to the ground state. This is known as population inversion.[5, 6] A population inversion is beneficial in the sense that the laser efficiency (lasing action) is increased, as more molecules are excited with the same electric current supplied.

The excimer laser at the Chemical Dynamics Beamline 9.0.2 at the Advanced Light Source is operated at 4 Hz with a fluence of 10-60 mJ $cm^{-2}$ and pulse-width of 20 ns. These specifications, along with the total flow rate of the gas at 400 cm $s^{-1}$, allows for the analysis of temporal behavior for up to 150 ms.

### 3.1.2 Sample Preparation, Bubbler

The hydrocarbons of interest are commercially obtained, most commonly from Sigma-Aldrich, in liquid form. The samples are first purified via the freeze-pump-thaw method using a bubbler, as shown in Figure 3.1.2a. The bubbler is connected to a vacuum pump through a steel line with an Ultratorr connector and Swageloks. The sample is first frozen using a vat of liquid nitrogen, and then the valve to the vacuum is opened to remove any dissolved gas in the sample, as well as air in the bubbler. Once the solid begins to melt, the vacuum valve is shut and time is provided for thawing. This process usually is repeated two more times to ensure the vapor is purely that of the sample.
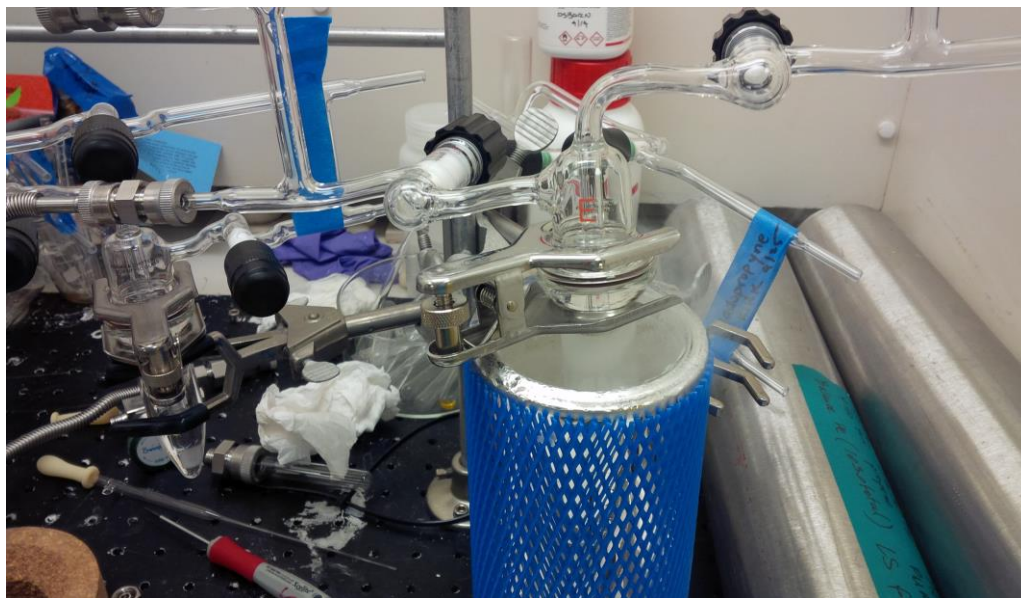
**Figure 3.1.2a:** Photo taken on April 25, 2014 in the chemical sample preparation room at the LBNL. The bubbler is sealed shut and connected to vacuum and contains the liquid hydrocarbon that is frozen in the liquid nitrogen vat (blue).

The steel line shown in Figure 3.2.1b is connected to MKS transducers and Baratron® digital readers, one for high pressure up to 10,000 Torr (left, top) and another for low pressure between 1 – 10 Torr (left, bottom). Cylinders on the right side of Figure 3.2.1b have been "flushed" with up to ~2500 – 3000 Torr of helium several times to remove any "sticky" gas molecules from previous experiments. Then, they have been vacuum pumped for a period of time until the pressure stabilizes around ~0.001 – 0.004 Torr. These vacuum-pumped cylinders are connected to the setup with closed valves. When the freeze-pump-thaw method is finished, the valves to the clean cylinders can all be opened slowly, in which case the liquid sample is able to bubble and the vapor is effused into the cylinders. The vapor

pressure of the sample in the cylinder should be documented. The cylinder is closed, the lines are vacuumed to remove extra molecules.
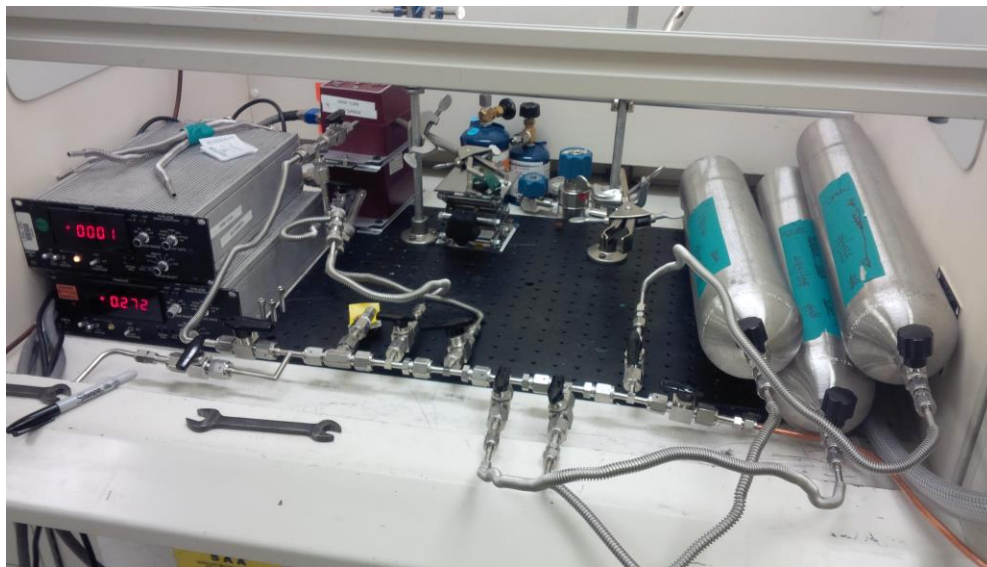


**Figure 3.2.1b:** The fume hood in the chemical sample preparation room at the LBNL. Empty cylinders (right) are connected to a vacuum pump system and two MKS pressure transducers and Baratron® digital pressure readers. The top digital reader is connected to high-pressure MKS transducer, up to 10,000 Torr. The bottom is connected to low-pressure MKS transducer, which precisely reads pressures from 1 – 10 Torr.

A high-pressure cylinder of helium is connected to the main line with the pressure gauges and valves. Helium can be dispensed into the gas cylinder containing the sample to reach a 1% sample partial pressure. Since the flow rate of the gas should be constant, and the experiments can last up to several hours depending on the measurements desired, the pressure of the tank should be sufficient for the need. If the vapor pressure of the sample is too low, adding helium to reach a 1% concentration may result in a total pressure too low to sustain the

tank's life for experimentation. In these cases, a greater amount of helium is required to ensure the total pressure meets the needs of the experiment. Usually, between 2,000 and 2,400 Torr is sufficient. The cylinders are then brought to the beamline for experimentation.

### 3.1.3 The Schematic/Apparatus

Calculations and literature research should be conducted prior to conducting experiments in that the approximate adiabatic ionization energy (AIE) is used to decide the range in photon energy for photoionization. Typically, it is also good practice to take "shots" at a few different energies to determine if the signal is sufficient for analysis. Absolute PIE scans are taken without the photolysis laser, i.e., no reaction is occuring. They are used to obtain the absolute photoionization efficiency curve of the parent molecular ion and any fragment ions that may result. This is done when calibration gas (a known concentration of ethane, propene, and 1-butene) is flowed along with the sample and ionized at the end to determine relative photoionization cross sections.

A cross section view of the MPIMS is displayed in Figure 3.1.3.[7] For the bimolecular reactions, the hydrocarbon sample of interest is flowed with oxygen, chlorine, and helium buffer gas into a heatable, 62 cm long slow flow quartz tube with a 1.05 cm internal diameter.[8-10] The flow rate of all gases are measured and can be controlled with calibrated mass flow controllers (MFCs). Using the measured flow rate of the reactants, the concentration can be determined by

64

$$Concentration = (3.24 \times 10^{16})(P)\left(\frac{F_R}{F_T}\right)\left(\frac{T}{298.15}\right)^{-1} \qquad (3.1.3)$$

where $F_R$ is the flow rate of the reactant, $F_T$ is the total flow rate, and T is the temperature of the reactor. The concentration can be determined in units of molecules $cm^{-3}$.
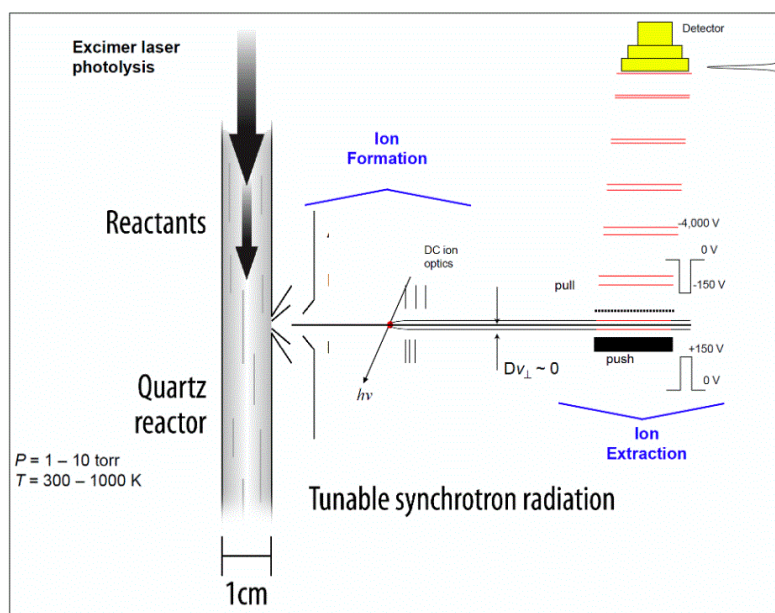


**Figure 3.1.3:** The multiplexed chemical kinetics orthogonal time-of-flight mass spectrometer.[11]

The mixture flows into the reactor tube where a 351 nm excimer laser can generate Cl· from $Cl_2$. There, newly-generated hydrocarbon radicals are formed via H-abstraction and can react with $O_2$. The tube is insulated by 18 μm thick Nichrome tape for thermal insulation and temperature uniformity. The temperature of the reactor can be set and measured using a closed-loop circuit.[10] The pressure is also maintained by a capacitive manometer and controlled with closed-loop feedback

valve in conjunction with the Roots pump, which is a 3200 L s$^{-1}$ oil-free turbomolecular pump.[7] The pressure is maintained typically at either 4 Torr or 8 Torr. The continuous gas flow of 400 cm s$^{-1}$ and the 4 Hz repetition of the excimer laser ensure that a fresh sample is introduced into the reactor tube for reaction and detection.

The opening approximately halfway down the quartz reactor tube is approximately 650 μm in size (Figure 3.1.3). A small portion of the gaseous mixture flows through the pinhole, forming an effusive molecular beam at a slight angle. As such, a 0.15 cm diameter skimmer is placed 0.2 – 0.3 cm downstream from the location of the pinhole to direct the molecular beam to the differentially pumped ionization chamber.[7]

Once in the ionization chamber, the molecular beam of excess reactants and photoxidation products are ionized with synchrotron radiation and are subsequently detected. Typically, there are 150 – 250 laser shots at each particular photon energy and the energy is scanned in step-sizes of 0.025 eV. Two additional vacuum pump systems of 1600 s$^{-1}$ and 700 L s$^{-1}$ are used for the ionization and detection regions.

## 3.1.4 Vacuum Pumps

Vacuum pumps are essential to ensure that the regions of the apparatus remain contaminant-free. Three turbomolecular pumps are used in the experimental setup. The largest vacuum pump, a 3200 L s$^{-1}$ turbomolecular vacuum coupled with a Roots pump and backing scroll pump, is located at the end of the slow flow reactor

tube. A 1600 L s$^{-1}$ pump is placed in the ionization region and a 600 L s$^{-1}$ is in the detector region.

Turbomolecular pumps are systems of moving and stationary blades, termed "rotors" and "stators," respectively. These are arranged in levels.[12] As the gas molecules enter the vacuum, the blades hit the molecules and provide momentum toward a stator due to the angle of the blades (Figure 3.1.4a). The stator directs them to the next rotor, thereby moving them further along in a single direction toward higher pressure. These pumps aim to compress the molecules to atmospheric pressure. The efficiency of the turbopumps can be expressed in equations 3.1.4a and 3.1.4b, in terms of the compression ratio, K:

$$K = \frac{P_{outlet}}{P_{intake}} \tag{3.1.4a}$$

$$K_{max} = \left\{ exp\left[ \frac{\sqrt{v_B M}}{\sqrt{2K_B N_A T}} \right] f_\phi \right\}^n \tag{3.1.4b}$$

where P is the pressure at the outlet and inlet, M is the molar mass of the gas, $v_B$ is the average tangential velocity of the blades, T is the temperature, $N_A$ is Avogadro's number, $K_B$ is Boltzmann's constant, $f_{(\phi)}$ is a function of the blade angle, and n is the number of the blades in the pump.[13, 14] From Equation 3.1.4b it can be understood that the compression ratio is low for molecules with low molecular weight. The pumping efficiency, however, can be increased with higher rotational speeds ($v_B$).

The turbomolecular pumps are backed by dry scroll pumps, which use interleaved spiral-shaped scrolls to pump the gas molecules. The two scrolls are aligned on top of one another. One of them stays fixed while the other one oscillates

67

over it in a circular motion, but the scroll itself does not rotate. Figure 3.1.4b

visualizes this movement. Once the inlet connection is closed, the trapped gas is

compressed by the "orbiting" of the scroll until it reaches a high pressure. The gas is

able to escape at the center of the spiral, shortly after which the inlet is opened to

allow the next sample to be exhausted. Because the scroll pumps are oil-free, the

contamination to the system is significantly minimized. These pumps have a speed

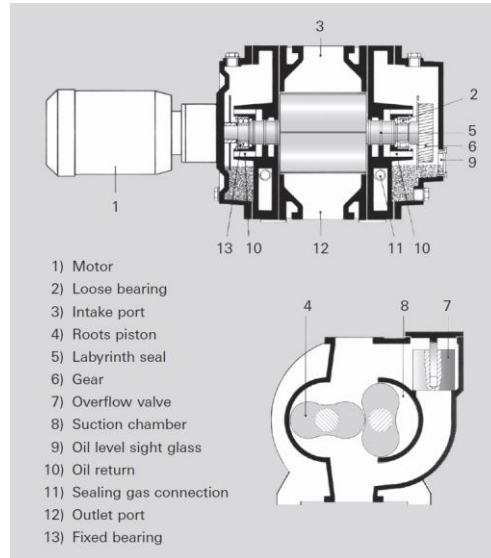from 20 – 50 $m^3$ $h^{-1}$ with an operational range of 1000 – $10^{-2}$ mbar.[10]
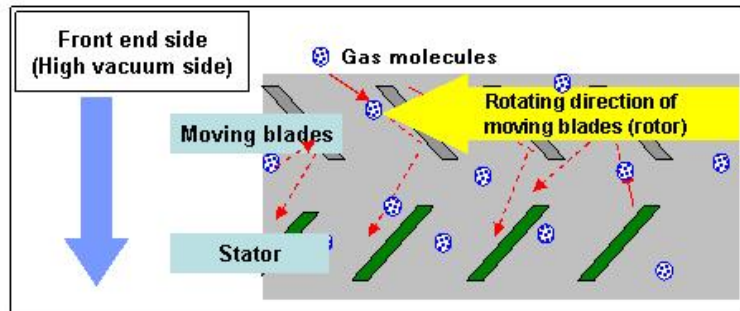


**Figure 3.1.4a:** The gas molecules are forced from the inlet toward the outlet in one direction.[15]
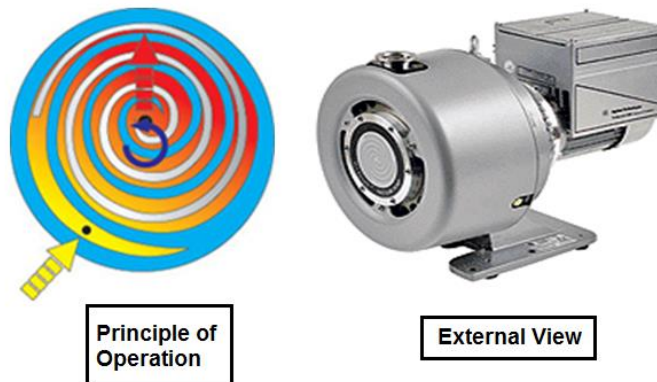


**Figure 3.1.4b:** The movement of a scroll pump (left) and the external view (right).[16]

Essentially, the Roots pump that is used with the 3200 L s$^{-1}$ turbomolecular pump contains two rotors in the shape of an "8". These pieces rotate in oppose directions, but are separated enough from one another that they never gain contact. They are labeled as (4) in Figure 3.1.4c.



1) Motor
2) Loose bearing
3) Intake port
4) Roots piston
5) Labyrinth seal
6) Gear
7) Overflow valve
8) Suction chamber
9) Oil level sight glass
10) Oil return
11) Sealing gas connection
12) Outlet port
13) Fixed bearing

**Figure 3.1.4c:** The labeled components of a Roots pump.[17]

The gas is moved from the inlet port (3) to the outlet port (2) as the rotors rotate through the phases shown in Figure 3.1.4d.[17] In Phase 1 the rotors take in a small volume of gas, and in Phase 5 the gas is expelled to the exhaust. If they rotate with a very high velocity, high volumes of gas can be evacuated. In fact, the Roots pump system has a range of 75 to 30,000 m$^3$ h$^{-1}$ with operating range from 10 to 10$^{-3}$ mbar total pressure.[3]
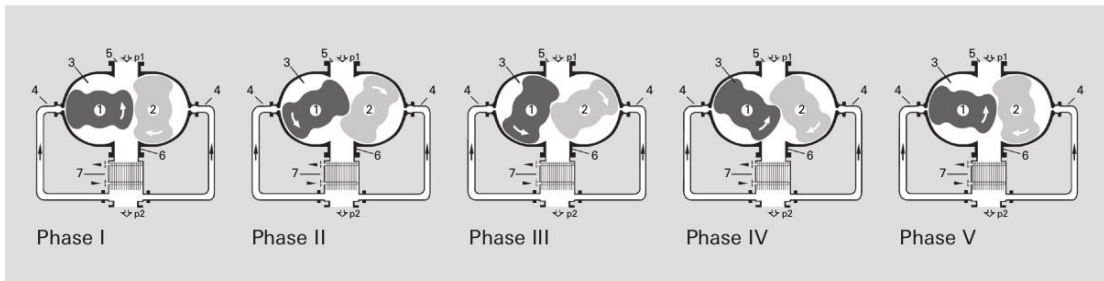
**Figure 3.1.4b:** The phases of a Roots pump.[17]

## 3.1.5 Photoionization Source

The Advanced Light Source at the Lawrence Berkeley National Lab is a third-generation synchrotron. Electrons are initially generated by the electron gun, where electrons are made at the cathode by thermionic emission from heated barium aluminate.[3] The electron gun is one component of the linear accelerator (Linac). Through a series of electric fields, the speed of the electrons is increased, and they are subsequently lead into the booster ring where they are further accelerated to nearly the speed of light (Figure 3.1.5a). Finally, the electron beam is directed to the 1.9 GeV electron storage ring, where the electrons continue to travel circularly with the aid of undulators.

The shape of the ring is not exactly circular. In fact, it is dodecagonal, and to keep the electrons from colliding with the wall there are insertion devices known as undulators. These are bending magnets with alternating poles that are able to change the direction of the electrons. Synchrotron radiation is emitted with each change in electron trajectory (Figure 3.1.5b).
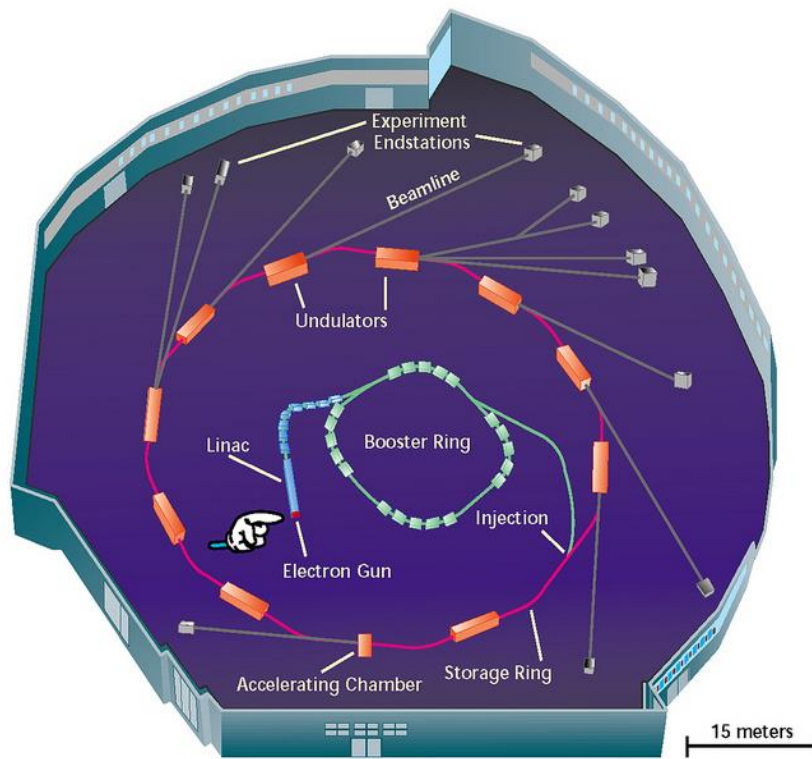
**Figure 3.1.5a:** General schematic of electron generation, storage, and light production at the Lawrence Berkeley National Lab.
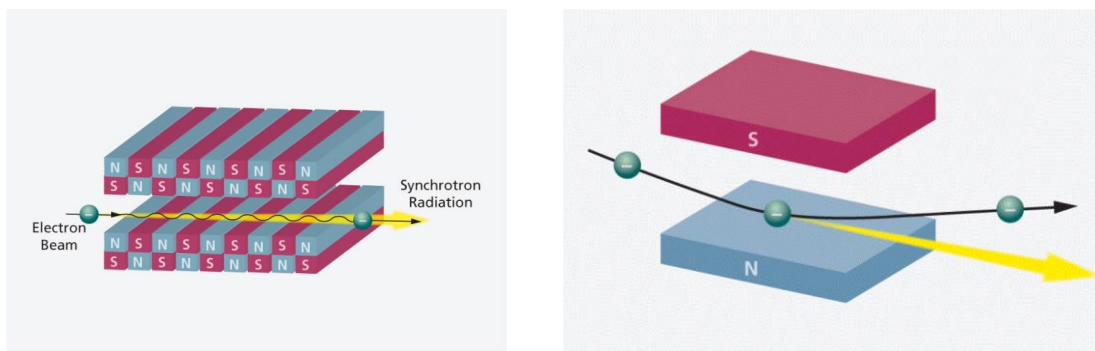


**Figure 3.1.5b:** Left: the bending of an electron beam due to the effect of undulators, such as those used at LNBL. Right: At each turn of electron beam, radiation is emitted

Each of the beamlines at the ALS are positioned at the undulators, and the radiation can be harvested from the storage ring. To determine the amount of photon energy released from an undulator, equation 2.2.2b is reintroduced here as 3.1.5a for clarity:

$$E = hv \tag{3.1.5a}$$

E is the photon energy, h is Plank's constant and v is the frequency of the photon. Note that frequency is also the inverse of wavelength, λ:

$$v = \frac{1}{\lambda} \tag{3.1.5b}$$

The wavelength ($\lambda_x$) of synchrotron radiation obtained from the undulator can be written as

$$\lambda_x = \frac{\lambda_u}{2\gamma^2}\left(1 + \frac{K^2}{2} + \gamma^2\theta^2\right) \tag{3.1.5c}$$

where $\lambda_u$ is the wavelength of the magnetic field alternating along the undulator based on spacing between the magnets, γ is the energy of the beam, θ is the direction of radiation emission, and K is the undulator strength parameter.[18] Figure 3.1.5c presents a schematic relating the variables, as provided by the Advanced Light Source.[19] K can be defined by:

$$K = \frac{eB_0\lambda_u}{2\pi m_0 c} \tag{3.1.5d}$$

In the above equation, e is the charge of the electron, $m_0$ is the mass of an electron at rest, c is the speed of light, and $B_0$ is the strength of the magnetic field.

# ALS Radiation is Produced by Bend Magnets and Undulators
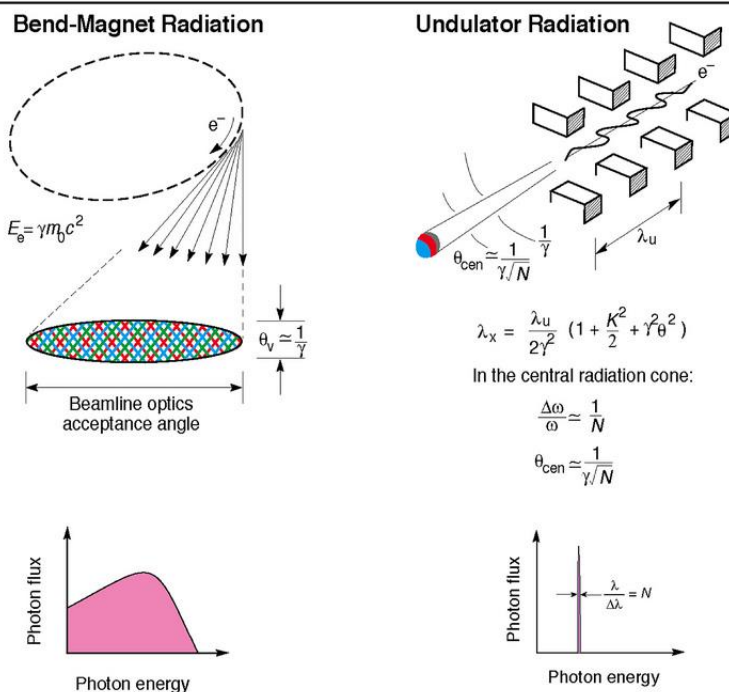
**Figure 3.1.5c:** Synchrotron radiation generated at the ALS as a result of bend-magnets and undulators.[19]

Equations 3.1.5c can be combined with equations 3.1.5a and 3.1.5b to yield the following equation provided by Margaritondo[3, 20]:

$$E = (\frac{2h\gamma^2}{\lambda_u})(\frac{1}{1+\frac{1}{2}K^2 + \theta_u{}^2\gamma^2}) \tag{3.1.5e}$$

The period of the undulators at the Advanced Light Source is 10 cm, which provides a flux of $10^{16}$ photons s$^{-1}$ (Figure 3.1.5a).[7] The beamline utilized for our studies is the Chemical Dynamics Beamline (9.0.2), which has a windowless gas filter of 30 Torr of either Ar or Kr to remove higher-order harmonic photons from the undulator.[21] Other noble gases are available at the ALS for use upon request,

including helium, neon, and xenon.[22] The extent of suppression of the higher-order harmonic photons is calculated by Beer's Law:

$$\frac{I}{I_0} = e^{-\sigma l N} \tag{3.1.5f}$$

I is the transmitted photon intensity, $I_0$ is the incident photon intensity, l is the length of the gas cell, N is the density of the gas and σ is the photoabsorption cross section of the noble gas.[22, 23]

The light then reaches a 3 m off-plane Eagle monochromator. Figure 3.1.5d shows the off-plane Eagle monochormator used at the ACO (Anneau de Collisions d'Orsay) light source in France and is comparable to the one used at the ALS in Berkeley.[24]

A monochromator is an optical system that enables the selection of a narrow band of wavelengths from a much wider range at the input. While the undulator is able to roughly extract a selected energy of radiation by reducing the spacing between the magnets ($\lambda_u$), the monochromator enables the synchrotron light to be focused to specific, monochromatic beams with a desired wavelength corresponding to an energy in the range of 7.2 – 25.4 eV.

In Figure 3.1.5d, the synchrotron radiation generated from the undulator is directed to a set of diffraction gratings through a gas filter with the aid of toroidal mirrors. These mirrors simply help to focus the light through the gas filter and entrance slit.

Diffraction gratings are a series of parallel and closely spaced grooves carved into a reflective surface, such as glass or mirror, and a general schematic is represented by Figure 3.1.4e.
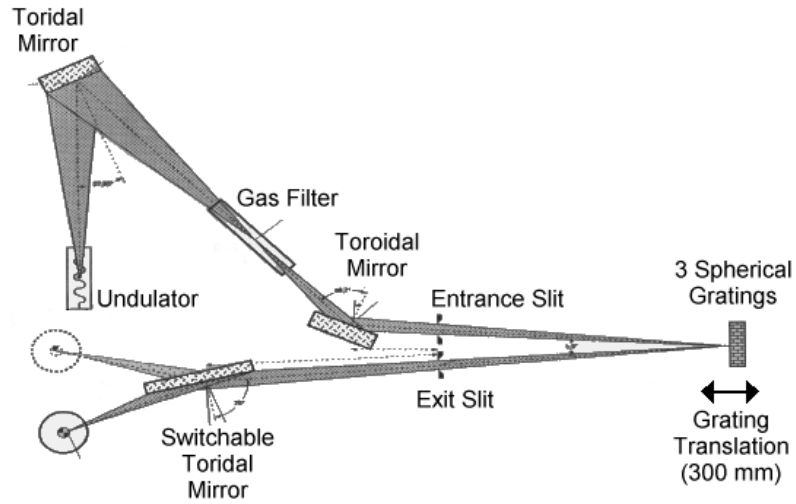


**Figure 3.1.5d:** The schematic of an Eagle off-plane beamline Optical Layout[24]
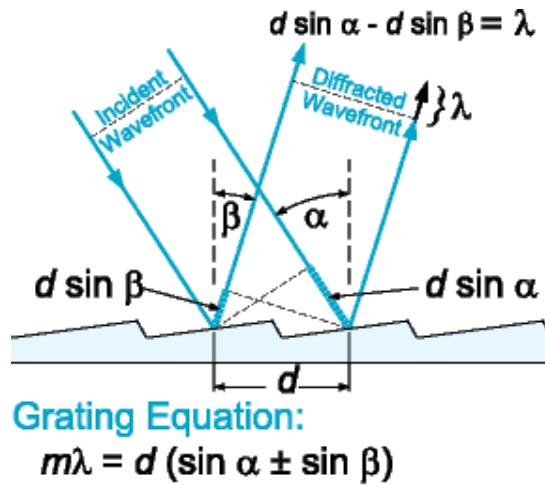


**Figure 3.1.5e:** Mathematical interpretation of reflective diffraction of polychromatic light. Graph courtesy of International Light, Inc.[25]

The equation used to separate polychromatic radiation into specific wavelengths is written as

$$n\lambda = d\,(\sin\alpha \pm \sin\beta_n) \tag{3.1.5g}$$

where n is the order number of diffraction, $\lambda$ is the diffracted wavelength corresponding to the photon energy desired, d is the distance between the grooves, $\alpha$ is the incidence angle measured from the grating normal, and $\beta_n$ is the angle of diffraction of the nth order (also measured from the grating normal).[26] Thus, the diffraction grating can be rotated to diffract monochromatic light at a specific wavelength. At the ALS, specifically, the Eagle monochromator can achieve a narrower spectral bandwidth (10 – 50 meV) at the expense of photon flux (~ $10^{13}$ – $10^{14}$ photons $^{-1}$).[7] Once the radiation has passed through the exit slits of the monochromator, the photon beam then intersects the molecular beam inside the ionization region.

### 3.1.6 Detection: TOF Mass Spectrometer and Channeltron Plates

A McLaren time of flight mass spectrometer enables continuous detection of reactants and products simultaneously over a range of masses. When the molecular beam is crossed with the synchrotron radiation generated by the undulator, the molecules will be ionized only if the energy of the light is greater than the ionization energy of the species.

From Figure 3.1.3, it should be noted that the cations pass through a series of DC electric fields to focus the beam towards the end of the flight tube, where they

are met by a "puller" and a "pusher", which are negative and positive electric fields of ~150 V, respectively, to direct the trajectory of the electrons toward the channeltron plates for detection. Because the force imposed on the cations is uniform, and the length of the tube remains unchained, then the kinetic energy (KE) obtained is equal for each ion. As the inertia of the molecule is dependent upon its mass, then the final velocity of each ion is inversely proportional to the square root of its mass-to-charge ratio ($m/z$).[27] The kinetic energy of the ion can be determined by equation 3.1.6a:

$$KE = \frac{mv^2}{2} = zV \tag{3.1.6a}$$

where m is the mass of the ion, v is the velocity, z is the charge of the ion, and V is the voltage applied for the electric field.[28] Typically, z is equal to 1, as the energy used to ionize is not substantial enough for double ionization. The time of flight ($T_f$) required for the ion to travel through the length of the flight tube (L) is:

$$T_{f=\frac{L}{v}} \tag{3.1.6b}$$

The relationship between the mass and time of flight is visualized in Figure 3.1.6b.

If multiple ions with known masses are detected at a specific TOFs, then a calibration equation can be generated to solve for the intercept and slope. The equation for the linear relationship is created by combining equations 3.1.6a and 3.1.6b together:

$$T_f = \alpha + \beta\sqrt{m/z} \tag{3.1.6c}$$

In the above linear relationship relating the mass of the ion to its time of flight, α is the y-intercept and β is the slope. Once the linear relationship is generated, it is possible to detect TOFs of ions of unknown mass, and as long as pertinent parameters of the equipment remain constant the *m/z* of the ion can be determined.



Inlet/ion source          drift region                    detector
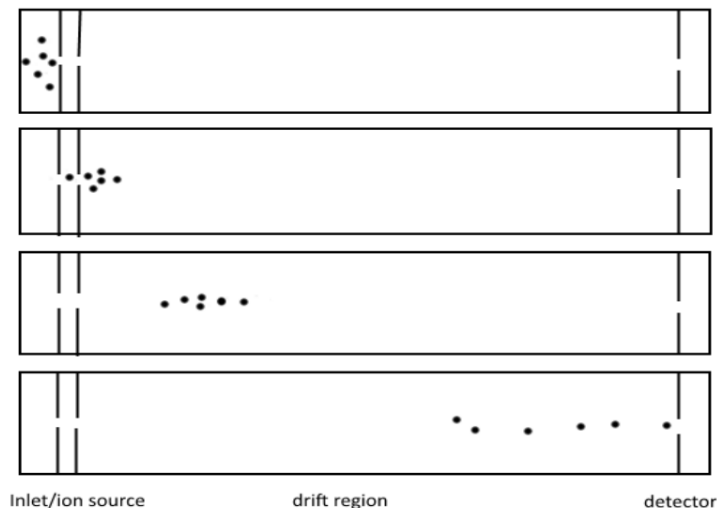
**Figure 3.1.6b:** A diagram recreated from other sources, showing that as time passes, the ions are separated.[29]

Ions with *m/z* = 14 – 155 are able to be detected at the end of the drift tube by a time- and position-sensitive Chevron style microchannel plate (MCP) detector with a delay-line anode.[7, 30] A side view of the detector is provided in Figure 3.1.6c.

MCPs are comprised of several channel electron multipliers (CEM) and have the function of transferring and intensifying the ionic image. The schematic of how MCPs and CEMs work is shown in Figure 3.1.6d. Because CEM tubes are usually each a micrometer in diameter and are placed into an array very closely together, as well as at an angle with respect to the incoming ion beam, there is a high probability

78

that the ions will hit one of the inside surfaces of a CEM.[31] In addition, the surfaces of

the CEM are made of semiconductor material, and when the ions hit the CEM with a

substantial velocity, secondary electrons are generated. The greater the velocity of

the incoming ion beam, the larger the ion cloud that is generated as a result.
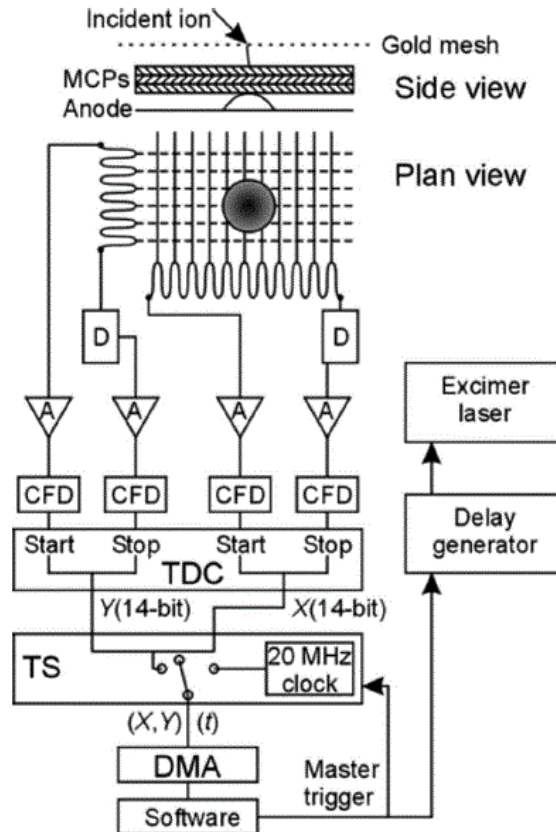


**Figure 3.1.6c:** The components of the TOF mass spectrometer: (D) delay, (A) fast analog amplifier, (CFD) constant fraction discriminator, (TDC) time to digital converter, (TS) time stamping board, and (DMA) dynamic memory access data acquisition card.[7]

Another MCP can be lined up close to the output end of the first MCP to

amplify the electron signal from the first MCP. In that the electrons from the first

should hit the wall of the second CEM, a "chevron" orientation (v-shaped) is the preferred orientation. If three or more MCPs are "stacked" in the type of alternating, zig-zag orientation shown in Figure 3.1.6e, then the electron gain is approximately $10^8$.[32]
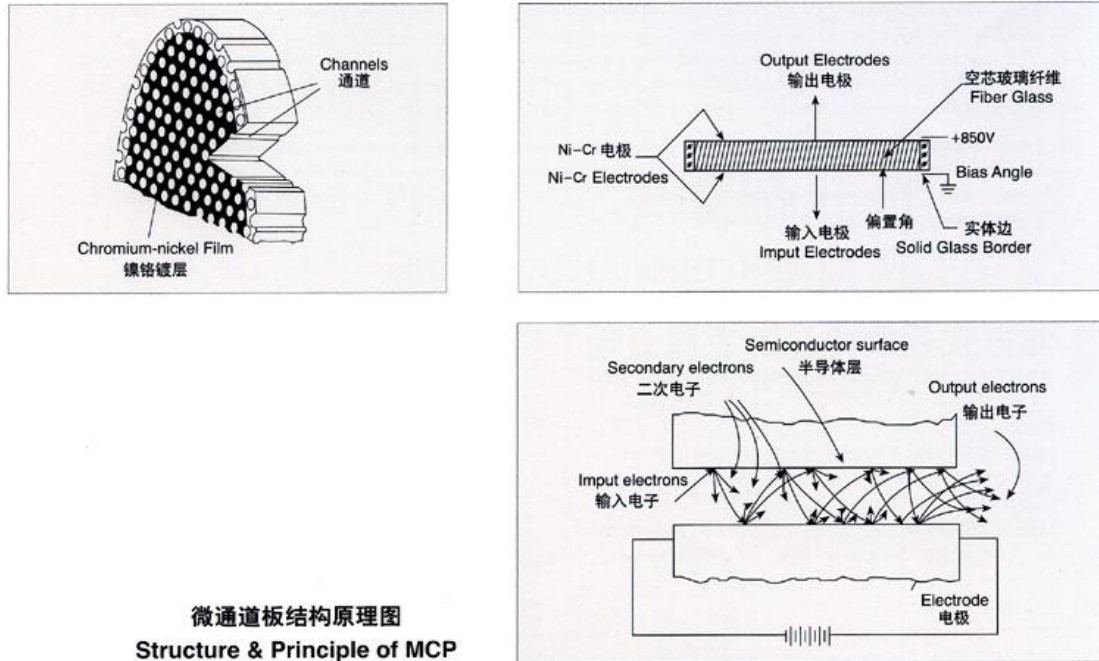


**Figure 3.1.6d:** Top left: Image of the microchannel plate (MCP) with the channel electron multipliers (CEM). Top right: view of the MCP from above. Bottom right: a side view of the CEM showing input ions, the generation of electrons and secondary electrons. Note cations can be used for input, as well.[33]

As presented in Figure 3.1.6e, the electron cloud is eventually directed through constant fraction discriminators and enter a "start" and "stop" inputs of time to a digital converter (TDC).[7] The time delays are converted to 14-bit digital numbers, and if valid start and stop pulses are received, then a 20 MHz oscillator on a

homemade time stamping (TS) board creates a 32-bit number corresponding to the time of arrive of a specific ion. The position and time with respect to the laser are recorded for each ion onto the computer's hard drive. The cycle begins 20 ms before the laser pulse and lasts 150 ms.
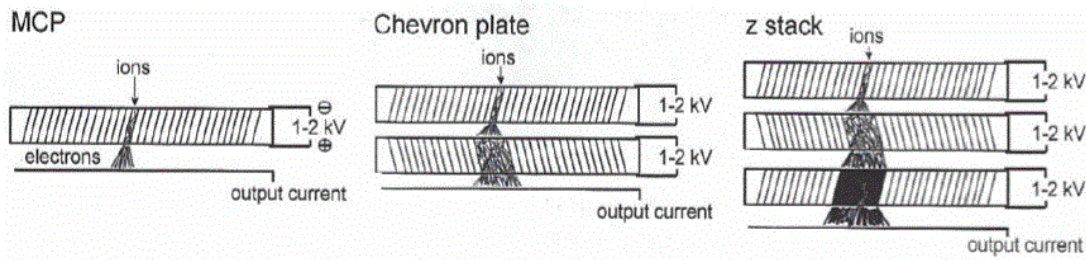


**Figure 3.1.6e:** Left: one MCP with an array of CEMs. Middle: a chevron-plate orientation with two MCPs. Right: a "z stack" orientation of three or more MCPs.[3]

## 3.1.7 Data Analysis

A three-dimensional data set is obtained from reactions using the MPIMS, as shown in Figure 3.1.7. For each particular TOF of an ion, the *m/z* can be determined using the calibrated linear equation (3.1.6c). As such, a mass spectrum can be obtained, with the total ion signal (s) at each photon energy (E). Also, the reaction time (t) has been recorded using the "start" and "stop" constant fraction discriminators and TDC described in section 3.1.6.
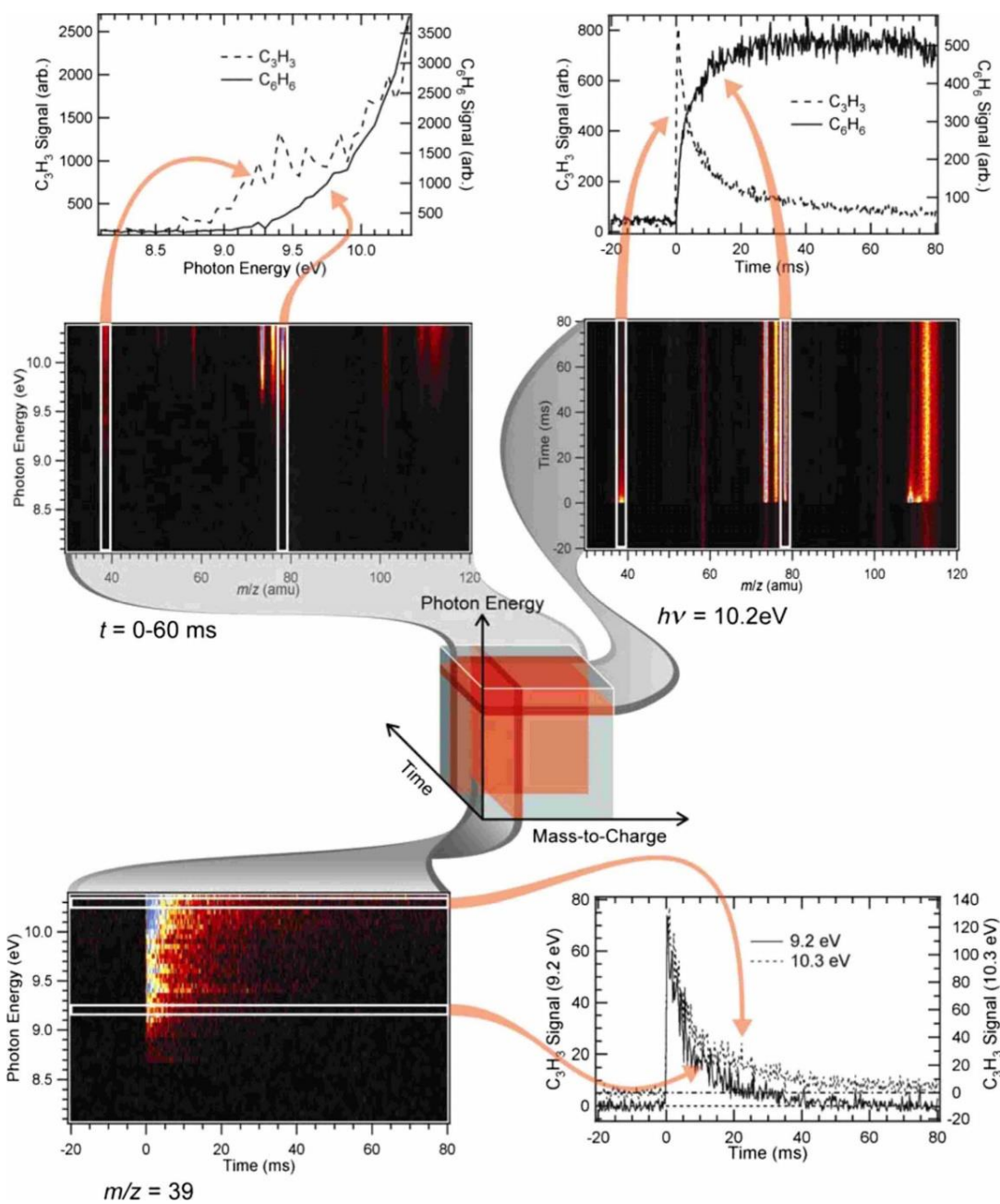
**Figure 3.1.7:** The three-dimensional dataset obtained from photooxidation reactions using MPIMS at the Chemical Dynamics Beamline 9.0.2 at the ALS in Berkeley, CA.[7]

The analysis begins with IGOR Pro by Wavemetrics.[34] The procedure file is a custom-made ALS kinetics file that enables higher-level computation to compile the data with greater ease. The pre-laser shot (before 20 ms) background can be subtracted. A calibrated vacuum ultraviolet sensitive photodiode provides a measured photocurrent, enabling the ion signal to be normalized at each photon energy.

The three-dimensional data block is difficult to analyze. However, 2-dimensional slices of the data can be taken while holding the last variable constant. In this way, mass spectra can be visualized. These are the colored spectra in Figure 3.1.7, with the setting in IGOR pro at "BlueHot256" to show intensity differences. Furthermore, vertical slices of the 2D data sets can be taken to arrive at 1D graphs. The most useful slices are photoionization efficiency curves (PIE curves), as described in the previous chapter of this thesis, and time-traces.

PIE curves examine the ion signal intensity (S) as a function of photon energy (E) at a particular *m/z*. In this case, the observation of a PIE is independent of time. These PIE curves are represented top left image in Figure 3.1.7. As discussed in Chapter 2, these curves are highly useful in identifying the ion in that the onset of the curve corresponds to the adiabatic ionization energy of the species. In addition, the shape of the experimental curve should match the photoionization cross section of the molecule. Note that the vertical slices obtained from reactions can possess contributions from more than one ion. Equations 2.2.5a and 2.2.5b presented in the previous chapter become useful in this scenario.

Time-traces, or kinetic traces, show the ion signal intensity (S) as a function of time (t). A fraction of the reactants deplete at the time of laser firing, $t_0$, as a portion of the initial concentration of starting material is consumed by the H-abstraction by chlorine radicals. Primary products of interest to combustion processes should be detected with an inverse slope equal to the depletion of the parent molecule. If the timescale of a product formation is much later, it likely is due to secondary reactions (i.e., further reactions with chlorine, self-reactions, etc.). Radicals, which are substantially more reactive and short-lived than product molecules, possess very sharp kinetic traces, where there is a detection in formation followed a sudden depletion. The dotted line in the top right 1D spectrum of Figure 3.1.6 is symptomatic of radical instability and is a general representation of the short lives of these species.

## 3.2 Aerosol Photoelectron Spectroscopy

Research was conducted at the National Synchrotron Radiation Research Center in Hsinchu City, Taiwan in the Spring of 2015. The focus of the experiment was to determine an effect of an acidic environment on the electronic behavior of isoprene and gamma-valerolactone. As aerosol research is a fairly new and emerging field of interest, there have been a limited number of studies conducted in the fashion reported in this thesis. The aerosol work reported here was inspired by, and in collaboration with, Dr. Chia Wang of National Sun Yat-sen University in Kaohsiung, Taiwan.[35]

### 3.2.1 Sample Preparation

The samples can be prepared in the chemical instrumentation room along the main circumference of the beamline floor. In order to be able to witness any changes in photoelectron spectrum as a result of pH, many dilute solutions (sample + $H_2O$ + HCl) of known concentration (anywhere from 0.01M to 0.25M) are prepared. In some cases, alternative solvents such as dimethyl sulfoxide (DMSO) can be used. The pH of each solution is measured using a Suntex SP-701 pH meter, as shown in Figure 3.2.1.
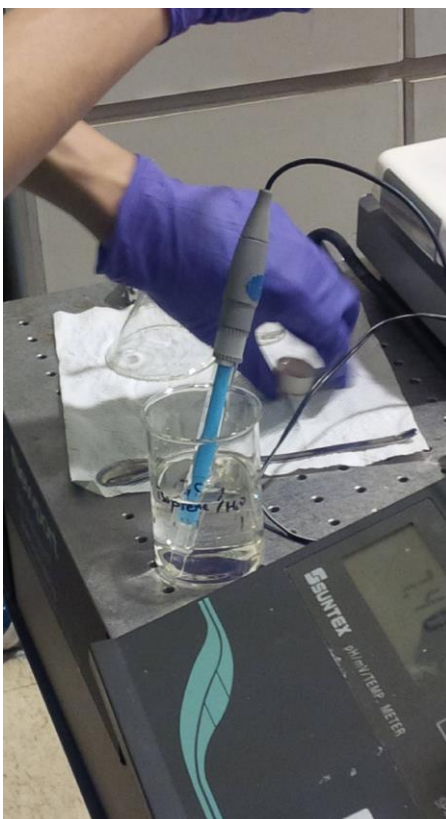


**Figure 3.2.1:** The preparation of 0.1M isoprene + HCl solution. Photo taken in March of 2015 at the NSRRC.

## 3.2.2 The Apparatus and Overall Reaction

The overall apparatus is pictured in Figure 3.2.2a, including an aerosol source region, a differential pumping region, and the ionization region.
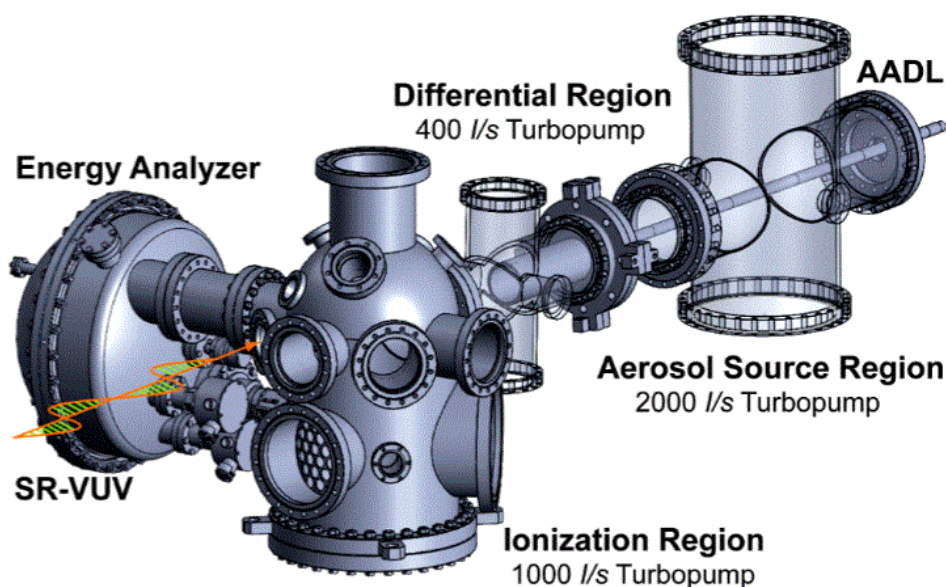


**Figure 3.2.2a:** The view of the aerosol VUV photoelectron spectroscopy apparatus at the BL21B2 beamline at the NSRRC in Hscinchu City, Taiwan.[35]

The overall reaction begins with a beam of neon gas flowing from a cylinder into the Model 9306 atomizer[36] where the pressure is managed by a regulator and gauge on the atomizer. The aerosol is generated as the liquid sample is forced through small nozzles and the particles are suspended in the carrier inert gas through the output nozzle (Figure 3.2.2b). It enters the aerosol source chamber, where it proceeds through the adjusted aerodynamic lens (AADL) system for the purpose of better size-selection, as well as the formation of a highly collimated beam. The average droplet size of the particles is ~100 nm. The aerosol source region is

pumped by a turbomolecular pump of 2000 L s$^{-1}$ and the pressure in the aerosol source chamber is maintained at ~$10^{-3}$ Torr.
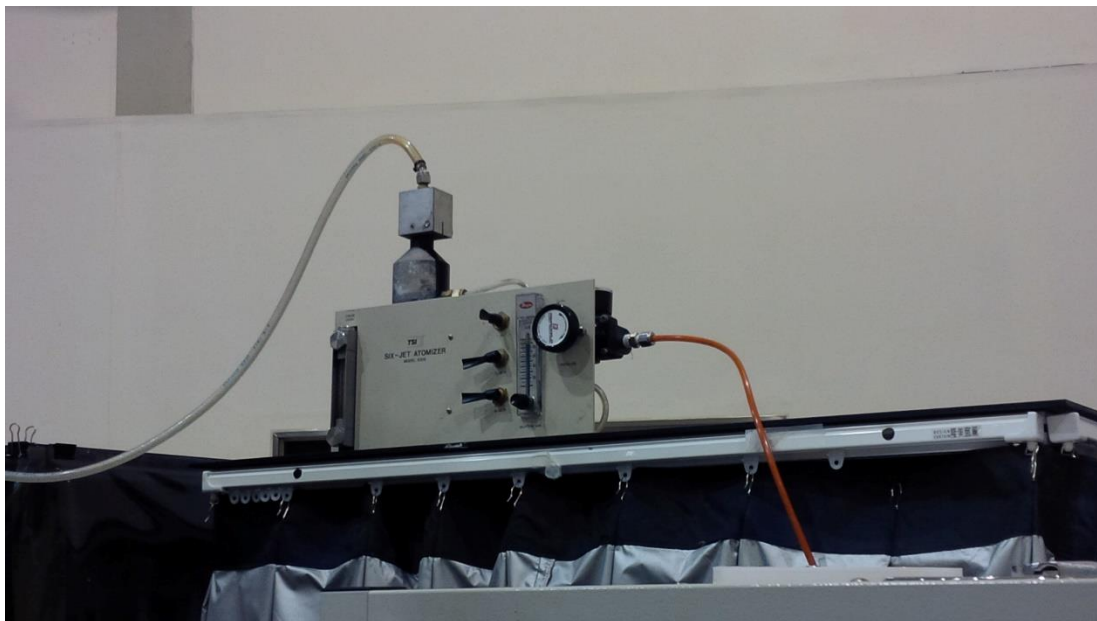


**Figure 3.2.2b:** The atomizer is attached to a pressurized neon cylinder and the output it connected to the aerosol source chamber. Photon taken in March of 2015.

After passing through the aerosol source region, the collimated aerosol beam continues through the differential pumping region with a 400 L s$^{-1}$ turbomolecular pump. It enters the ionization region where it crosses with the VUV synchrotron light of a particular energy, as defined by the parameters of the monochromator. The beam was manually directed using a set of adjustable flanges and visually inspected to determine the overlap with the photon beam. In addition, the photoelectron signals provided insight to how well the beams intersected. The ionization region is pumped with a 1000 L s$^{-1}$ turbomolecular pump.

Electrons are released upon intersection of the photon and aerosol beams if the energy is sufficient for photoionization. A R3000 model (Scienta Omicron)[37] hemispherical electron energy analyzer is installed at 54.7° with respect to the direction of the photon beam and is used to detect the kinetic energy distribution of the ejected photoelectrons.[35] The acceptance angle of the analyzer is 10°. A general idea of the direction of the photon beam, aerosol beam, and ejected electron trajectory are shown in Figure 3.2.2c.
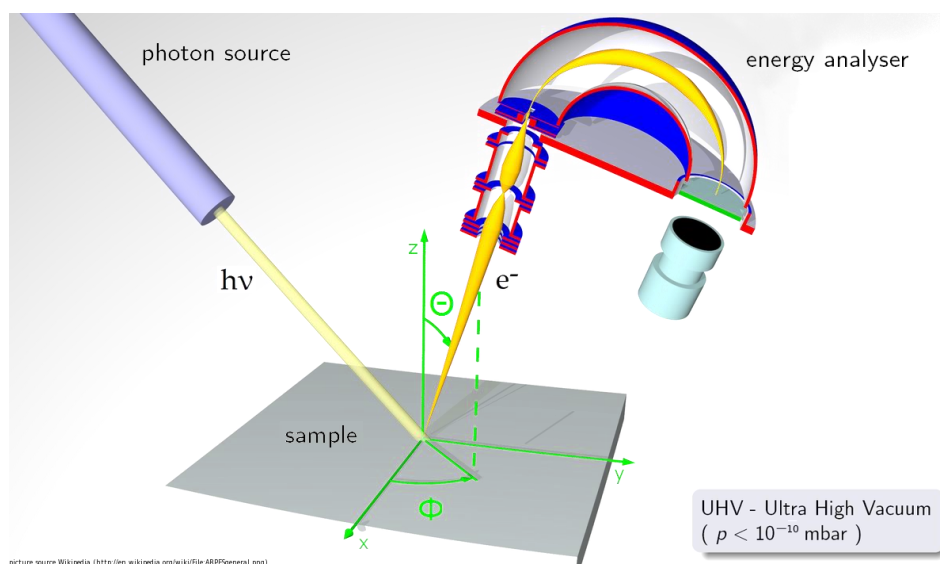


**Figure 3.2.2c:** The intersection of the photon and aerosol beams to generate the photoelectron beam. The hemispherical electron energy analyzer used at the NSRRC is analogous to that drawn in this image.

If the photon energy of the VUV beam is known (hv), and the kinetic energy of the electron is measured, then the electron binding energy can be determined. Information on the electronic characteristics of the molecule in question can be ascertained as described in the section on photoelectron spectroscopy previously

88

discussed in this thesis (section 2.2.4), and equation 2.2.4d is written again here as equation 3.2.2 for clarity:

$$eKE = h\nu - BE \tag{3.2.2}$$

### 3.2.3 Aerosol Generation and Sizing

The prepared samples with specific pHs were added into a TSI Inc. Model 9305 six-jet atomizer[36] (Figure 3.2.3a). This model atomizer has a built-in pressure regulator and gauge, and any combination of the six particle-generating atomizer jets can be selected at a time. Each of the jets can produce particle concentrations greater than $10^7$ particles cm$^{-3}$ at 6.5 L/min. The particle number concentration and total particle output are able to be manipulated, as well.[36] The liquid sample can be added to the atomizer on the top towards the left and monitored with a window to observe the liquid level. The inert gas inlet is located on the right side of the atomizer through the pressure regulator and to the atomizer. The outlet nozzle is located at the top, from where the aerosol can be transported to the aerosol source region.

The atomizer is able to use the pressure of the inlet carrier gas to force the liquid through small nozzles on any of the six small jets. As it does so, the liquid particles are separated into much smaller particles that are able to suspend into the carrier gas. To determine the size distribution and number density of the aerosol particles, a scanning mobility particle sizer (Model 3936, TSI Inc.) was used along with a condensation particle counter (CDC), as well as a differential mobility analyzer (DMA). Figure 3.2.3b shows the size distribution among the detected particles measured by Su et al. in a recent measurement using cysteine.[35]

**Figure 3.2.3a:** The six-jet TSI Inc. Model 9306 atomizer used in the photoelectron spectroscopic studies at the NSRRC.
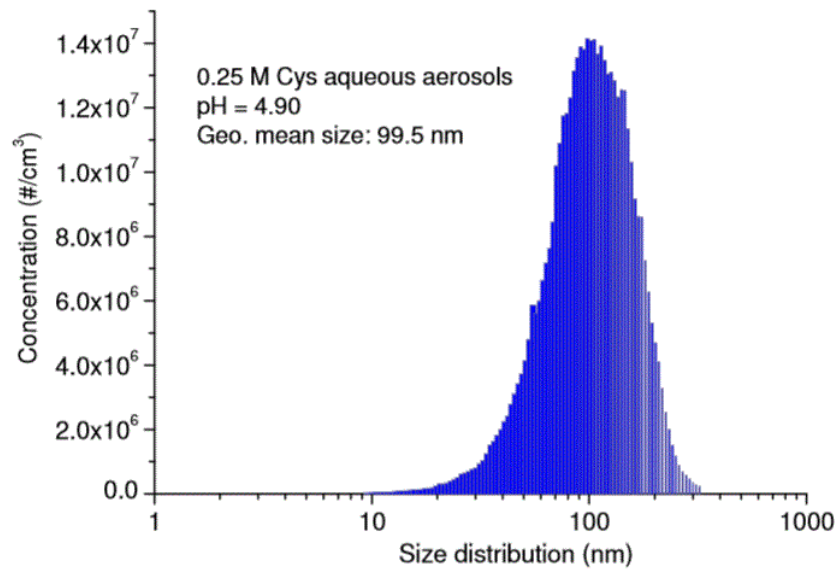


**Figure 3.2.3b:** Size distribution of 0.25 M Cysteine aqueous aerosols, measured by the scanning mobility particle sizer. The geometric mean size is 99.5 nm.[35]

The polydisperse size distribution underscores the need to select the size for more precise aerosol investigation. In which case, the output of the atomizer is attached to an adjustable aerodynamic lens (AADL).

Liu et al.[38, 39] described the formation of a particle beam by expanding an aerosol through a nozzle into an evacuated chamber. The narrowness of the particle beam can be improved by utilizing axisymmetric flow contractions and enlargements upstream of the nozzle. These contractions and enlargements of aerosol particles are known as "aerodynamic lenses."

The overall aim of the aerodynamic lenses is to focus intermediate-sized particles. The small particles follow gas streamlines and are not focused, while the large particles are defocused by the lens. A general schematic with the labeled parts is provided in Figure 3.2.3c.
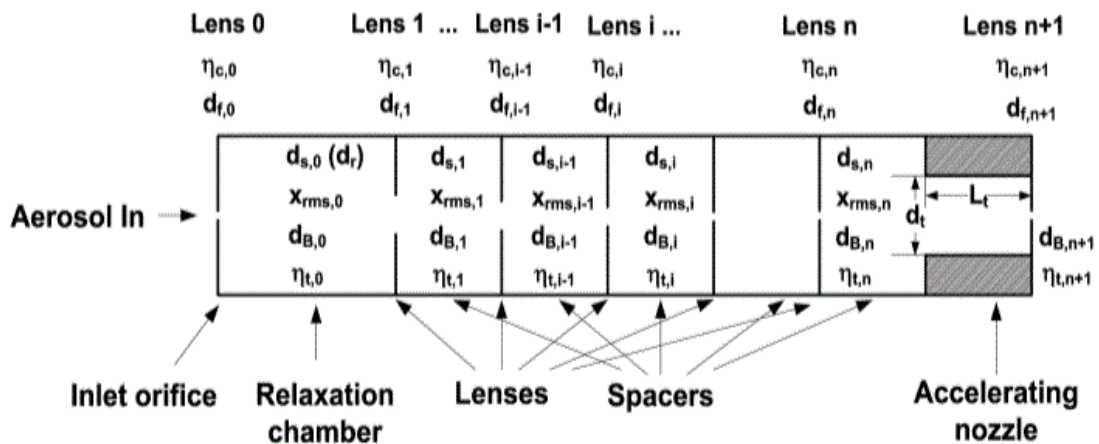


**Figure 3.2.3c:** Diagram of an aerodynamic lens system.[40]

Consider a steady flow of particles in a carrier gas with radial streamline $r_o(-\infty)$ in Figure 3.2.2d. The particle radical position $r_p(-\infty)$ will typically separate from the carrier streamline radial position due to inertial effects. The degree to which this occurs is known as the particle stream contraction factor ($n$), calculated as

$$n = \frac{r_p(\infty)}{r_0(\infty)} \tag{3.2.3a}$$



$$\text{Particle Stream Contraction Factor } \eta = \frac{r_p(\infty)}{r_0(\infty)}$$
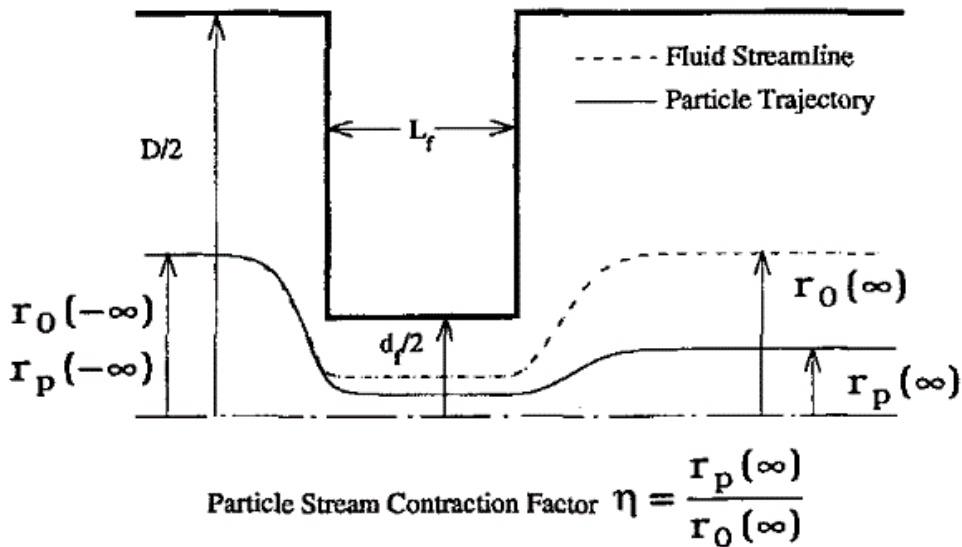
**Figure 3.2.3d:** A closer look at the inside of an AADL. Particle with carrier gas flow begins at the left, shown as $r_0(-\infty)$.[38]

In figure 3.2.3d, the fluid or mixture passes through a tube that has an inner diameter of D. There is a cylindrical constriction (the lens) with an inner diameter of $d_f$ and a length of $L_f$. Spacers are the separation distances between lenses. These distances should be long enough for allowing the converging and diverging patterns of the beams, although there is currently no guideline on the spacer length.[40]

The degree to which the trajectory deviates is mostly due to the Stokes number (S). The Stokes number is the ratio of the particle stopping distance at the average orifice velocity (u) to the orifice diameter ($d_f$).[40]  It is determined by

$$S = \frac{\tau u}{d_f} = \frac{2\rho_p d^2{}_p C_c m}{9\pi \rho_1 \mu d^3{}_f} \qquad (3.2.3b)$$

where $\tau$ is the particle relaxation time, $d_f$ is diameter of the lens aperture, $d_p$ is the diameter of the particle, $\rho_p$ is the particle material density, $\rho_1$ is the carrier gas density, $\mu$ is the carrier gas viscosity, $C_c$ is the Cunningham slip correction factor, and m is the mass flowrate.[40] The Cunningham slip correction factor is determined using the Knudsen number (Kn) in the following two equations:

$$C_c = 1 + Kn_p(1.257 + 0.4e^{\frac{-1.1}{Kn_p}}) \qquad (3.2.3c)$$

$$Kn_p = \frac{2\lambda_1}{d_p} \qquad (3.2.3d)$$

The relationship between the Stokes number (S) and the particle stream contraction factor (*n*) is easily visualized by Figure 3.2.2e. It can be observed that a multi-lens system with similar lenses is effective for focusing particles with sizes close to the desired size. The spacing, size, and locations of the lenses enable the selection of a particle size of interest for use in experimentation, and the Aerodynamic Lens Calculator[41] can be used in the determination of these parameters.

The accelerating nozzle is located at the exit of the tube AADL system and is depicted at the far right of the schematic shown Figure 3.2.3c. The nozzle is important for the regulation of particle beam shape, which is contingent upon the

93

shape of the nozzle itself. The nozzle geometry is cylindrical, and as a result the particle is accelerated to an inward direction to form a narrow, low divergence beam.[38]

The AADL at the NSRRC beamline BL21B2 has an internal diameter of 10 mm. The inlet nozzle of the AADL is 300 μm, while the four orifices are equal to 5.0, 4.5, 4.0, and 3.5 mm in diameter with a spacing of 50 mm. The accelerating nozzle is 3.0 mm. The series of decreasing orifices (by size) enables the bulk of particle-free gas to be stripped away, enabling only aerosol particle-containing beams to be channeled to a collimated beam. The average size of the aerosol particles in the beam is ~ 100 nm.
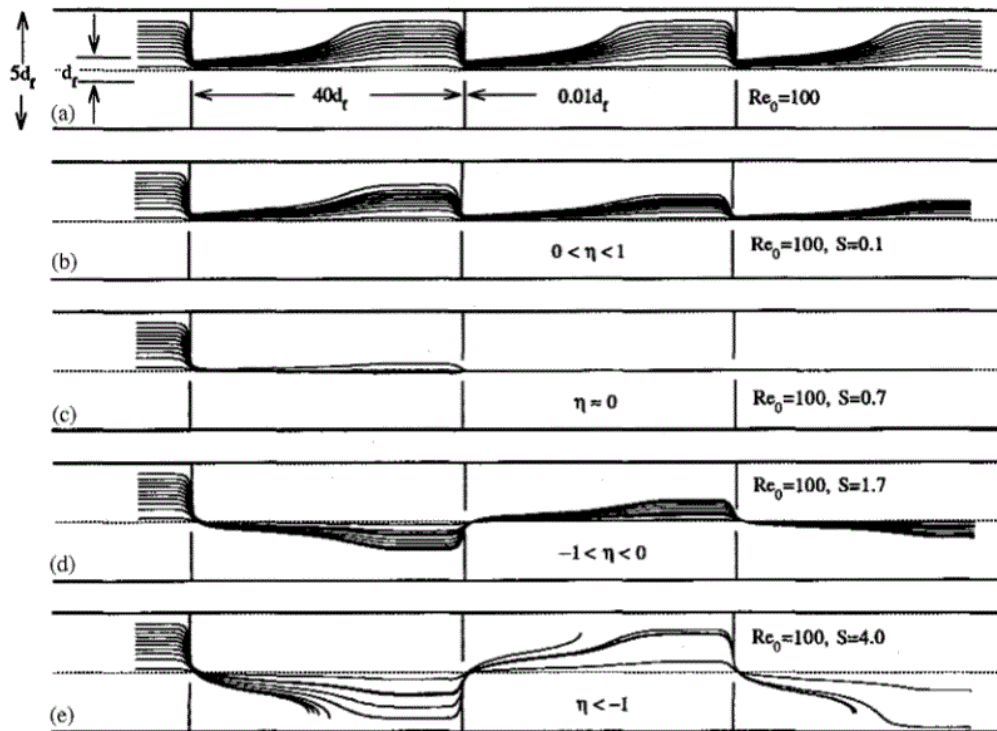


**Figure 3.2.3e:** The motion of particles in a three-lens AADL system.[38]

94

## 3.2.4 The Photoionization Source

The general schematic of the photoionization source at the gas phase spectroscopy beamline (BL21B2) at NSRRC is similar to that previously described for the Chemical Dynamics Beamline 9.0.2 at the Advanced Light Source. At the synchrotron, electrons are emitted from an injector, which is composed of an electron gun and a 50-MeV linear accelerator (Linac), shown on the right side of Figure 3.2.4a. The beam of electrons enter a booster ring of 72 meter circumference and reach 99.999995% the speed of light and are then injected into a storage ring through a transport line of 70 m. The storage ring at the NSRRC is hexagonal, as opposed to the dodecagonal shape at the ALS. The circumference of the storage ring is 120m.
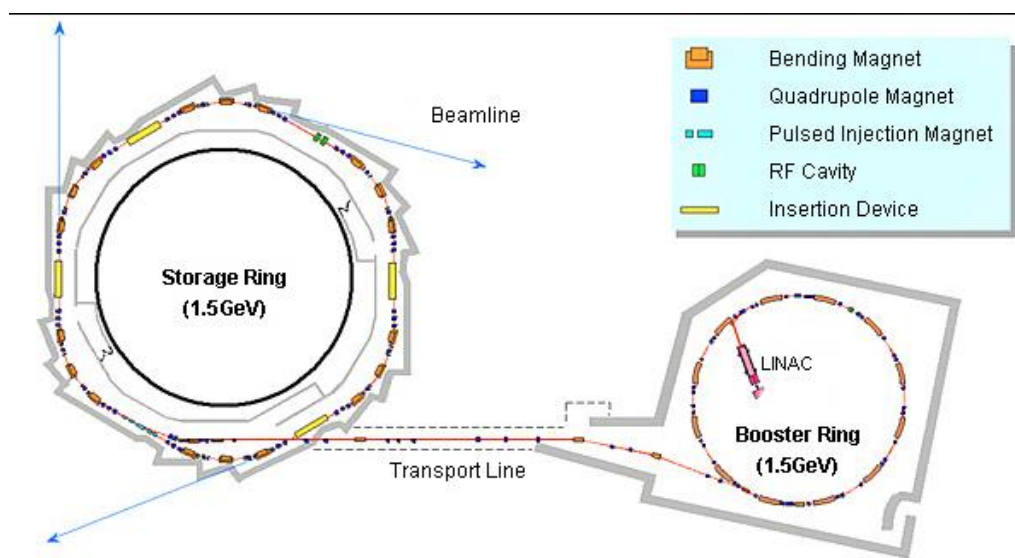


**Figure 3.2.4a:** A layout of the synchrotron and electron path. Synchrotron radiation is emitted in the form of photon beams (blue lines) that extend to the beamlines via undulator ports.[42]

95

The beamlines have different undulators available, depending on the need of the experiment. A 3.9 m U9 hybrid model undulator is used at the BL21B2 beamline to generate radiation when the electron beams travel through and are bent. The U9 undulator has a period of 9 cm with a total of 48 periods, the flux at $10^{12}$ photons s$^{-1}$, and the photon energy generated can range from 5 to 100 eV.[43]

Analogous to the beamline at the ALS, the multi-harmonic synchrotron radiation generated by the U9 undulator and magnetic fields should be filtered. Since only the first harmonic photons are desirable, a gas cell containing noble gas is used to absorb light above the ionization energy of the gas. An image of the light absorption cell is provided in Figure 3.2.4b, courtesy of the NSRRC.
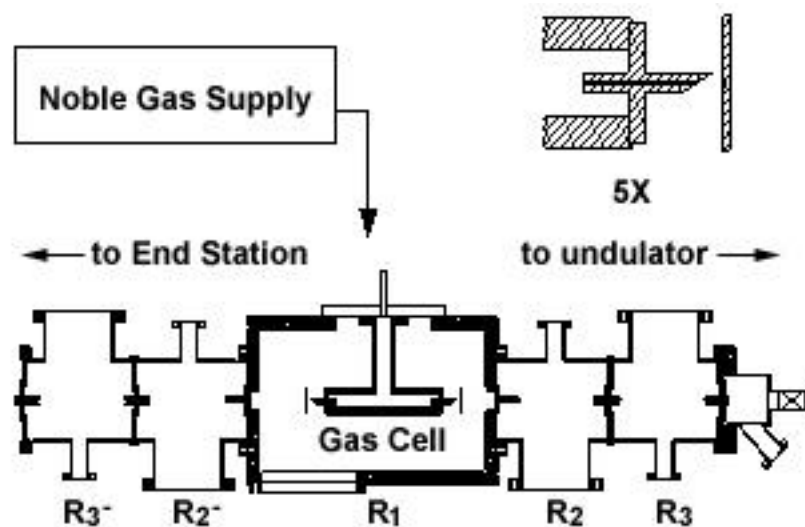


**Figure 3.2.4b:** Schematic of the gas filter that suppresses higher-order harmonic light from the undulator before progressing through the entrance slits of the monochromator.[15]

The 6 m cylindrical grating monochromator (6-M CGM) provides two energy branches that use separate entrance slits, where the low energy branch includes a grating angle of 150° to provide photon energies from 5 to 30 eV (Figure 3.2.4c). The high energy branch includes a grating angle of 130° to provide photon energies from 15 to 100 eV.

The bandwidth (BW) of a photon beam refers to the range of wavelengths ($\Delta\lambda$) about a specific wavelength ($\lambda$), and as the light produced by undulators is relatively monochromatic the bandwidths are written in units of 1/1000 or 0.1% BW:

$$0.1\% \ BW = \frac{\Delta\lambda}{\lambda}$$
3.2.4

The flux of $10^{12}$ photons s$^{-1}$ generated by the U0 undulator signifies the number of photons per second per 0.1% BW, while the brightness of the beam takes into account the direction of all photons.[44] If photons diverge, the brightness of the light is diminished. Alternatively, if photons travel parallel and in the same direction then the brightness is much more intense. The brilliance demonstrates the intensity of photons able to be focused onto a small area, which is determined by the cross-section area of the undulator. The smaller the area of the photon source, holding divergence and flux constant, the greater the brilliance of the light. The U9 undulator produces a brilliance of light on the order of $10^{16}$ to $10^{17}$ photons/sec/mm$^2$/mrad$^2$/0.1%BW/200mA, where 200 mA is the ring current.
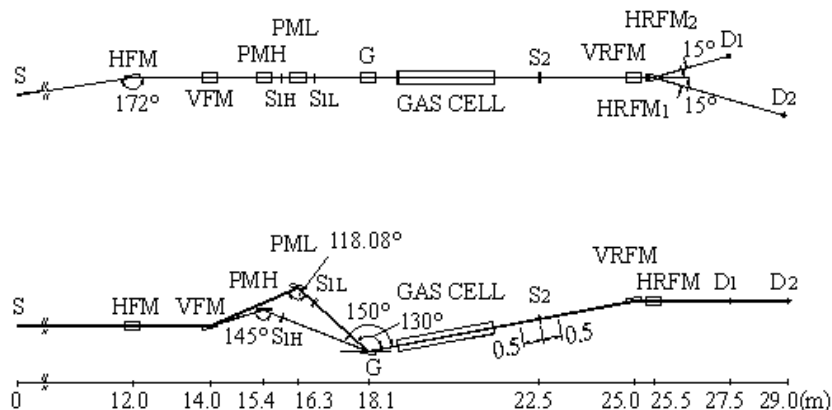
**Figure 3.2.4c:** The two energy branches of the U9-CGM (cylindrical grading monochrometer).Top: lower-energy branch up to 30 eV of photon energy. Bottom: higher-energy branch up to 100 eV of photon energy. The radiation source is represented by S, HFM is the horizontal pre-focusing mirror, VFM is the vertical prefocusing mirror, $S_{1H}$ and $S_{1L}$ are the entrance slits. PMH and PML are the plane mirrors, G are the gratings, VRFM is the vertical refocusing mirror, $HRFM_1$ and $HRFM_2$ are the horizontal refocusing mirrors, and D1 and D2 are the sample positions.[45]

## 3.2.5 Analysis

The ejected electrons from the photoionization of the aerosol beam are passed through a set of microchannel plates (MCP), and are then detected with a hemispherical energy analyzer (R3000)[37] with an acceptance angle of 10° and resolution of approximately 3 meV at 50 eV.[46] The pulse counting mode can be used to measure photoelectron signal.

The electron signals are recorded onto the hard drive of the computer and can be visualized as shown in Figure 3.2.5a, with the integrated counts in arbitrary units (a.u.) on the y-axis and the kinetic energy (eKE) on the x-axis in eV.
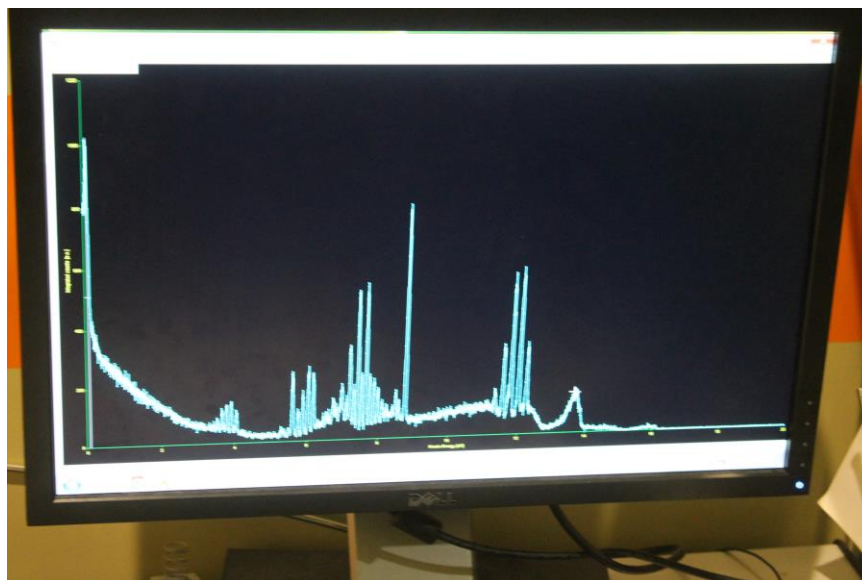


**Figure 3.2.5a:** The visualization of the PE spectrum of an aerosol measured at the NSRRC in March 2015.

Water can be used to calibrate the energy scale of the spectra by obtaining the photoelectron spectra of atomized water and matching known bands. Su et al.'s[35] work on aerosols at the BL21B2 beamline demonstrates the resulting PE spectrum, shown in Figure 3.2.5b. Using pure water in the atomizer, the contribution of both the gas phase and condensed phase (water particles of ~100 nm) are visually observable. It was found that the ionization energy of the condensed droplets was 1.79 ± 0.05 eV less than that of the gaseous water molecules. The vibrationally-

resolved bands of gas-phase water (0,0,0) and (1,0,0) are used to calibrate the energy scale.
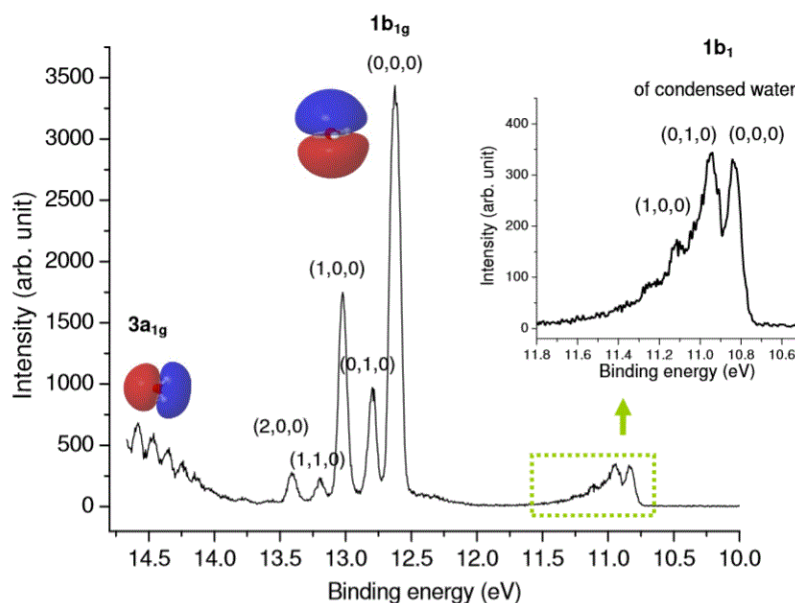


**Figure 3.2.5b:** The VUV photoelectron spectra of pure water aerosols at 25 eV. The gas-phase water molecules have a higher ionization energy (~12.52 eV) than the condensed phase (10.83 eV ± 0.05 eV). As such, the gas-phase spectrum is toward the left of the graph and the condensed phase is toward the right, also magnified in the inset of the image.[35]

The solvent utilized to make the sample solution must be atomized and its photoelectron spectrum obtained at the same photon energy for reference. Literature PE spectra of gas-phase molecules of interest are also highly useful as guides in examining the resultant experimental photoelectron spectrum.

Once the photoelectron spectra have been deconvoluted and the spectrum of sample aerosol isolated at each pH value, it can be observed if the there is a change in molecular orbital character as a function of pH. If so, the distinct band shapes in

the photoelectron spectra can be explained using Gaussian[47] calculations that can help determine the structural form of the molecule.[48]

## 3.3 TPEPICO at University of the Pacific, Stockton

Threshold Photoelectron Photoionization (TPEPICO) spectroscopy studies the unimolecular photodissociation dynamics of a molecule of interest. It is a combination of photoionization mass spectrometry and photoelectron spectroscopy, both presented earlier in this thesis in sections 3.1 and 3.2, respectively.

The apparatus is currently housed at the University of the Pacific with Professor Bálint Sztáray. It was originally built at the University of North Carolina, Chapel Hill with support from the U.S. Department of Energy (DOE).

### 3.3.1 The Experiment and Apparatus

A block diagram for the apparatus is represented in Figure 3.3.1a.
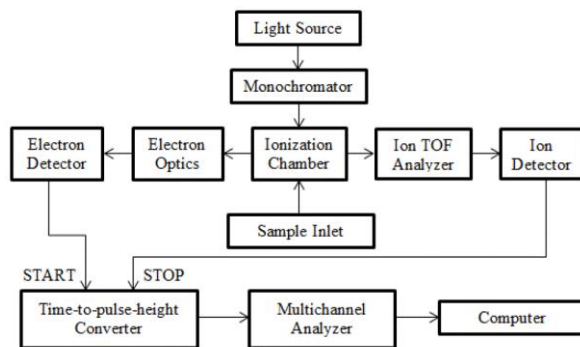


**Figure 3.3.1a**: A block diagram of the TPEPICO apparatus at the University of the Pacific, Stockton.[49]

Photons are generated via a hydrogen discharge lamp that operates at approximately 1 – 1.5 Torr $H_2$. Generally speaking, a hydrogen discharge lamp contains a pair of electrodes inside a glass tube. The glass tube has a small section containing quartz or silica through which the generated photon beam is able to be transmitted. The photons are generated when an electric current is passed through the electrodes and a high voltage is reached. At this point the hydrogen molecules are excited to higher level orbitals, and when they relax there is an emission of radiation in the form of light. The hydrogen lamp is on the right side of Figure 3.2.1b labeled "Danger High Voltage".
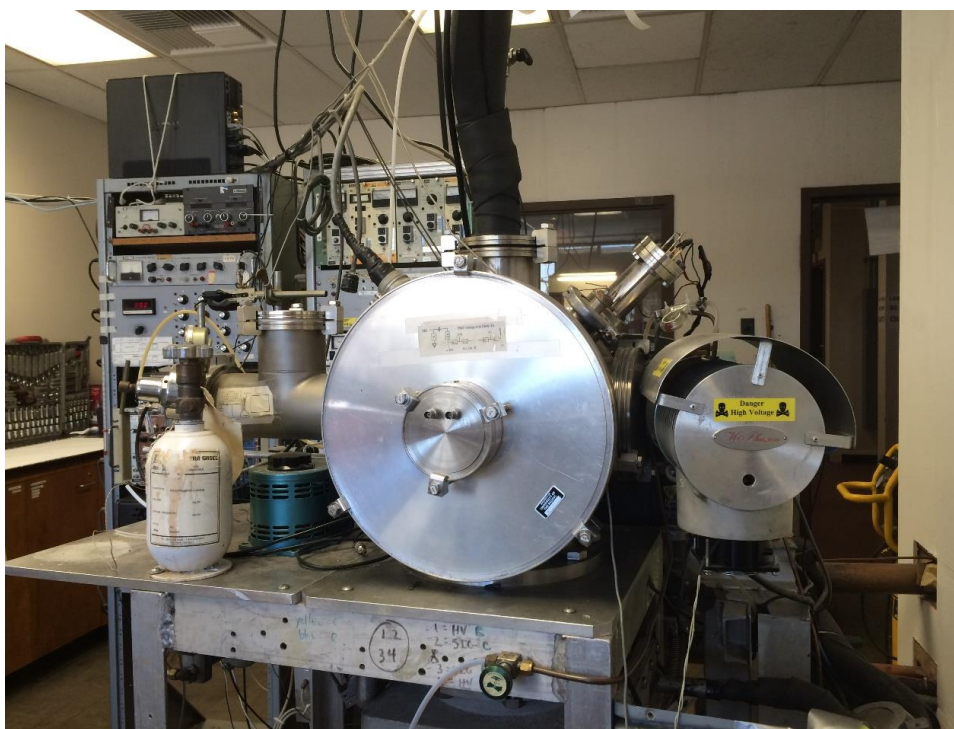


**Figure 3.3.1b:** View from the end of the ionization chamber. The hydrogen lamp is covered and labeled with "Danger High Voltage". Image taken at the University of the Pacific, Stockton in June 2015.

The wavelength corresponding to a particular photon energy can be selected with a 1 m normal incidence monochromator, where the entrance and exit slits are set to 100 μm. The photon energy can be varied from 6 to 14.5 eV, and the 1 Å wavelength resolution of the monochromator corresponds to 8 meV at 10 eV.[50] The photon energy was calibrated using Lyman-α and Lyman-β emission lines at 1216 Å and 1026 Å, respectively. The monochromator (green) can be visualized in Figure 3.3.1c.
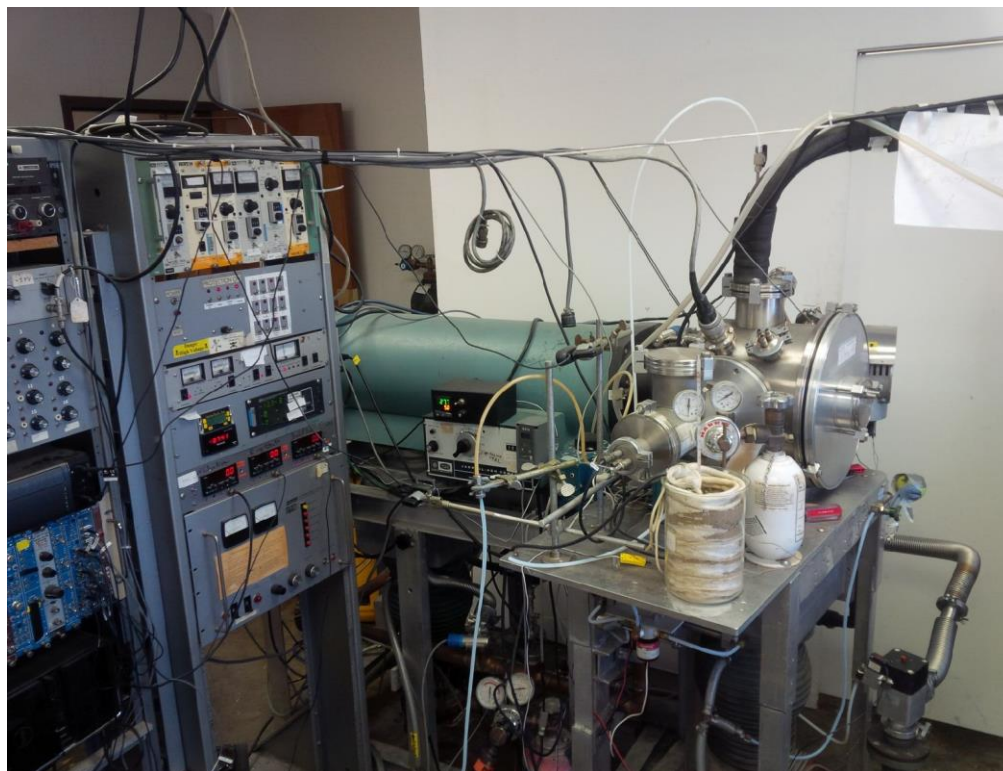


**Figure 3.3.1c:** The TPEPICO apparatus at the University of the Pacific, Stockton. The vapor sample inlet is attached to the ionization chamber (right), where the molecular beam is orthogonally intercepted by VUV photons coming from the hydrogen lamp (behind the ionization chamber) through the monochromator (green). Photo taken in October 2015.

The pressure in the ionization chamber before adding the sample is typically ~3 x $10^{-7}$ Torr. The vapor of the liquid sample is effusively introduced into the ionization chamber via a needle valve. The pressure can be monitored throughout the experiment to ensure there is no change. The molecular beam of the sample is orthogonally intercepted by the VUV photon beam. If the energy of the photon beam is greater than the ionization energy of the molecule, then it will ionize. The ions resulting from this process travel in one direction toward the linear time-of-flight (LinTOF) mass spectrometer, while the ejected photoelectrons travel in the other direction to the electron analyzer (Figures 3.3.1d and 3.3.1e).

The ions are directed with Wiley-McLaren[51] space-focusing geometry and accelerated to 100 eV in a long acceleration region of 5 cm. After the first region, they are quickly accelerated to 260 eV in a short acceleration region of 5 mm. In this case, the force on the ions is constant and the kinetic energy of each molecule is equal. As described previously in section 3.1.6 and represented by equations 3.1.6a-c, the velocity of the ion is inversely proportional to its mass and the time of flight is inversely proportional to the square root of the mass of the ion. Once they have surpassed the acceleration regions, they enter a 34 cm field-free drift region and encounter a set of Chevron-style Burle (now Photonis) microchannel plates (MCPs).[52]

The photoelectrons are extracted through a 6.75 mm long field of 20 V cm$^{-1}$ and are accelerated into a 13 cm drift tube set to 77 V. A mask at the end of the drift region contains a 1.4 mm aperture for the Channeltron detector (center) and 2 x 8
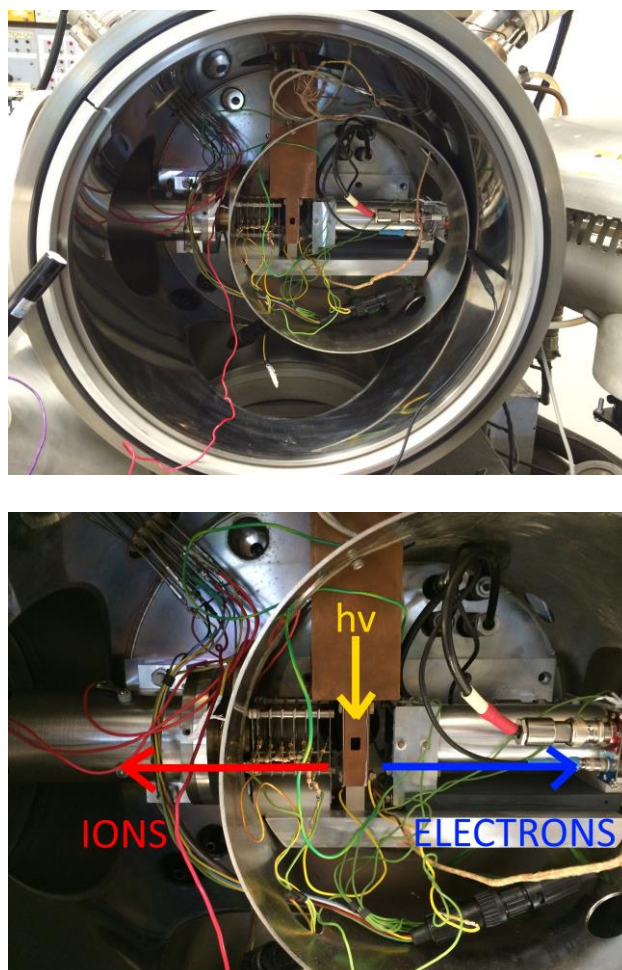
**Figure 3.3.1d:** Top: the inside of the ionization chamber. Bottom: A zoomed-in photograph with
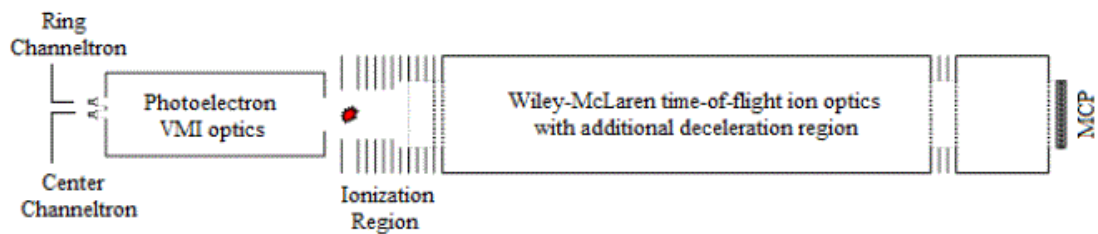


**Figure 3.3.1e:** A labeled schematic of the image shown at the bottom of Figure 3.3.2d.

mm opening for the hot electron detector. The velocity map imagining technique (VMI) was first introduced to the TPEPICO apparatus by the Baer group,[53] and enables the photoelectrons to be focused onto rings depending on their velocity perpendicular to ejection.[53] Zero kinetic energy threshold electrons are detected at the center. While some hot electrons are still able to be detected by the center, the hot electron detector provides a well-defined fraction of energetic electrons that have contaminated the center. Hot electrons can be subtracted from the signal of the central detector.[49, 54]

The ejection of an electron and the corresponding ion are detected in coincidence, meaning that they result from the photoionization of the same type of molecule. First, the near-weightless electron is detected (on either the "center" or the "ring"), signaling the "start" time that is logged into a time-to-pulse-height converter (TPHC). When the corresponding ion is detected, another TPHC logs the "stop" time and the information is sent to Ortec multichannel analyzer (MCA) cards. These MCA cards assess a stream of voltage pulses and organize the points into a histogram of counts vs. pulse-height.[55] Each histogram can be displayed as the time of flight spectra at each particular photon energy.

The reaction can be "tested" at a particular temperature, pressure and photon energy. Holding the pressure and temperature constant, more tests can be conducted. If the signals are agreeable, the monochromator is configured to scan a photon energy range designated by the user. In this particular apparatus, the $H_2$ photon flux is not constant from one energy to another, and to obtain the threshold

photoelectron spectrum (TPES), theoretically the signals at each energy can be normalized by time and pressure. However, in terms of breakdown diagram generation, the TOF signals are normalized as fractional abundance at each specific photon energy, where flux variance between measurements do not affect the analysis of dissociation dynamics.

A TOF spectrum is generated at each photon energy. The parameters of the "run" are input as a script to the TPEPICO control computer by defining the starting photon energy for the experiment, as well as the step-size, number of steps, and length of time for each photon energy. The amount of time at each photon energy increases the number of counts detected, providing a larger sample size and greater precision in measurement.

### 3.3.2 Programs and Analysis

The data obtained from the Ortec MCA cards are written to the hard drive in .tdat file format. These files can be opened using Notepad, Wordpad, or most other text-based processes. The TPHC enables the coincidence counts from both the center detector, as well as the ring detector, to be listed in a series of numbers. The total number of points depends on the number of active channels in the multi-channel analyzer (MCAS number). This can be controlled by the TPEPICO input script, as it is the range of the TOF divided by the TOF resolution.

The points can be visualized by plotting the point number (1,2,3…) on the x-axis and the output signal on the y-axis using IGOR Pro 6[34]. The first half of the numbers correspond to the detection of electrons on the center, while the second

half of the numbers relate to the detection of hot electrons on the ring. For example, if the signal is recorded in a series of 10,000 data points, the first 5,000 points of the .tdat text file correspond to hits on the center detector and the second 5,000 are hits on the ring detector. This is useful to visualize the signal, but is also useful in the deconvolution of adjacent peaks and adjusting for isotopologues, which will be described in greater depth later in this section.

A custom-made TPEPICO Data Processing program (version 1) provided by the Sztáray group at the University of the Pacific automatically converts the multichannel analyzer number (MCAS) to the appropriate TOF in µs. In addition, the center counts and the ring counts are overlapped for easy visualization. Figure 3.3.2a shows a TOF spectrum of ethylenediamine (EN) and its dissociative fragments at a photon energy of 9.501 eV. The red peaks are hot electrons from the ring and the blue are threshold electrons from the center.

A weighted factor can be used to determine the count of zero kinetic energy electrons. This factor can be experimentally found by using spectra obtained at various energies above the dissociation limit of the parent ion, where the parent ion should no longer exist. The average ratio between the parent ion intensities at both the center and the ring can be obtained, and this factor can be multiplied by the hot-electron count on the ring and then subtracted from the count at the center.[49]

The white text box at the very top of the TPEPICO Data Processing program (Figure 3.3.2a) is used for script input for the integration of time of flight peaks. Since the time of flight of an ion is inversely proportional to the square root of its mass

108

(3.1.6c), each TOF peak corresponds to a particular *m/z*. For fast dissociations where the TOF peaks are Gaussian-shaped, the peaks can be integrated from the tail of one end of the curve to that of the other to determine the total intensity of ions formed at each *m/z*. The integration ranges, in units of μs, can be typed as a script and executed in the TPEPICO Data Processing program.
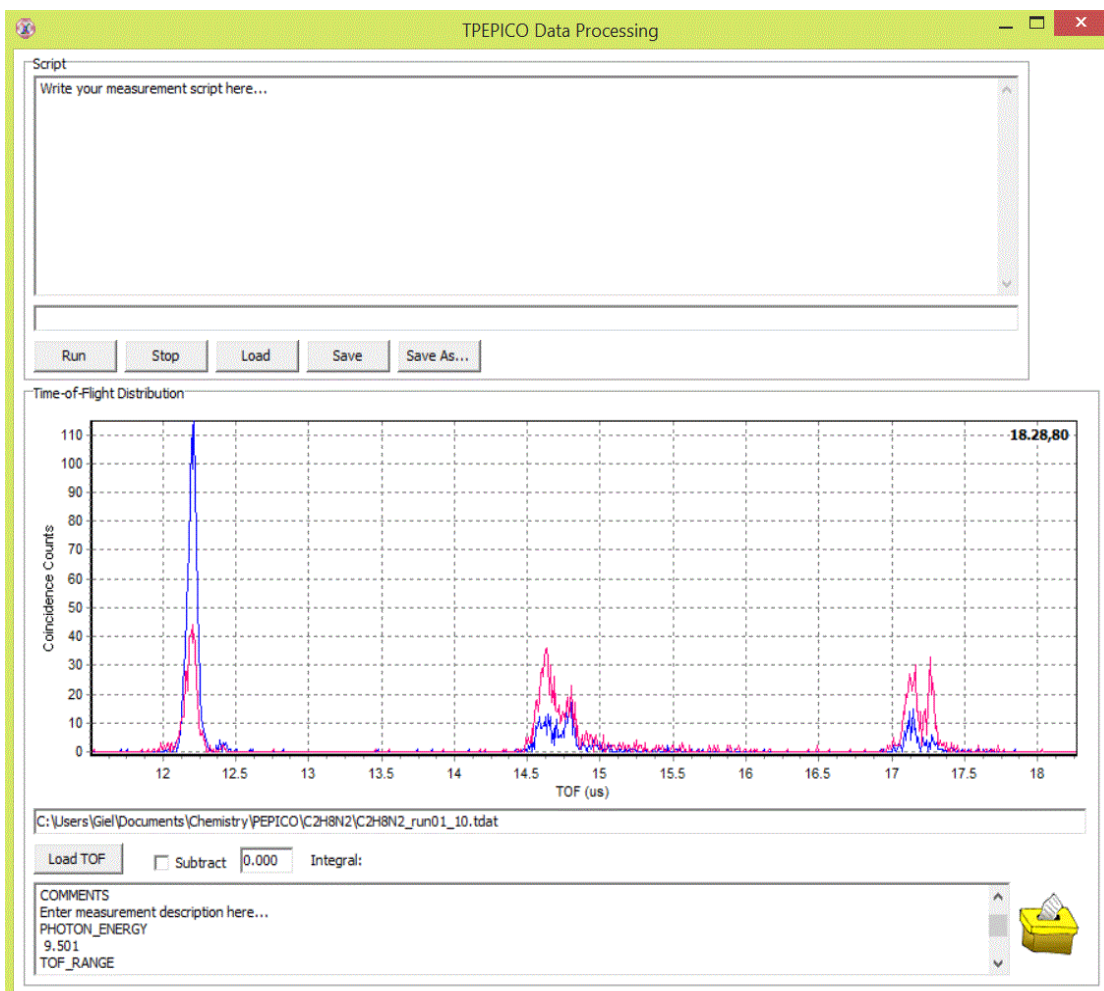


**Figure 3.3.2a:** A TOF spectrum of 0 K ethylenediamine (EN) photodissociation at 9.501. EN⁺· and its isotopologue peak are shown on the right. The ring signal (red) is

multiplied by a weighted factor and subtracted from the center detector signal (blue) to arrive at the count of zero kinetic energy electrons.

Slow dissociations occur when the parent ion does not dissociate immediately, but rather while traveling through the drift tube. Slow dissociations are manifested in asymmetric TOF peaks, an example of which is shown in Figure 3.3.2b. However, when the parent ion possesses greater internal energies in excess of the dissociation limit, the dissociation becomes faster and the peak resolves itself to a more normal distribution (Figure 3.3.2c).[56, 57]



**Figure 3.3.2b:** An asymmetric TOF peak is detected in 0 K ethylenediamine photodissociation at 9.125 eV using TPEPICO. Data taken at University of the Pacific on May 31, 2015. The signal from the center detector is blue, the signal from the ring detector is red, and the corrected center signal using a factor of 0.22 is shown in green. These non-Gaussian peak shapes are representative of slow dissociation reactions.

If there are no adjacent TOF peaks, the asymmetric TOF peak can be integrated in the same way as fast dissociation peaks to determine the intensity of the cationic fragment. However, if nearby peaks are detected it is important to adjust

the integration range in the script, as the right tail end of the curve shifts with an increase in energy to become more Gaussian.
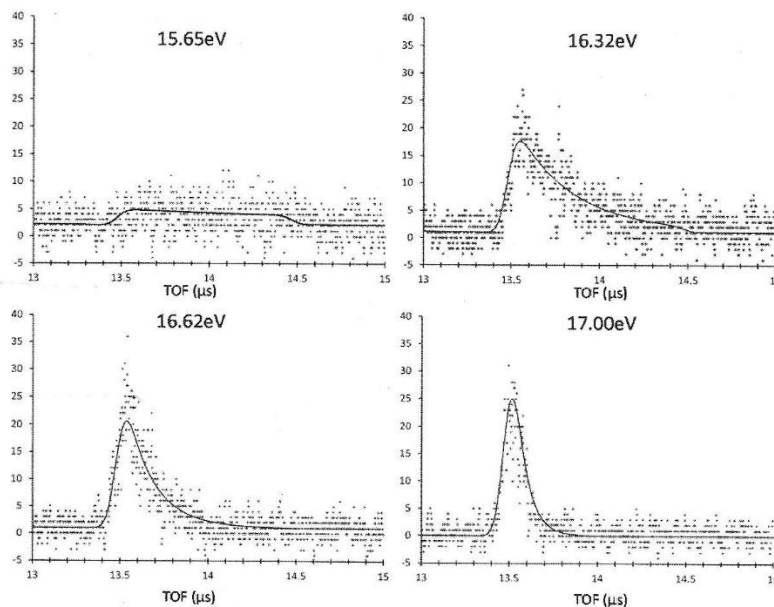


**Figure 3.3.2c:** A PEPICO study of the naphthalene radical cation dissociation. As the photon energy increases, it can be seen that the TOF peak grows increasingly more Gaussian. The dots are experimental TOF counts while the solid lines are modeled using theoretical techniques.[57]

The deconvolution of adjacent peaks can be tedious in that there is an overlap of the signals. A custom-made program by Krisztian Torma of the Sztaray group at University of the Pacific aims to deconvolute peaks and can be useful in specific instances. In addition, the multi-peak fitting tool in Igor Pro[34] has several mathematical curve-fitting features that enable the user to distinguish the contribution of each curve to the overlap between them. The images in Figure 3.3.2d, for instance, were generated by plotting the counts of threshold electrons vs

multichannel number (MCAS) in the ethylenediamine TPEPICO photodissociation experiment presented in Chapter 6. Here, ethylenediamine and its $^{13}$C isotopologue were visualized at a photon energy between its ionization energy and its first dissociation limit. A mathematical equation was fit to each curve and the area underneath was calculated. The isotopic ratio of $^{13}$C to $^{12}$C was verified in this way (~2.2%). In addition, the contribution of each isotopologue to the overlap can be assessed by subtracting the area of the mathematical fit of one curve from the total area underneath both curves.
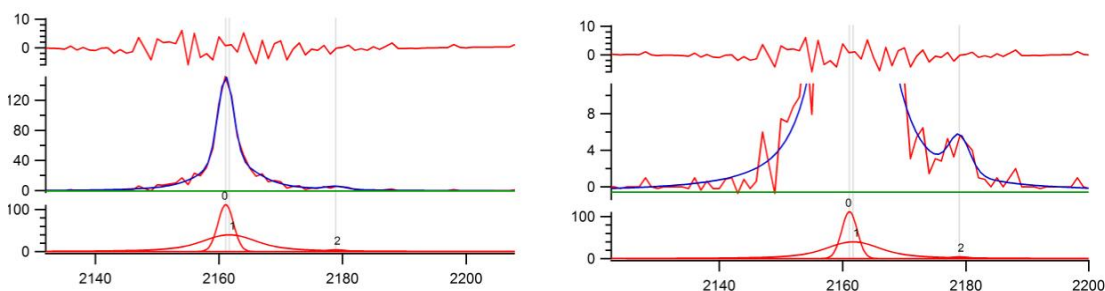


**Figure 3.3.2d:** The IGOR multi-peak fitting in the deconvolution and determination of isotopologue contributions to adjacent peaks. Shown above is parent ion *m/z* = 60 and the ~ 2.3% $^{13}$C and $^{15}$N isotopologue contribution at 8.8 eV.

Average background noise is determined by integrating flat areas in the TOF spectrum, both on the left side of the detected peaks as well as the right. The integrated values of all of the TOF and noise peaks are printed by the TPEPICO Data Processing program.

The intensity of each *m/z* at the respective photon energy is input into an Excel spreadsheet, and the background intensity and isotopologue signal can be accounted for through appropriate subtraction and addition where necessary.

The breakdown diagram can be generated as the fractional abundance of the parent and daughter ions at each photon energy via the Excel spreadsheet. All intensities are normalized by dividing the signal of each $m/z$ by the total number of counts at each photon energy.

The breakdown diagram can then be imported into MiniPEPICO[58] computational software for analysis. Quantum mechanical calculations using Gaussian 09[47] suite can be completed as described in section 2.4 of this thesis. The rotational constants and frequencies of the neutral species, as well as the frequencies of the parent cationic radical, are required for input into MiniPEPICO.[58] From these optimized Gaussian structures, the calculated adiabatic ionization energy (2.2.4c) is determined and entered into the software, as well. This energy serves as the baseline (0) for all relative barrier energies used in the program.

Transition states are visually inspected using GaussView[59] to ensure it is the saddle point on the potential energy surface for the correct transition. The real frequencies for each state, along with the calculated dissociation barrier are entered into the program. The lowest frequencies of calculated transition states are scaled to match experimental data.[49] MiniPEPICO[58] is then able to calculate all necessary density and number of states functions, internal energy distributions, and dissociation rates to model a theoretical breakdown diagram for direct comparison with the experimental. In the case of slow dissociations, modeled TOF spectra also need to match the experimental results, as shown in Figure 3.3.2e. The optimized, modeled

breakdown diagram from MiniPEPICO provides the experimentally-extracted photoionization onset (appearance energy) of each fragment.

With appropriate data analysis, the reaction rates for each dissociation channel can be obtained with MiniPEPICO[58] through statistical modeling. Three unimolecular rate theories are included in the software program: the RRKM Theory,[60-62] the variational transition state theory (VTST)[63], and the simplified statistical adiabatic channel model (SSACM).[64] The reaction rates are printed into a .rat file that can also be opened using Notepad, Wordpad, or other text-based programs.
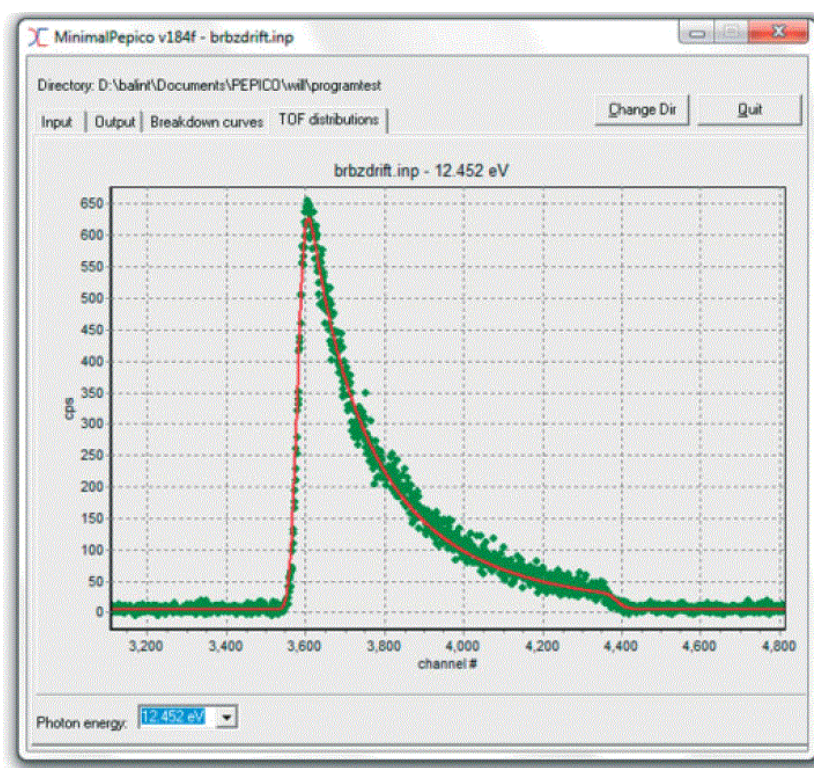


**Figure 3.3.2e:** A slow TOF distribution is modeled using MiniPEPICO; the green dots are experimental, the solid red line is the modeled curve.[58]

114

## 3.4 References

1.  Khanin, Y.I., *Fundamentals of Laser Dynamics*. 2006, Cambridge: Cambridge International Science Publishing.
2.  Svelto, O. and D.C. Hanna, *Principles of Lasers, 3rd ed.* 1989, New York: Plenum Press.
3.  Ng, M.Y.-H., *The Investigation of the Low Temperature Combustion of Mesitylene and Tert-Amyl Methyl Ether by Synchrotron Photoionization Mass Spectrometry*, in *Chemistry*. 2015, University of San Francisco: San Francisco.
4.  *Principles of Light Sources for Lithography*. 2014 [cited 2015 December 19, 2015]; Available from: http://www.martini-tech.com/principles-of-light-sources-for-lithography/.
5.  He, Q., *Investigation of Gamma-Valerolactone + OH and Isobutanol + OH Combustion Systems Using Synchrotron Photoionization Mass Spectrometry*, in *Chemistry*. 2011, University of San Francisco: San Francisco, CA.
6.  Svelto, O., *Principles of Lasers, 4th ed.* 1998, New York, USA: Springer.
7.  Osborn, D.L., et al., *The multiplexed chemical kinetic photoionization mass spectrometer: A new approach to isomer-resolved chemical kinetics.* Review of Scientific Instruments, 2008. **79**: p. 104103-1/104103-10.
8.  Ng, M.Y., et al., *Synchrotron Photoionization Study of Mesitylene Oxidation Initiated by Reaction with Cl (2P or O(3P) Radicals.* J. Phys. Chem. A, 2014. **118**: p. 3735-3748.
9.  Czekner, J., et al., *Absolute photoionization cross-sections of selected furanic and lactonic potential biofuels.* International Journal of Mass Spectrometry, 2013. **348**: p. 39-46.
10. Smith, A.R., *Absolute photoionization cross sections of furanic fuels: 2-ethylfuran, 2-acetylfuran and furfural.* Journal of Mass Spectrometry, 2015. **50**: p. 1206-1213.
11. Ray, A., *Characterization of Ethene + OH Products and Cyclohexene Ring-Opening Mechanism Elucidation Via Synchrotron Photoionization Mass Spectrometry*, in *Chemistry*. 2010, University of San Francisco: San Francisco.
12. *Turbo Molecular Pumps (Compound Molecular Pumps) Exhaust Theory*. 2010 [cited 2015 December 14, 2015]; Available from: http://www.osakavacuum.co.jp/en/products/pump_turbo/genri.html.
13. Delchar, T.A., *Vacuum Physics and Techniques*. 1993: Chapman & Hall.
14. *4.1.4 Compression Ratio*. 2015 [cited 2015 December 20, 2015]; Available from: https://www.pfeiffer-vacuum.com/en/know-how/vacuum-generation/vacuum-pumps-working-principles-and-properties/compression-ratio/.
15. *Research Facility/End Station*. 2010 [cited 2015 December 12, 2015]; Available from: www.nsrrc.org.tw/english/research8_1_Crossed_Molecular.aspx.
16. *Scroll Pumps*. 2013 [cited 2015 December 14, 2015]; Available from: http://hivatec.ca/our-services/vacuum-pump-maintenance-repair/scroll-pumps/.

17. *Design / Operating Principle*. 2015  [cited 2015 December 13, 2015]; Available from: https://www.pfeiffer-vacuum.com/en/know-how/vacuum-generation/roots-vacuum-pumps/.

18. Attwood, D. *Undulator Equation and Radiated Power*. 2007  [cited 2015 December 9, 2015]; Available from: http://www.eecs.berkeley.edu/~attwood/sxr2009/lecnotes/10_UndulatorEquatnRadPwr_2009.pdf.

19. *ALS Radiation is Produced by Bend Magnets and Undulators*. 2005  [cited 2015 December 9, 2015]; Available from: https://www.flickr.com/photos/advancedlightsource/4208770503/in/photostream/ .

20. Margaritondo, G., *A Primer in Synchrotron Radiation: Everything You Wanted to Know About Sex (Synchrotron emission of X-Rays) but Were Afraid to Ask.* Journal of Synchrotron Radiation, 1995. **2**: p. 148-154.

21. Suits, A.G., et al., *A differentially pumped harmonic filter on the chemical dynamics beamline at the Advanced Light Source.* Review of Scientific Instruments, 1997. **66**: p. 4841-4844.

22. *Hardware: Gas Filter*. 2015  [cited 2015 December 12, 2015]; Available from: www.chemicaldynamics.lbl.gov/gasfilter.html.

23. Heimann, P.A., et al., *Performance of the Vacuum Ultraviolet High-Resolution and High Flux Beamline for Chemical Dynamics Studies at the Advanced Light Source.* Review of Scientific Instruments, 1997. **68**: p. 1945-1951.

24. *Eagle off-plane beamline Optical Layout*. 2015  [cited 2015 December 9, 2015].

25. Ryer, A., *Light Measurement Handbook*. 1997, International Light, Inc.

26. Medway Optics, L. *Diffraction Gratings*. 2006  [cited 2015 December 10, 2015]; Available from: http://www.medwayoptics.com/product4.htm.

27. Smith, R.M., *Understanding Mass Spectra: A Basic Approach*. 2004, Hoboken, New Jersey: Wiley.

28. Herbert, C. and R. Johnstone, *Mass Spectrometry Basics*. 2003, New York: CRC Press.

29. Hoffman, E.D. and V. Stroobant, *Mass Spectrometry: Principles and Applications, 2nd ed.* 2001, England: Wiley.

30. Vallerga, J.V. and O.H.W. Siegmund, *2K x 2K resolution element photon counting MCP sensor with > 200 kHz event rate capability.* Nuclear Instruments and Methods in Physics Research Section A: Accelerators, Spectrometers, Detectors and Associated Equipment, 2000. **442**(1-3): p. 159-163.

31. Skoog, D.A., F.J. Holler, and S.R. Crouch, *Principles of Instrumental Analysis, 6th ed.* 2007, United States: Cengage Learning.

32. Gross, J.H., *Mass Spectrometry, 2nd ed.* 2011, Berlin Heidelberg: Springer.

33. *Microchannel Plate*. 2002  [cited 2015 December 10, 2015]; Available from: http://www.hioptic.com/night-vision-equipment/MCP-microchannel-plates/.

34. *IGOR Pro* 2013, Wavemetrics, Inc.: Portland, OR.

35. Su, C.-C., et al., *VUV Photoelectron Spectroscopy of Cysteine Aqueous Aerosols: A Microscopic View of Its Nucleophilicity at Varying pH Conditions.* Journal of Physical Chemistry Letters, 2015. **6**(5): p. 817-823.

36. *Six-Jet Atomizer 9306*. 2015, TSI Inc.: Shoreview, Minnesota.

37. *R3000 A Compact and Powerful Analysis Tool*. 2015 [cited 2015 December 12, 2015]; Available from: www.scientaomicron.com/en/products/357/1206.

38. Liu, P., et al., *Generating Particle Beams of Controlled Dimensions and Divergence: I. Theory of Particle Motion in Aerodynamic Lenses and Nozzle Expansions.* Aerosol Science and Technology, 1994. **22**: p. 293-313.

39. Liu, P., et al., *Generating Particle Beams of Controlled Dimensions and Divergence: II. Experimental Evaluation of Particle Motion in Aerodynamic Lenses and Nozzle Expansions.* Aerosol Science and Technology, 1995. **22**: p. 314-324.

40. Wang, X. and P.H. McMurry, *A Design Tool for Aerodynamic Lens Systems.* Aerosol Science and Technology, 2006. **40**: p. 320-334.

41. Wang, X. and P.H. McMurry, *Instruction Manual for the Aerodynamic Lens Calculator.* Aerosol Science and Technology, 2006. **40**: p. 1-10.

42. *Research Facility/Accelerator*. 2010 [cited 2015 December 11, 2015]; Available from: www.nsrrc.org.tw/english/accelerator.aspx.

43. *BL21B U9-CGM Spectroscopy Beamline*. 2010 [cited 2015 December 11, 2015]; Available from: edf.nsrrc.org.tw/manage/fck_fileimage/file/bldoc/21BU9CGM.htm.

44. Gruner, S., D. Bilderback, and M. Tigner, *Synchrotron Radication Sources for the Future*, in *ERL White Paper*. 2000, Cornell University: Ithaca, New York.

45. Song, Y.F., et al., *Design of an ultra-high resolution and high flux cylindrical grating monochromator undulator beamline.* Nuclear Instruments and Methods in Physics Research Section A: Accelerators, Spectrometers, Detectors and Associated Equipment, 2001. **467-468 Part 1**: p. 496-499.

46. Cochran, E. and G. Meloni, *Hypervalence in monoxides and dioxides of superalkali clusters.* Journal of Chemical Physics, 2014. **140**: p. 204319-1/204319-13.

47. Frisch, M.J., et al., *Gaussian 09*. 2009, Gaussian, Inc.: Wallingford, CT.

48. Jagoda-Cwiklik, B., et al., *Ionization of Aqueous Cations: Photoelectron Spectroscopy and ab Initio Calculations of Protonated Imidazole.* J. Phys. Chem. B, 2008. **112**: p. 7355-7358.

49. Borkar, S.N., *Very Accurate Gas-Phase Thermochemistry Through Photoelectron Photoion Coincidence (PEPICO) Spectroscopy*, in *Chemistry*. 2013, University of the Pacific: Stockton, California.

50. Hornung, B., et al., *Dissociative Photoionization of $X(CH_3)_3$ (X = N, P, As, Sb, Bi): Mechanism, Trends, and Accurate Energetics.* J. Phys. Chem. A, 2009. **113**(28): p. 8091-8098.

51. Wiley, W.C. and I.H. McLaren, *Time-of-Flight Mass Spectrometer with Improved Resolution.* The Review of Scientific Instruments, 1955. **26**(12): p. 1150-1157.

52. *Microchannel Plates*. 2015 [cited 2015 December 12, 2015]; Available from: https://www.photonis.com/en/microchannel-plates.

53.     Baer, T. and Y. Li, *Threshold Photoelectron Spectroscopy with Velocity Focusing: An Ideal Match for Coincidence Studies.* International Journal of Mass Spectrometry, 2002. **219**: p. 381-389.

54.     Sztaray, B. and T. Baer, *Suppression of Hot Electrons in Threshold Photoelectron Photoion Coincidence Spectroscopy Using Velocity Focusing Optics.* Review of Scientific Instruments, 2003. **74**(8): p. 3763-3768.

55.     *Multichannel Analyzers*. 2014   [cited 2015 December 24, 2015]; Available from: http://www.ortec-online.com/Solutions/multichannel-analyzers.aspx.

56.     Bodi, A., Hemberger, P., *Imaging breakdown diagrams for bromobutyne isomers with photoelectron-photoion coincidence.* Physical Chemistry Chemical Physics, 2014. **16**: p. 505-515.

57.     West, B., Joblin, C., Blanchet, V. ,Bodi, A., Sztaray, B., Mayer, P.M., *On the Dissociation of the Napthalene Radical Cation: New iPEPICO and Tandem Mass Spectrometry Results.* Journal of Physical Chemistry, 2012. **116**: p. 10999-11007.

58.     Sztaray, B., Bodi, A., Baer, T., *Modeling unimolecular reactions in photoelectron photoion coincidence experiments.* Journal of Mass Spectrometry, 2010. **45**: p. 1233-1245.

59.     Dennington, R., T. Keith, and J. Millam, *GaussView*. 2009, SemiChem Inc.: Shawnee Mission, KS.

60.     Marcus, R.A. and O.K. Rice, *The kinetics of the recombination of methyl radicals and iodine atoms.* J. Phys. Colloid Chem., 1951. **55**: p. 894.

61.     Rice, O.K. and H.C. Ramsperger, *Theories of unimolecular reactions at low pressures II.* J. Am. Chem. Soc., 1928. **50**: p. 617.

62.     Rice, O.K. and H.C. Ramsperger, *Theories of unimolecular reactions at low pressures.* J. Am. Chem. Soc., 1927. **49**: p. 1617.

63.     Hase, W.L., *Variational unimolecular rate theory.* Acc. Chem. res., 1983. **16**: p. 258.

64.     Baer, T. and W.L. Hase, *Unimolecular Reaction Dynamics: Theory and Experiments*. 1996, New York: Oxford University Press.

# Chapter 4: Low Temperature Chlorine-Initiated Oxidation of Small-Chain Methyl Esters: Quantification of Chain-Terminating HO₂-Elimination Channels

Giel Muller[†], Adam Scheer[§], David L. Osborn[‡],

Craig Taatjes[‡]*, and Giovanni Meloni[†]*

†University of San Francisco, San Francisco, California 94117

§Pacific Gas and Electric Company, 245 Market St. San Francisco, California 94111

‡Sandia National Laboratories, Livermore, California 94551

## 4.1 Abstract

Cl-initiated oxidation reactions of three small-chain methyl esters, methyl propanoate ($CH_3CH_2COOCH_3$; MP), methyl butanoate ($CH_3CH_2CH_2COOCH_3$; MB) and methyl valerate ($CH_3CH_2CH_2CH_2COOCH_3$; MV) are studied at 1 or 8 Torr and 550 and 650 K. Products are monitored as a function of mass, time, and photoionization energy using multiplexed photoionization mass spectrometry coupled to tunable synchrotron photoionization radiation. Pulsed-photolysis of molecular chlorine is the source of Cl radicals, which remove an H atom from the ester, forming a free radical. In each case, after addition of $O_2$ to the initial radicals, chain-terminating HO₂-elimination reactions are observed to be important. Branching ratios among competing HO₂-elimination channels are determined via absolute photoionization spectra of the unsaturated methyl ester coproducts. At 550 K, HO₂-elimination is observed to be selective, resulting in nearly exclusive production of the conjugated methyl ester coproducts, methyl propenoate, methyl-2-butenoate, and

methyl-2-pentenoate, respectively. However, in MV, upon raising the temperature to 650 K, other $HO_2$-elimination pathways are observed that yield methyl-3-pentenoate and methyl-4-pentenoate. In each methyl ester oxidation reaction, a peak is observed at a mass consistent with cyclic ether formation, indicating chain-propagating OH loss/ring formation pathways via QOOH intermediates. Evidence is observed for the participation of resonance-stabilized QOOH in the most prominent cyclic ether pathways. Stationary point energies for $HO_2$-elimination pathways and select cyclic ether formation channels are calculated at the CBS-QB3 level of theory and assist in the assignment of reaction pathways and final products.

Keywords: Biodiesel, Biofuels, Esters, Fatty Acid Methyl Esters, Methyl Butanoate, Oxidation, Combustion

*Corresponding Authors email: [cataatj@sandia.gov](mailto:cataatj@sandia.gov); gmeloni@usfca.edu

## 4.2 Introduction

Liquid fuels are a significant generator of $CO_2$ emissions in the United States, with combustion of transportation fuels accounting for 26% of U.S. greenhouse gas emissions in 2013.[1-2] Finding, characterizing, and developing carbon neutral sources of liquid fuels will be essential in a broader strategy to reduce the global warming impact of transportation.

Biodiesel derived from biomass is a potentially carbon-neutral energy source that could be scaled to much greater levels of production if more economical means of conversion are developed. Current biodiesel fuel typically consists of a mixture of long-chain hydrocarbons, predominantly fatty acid methyl esters (FAMEs), in which a

methyl ester functional group is attached to a hydrocarbon chain.[3] FAMEs are currently the leading biofuel in the European Union and are most often derived from industrial transesterification processes of vegetable oils or animal fats.[4] FAMEs are easily blended with petroleum fuels, enabling mixtures that can improve efficiency and help reduce dependence on traditional fossil fuel resources.[5-7]

In addition to increasingly stringent efficiency regulations, much effort has been devoted to measuring and comparing CO, NO, and particulate matter emissions from both petroleum and biodiesel blend combustion.[8] The nitrogen oxide species, $NO_x$, are the primary precursors for the generation of photochemical smog, which is known to pose serious health risks. Carbon monoxide emissions and particulate matter from fuel combustion are also harmful pollutants.[9] Combustion experiments consistently show that biodiesels often yield higher thermal efficiencies, less CO and reduced soot emissions compared to traditional petroleum fuels. However, biodiesel combustion also results in greater NO emissions than its petroleum counterparts.[10-14]

Because each biofuel source and blend is unique, the combustion of a particular fuel yields a distinct product mix. Thus, a number of recent studies are devoted to characterizing the combustion of oils derived from soybeans, canola, rapeseed, sunflower, palm, and Mahua, as well as their mixtures.[15-22] Regardless of the organic source of biodiesel, incomplete combustion of FAMEs in engines, causing release of unburned esters, which undergo subsequent atmospheric oxidation, is of major concern. As a result, these reactions and the resulting products need to be analyzed in order to ascertain the environmental effects that use of ester

121

fuels has on atmospheric chemistry.

Though a great deal of research is still needed to characterize ester combustion, oxidation and the associated atmospheric effects, concerted effort has been devoted to investigating combustion of $C_6$ - $C_{10}$ methyl esters, encompassing a relatively wide range in the number of carbons on the aliphatic main chain.[23-26] Dayma et al.[27] studied the oxidation of methyl hexanoate and reported a distinct negative temperature coefficient (NTC) zone, while Herbinet et al.[28] combined kinetic models of methyl decanoate, methyl-9-decanoate, and n-heptane in order to obtain a blended surrogate mechanism intended to approximate the combustion of biodiesel fuels derived from rapeseed oil. Models indicate that longer hydrocarbon chains in FAMEs yield more pronounced NTC behavior, which highlights the importance of the hydrocarbon chain in directing the low temperature oxidation chemistry.

Smaller saturated esters in fact do not exhibit an NTC region[29], and these compounds provide a means to isolate the oxidation chemistry specific to the ester moiety.[30-33] In particular, in an effort to minimize complexity and inform biofuel combustion models a great deal of attention has been devoted to the $C_4$ methyl ester, methyl butanoate (MB).[34-36] The MB oxidation mechanism mechanism posed by Fisher et. al[37] is often credited for sparking interest in MB as a potentially novel biofuel and studies have focused on its ignition properties over the last fifteen years.[38-40] Lin et al.[41] aimed to isolate the effect of the methyl ester moiety on combustion properties via kinetic modeling investigations of MB compared to *n*-butane. Because *n*-butane combustion displays NTC behavior while MB does not, it appears that the methyl ester functional group has a large influence on the oxidation

122

of smaller chain FAMEs.

Here we present a study of the initial reactions expected for low temperature autoignition of a series of short chain esters, methyl propanoate ($CH_3CH_2COOCH_3$; MP), methyl butanoate ($CH_3CH_2CH_2COOCH_3$; MB) and methyl valerate ($CH_3CH_2CH_2CH_2COOCH_3$; MV) (Scheme 4.2) at 1 or 8 Torr and 550K and 650K. The results presented here are expected to provide insight into the gas phase oxidation chemistry for both short chain FAMEs as well as carbon-centered radicals formed relatively close to the ester moiety of longer chain esters. These results should also serve as a valuable validation tool for the development of FAME kinetic models.
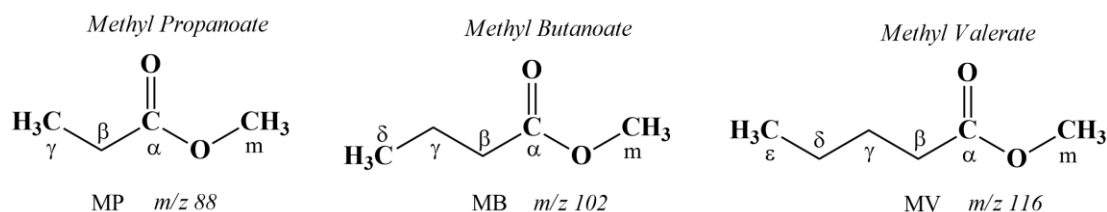


**Scheme 4.2:** The methyl ester reactants studied in these experiments with the main carbon chain labeled with Greek letters and the ester methyl group designated with an 'm.' This convention will be used throughout the text.

### 4.2.1 Fundamental Low Temperature Oxidation Chemistry of Oxygenates

Several recent studies of the low temperature oxidation chemistry of complex oxygenates demonstrate that while the conventional R + $O_2$ pathways remain important, the oxygenated functional groups can introduce new pathways and drive the outcome of $RO_2$ decomposition.[42-44] For a typical hydrocarbon peroxy radical ($RO_2$), a number of well-defined decomposition pathways are available. Concerted elimination of $HO_2$ yields an unsaturated coproduct. These reactions are effectively chain-terminating below ~1000 K due to the unreactive nature of the $HO_2$ radical

123

carrier. Alternatively, RO$_2$ can undergo isomerization via intramolecular H abstraction reactions that yield hydroperoxyalkyl radicals (QOOH) in which the radical center has shifted from the terminal peroxy oxygen to a carbon. These QOOH can undergo a second O$_2$ addition followed by a series of reactions leading to chain branching.[45] Of greater significance to this work, the QOOH can also undergo unimolecular decomposition reactions that yield OH and a stable cyclic ether coproduct. The OH is a reactive chain carrier and these reactions are thus deemed chain propagating. For an extensive discussion of the fundamental chemistry that governs hydrocarbon ignition, including chain-terminating HO$_2$-elimination channels, as well as chain-propagating and chain-branching pathways involving QOOH, we refer the reader to the work of Zádor, Taatjes and coworkers.[43-46]

In recent studies of ketone oxidation under similar low temperature, low pressure conditions, resonance-stabilized QOOH formation pathways were shown to greatly enhance chain propagation channels. In particular, channels that yield 5-membered ring cyclic ethers via low-strain 5-membered ring transition states were especially prominent[44, 47] The short MB hydrocarbon chain does not permit the production of 5-membered cyclic ether rings. However, radical formation at the terminal methyl group of the saturated 5-carbon chain of MV makes possible the formation of a resonance-stabilized QOOH and the subsequent 5-membered ring cyclic ether. Here we investigate the low temperature oxidation reactions of MP, MB and MV (Scheme 4.2) with the goal of identifying product formation channels and investigating differences in low-temperature oxidation chemistry as a function of chain length.

124

## 4.3 Experiment

The chlorination and oxidation reactions of MP, MB, and MV were studied at the Advanced Light Source (ALS) of Lawrence Berkeley National Laboratory. The details of these experiments have been presented in prior work[44, 48-49] and will only be briefly outlined here.

A mixture of reactants and He buffer gas is introduced into a heated 1.05 cm i.d. quartz flow tube via calibrated mass flow controllers. Pressure inside the tube is maintained at 8 Torr for the MB and MV experiments and at 1 Torr for the MP experiments. A pinhole approximately 650 μm in diameter is located along the side of the reactor. Effluent is continually sampled through a 1.5 mm diameter skimmer, creating a molecular beam that is directed into a differentially pumped ionization chamber. The molecular beam is orthogonally intersected by quasi-continuous, tunable ionizing vacuum ultraviolet radiation generated by the ALS synchrotron and the resulting ions are accelerated into a linear time-of-flight mass spectrometer. Products are observed as a function of time, mass, and photoionization energy, resulting in a three-dimensional dataset that can be sliced and integrated to attain the photoionization spectra and time profiles for each species.[48, 50]

An unfocused 351 nm excimer laser pulsed at 4 Hz provides the initial source of Cl· via photolysis of $Cl_2$. Approximately 1.5% of molecular $Cl_2$ is converted to Cl·.[51] The average pre-photolysis background signal is subtracted yielding mass spectra with positive signals for post-photolysis products. Signals are dependent on ionization energy and are normalized to the synchrotron photon current measured by a calibrated photodiode.

All reactant concentrations are provided in Table 1. MP, MB, and MV were commercially available with labeled purities of 99%. Methyl 2-propenoate, methyl 2-butenoate and methyl 3-butenoate were obtained commercially with noted purities of 99%, 98%, and 97%, respectively. Methyl 2-pentenoate and methyl 4-pentenoate were each obtained at 95% and trans-methyl 3-pentenoate at >90% purity. The absolute photoionization energy curves are generated as a result of flowing sample gas with a mixture of ethene, propene, and butene (calibration gases), compounds with known concentration for which the absolute photoionization cross sections are well-known. Absolute photoionization cross sections are determined as in Welz et al.[52] Each sample was freeze-pump-thawed to remove any dissolved gases before they were prepared to use in the experiment.

**Table 4.3**: Initial reactant concentrations (cm-3) used in the oxidation experiments. Helium was added to provide a total pressure of 8 Torr in all experiments, aside from methyl propanoate (MP) where the total pressure was 1 Torr.

| | Temp (K) | $[Precursor]_0$ | $[O_2]$ | $[Cl_2]$ | $[Cl\cdot]_0$ |
|---|---|---|---|---|---|
| MP | 550 | $5.1 \times 10^{12}$ | $7.8 \times 10^{14}$ | $9.3 \times 10^{12}$ | $9.7 \times 10^{10}$ |
| MP | 650 | $4.3 \times 10^{12}$ | $7.8 \times 10^{14}$ | $7.8 \times 10^{12}$ | $8.2 \times 10^{10}$ |
| MB | 550 | $7.0 \times 10^{13}$ | $2.0 \times 10^{16}$ | $6.7 \times 10^{13}$ | $7.0 \times 10^{11}$ |
| MB | 650 | $5.9 \times 10^{13}$ | $1.7 \times 10^{16}$ | $5.7 \times 10^{13}$ | $6.0 \times 10^{11}$ |
| MV | 550 | $6.9 \times 10^{13}$ | $2.0 \times 10^{16}$ | $6.7 \times 10^{13}$ | $7.0 \times 10^{11}$ |
| MV | 650 | $4.4 \times 10^{13}$ | $1.7 \times 10^{16}$ | $5.7 \times 10^{13}$ | $6.0 \times 10^{11}$ |

All geometry optimizations and energies have been calculated at the CBS-QB3 level of theory[53-55] with the Gaussian 09 suite.[56] Transition states, with one negative imaginary frequency, were determined by using the Synchronous Transit-Guided Quasi-Newton (STQN) method[57] at the B3LYP/6-31G(d) level/basis set with CBS-QB3 optimizations. Transition states were visually inspected using Gaussview.[58]

CBS-QB3 calculations have a mean absolute deviation (MAD) of $\pm$ 1.1 kcal $mol^{-1}$ compared to experimental dataof the G2/97 test set[55, 59-60]

## 4.4 Results and Discussion

### 4.4.1 Computational Results

Bond dissociation energies have been calculated for each C-H bond in MP with results given in Scheme 4.4.1a. The $C_\gamma$-H bond is calculated to be the strongest at 100.9 kcal $mol^{-1}$. Given the $BDE_{0K}$ of HCl (102.3 $\pm$ 0.05 kcal $mol^{-1}$), all hydrogen removals are exothermic.[61]
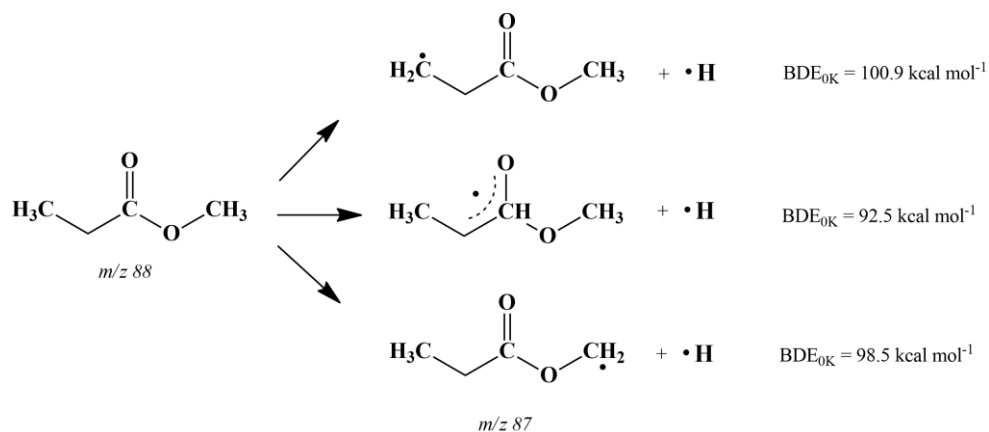


**Scheme 4.4.1a:** Adiabatic bond dissociation energies ($BDE_{0K}$) of methyl propanoate calculated at the CBS-QB3 level.

Thus each hydrogen represents an energetically accessible radical site. The weakest bond by more than 6 kcal $mol^{-1}$ is $C_\beta$-H due to the resonance stabilization of the resulting radical, as shown in Scheme 4.4.1b. Production of this radical is calculated to be exothermic by 9.8 kcal $mol^{-1}$. The large concentration of parent ester (Table 1) relative to initial Cl· concentration ensures that Cl· reacts primarily with parent ester

as opposed to the initial ester radials or subsequent products. The ratio of $O_2$ to initial Cl· is also kept large ($[O_2]/[Cl·] \sim 50$) to promote immediate consumption of the ester radicals by the desired $O_2$-addition reaction, while minimizing secondary chlorine chemistry.[44]
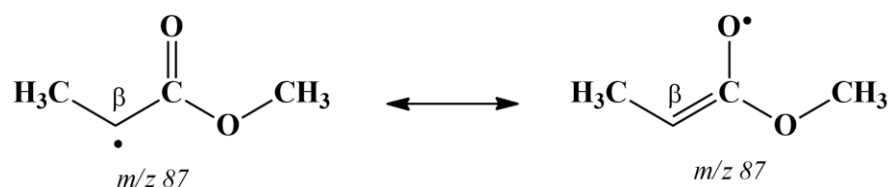


**Scheme 4.4.1b:** Resonance structures of the initial radical ($R_\beta$) at the $\beta$ -carbon site.

Figure 4.4.1a shows the CBS-QB3 stationary points calculated on the surfaces for the $R_\beta + O_2$ reactions of the three esters. Because these reactions yield conjugated coproducts, they are expected to be the lowest energy decomposition pathways for the $R_\beta O_2$ radicals.[42, 44, 47] In each case, the $RO_2$ well resulting from $O_2$ addition to the resonance-stabilized initial radical is shallow ($23 – 26$ kcal mol$^{-1}$). As a result, barriers for $R_\beta O_2$ back dissociation to $R_\beta + O_2$ reactants are calculated to be close to or below those for the further unimolecular $RO_2$ chemistry discussed above. Consequently, despite the high $O_2$ concentration, the initial $R_\beta$ are susceptible to secondary chemistry including reactions with Cl· and $Cl_2$ as well as self-reaction, reaction with other radicals (OH, $HO_2$, etc.) and possible reaction with the reactor walls. Indeed chlorinated products resulting from addition of Cl· to $R_\beta$ (Scheme 4.4.1c) are observed and are discussed further below.
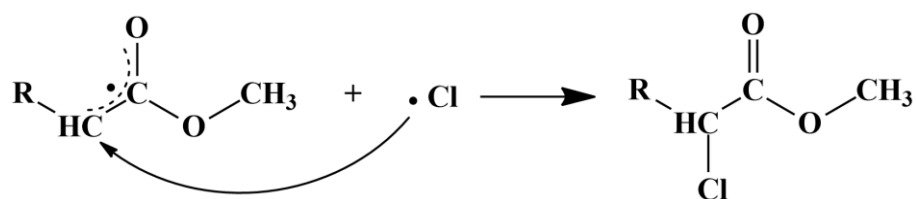
**Scheme 4.4.1c:** Resonance stabilization leads to long-lived initial radicals susceptible to secondary reactions, including addition of Cl·.
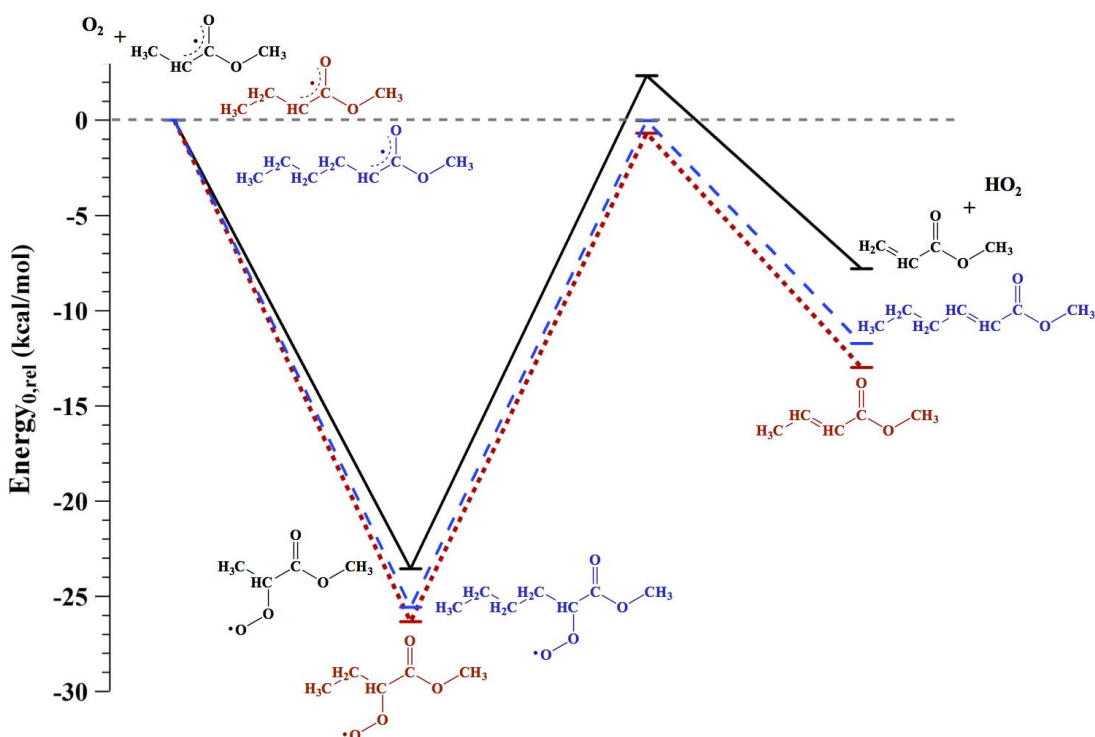


**Figure 4.4.1a:** Potential energy surface for the reaction of the initial methyl propanoate, methyl butanoate and methyl valerate radicals $R_\beta$ with $O_2$ followed by $HO_2$-elimination. Energies at 0 K are at the CBS-QB3 level. Cyclic ether formation channels are not expected to be favored and are thus not included (see text). Several β-scission channels are also possible but for clarity are not included.

Figures 4.4.1b – 4.4.1d show the potential energy surfaces calculated for the reaction of $O_2$ with the other initial radicals of MP (Figure 4.4.1b), MB (Figure 4.4.1c),

and MV (Figure 4.4.1d). In comparison to $R_\beta O_2$, $O_2$-addition to radicals generated elsewhere along the chain have significantly deeper wells relative to back dissociation (32 – 40 kcal mol$^{-1}$). In each case, peroxy radicals originating at the γ carbon have a low energy $HO_2$-elimination pathway (through a 5-member ring transition state) that yields a conjugated unsaturated ester coproduct. Peroxy radicals generated elsewhere along the main aliphatic chain have thermodynamically competitive channels to both $HO_2$-elimination yielding non-conjugated unsaturated esters and isomerization to QOOH followed by ejection of OH upon cyclic ether formation. No concerted $HO_2$-elimination channel is available for radicals at the terminal ester methyl group. In these cases, cyclic ether + OH channels are energetically plausible and β-scission pathways may also become important. Several cyclic ether formation pathways are considered unfavorable due to energetic or entropic considerations and were not calculated. Cyclic ether channels were only investigated for 6-membered or smaller rings due to the high entropy in the reactions yielding larger rings. Oxetane formation pathways typically have very high QOOH $\rightarrow$ Cyclic Ether + OH barriers. Thus the only oxetane channels anticipated to be energetically competitive are those that proceed via a resonance-stabilized QOOH[44] and other oxetane channels were not calculated. Due to high $RO_2 \rightarrow$ QOOH barriers, 3-membered ring cyclic ether (oxirane) channels are not expected to be competitive with $HO_2$-elimination and were also not calculated. The remaining $HO_2$-elimination and cyclic ether formation channels are the focus of the following sections.

130
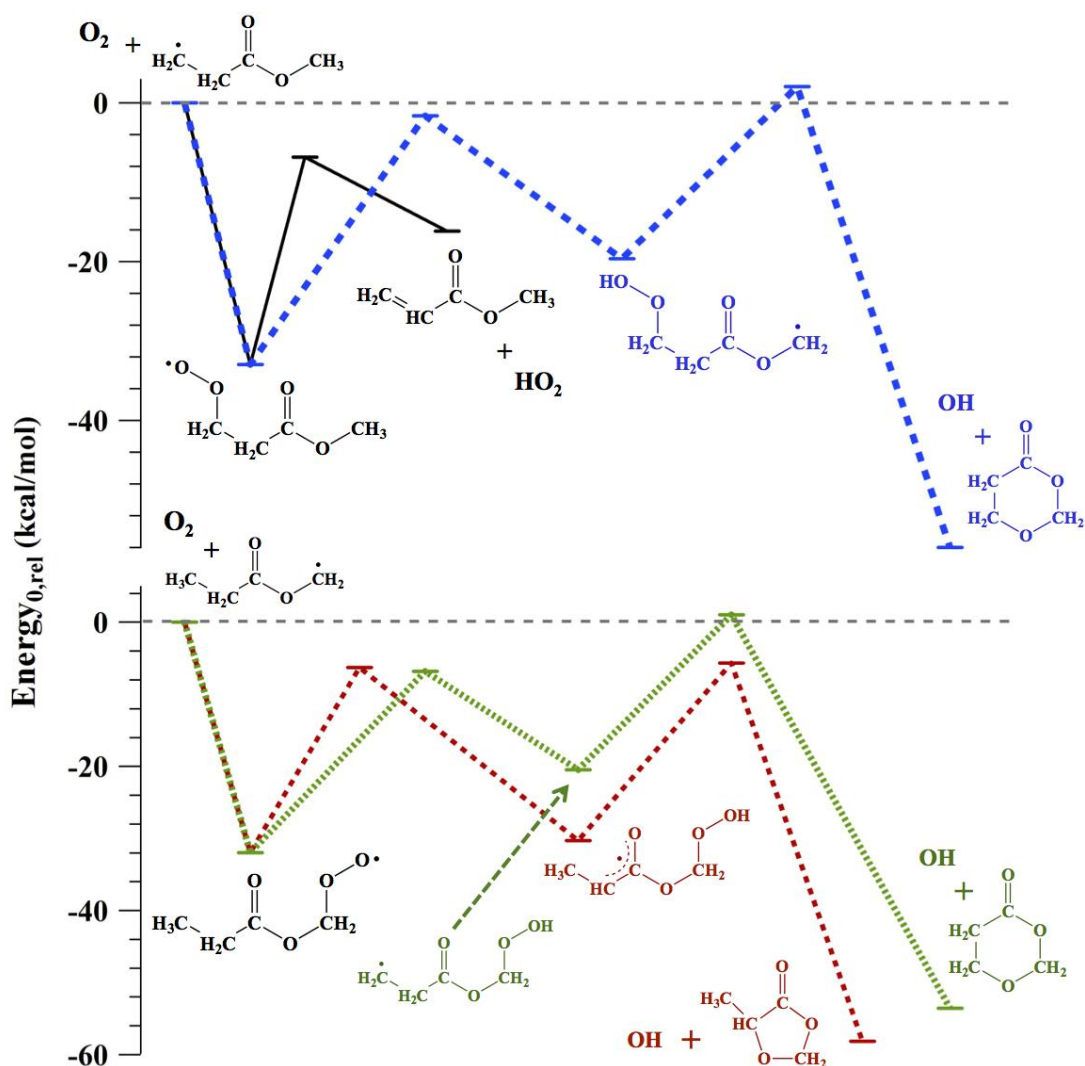
**Figure 4.4.1b.** Potential energy surface for the reaction of the initial methyl propanoate radicals $R_\gamma$ (top) and $R_m$ with $O_2$. Energies at 0 K are at the CBS-QB3 level. Certain cyclic ether formation channels are not expected to be favored and are thus not included (see text). Several β-scission channels are also possible but for clarity are not included.
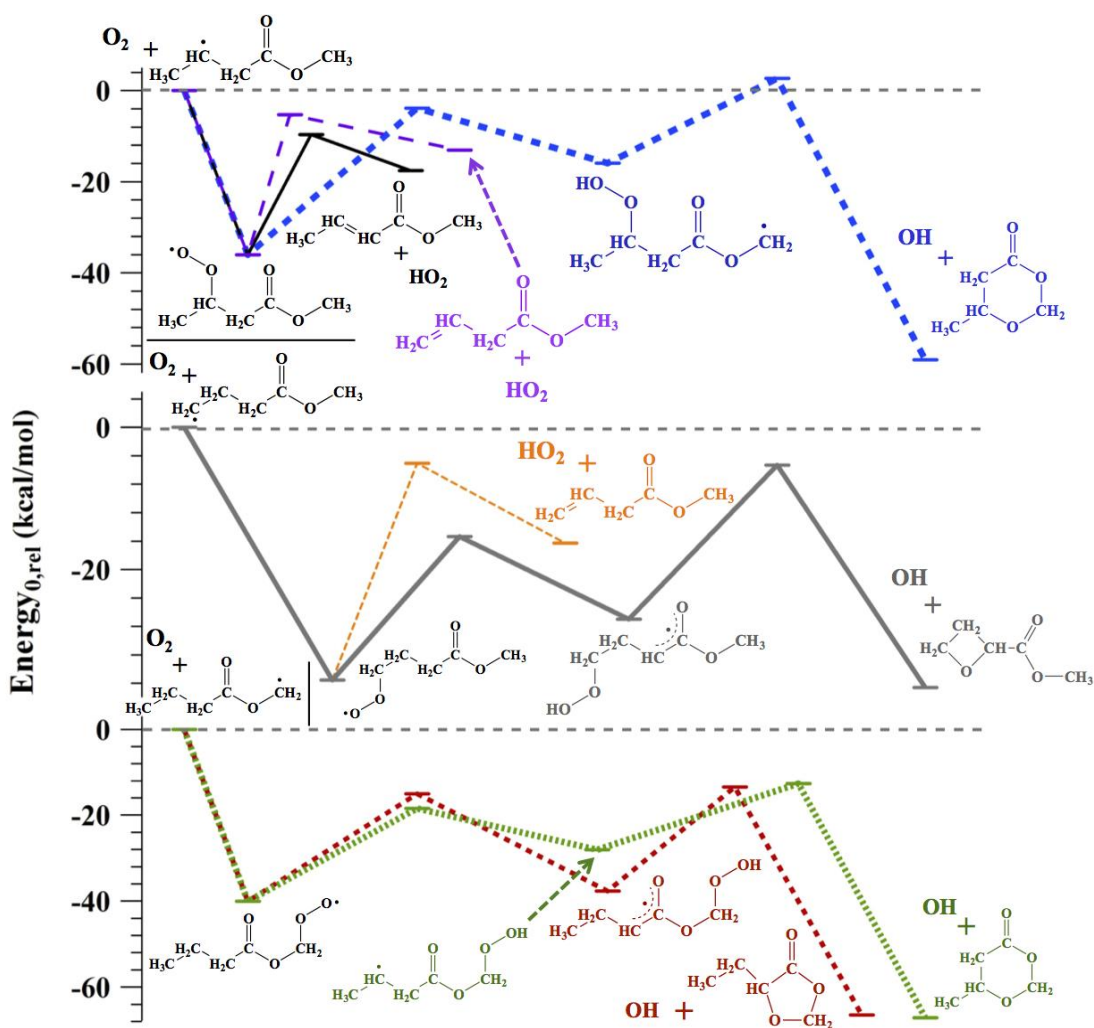
**Figure 4.4.1c:** Potential energy surface for the reaction of the initial methyl butanoate radicals, $R_\gamma$ (top), $R_\delta$ (middle) and $R_m$ (bottom) with $O_2$ with $O_2$. Energies at 0 K are at the CBS-QB3 level. Certain cyclic ether formation channels are not expected to be favored and are thus not included (see text). Several β-scission channels are also possible but for clarity are not included.
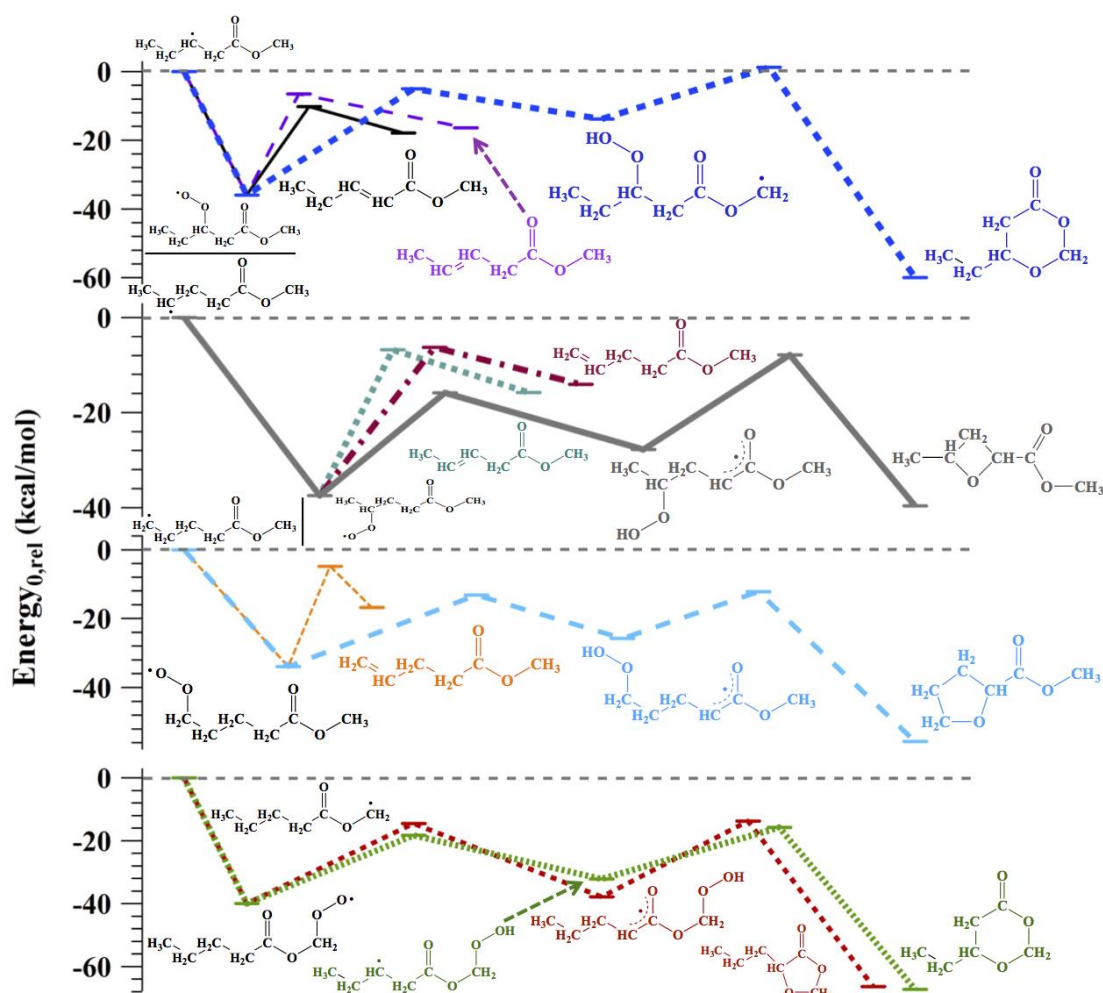
**Figure 4.4.1d:** Potential energy surface for the reaction of the initial methyl valerate radicals $R_\gamma$ (top), $R_\delta$ (top middle), $R_\varepsilon$ (bottom middle) and $R_m$ (bottom) with $O_2$. Energies at 0 K are at the CBS-QB3 level. Certain cyclic ether formation channels are not expected to be favored and are thus not included (see text). Several β-scission channels are also possible but for clarity are not included.

## 4.4.2. HO$_2$-Elimination Channels and Branching

All three ester compounds contain a terminating methyl group bound to the ester oxygen. With no neighboring C-H bonds, concerted HO$_2$-elimination channels from these radical sites ($R_m$) are not expected. A variety of HO$_2$-elimination channels

centered on the hydrocarbon chains are available (Scheme 4.4.2) and are the focus of this section. Figures 1 - 2 and Scheme 4.4.2 show that $HO_2$-elimination channels originating from both $R_\beta$ or $R_\gamma$ of MP yield methyl propenoate. The $m/z = 86$ product signal from MP oxidation is small and the associated photoionization spectrum is somewhat noisy (Figure 4.4.2a). However, Figure 4.4.2a shows that the $m/z = 86$ product spectrum is consistent with that of a methyl propenoate standard at both 550 and 650 K. The adiabatic ionization energy (AIE) of methyl propenoate is calculated to be 10.1 eV[62] and determined experimentally to be 9.9 eV, in good agreement with that observed for the $m/z = 86$ MP oxidation product. Corroborating this assignment is the observation of strong fragment ion signals from methyl propenoate at $m/z = 58$ and $m/z = 85$ that closely match the corresponding signals in the MP oxidation (Supplementary Figure 4.7a). With no other concerted $HO_2$-elimination reactions expected from MP radicals, this result is not surprising.
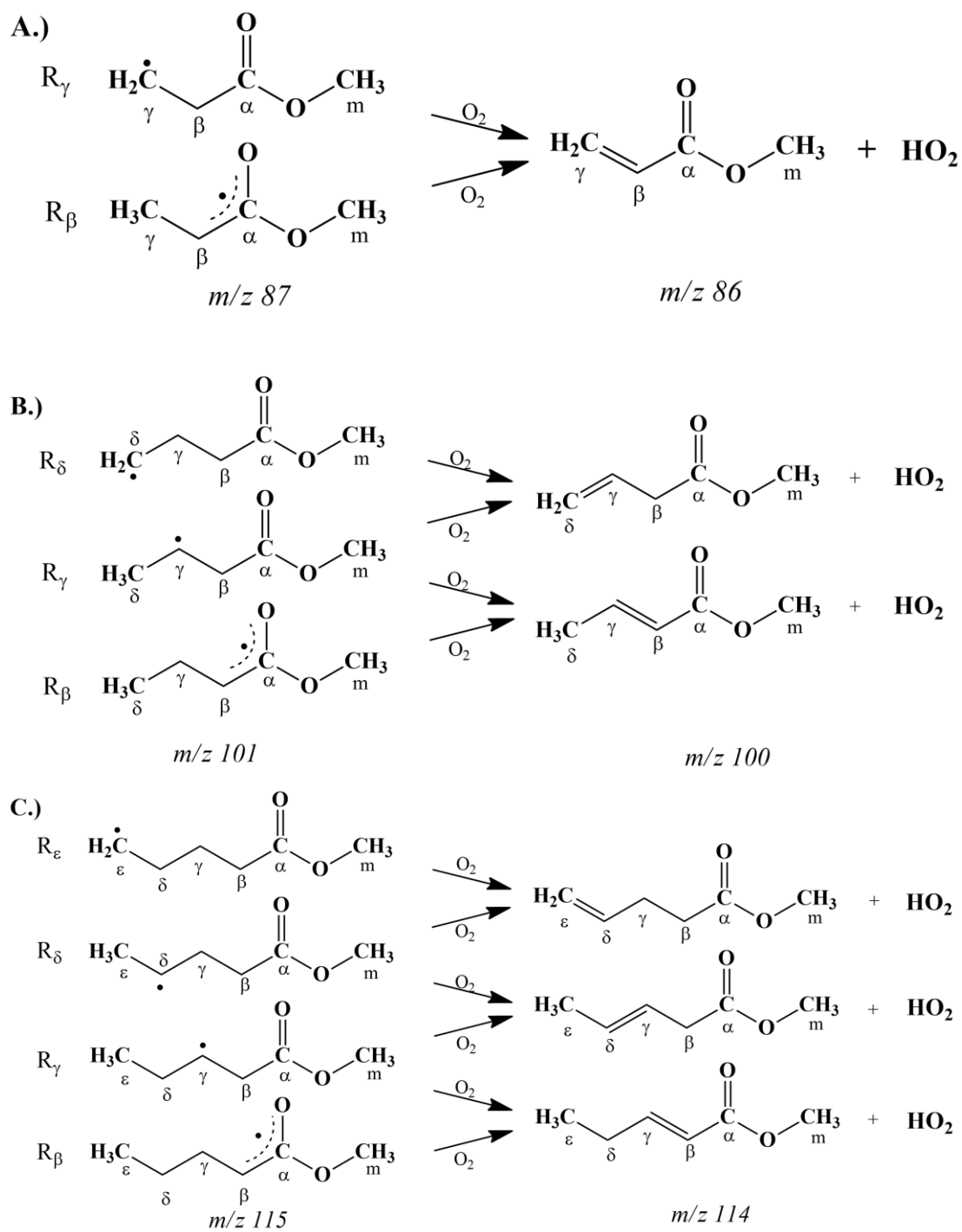
**Scheme 4.4.2:** Possible $HO_2$-elimination channels for A.) MP, B.) MB and C.) MV.

135
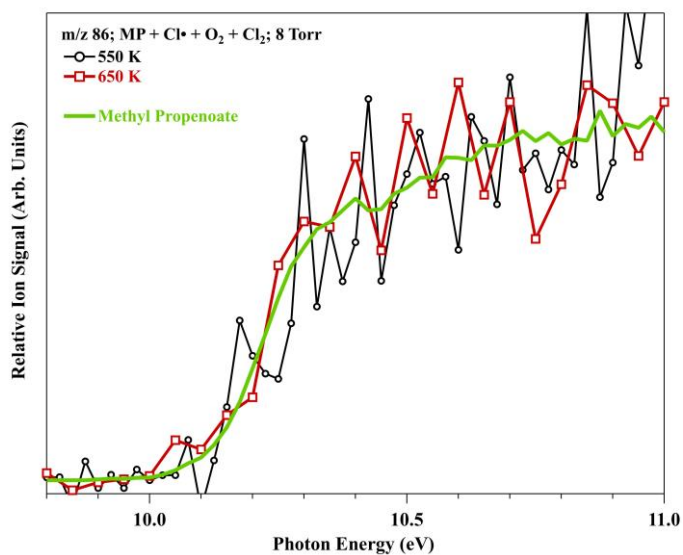
**Figure 4.4.2a:** Photoionization spectra for the *m/z* = 86 peak observed in Cl-initiated oxidation of methyl propanoate at 550 and 650 K compared to a methyl propenoate standard.
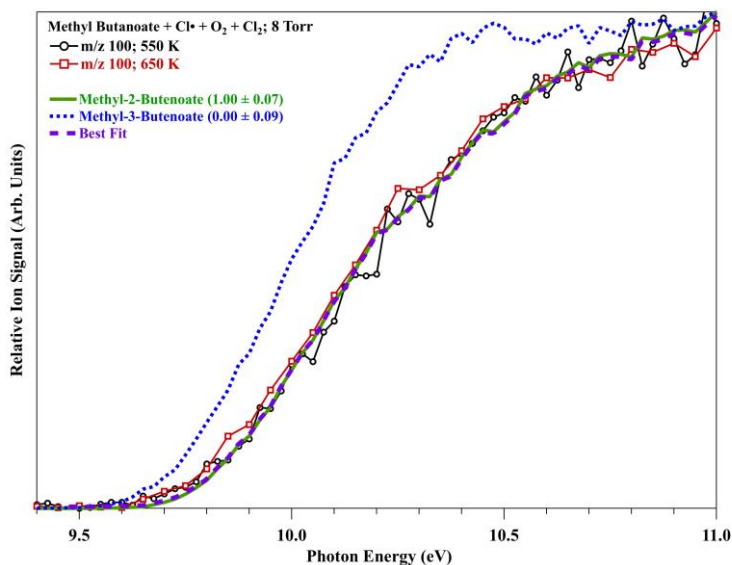


**Figure 4.4.2b:** Photoionization spectra for the *m/z* = 100 peak observed in Cl-initiated oxidation of methyl butenoate at 550 and 650 K compared to methyl-2-butenoate and methyl-3-butenoate standards. The line of best fit (solid purple) results from a least squared regression and indicates a 100% contribution from the conjugated methyl-2-butenoate.

Analogous to $R_\beta$ in MP, $HO_2$-elimination from the resonance-stabilized MB radical can only yield methyl-2-butenoate. However, multiple $HO_2$-elimination channels are available via the secondary $R_\gamma$ and both methyl-2-butenoate and methyl-3-butenoate (Scheme 4.4.2B) are possible. Finally, $HO_2$-elimination from the primary MB carbon radical ($R_\delta$) can only yield methyl-3-butenoate.

The photoionization spectrum of the $m/z = 100$ product of MB oxidation at 550 K matches that of methyl-2-butenoate nearly exactly (Figure 4.4.2b). Taking the methyl-2-butenoate and methyl-3-butenoate spectra as basis functions in a least-squares fit of the $m/z = 100$ product results in a 100% contribution of methyl-2-butenoate to the best fit, which is shown as the purple curve in Figure 4.4.2b. The maximum contribution of methyl-3-butenoate is calculated to be less than 10% at a 2σ error tolerance. Figure 4.4.2b shows that when the temperature is raised to 650 K, the nearly perfect match to methyl-2-butenoate remains. The signals observed at $m/z = 69$ and 85 in MB oxidation are consistent with daughter ions observed in pure methyl-2-butenoate photoionization. (Supplementary Figure 4.7b). Results of stationary point calculations shown in Fig. 4.4.1c indicate that formation of methyl-2-butenoate is the lowest energy $R_\gamma O_2$-decomposition channel. This is expected due to the stability of the conjugated π-system of the methyl-2-butenoate product. The barrier to formation of the non-conjugated methyl-3-butenoate is calculated to be 4.3 kcal mol$^{-1}$ higher. In contrast to the reactions available from $R_\gamma O_2$, the middle panel of Figure 4.4.1c shows that the barrier for QOOH formation from $R_\delta O_2$ is significantly less than that for concerted $HO_2$-elimination. The energy of the subsequent transition state to form a cyclic ether product is still below the saddle point along the path from

137

$R_\delta O_2$ to $HO_2$ + methyl-3-butenoate. It is therefore probable that QOOH chemistry is favored from $R_\delta O_2$. These considerations explain the conjugated methyl-2-butenoate as the exclusive $HO_2$-elimination coproduct.

Methyl valerate presents yet a more complex system. Scheme 4.4.2C shows the three radicals on the hydrocarbon chain can yield three different unsaturated products via $HO_2$-elimination. Each of these compounds (methyl-2-pentenoate, trans-methyl-3-pentenoate and methyl-4-pentenoate) is commercially available and absolute photoionization spectra were obtained for each. Cis-methyl-3-pentenoate was not available for purchase and no attempt to synthesize it was undertaken. Our CBS-QB3 calculations indicate the trans isomer is more stable by 1.3 kcal mol$^{-1}$ The top panel of Figure 4.4.2c shows the photoionization spectrum of the $m/z$ = 114 product signal from MV oxidation at 550 K alongside the standard spectra. The high energy portion of the product signal is reproduced well by that of the conjugated methyl-2-pentenoate, a result consistent with those of MP and MB oxidation. However, the low energy portion of the product curve is not well reproduced by the methyl-2-pentenoate spectrum, indicating a contribution from the other possible isomers, which have earlier photoionization onsets (Figure 4.4.2c). A best fit analysis reveals a 90% contribution from methyl-2-pentenoate, a 10% contribution from methyl-3-pentenoate and no contribution from methyl-4-pentenoate. Figure 4.4.1d shows that formation of methyl-3-pentenoate is energetically more favorable from $R_\delta O_2$ than methyl-4-pentenoate. As discussed below, the lowest energy pathway for $R_\epsilon O_2$ decomposition is cyclic ether formation. Therefore, a large contribution from methyl-4-pentenoate is not expected.
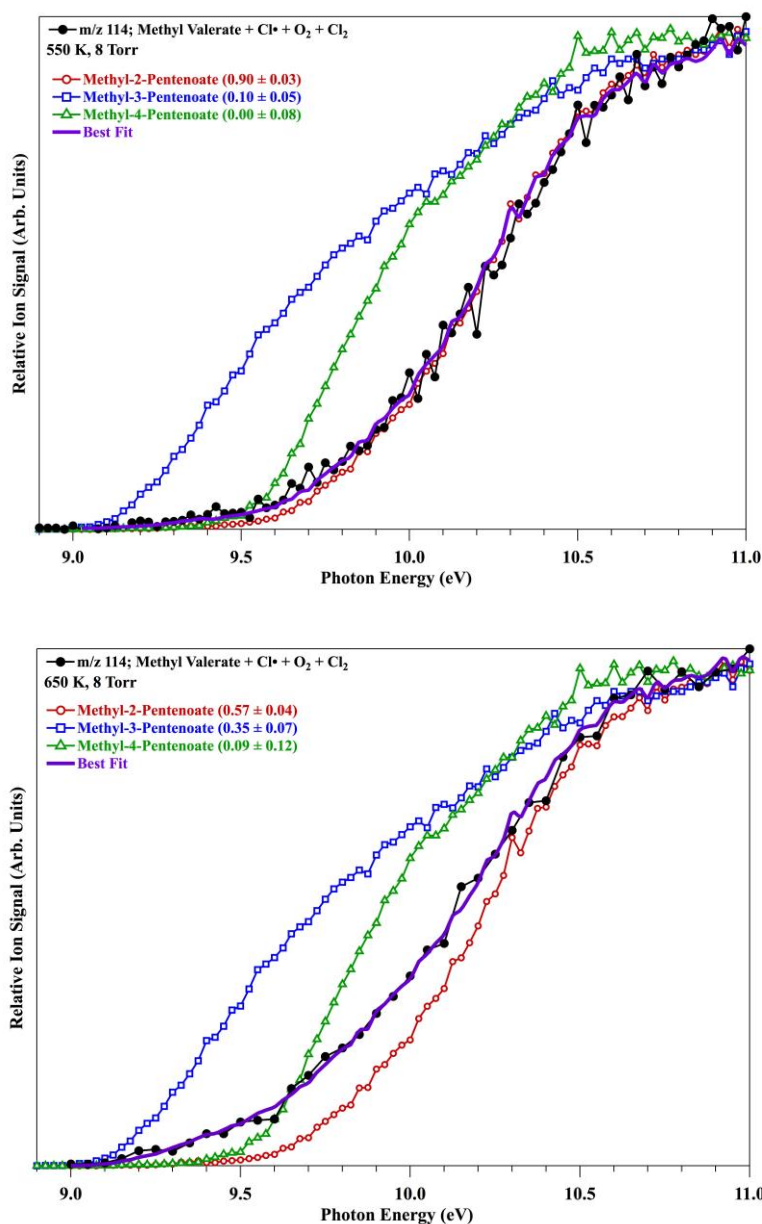
138

**Figure 4.4.2c.** Top: Photoionization spectra for the *m/z* = 114 peak observed in Cl-initiated oxidation of methyl valerate at 550 K compared to methyl-2-pentenoate, methyl-3-pentenoate and methyl-4-pentenoate standards. The line of best fit (solid purple) results from a least squared regression and indicates a 90% contribution from the conjugated methyl-2-pentenoate. Bottom: The same for 650 K. The least squares fit indicates contributions from each isomer.

139

In contrast to MB oxidation, when the temperature is increased to 650 K, a dramatic change in the HO$_2$-elimination product curve is observed (bottom panel of Figure 4.4.2c). The earlier onset of the $m/z$ = 114 product photoionization spectrum at 650 K can be explained only by a greater contribution from methyl-3-pentenoate, which displays the earliest ionization onset of the three methyl-pentenoate isomers at 9.1 eV, matching that observed for the $m/z$ = 114 product at 650 K. The best fit analysis indicates formation of all three isomers (57% methyl-2-pentenoate, 35% methyl-3-pentenoate and 9% methyl-4-pentenoate). The conjugated product is still the primary contributor, but at a significantly reduced level. Methyl-2-pentenoate displays fragment ions at m/z = 82 and m/z = 83 while methyl-3-pentenoate and methyl-4-pentenoate each produce fragment ions at $m/z$ = 54 and $m/z$ = 72. All of these fragment ions are consistent with signals observed in the oxidation of MV (Supplementary Figures 4.7c and 4.7d).

### 4.4.3. Cyclic Ether Formation

Integrated product mass spectra for all three esters studied here (Figures 4.4.3a – 4.4.3c) display a peak at a mass of parent + 14, consistent with formation of cyclic ethers + OH via QOOH intermediates. Scheme 4.4.3 shows the expected cyclic ether products along with their calculated AIEs. The oxiranes and the oxetanes produced via non-resonance-stabilized QOOH were excluded from consideration because of the high barriers expected to their formation. None of the cyclic ethers anticipated from MP or MB oxidation were available commercially and no attempt was made to synthesize them. Both cyclic ether products likely from MP oxidation have calculated AIEs of 10.1 eV. Unfortunately, the signal for $m/z$ = 102 in MP is too

weak to yield a reasonable photoionization spectrum. In contrast, the photoionization spectrum of $m/z = 116$ in MB displays a clear onset at 9.6 eV, in agreement with the lowest value calculated for the three expected cyclic ether products shown in Scheme 4.4.3. Formation of this oxetane product occurs via a resonance stabilized QOOH and is in direct competition with methyl-3-butenoate formation via $HO_2$ elimination from $R_\delta O_2$. As discussed above, no methyl-3-butenoate was observed, lending support to the conclusion that $R_\delta O_2$ decomposition proceeds primarily via QOOH. Figure 4.4.1c shows that the barrier to formation of the resonance-stabilized QOOH from $R_\delta O_2$ (20.3 kcal mol$^{-1}$) is much lower than that for concerted $HO_2$-elimination (30.4 kcal mol$^{-1}$) while the subsequent barrier to form methyl oxetane-2-carboxylate is calculated to be 21.7 kcal mol$^{-1}$. The 6-membered ring cyclic ether has a calculated AIE of 10.0 eV, but its formation from $R_\gamma O_2$ is not expected due to the associated QOOH → Cyclic Ether + OH barrier lying above the $R_\gamma + O_2$ entrance channel. A contribution from the 5- and 6- membered ring cyclic ethers originating from $R_m O_2$ cannot be excluded based on the calculated AIEs or the stationary point calculations presented in the lower panel of Figure 4.4.1c.
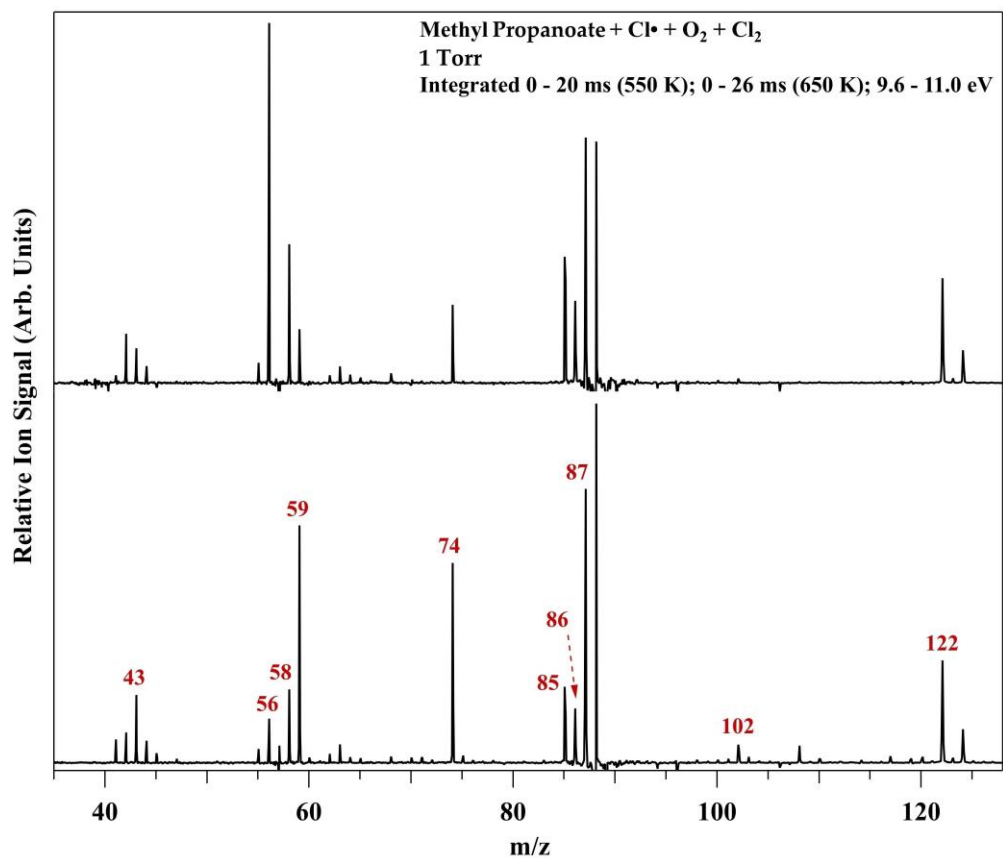
**Figure 4.4.3a:** Difference mass spectra of Cl-initiated oxidation of methyl propanoate at 550 K (bottom) and 650 K (top) normalized to photocurrent resulting from integrating the ion signal for the 32 ms timeframe immediately following photolysis and over ionizing photon energies from 9.0 –11.0 eV. Averaged background signal before photolysis has been subtracted, and negative signal arising from consumption of MP is omitted for clarity.
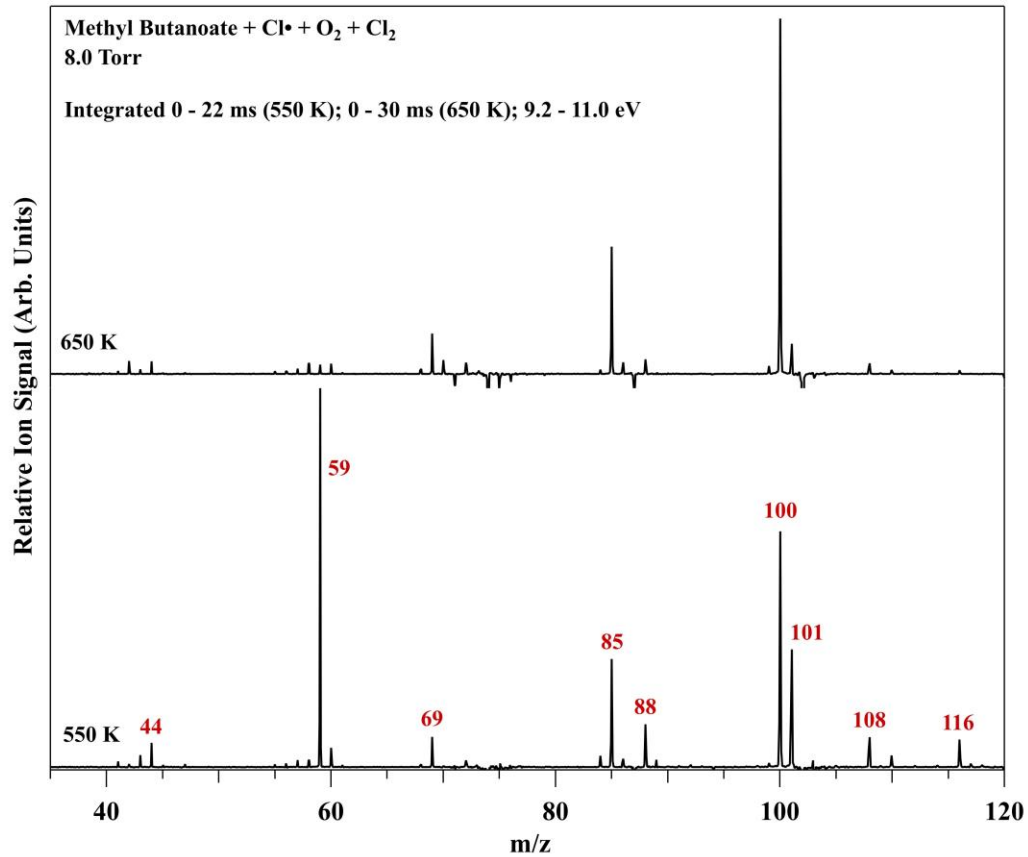
**Figure 4.4.3b:** Difference mass spectra of Cl-initiated oxidation of methyl butanoate at 550 K (bottom) and 650 K (top) normalized to photocurrent resulting from integrating the ion signal for the 32 ms timeframe immediately following photolysis and over ionizing photon energies from 9.0 –11.0 eV. Averaged background signal before photolysis has been subtracted, and negative signal arising from consumption of MB is omitted for clarity.
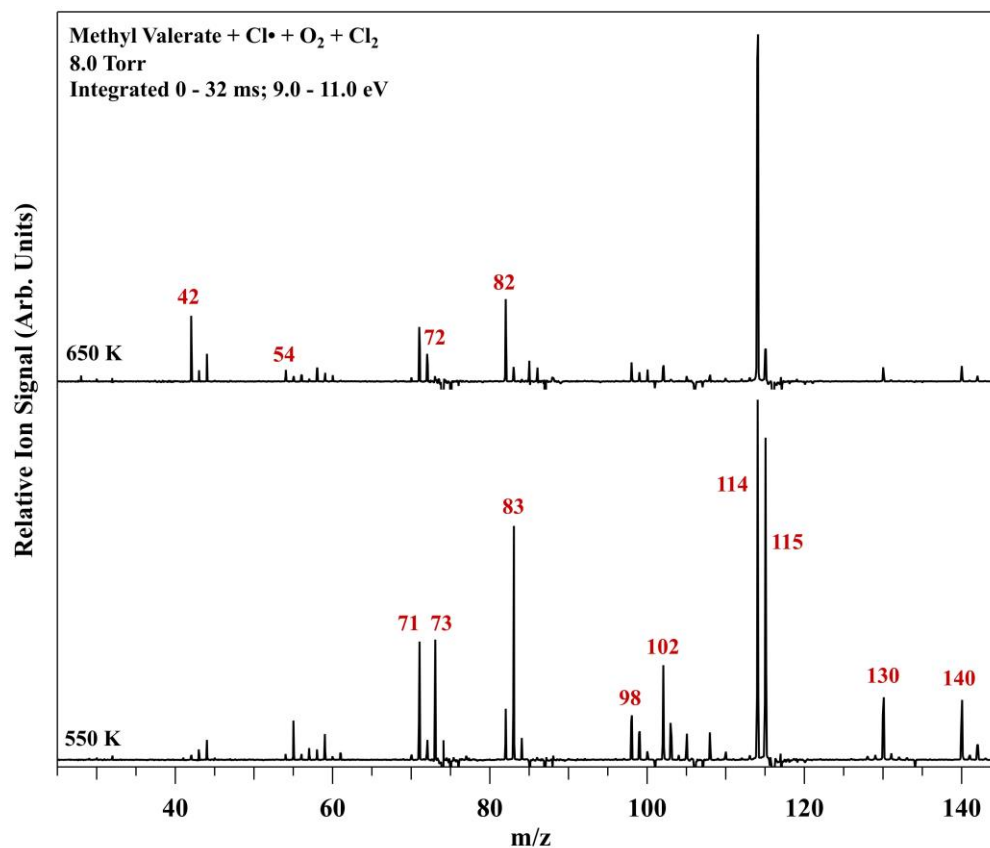
**Figure 4.4.3c:** Difference mass spectra of Cl-initiated oxidation of methyl valerate at 550 K (bottom) and 650 K (top) normalized to photocurrent resulting from integrating the ion signal for the 32 ms timeframe immediately following photolysis and over ionizing photon energies from 9.0 –11.0 eV. Averaged background signal before photolysis has been subtracted, and negative signal arising from consumption of MV is omitted for clarity.

**MP**   **MB**   **MV**



methyl oxetane-2-carboxylate   9.6

methyl 4-methyloxetane-2-carboxylate   9.4 (cis and trans)

5-methyl-1,3-dioxolan-4-one   10.1

5-ethyl-1,3-dioxolan-4-one   10.1

5-propyl-1,3-dioxolan-4-one   10.0

1,3-dioxan-4-one   10.1

6-methyl-1,3-dioxan-4-one   10.0

6-ethyl-1,3-dioxan-4-one   10.0

methyl tetrahydrofuran-2-carboxylate   9.2
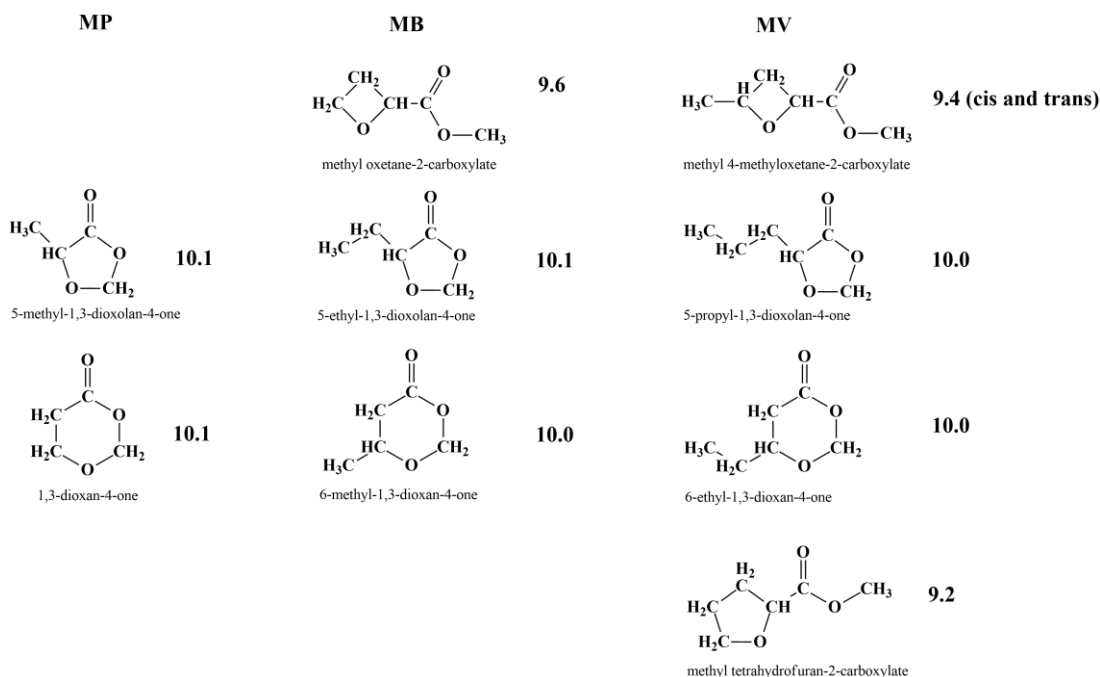
**Scheme 4.4.3:** The calculated adiabatic ionization energies of select cyclic ether products for the respective methyl esters.

For MV $RO_2$ radicals, the only cyclic ether channel with a calculated highest barrier lying below the competing $HO_2$-elimination barrier is formation of the 5-membered ring, methyl-tetrahydrofuran-2-carboxylate (Me-THF-2-carboxylate) originating from $R_\varepsilon O_2$. This channel benefits from low ring strain in the 7-membered $RO_2 \rightarrow QOOH$ transition state as well as the 5-membered $QOOH \rightarrow$ cyclic ether + OH transition state. Furthermore, the QOOH radical is resonance-stabilized, which is expected to yield a longer-lived radical that may drive reaction flux to the cyclic ether product.[44, 63] As discussed above, a similar channel has been shown to be dominant in open-chain ketones.[44, 47] Neither MP nor MB have an analogous channel available. The photoionization spectrum of Me-THF-2-carboxylate was obtained as described

145

above. The parent cation showed an extremely weak signal, but strong signals from multiple fragment ions ($m/z$ = 102 and $m/z$ = 71) were observed. Both of these masses are seen in MV oxidation (Figure 4.4.3c bottom panel) and the corresponding photoionization spectra are in good agreement with the fragment ions of the Me-THF-2-carboxylate standard from 9.0 – 10.0 eV, before also displaying contributions from other sources (Figure 4.4.3d). The peak at $m/z$ = 130 indicates an additional contribution from other cyclic ether channels, as would be expected from the observation of cyclic ether products in both MP and MB oxidation, where analogous channels to 5-membered ring products are not available. The onset of the $m/z$ = 130 product of MV oxidation is observed near 9.5 eV, in good agreement with methyl 4-methyloxetane-2-carboxylate. This product would be expected by analogy to the oxetane channel from $R_\delta O_2$ via a resonance-stabilized QOOH observed in MB oxidation. Disproportionation reactions[64] involving $RO_2$ are possible and would produce a bicarbonyl at an $m/z$ of parent + 14 with an identical formula to the cyclic ether. However the lack of corresponding peaks due to an alcohol coproduct at an $m/z$ of parent + 16, fails to corroborate this alternative.
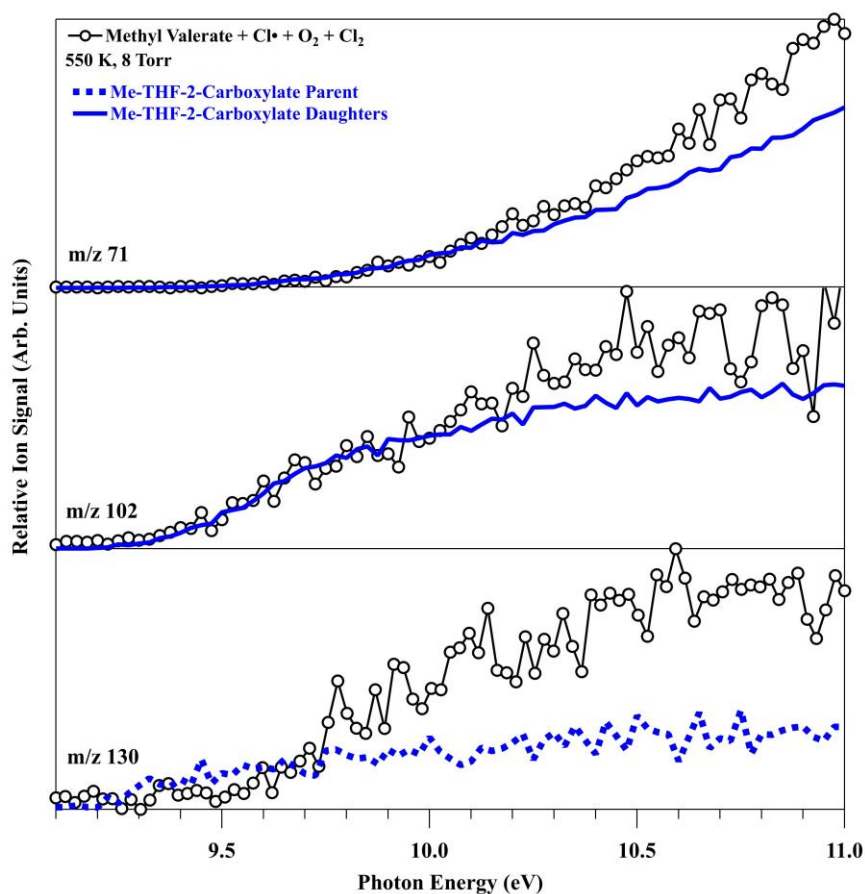
**Figure 4.4.3d:** Photoionization spectra for the *m/z* = 130 (bottom), *m/z* = 102 (middle) and *m/z* = 71 (top) peaks observed in Cl-initiated oxidation of methyl valerate at 550 K. The signals are compared to those from a methyl-tetrahydrofuran-2-carboxylate standard. The parent Me-THF-2-carboxylate displays only a very weak signal. However, the strong daughter ion signals agree with the respective oxidation peaks below 10.0 eV before other contributions at these values of *m/z* become apparent.

## 4.4.4. Other Products and Fragment Ions

In the Cl-initiated oxidation of MB, Figure 4.4.3b displays strong signals at *m/z* = 116, 108, 101, 100, 88, 85, 69, 59, 44 and 30 (not shown). The signals at *m/z*

147

= 116 and 100 have already been identified as cyclic ether products and the coproduct of $HO_2$-elimination, respectively. Similarly, the peak at $m/z$ = 85 has been assigned as a fragment ion of the $HO_2$-elimination coproduct methyl-2-butenoate (Figure 4.7b). Similarly, Figure 4.7b shows the peak at $m/z$ = 69 is partially due to a fragment ion of methyl-2-butenoate. The peak at $m/z$ = 101 corresponds both to the initial MB radicals and fragment ions of the associated MB peroxy ($RO_2$) radicals. The kinetic time trace (Supplementary Figure 4.7g) of the $m/z$ = 101 signal shows a sharp rise, consistent with the initial radical formation via H-abstraction reactions with Cl·, followed by a relatively constant signal that likely results from $RO_2$ formation and fragmentation via: $[RO_2]^+ \rightarrow [R]^+ + O_2$. The signal at $m/z$ = 108 is also observed in the absence of $O_2$ (Supplementary Information Figure 4.7k), displays a sharp rise consistent with chlorinated product formation, and is paired with a peak at $m/z$ = 110, which, relative to the $m/z$ = 108 signal, is observed in the natural abundance of the $^{37}Cl$:$^{35}Cl$ isotope ratio. These peaks likely result from Cl· addition to the long-lived resonance-stabilized $R_\beta$ to form $R_\beta Cl$ followed by fragmentation via: $[CH_3CH_2CHClCOOCH_3]^+ \rightarrow [CHClCOOCH_3]^+ + CH_3CH_2$. The peak at $m/z$ = 88 is consistent with fragment ion formation via loss of neutral CO from the cyclic ether cation. Such a reaction has been observed in the low temperature oxidation a number of ketones[44, 47, 51] and again here in the photoionization of methyl-tetrahydrofuran-2-carboxylate. The peak at $m/z$ = 59 is only observed in the presence of $O_2$ and has a time profile showing a fast rise followed by partial decay. The origins of this peak are not immediately obvious, but the time profile indicates that it is due, at least in part, to a fragment ion. Finally, peaks at $m/z$ = 30 and 44 are

only observed in the presence of $O_2$. Their photoionization spectra align with the well-known spectra of formaldehyde ($CH_2O$) and acetaldehyde ($CH_3CHO$), respectively. These small molecule products may originate from numerous bimolecular channels and we do not attempt to identify specific pathways here. A number of analogous peaks are observed in MP and MV oxidation and for brevity we omit similar detailed explanations. Product time profiles and photoionization spectra are included in the Supplementary Information section 4.7 as Figures 4.7e – 4.7j for the 550 K Cl-initiated oxidation experiments of the three esters studied here.

## 4.5 Conclusions

The Cl-initiated oxidation reactions of $C_3$-$C_5$ methyl esters have been studied with multiplexed photoionization mass spectrometry utilizing tunable synchrotron ionization radiation. The β-carbon radical, $R_\beta$, formed from H-abstraction is resonance-stabilized and thus addition of $O_2$ results in a shallow $R_\beta O_2$ well. As a consequence, traditional $RO_2$ exit channels lie near or above the $R_\beta + O_2$ entrance channel. Despite the low energy conjugated coproduct, in the conditions studied here other secondary pathways are expected to compete with $HO_2$-elimination. In contrast, other initial radicals form more strongly bound peroxy radicals, and the products of both chain-terminating $HO_2$-elimination and chain-propagating cyclic ether formation pathways are observed. Though a number of reactions are possible from decomposition of $R_\gamma O_2$, $HO_2$-elimination to form the conjugated methyl-2-propenoate, methyl-2-butenoate, and methyl-2-pentenoate are observed to be dominant at 550 K. Interestingly, as the temperature is raised to 650 K, selectivity is

lost in the $HO_2$-elimination pathways of MV and a mix of methyl-2- 3- and 4-pentenoate are observed. At 550 K, cyclic ether formation channels via QOOH radicals are observed to be competitive. In MB and MV, formation of oxetane cyclic ethers appears to be important via resonance-stabilized QOOH, with the radical site at the β carbon. Due to the longer hydrocarbon chain, a favorable pathway exists to form a 5-membered ring cyclic ether, methyl-tetrahydrofuran-2-carboxylate (Me-THF-2-carboxylate), via low ring strain transition states in both the $RO_2 \rightarrow$ QOOH and QOOH $\rightarrow$ cyclic ether + OH reactions. Though photoionization results in a very short lived Me-THF-2-carboxylate cation, its fragment ions are observed in the oxidation of MV, confirming the presence of this channel.

## 4.6 Acknowledgements

## 4.7 Supplementary Information



**Figure 4.7a:** Photoionization spectra for the *m/z* = 85 (bottom) and *m/z* = 69 (top) peaks observed in Cl-initiated oxidation of methyl butanoate at 550 K. The signals are compared to those from daughter ions originating from a methyl-2-butenoate standard.
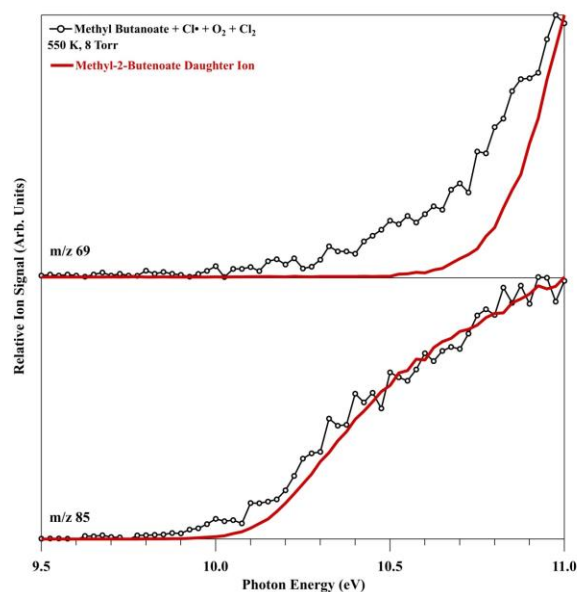
**Figure 4.7b:** Photoionization spectra for the *m/z* = 85 (bottom) and *m/z* = 69 (top) peaks observed in Cl-initiated oxidation of methyl butanoate at 550 K. The signals are compared to those from daughter ions originating from a methyl-2-butenoate standard.
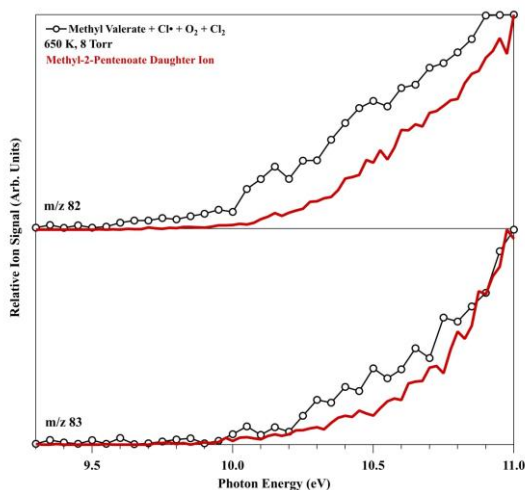


**Figure 4.7c:** Photoionization spectra for the *m/z* = 83 (bottom) and *m/z* = 82 (top) peaks observed in Cl-initiated oxidation of methyl valerate at 650 K. The signals are compared to those from daughter ions originating from a methyl-2-pentenoate standard.

152
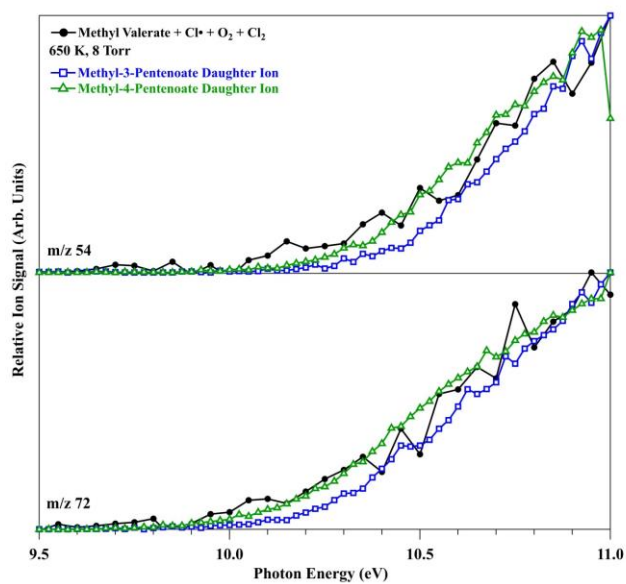
**Figure 4.7d:** Photoionization spectra for the *m/z* = 72 (bottom) and *m/z* = 54 (top) peaks observed in Cl-initiated oxidation of methyl valerate at 650 K. The signals are compared to those from daughter ions originating from a methyl-3-pentenoate and methyl-4-pentenoate standards.
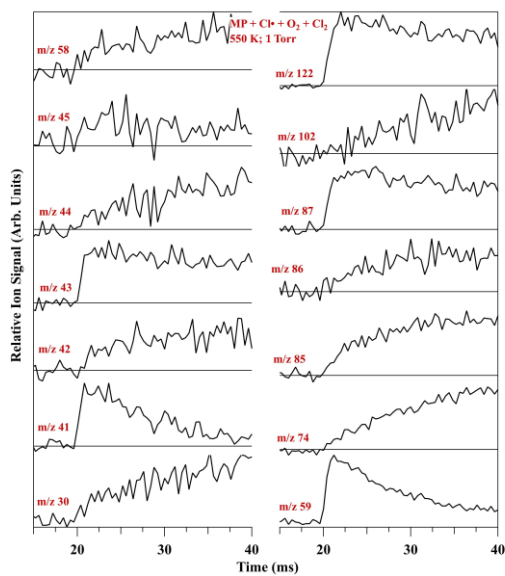


**Figure 4.7e:** Time traces for products observed in the Cl-initiated oxidation of methyl pentanoate at 550 K and 1 Torr. The photolysis laser fires at 20 ms.

153
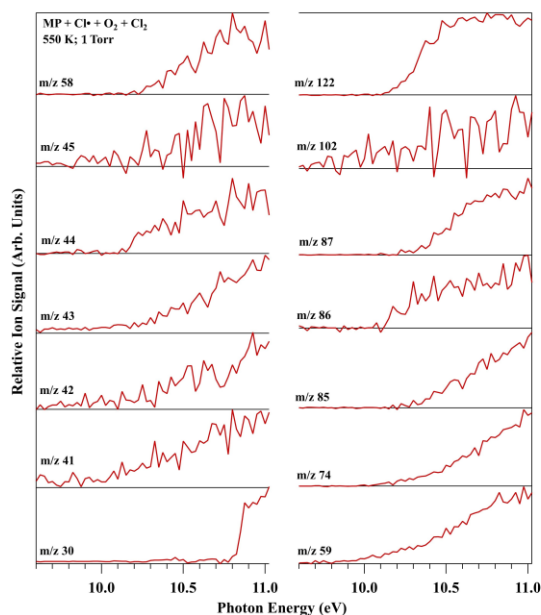
**Figure 4.7f:** Photoionization spectra for products observed in the Cl-initiated oxidation of methyl pentanoate at 550 K and 1 Torr.
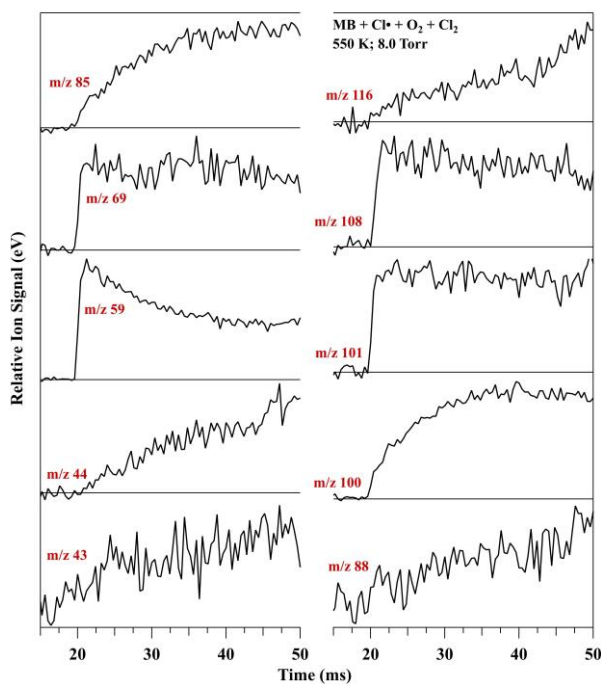


**Figure 4.7g:** Time traces for products observed in the Cl-initiated oxidation of methyl butanoate at 550 K and 8 Torr. The photolysis laser fires at 20 ms.
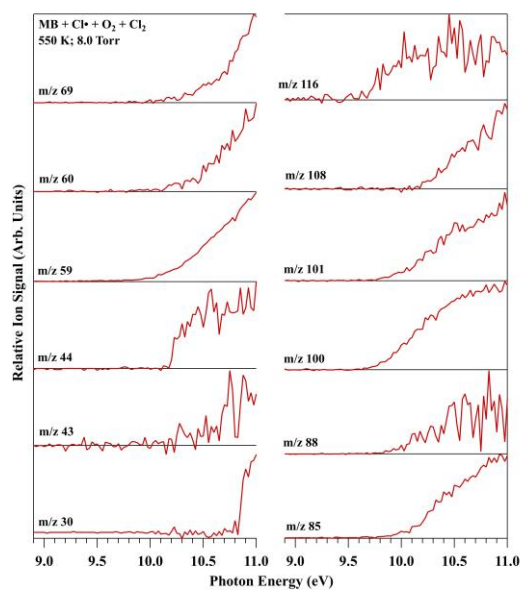
**Figure 4.7h:** Photoionization spectra for products observed in the Cl-initiated oxidation of methyl butanoate at 550 K and 8 Torr.
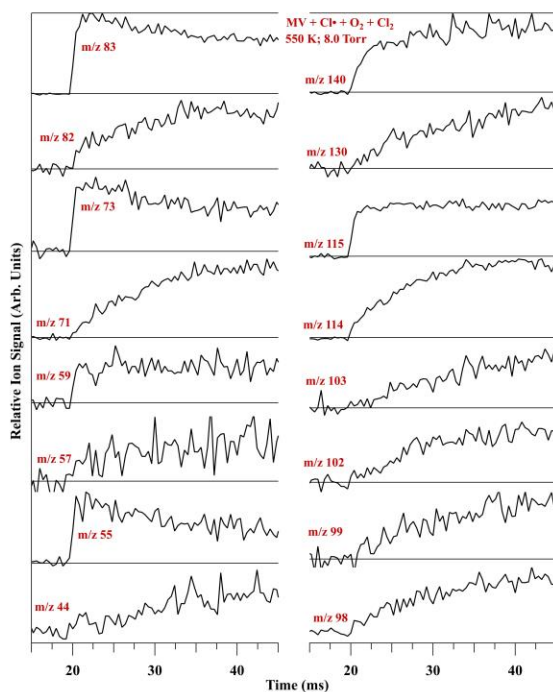


**Figure 4.7i:** Time traces for products observed in the Cl-initiated oxidation of methyl valerate at 550 K and 8 Torr. The photolysis laser fires at 20 ms.
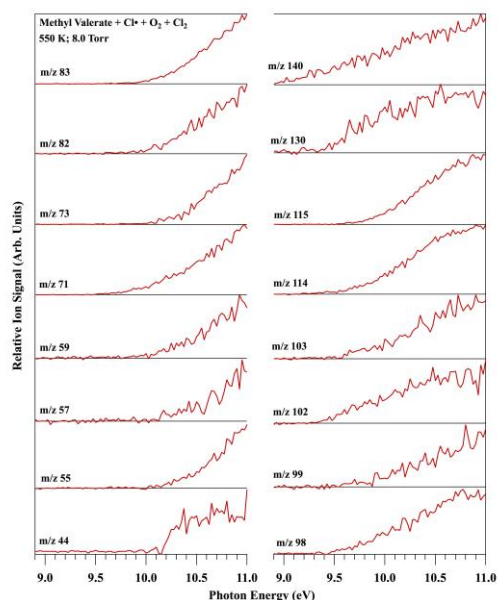
**Figure 4.7j:** Photoionization spectra for products observed in the Cl-initiated oxidation of methyl valerate at 550 K and 8 Torr.
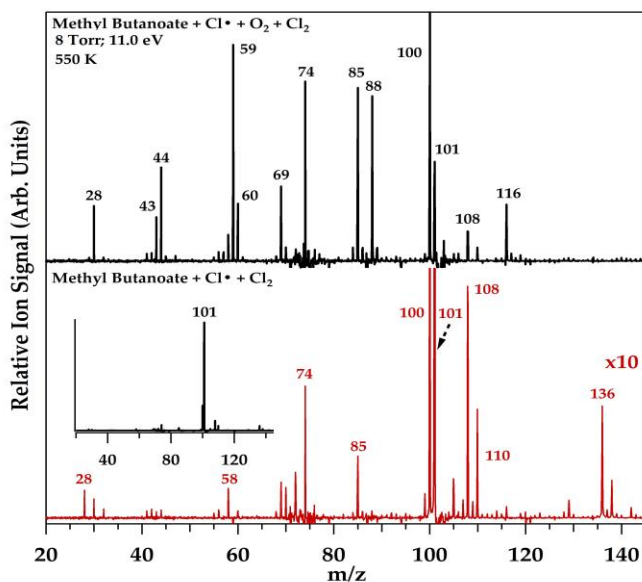


**Figure 4.7k:** Difference mass spectra of Cl-initiated oxidation of methyl butanoate at 550 K, 8 Torr and 11.0 eV. The bottom spectrum was recorded with no $O_2$ flow. Averaged background signal before photolysis has been subtracted, and negative signal arising from consumption of MB is omitted for clarity.

156

## 4.8 References

(1.)     *Carbon Dioxide Emissions From Energy Consumption by Source*; United States Energy Information Administration: 2014, 2014; pp 157-169.

(2.)     Metz, B.; Davidson, O. R.; Bosch, P. R.; Dave, R.; (eds), L. A. M. *Climate Change 2007: Mitigation. Contribution of Working Group III to the Fourth Assessment Report of the Intergovernmental Panel on Climate Change. Transport and its Infrastructure.*; United Nations: 2007, 2007.

(3.)     Lois, E., Definition of Biodiesel. *Fuel* **2007,** *86*, 1212-1213.

(4.)     Alhassan, Y.; Kumar, N.; Bugaje, I. M.; Pali, H. S.; Kathkar, P., Co-solvents Transesterification of Cotton Seed Oil Into Biodiesel: Effects of Reaction Conditions on Quality of Fatty Acids Methyl Esters. *Energ. Convers. Manage.* **2014,** *84*, 640-648.

(5.)     Pramanik, K., Properties and Use of Jatropha Curcas Oil and Diesel Fuel Blends in Compression Ignition Engine. *Renew. Energ.* **2003,** *28*, 239-248.

(6.)     Lenin, A. H.; Rex, C. R. B. S.; Thyagarajan, K.; Saravanan, M. S. S., Experimental Investigations on a Diesel Engine Using Blends of Methyl Esters of Pongamia Oil as the Fuels. *Eur. J. Sci. Res.* **2012,** *72* (2), 273-284.

(7.)     Conceicao, M. M.; Candeia, R. A.; Dantas, H. J.; Soledade, L. E. B.; Fernandes, V. J.; Souza, A. G., Rheological Behavior of Castor Oil Biodiesel. *Energ. Fuel.* **2005,** *29*, 2185-2188.

(8.)     Schumacher, L.; Marshall, W.; Krahl, J.; Wetherell, W.; Grabowski, M., Biofuel Emissions Data from Series 60 DDC Engines. *Trans. Am. Soc. Ag. Eng.* **2001,** *44*, 1465-1468.

(9.)     Rani, B.; Singh, U.; Chuhan, A. K.; Sharma, D.; Maheshwari, R., Photochemical Smog Pollution and Its Mitigation Measures. *J. Adv. Sci. Res* **2011,** *2* (4), 28-33.

(10.)    Bari, S., Performance, Combustion and Emission Tests of a Metro-bus Running on Biodiesel-ULSD Blended (B20) Fuel. *Appl. Energ.* **2014,** *124*, 35-43.

(11.)    Song, H.; Tompkins, B.; Bittle, J.; Jacobs, T., Comparisons of NO Emissions and Soot Concentrations from Biodiesel-Fueled Diesel Engine. *Fuel* **2012,** *96*, 446-453.

(12.)    Fontaras, G.; Kousoulidou, M.; Karavalakis, G.; Tzamkiozis, T.; Pistikopouos, P.; Ntziachristos, L.; Bakeas, E.; Stournas, S.; Samaras, Z., Effects of Low Concentration Biodiesel Blend Application on Modern Passenger Cars. Part 1: Feedstock Impact on Regulated Pollutants, Fuel Consumption and Particle Emissions. *Environ. Pollut.* **2010,** *158*, 1451-1460.

(13.)    Senthil, K. M.; Ramesh, A.; Nagalingam, B., An Experimental Comparison of Methods to use Methanol and Jatropha Oil in a Compression Ignition Engine. *Biomass Bioenerg.* **2003,** *25*, 309-318.

(14.)    Puhan, S.; Vedaraman, N.; Sankaranarayanan, G.; Ram, B. V. B., Performance

and Emission Study of Mahua oil Ethyl ester in a Four Stroke Natural Aspirated DI Diesel Engine. *Renew. Energ.* **2005,** *30* (99), 1269-1278.

(15.)    Aldana, C.; Parthasarathy, R. N.; Gollahalli, S. R., Combustion Properties of Spray Flames of Canola Methyl Ester and Diesel Blends at Lean Inlet Equivalence Ratios. *J. Petrol. Sci. Res.* **2014,** *3* (4).

(16.)    Lenin, A. H.; Ravi, R.; Arrumugham, S.; Thyagarajan, K., Performance, Emission and Combustion Evaluation of Diesel Engine Using Methyl Esters of Mahua oil. *Int. J. Env. Sci.* **2012,** *3* (1).

(17.)    Canakci, M.; Gerpen, J. V., Comparison of Engine Performance and Emissions for Petroleum Diesel Fuel, Yellow Grease Biofuel and Soybean Oil Biofuel. *Trans. Am. Soc. Ag. Eng.* **2003,** *46*, 937-944.

(18.)    Tsai, J.; Chen, S.; Huang, K.; Lin, Y.; Lee, W.; Lin, V.; Lin, W., PM, Carbon and PAH Emissions From a Diesel Generator Fueled with Soy-Biodiesel Blends. *J. Hazard. Mater.* **2010,** *79*, 237-243.

(19.)    Kruczynski, S. W.; Orlinski, P., Combustion of Methyl Esters of Various Origins in the Agricultural Engine. *Indian J. Eng. Mater. S.* **2013,** *20*, 483-491.

(20.)    V., H.; Kumar, G. M., Combustion Analysis of Algal Oil Methyl Ester in a Direct Injection Compression Ignition Engine. *J. Eng. Sci. Tech.* **2013,** *8* (1), 77-92.

(21.)    Sokoto, M. A.; Hassan, L. G.; Dangoggo, S. M.; Ahmad, H. G.; Uba, A., Influence of Fatty Acid Methyl Esters on Fuel Properties of Biodiesel Produced from the Seeds Oil of Curcubita pepo. *Nig. J. Basic Appl. Sci.* **2011,** *19* (1), 81-88.

(22.)    Rao, P. V., Effect of Properties of Karanja Methyl Ester on Combustion and $NO_x$ Emissions of a Diesel Engine. *J. Pet. Technol. Altern. Fuels.* **2011,** *2* (5), 63-75.

(23.)    Biet, J.; Warth, V.; Herbinet, O.; Glaude, P. A.; Battin-Leclerc, F., Modeling Study of the Low-Temperature Oxidation of Large Methyl Esters. In *European Combustion Meeting 2009*, Vienna, Austria, 2009; Vol. e-Print Archive, pp 1-6.

(24.)    Dayma, G.; Togbe, C.; Dagaut, P., Detailed Kinetic Mechanism for the Oxidation of Vegetable Oil Methyl Esters: New Evidence from Methyl Heptanoate. *Energ. Fuel.* **2009,** *23*, 4254-4268.

(25.)    Dayma, G.; Sarathy, S. M.; Togbe, C.; Yeung, C.; Thomson, M. J.; Dagaut, P., Experimental and Kinetic Modeling of Methyl Octanoate Oxidation in an Opposed-Flow Diffusion Flame and a Jet-stirred Reactor. *P. Combust. Inst.* **2011,** *33*, 1037-1043.

(26.)    Wang, W.; Gowdagiri, S.; Oehlschlaeger, M. A., Comparative Study of the Autoignition of Methyl Decenoates, Unsaturated Biodiesel Fuel Surrogates. *Energ. Fuel.* **2013,** *27*, 5527-5532.

(27.)    Dayma, G.; Gail, S.; Dagaut, P., Experimental and Kinetic Modeling Study of the Oxidation of Methyl Hexanoate. *Energ. Fuel.* **2009,** *22*, 1469-1479.

(28.)    Herbinet, O.; Pitz, W. J.; Westbook, C. K., Detailed Chemical Kinetic Mechanism for the Oxidation of Biodiesel Fuels Blend Surrogate. *Combust. Flame* **2010,** *157* (5), 893-908.

(29.)    Parsons, B. I.; Hinshelwood, S. C., 352. The Oxidation of Hydrocarbons and

Their Derivatives. Part II. Structural Effects in the Ester Series. *J. Chem. Soc.* **1956**, 1799-1803.

(30.)    Kerschgens, B.; Cai, L.; Pitsch, H.; Janssen, A.; Jakob, M.; Pischinger, S., Surrogate Fuels for the Simulation of Diesel Engine Combustion of Novel Biofuels. *Int. J. Engine Res.* **2014**.

(31.)    Poon, H. M.; Ng, H. K.; Gan, S.; Pang, K. M.; Schramm, J., Chemical Kinetic Mechanism Reduction Scheme for Diesel Fuel Surrogate. *Appl. Mech. Mater.* **2014,** *541-441* (Engineering and Manufacturing Technologies), 1006-1010.

(32.)    Hernandez, J. J.; Sanz-Argent, J.; Monedero-Villalba, E., A Reduced Chemical Kinetic Mechanism of a Diesel Fuel Surrogate (n-Heptane/Toluene) for HCCI Combustion Modelling. *Fuel* **2014,** *133*, 283-291.

(33.)    Bounaceur, R.; Glaude, P. A.; Fourtnet, R.; Warth, V.; Battin-Leclerc, F., Detailed Kinetic Models for the Low-Temperature Auto-Ignition of Gasoline Surrogates. In *European Combustion Meeting 2009*, Vienna, Austria, 2009; Vol. e-Print Archive, pp 1-6.

(34.)    Zhao, H., HCCI and CAI Engines for the Automotive Industry. **2007**, 524 pp.

(35.)    Barckholtz, T. A., Modeling the Negative Temperature Coefficient in the Low Temperature Oxidation of Light Alkanes. *Prepr. Pap.-Am. Chem. Soc., Div. Fuel Chem.* **2003,** *48* (2), 518-519.

(36.)    Coniglio, L.; Bennadji, H.; Glaude, P. A.; Herbinet, O.; Billaud, F., Combustion Chemical Kinetics of Biodiesel and Related Compounds (Methyl and Ethyl Esters): Experiments and Modeling- Advances and Future Refinements. *Prog. Energ. Combust.* **2013,** *39*, 340-382.

(37.)    Fisher, E. M.; Pitz, W. J.; Curran, H. J.; Westbook, C. K., Detailed Chemical Kinetic Mechanisms for Combustion of Oxygenated Fuels. *P. Combust. Inst.* **2000,** *28*, 1579-1586.

(38.)    Dooley, S.; Curran, H. J.; Simmie, J. M., Autoignition Measurements and a Validated Kinetic Model for the Biodiesel Surrogate, Methyl Butanoate. *Combust. Flame* **2008,** *153*, 2-32.

(39.)    Gail, S.; Sarathy, S. M.; Thomson, M. J.; Dievart, P.; Dagaut, P., Experimental and Chemical Kinetic Modeling Study of Small Methyl Esters Oxidation: Methyl(E)-2-butenoate and Methyl Butanoate. *Combust. Flame* **2008,** *155*, 635-650.

(40.)    Hakka, M. H.; Bennadji, H.; Biet, J.; Yahyaoui, M.; Sirjean, B.; Warth, V., Oxidation of Methyl and Ethyl Butanoates. *In. J. Chem. Kinet.* **2010,** *42*, 226-252.

(41.)    Lin, K. C.; Lai, J. Y. W.; Violi, A., The Role of the Methyl Ester Moiety in Biodiesel Combustion: a Kinetic Modeling Comparison of Methyl Butanoate and n-Butane. *Fuel* **2011,** *92*, 16-26.

(42.)    Scheer, A. M.; Welz, O.; Vasu, S. S.; Osborn, D. L.; Taatjes, C. A., Low Temperature (550-700 K) Oxidation Pathways of Cyclic Ketones: Dominance of HO2-Elimination Channels Yielding Conjugated Cyclic Coproducts. *Phys. Chem. Chem. Phys.* **2015,** *17*, 12124-12134.

(43.)    Zador, J.; Taatjes, C. A.; Fernandes, R. X., Kinetics of Elementary Reactions

159

in Low-Temperature Autoignition Chemistry. *Prog. Energ. Combust.* **2011,** *37*, 371-421.

(44.) Scheer, A.; Welz, O.; Zador, J.; Osborn, D. L.; Taatjes, C. A., Low-Temperature Combustion Chemistry of Novel Biofuels: Resonance-Stabilized QOOH in the Oxidation of Diethyl Ketone. *Phys. Chem. Chem. Phys.* **2014,** *16* (26), 13027-13040.

(45.) Fernandes, R. X.; Zador, J.; Jusinski, L.; Miller, J.; Taatjes, C. A., Formally Direct Pathways and Low-Temperature Chain Branching in Hydrocarbon Autoignition: the Cyclohexyl + 02 reaction at High Pressure. *Phys. Chem. Chem. Phys.* **2009,** *22* (9), 1320-1327.

(46.) Zador, J.; Huang, H.; Welz, O.; Zetterberg, J.; Osborn, D. L.; Taatjes, C. A., Directly Measuring Reaction Kinetics of QOOH- a Crucial but Elusive Intermediate in Hydrocarbon Autoignition. *Phys. Chem. Chem. Phys.* **2013,** *15*, 10753-10760.

(47.) Allen, J. W.; Scheer, A. M.; Gao, C. W.; Merchant, S. S.; Vasu, S. S.; Welz, O.; Savee, J. D.; Osborn, D. L.; Lee, C.; Vranckx, S.; Wang, Z.; Qi, F.; Fernandes, R. X.; Green, W. H.; Hadi, M. Z.; Taatjes, C. A., A Coordinated Investigation of the Combustion Chemistry of Diisopropyl Ketone, a Prototype for Biofuels Produced by Endophytic Fungi. *Combust. Flame* **2014,** *161* (3), 711-724.

(48.) Taatjes, C. A.; Hansen, N.; Osborn, D. L.; Kohse-Hoeinghaus, K.; Cool, T. A.; Westmoreland, P. R., Imaging Combustion Chemistry via Multiplexed Synchrotron-Photoionization Mass Spectrometry. *Phys. Chem. Chem. Phys.* **2008,** (10), 20-34.

(49.) Ng, M. Y.; Nelson, J.; Taatjes, C. A.; Osborn, D. L.; Meloni, G., Synchrotron Photoionization Study of Mesitylene Oxidation Initiated by Reaction with Cl(2P) or O(3P) Radicals. *J. Phys. Chem. A.* **2014,** *118* (21), 3735-3748.

(50.) Osborn, D. L.; Zou, P.; Johnsen, H.; Hayden, C. C.; Taatjes, C. A.; Knyazev, V. D.; North, S. Q.; Peterka, D. S.; Ahmed, M.; Leone, S. R., The Multiplexed Chemical Kinetic Photoionization Mass Spectrometer: A New Approach to Isomer-Resolved Chemical Kinetics. *Rev. Sci. Instrum.* **2008,** *79* (104103), 1-10.

(51.) Scheer, A.; Welz, O.; Sasaki, D.; Osborn, D. L.; Taatjes, C. A., Facile Rearrangement of 3-Oxoalkyl Radicals is Evident in Low-Temperature Gas-Phase Oxidation of Ketones. *J. Am. Chem. Soc.* **2013,** *135* (38), 14256-14265.

(52.) Welz, O.; Zador, J.; Savee, J. D.; Ng, M. Y.; Meloni, G.; Fernandes, R. X.; Sheps, L.; Simmons, B. A.; Lee, T. S.; Osborn, D. L.; Taatjes, C. A., Low-temperature Combustion Chemistry of Biofuels: Pathways in the Initial Low-Temperature (550 K - 750 K) Oxidation Chemistry of Isopentanol. *Phys. Chem. Chem. Phys.* **2012,** *14*, 3112-3127.

(53.) Ochterski, J. W.; Petersson, G. A.; Montgomery, J. A., A Complete Basis Set Model Chemistry. V. Extensions to six or More Heavy Atoms. *J. Chem. Phys.* **1996,** *104*, 2598-2619.

(54.) Montgomery, J. A.; Frisch, M. J.; Ochterski, J. W.; Petersson, G. A., A Complete Basis Set Model Chemistry. VI. Use of Density Functional Geometries and Frequencies. *J. Chem. Phys.* **1999,** *110*, 2822-2827.

(55.) Montgomery, J. A.; Frisch, M. J.; Ochterski, J. W.; Petersson, G. A., A Complete Basis Set Model Chemistry. VII. Use of the Minimum Population Localization Method. . *J. Chem. Phys.* **2000,** *112*, 6532-6542.

(56.) Frisch, M. J.; Trucks, G. W.; Schlegel, H. B.; Scuseria, G. E.; Robb, M. A.; Cheeseman, J. R.; Scalmani, G.; Barone, V.; Mennucci, B.; Petersson, G. A.; Nakatsuji, H.; Caricato, M.; Li, X.; Hratchian, H. P.; Izmaylov, A. F.; Bloino, J.; Zheng, G.; Sonnenberg, J. L.; Hada, M.; Ehara, M.; Toyota, K.; Fukuda, R.; Hasegawa, J.; Ishida, M.; Nakajima, T.; Honda, Y.; Kitao, O.; Nakai, H.; Vreven, T.; Jr., J. A. M.; Peralta, J. E.; Ogliaro, F.; Bearpark, M.; Heyd, J. J.; Brothers, E.; Kudin, K. N.; Staroverov, V. N.; Kobayashi, R.; Normand, J.; Raghavachari, K.; Rendell, A.; Burant, J. C.; Iyengar, S. S.; Tomasi, J.; Cossi, M.; Rega, N.; Millam, J. M.; Klene, M.; Knox, J. E.; Cross, J. B.; Bakken, V.; Adamo, C.; Jaramillo, J.; Gomperts, R.; Stratmann, R. E.; Yazyev, O.; Austin, A. J.; Cammi, R.; Pomelli, C.; Ochterski, J. W.; Martin, R. L.; Morokuma, K.; Zakrzewski, V. G.; Voth, G. A.; Salvador, P.; Dannenberg, J. J.; Dapprich, S.; Daniels, A. D.; Farkas, O.; Foresman, J. B.; Ortiz, J. V.; Cioslowski, J.; Fox, D. J. *Gaussian 09*, Gaussian, Inc.: Wallingford, CT, 2009.

(57.) Peng, C.; Schlegel, H. B., Combining Sychronous Transit and Quasi-Newton Methods to Find Transition States. *Israel J. Chem.* **1993,** *33* (449), 449-454.

(58.) Dennington, R.; Keith, T.; Millam, J. *GaussView*, SemiChem Inc.: Shawnee Mission, KS, 2009.

(59.) Curtiss, L. A.; Raghavachari, K.; Redfern, P. C.; Pople, J. A., Assessment of Gaussian-2 and Density Functional Theories for the Computation of Enthalpies of Formation. *J. Chem. Phys.* **1997,** *106*, 1063-1079.

(60.) Curtiss, L. A.; Redfern, P. C.; Raghavachari, K.; Pople, J. A., Assessment of Gaussian-2 and Density Functional Theories for the Computation of Ionization Potentials and Electron Affinities. *J. Chem. Phys.* **1998,** *109*, 42-55.

(61.) Jr., M. W. C., NIST-JANAF Thermochemical Tables, Fourth Edition. *J. Phys. Chem. Ref. Data* **1998,** *Ref. Data* (Monograph 9), 1-1951.

(62.) Dam, H. V.; Oskam, A., He (I) and He (II) Photoelectron Spectra of Some Substituted Ethylenes. *J. Electron Spectrosc. Relat. Phenom.* **1978,** *13* (3), 273-290.

(63.) Savee, J. D.; Papajak, W.; Rotavera, B.; Huang, H.; Eskola, A. J.; Welz, O.; Sheps, L.; Taatjes, C. A.; Zador, J.; Osborn, D. L., Direct Observation and Kinetics of a Hydroperoxyalkyl Radical (QOOH). *Science* **2015,** *347* (6222), 643-646.

(64.) Russel, G. A., Deuterium-Isotope Effects in the Autoxidation of Aralkyl Hydrocarbons. Mechanism of the Interaction of Peroxy Radicals. *J. Am. Chem. Soc* **1957,** *79*, 3871-3877.

# Chapter 5: Aerosol Photoelectron Spectroscopy

## 5.1 Abstract

Preliminary aerosol photoelectron spectra were obtained at the National Synchrotron Radiation Research Center (NSRRC) in Hsinchu City, Taiwan. PE spectra for isoprene in environments of varying levels of acidity (pH of 1, 7, and 12), as well as spectra for gamma-valerolactone with differing levels of aerosol concentrations (5%, 20%, 30%, and pure) are presented and discussed.

## 5.2 Introduction

Fossil fuels have been the primary source of energy for transportation. The depleting reserves and growing concern over combustion emissions underline the need to focus on alternative fuels. Biofuel is a potentially carbon-neutral source of energy, as necessary ingredients can be extracted from both plants and animals. Various types of molecules are used as biofuel components, or studied as biofuel candidates — including ethers, alcohols, esters, furans, saturated hydrocarbons, and lactones.[1-4]

The structure of these types of molecules can influence the combustion behavior, as evidenced by the role of the functional group in small-chain methyl ester oxidation described in Chapter 4. Photoelectron (PE) spectroscopy is a valuable method frequently employed to elucidate the electronic structures of molecules, and while there is a range of literature available for PE spectroscopy of structures in the solid,[5, 6] liquid,[7-9] and gaseous states,[7, 10, 11] only recently has aerosol photoelectron spectroscopy emerged.[12, 13] In addition, information regarding PE spectroscopy of biofuel-related aerosols is very scarce.

Aerosol particles (0.01 – 10 µm in diameter) are a subset of particulate matter (PM), which is a class of small-sized pollutants that contribute to global warming by scattering solar radiation.[14, 15] Biofuels, and fuels in general, are closely related to the formation of aerosol particles, either through the reaction of $NO_x$ with organic atmospheric particles or directly emitted as small-sized carbonaceous aggregates such as soot.[16-18] When volatile organic compounds (VOCs) come into contact with ozone, for example, a specific type of aerosol is formed and is designated as secondary organic aerosols (SOAs).[19, 20] These reactions are complex and many studies have been conducted in an effort to ascertain the ozonolysis process and kinetics of aerosol formation.[21, 22]

Recently, Su et. al.[13] experimented with cysteine in the aqueous aerosol phase through a biological perspective. Cysteine, an amino acid, regulates biological function of proteins,[23] and while *ab initio* studies have been conducted on the electronic structure of cysteine in the gas-phase,[24] it was of interest to study the compound under physiologically relevant conditions — particularly in an aqueous environment. The activity of cysteine had been interpreted by its nucleophilicity,[25] although clear evidence was not available in literature. The valence electronic structure of cysteine in the aqueous aerosol phase was obtained and the results showed distinct band shapes at varying pH conditions through photoelectron spectroscopy.[13]

The aerosol photoelectron spectroscopy of cysteine inspired the current investigation of two particular biofuels in the aerosol phase, isoprene and gamma-valerolactone. Isoprene is used to produce liquid aviation fuels,[26] and is naturally released into the atmosphere by many plants.[27, 28] For the reason that it has been

163

classified as one of the most dominant biogenic VOCs, emission algorithms such as MEGAN (Model of Emissions of Gases and Aerosols from Nature) model regional and global levels of isoprene.[29] In addition, the oxidation of isoprene (2-methyl-1,3-butadiene, C5H8) is known to lead to SOAs, which have been described to greatly influence the climate due to contribution toward cloud condensation and nucleation.[30, 31] The impact of surrounding $NO_x$ conditions and relative humidity levels (RH) in the atmosphere have also been investigated in the role of isoprene SOA formation.[32, 33]

The influence of an acidic environment on isoprene has been explored, showing polymerization capabilities on acidic sulfate aerosols using aerosol mass spectrometry.[34, 35] Lewandowski et al.[36] sought to understand the impact of acidity-influenced oxidation chemistry on SOA yields of isoprene, finding a direct relationship between aerosol acidity and increasing SOA formation from photooxidation of isoprene. In this investigation, photoelectron spectra of isoprene aerosols, with varying degrees of acidic environments, are obtained and analyzed.

In addition to isoprene, gamma-valerolactone (dihydro-5-methyl-2(3H)-Furanone, $C_5H_8O_2$) is a biofuel of interest in the present work. It can be produced by dehydration/hydrogenation of $C_6$-sugars or levulinic acid with the use of ruthenium catalysts.[37, 38] Gamma-valerolactone (GVL) is used as a high-quality fuel-additive, and can be converted to liquid alkenes for use as transportation fuels.[39, 40] As GVL can be used in new generation engines, such as homogenous compression ignition (HCCI), the relevant autoignition and combustion processes were investigated via ·OH-initiated photooxidation reactions at the Advanced Light Source by Giovanni Meloni's research group at University of San Francisco.[41] The absolute

164

photoionization cross-sections of GVL have also been reported by Czekner et al.[42] at USF. In continuation of this line of research, the photoelectron spectra of GVL in the aerosol phase are obtained as function of molecular beam concentration to determine changes in electronic structure.

## 5.3 Experiment

Photoelectron spectroscopy was conducted at the beamline BL21B2 at the National Synchrotron Radiation Research Center in Hsinchu City, Taiwan. In-depth details of the aerosol photoelectron spectroscopy apparatus are provided in section 3.2 of this thesis and a brief overview is provided here.

Prior to conducting the experiments, PE spectra of atomized water are taken to identify the vibrational bands. These are essentially used as "background" spectra, although depending upon the ionization energies of the aerosol species investigated, the subtraction of water may or may not be required to witness shifts in bands between experiments. When water is atomized, there are two specific contributions to the PE spectrum: condensed-phase water (onset ~10.75, eV binding energy) and gas phase water (onset ~12.50 eV, binding energy).

Three identical isoprene solutions were prepared by dissolving 0.14 mL into 200 mL of water to form 0.01 M solutions. HCl or NaOH was added to each solution and the pH was monitored with a Suntex SP-701 pH meter to form three isoprene solutions of pH 1, 7, and 12. Following a similar procedure, a 0.5 M solution of GVL was prepared by dissolving 10 mL into 200 mL of water.

For each experiment, the respective sample was placed into a Model 9306[43] atomizer where the pressure was controlled by a regulator. The liquid solution was forced through small nozzles via pressure generated by inert neon gas flow into the atomizer. This neon flow generated aerosol droplets on the order of 100 nm in diameter and carried the aerosol mixture to the aerosol source chamber, where it entered an adjusted aerodynamic lens (AADL) system for additional size-selection. Once entering the ionization region, the beam intersected VUV synchrotron radiation of 25 eV photon energy. The ejected electrons were collected with a R3000 model (Scienta Omicron)[44] hemispherical electron energy analyzer with an acceptance angle of 10°. The kinetic energy of the photoelectrons were recorded and subsequently converted to binding energy, and then compared with literature values and PE spectra where available. In addition, geometric optimizations, adiabatic ionization energies, and simulated PE spectra were achieved using Gaussian 09[45] suite at the CBS-QB3[46-48] level of theory with a mean average deviation of 0.05 eV.

## 5.4 Results and Discussion

### 5.4.1 Isoprene

The photoelectron spectra of isoprene solutions of pH 1, 7, and 12 are represented in Figure 5.4.1 for simplicity.

Literature reference for the valence shell electronic spectroscopy of isoprene in the gas phase is provided by Martins et al.,[49] where the first onset is reported at 8.842 eV, assigned to the ionization from the π(3a") orbital. The CBS-QB3 calculated adiabatic ionization energy of 8.86 ± 0.05 eV is in excellent agreement with

experimental value obtained by their investigation. However, perhaps due to the dilute mixture of the sample, as well as the low solubility of isoprene in water, isoprene is undetectable in the PE spectrum obtained from our experimentation.

The results are not optimal for analysis in that the condensed phase band of water typically appears ~10.83 eV, while it is shifted upward in the spectrum pertaining to pH 12 at ~11.3 eV. The relative intensity of the condensed phase water band is also substantially more prominent for the pH 12 aerosol compared to the more acidic environments.
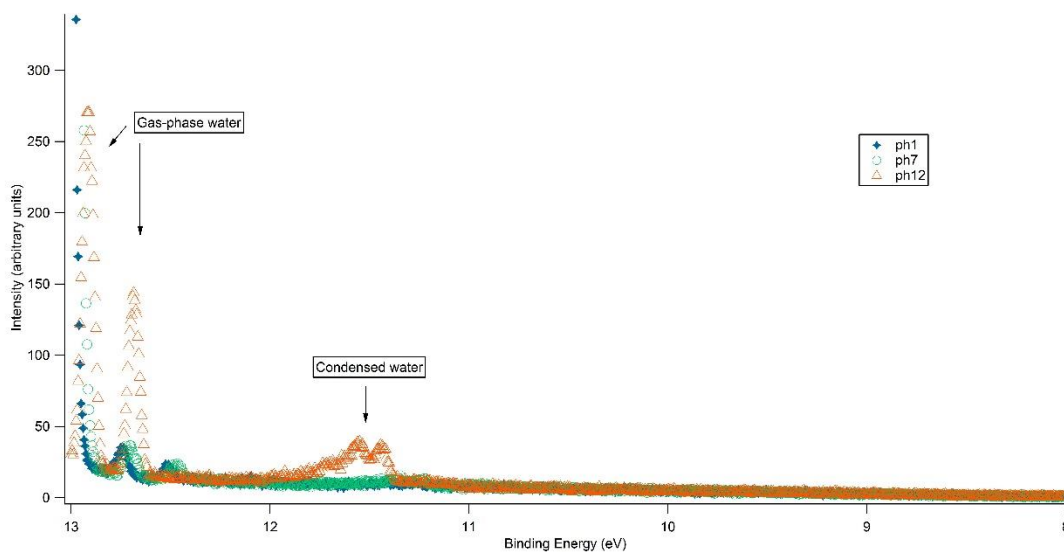


**Figure 5.4.1:** Photoelectron spectra generated at 25 eV for atomized solutions of isoprene + $H_2O$ at pH of 1, 7, and 12.

## 5.4.2 Gamma-Valerolactone

Photoelectron spectra of gamma-valerolactone in four different molecular-beam concentrations are shown in Figure 5.4.2a.
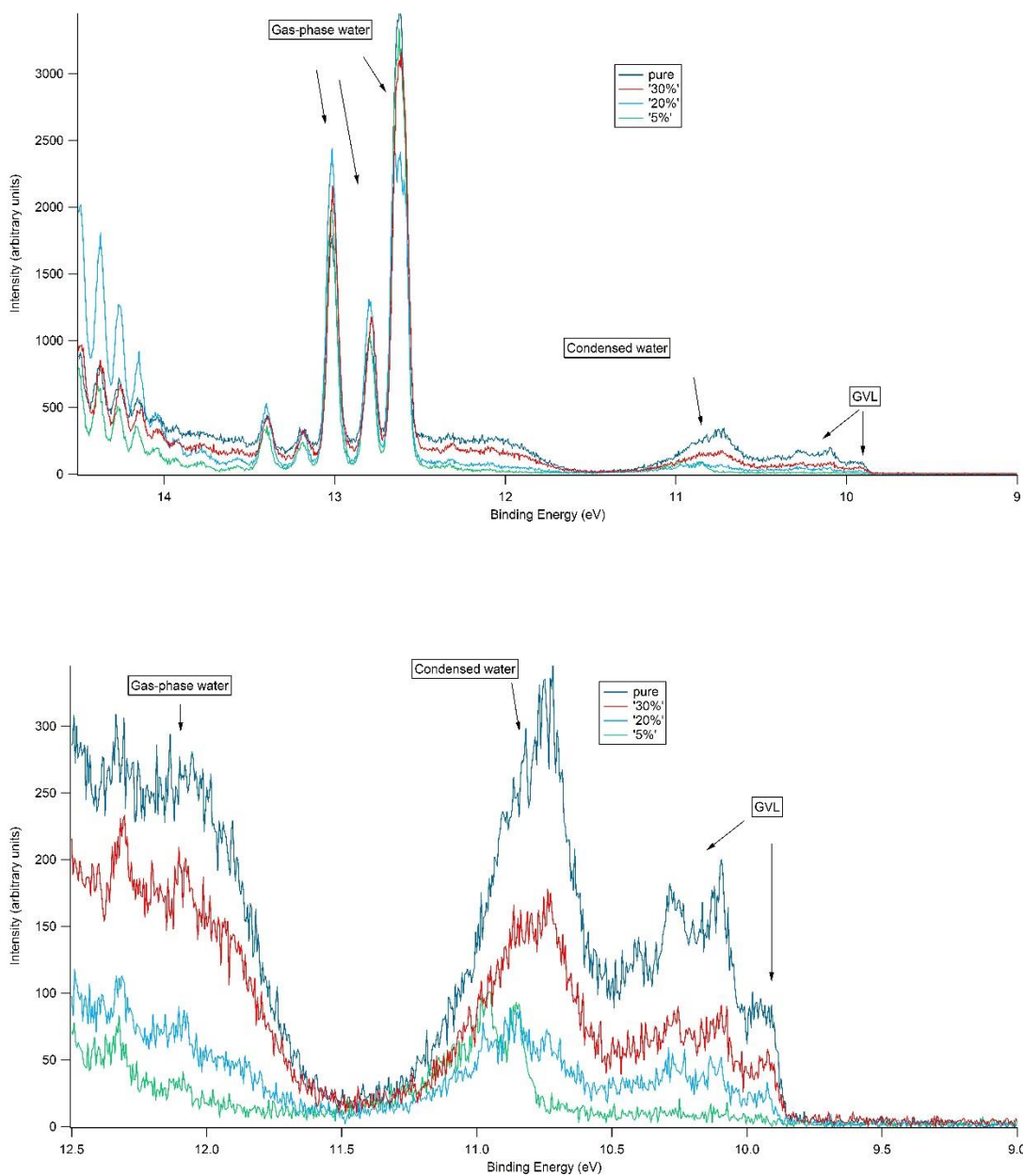
**Figure 5.4.2a:** Top: Photoelectron spectra of GVL "pure", 5%, 20%, and 30% aerosol beam concentrations in the range of 9.0 to 14.5 eV binding energy. Bottom: A closer image of the PE spectra, with binding energy from 9.0 to 12.5 eV.

Although the photoelectron spectrum of GVL is not currently available in literature, the CBS-QB3 calculated adiabatic ionization energy of 9.98 ± 0.05 eV by Czekner et al.[42] is in good agreement with the measured onset of GVL shown in Figure 5.4.2a. The lowest-energy structure optimized at the CBS-QB3 level of both neutral and cationic GVL are shown in Figure 5.4.2b, and the simulated PE spectrum is visualized in Figure 5.4.2c.

The results of GVL aerosol photoelectron spectroscopy resulting from varying aerosol concentrations are not compelling, as the bands do not seem to shift. However, a potentially interesting investigation for future study would involve the shift in relative peak intensities from the gas-phase to the aerosol phase. In the simulated gas phase PE spectrum shown in Figure 5.4.2c, the third peak vibrational band is the most intense at approximately 10.3 eV (binding energy). However, in the pure aerosol PE spectrum shown in Figure 5.4.2a, the second band at approximately 10.1 eV is the most intense vibrational transition. Additional measurements, both in the gas phase as well as aqueous aerosol phase, would need to be conducted in order to understand the shift.
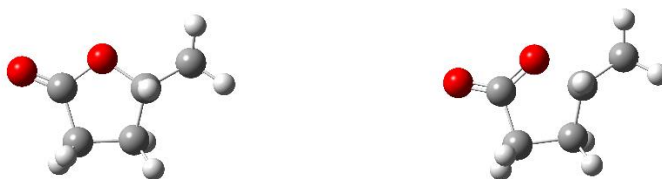


**Figure 5.4.2b:** Left: The neutral species of GVL. Right: The cationic GVL species. Both geometries optimized at the CBS-QB3 level of theory.
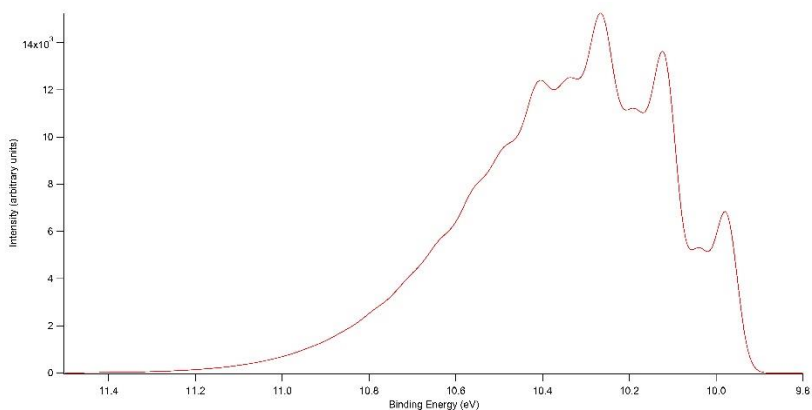
**Figure 5.4.2c:** The Gaussian-simulated gas phase photoelectron spectrum of gamma-valerolactone calculated at the CBS-QB3 level of theory.

## 5.5 Conclusion:

This preliminary investigation to aerosol photoelectron spectroscopy for biofuels serves as a foundation for future experimentation. While these results do not present persuasive evidence to support changes in electronic structure in the two experiments, there are changes that can be made that may improve our understanding of behavior in the aerosol state. Namely, it would be of interest to study an experiment involving two source regions, i.e., one for pure isoprene aerosol and another for acidic aqueous aerosol. In this way, solubility and liquid-phase chemistry processes are eliminated and perhaps this will closer emulate natural atmospheric interaction. In addition, particle sizers and counters would be of use to differentiate changes in photoelectron spectra based on the aerosol particle size.

**5.6 Acknowledgements**

## 5.7 References

1.      Schuchardta, U., R. Serchelia, and R.M. Vargas, *Transesterification of Vegetable Oils: A Review.* Journal of the Brazilian Chemical Society, 1998. **9**: p. 199-210.

2.      Agarwal, A.K., *Biofuels (alchols and biodiesel) Applications as Fuels for Internal Combustion Engines.* Progress in Energy and Combustion Science, 2007. **33**: p. 233-271.

3.      Roman-Leshkov, Y., et al., *Production of Dimethyl-furan for Liquid Fuels from Biomass-derived Carbohydrates.* Nature, 2007. **447**: p. 982-985.

4.      Horvath, I.T., et al., *-Valerolactone - a Sustainable Liquid for Energy and Carbon-Based Chemicals.* Green Chemistry, 2008. **10**: p. 238-242.

5.      Green, J.C., *Photoelectron Spectroscopy: Study of Valence Bands in Solids.* Annual Review of Physical Chemistry, 1977. **28**: p. 161-183.

6.      Campbell, M.J., et al., *Ultraviolet Photoelectron Spectroscopy of the Valence Bands of Solid $NH_3$, $H_2O$, $CO_2$, $SO_2$, and $N_2O_4$.* Journal of Physics C: Solid State Physics, 1982. **15**(11): p. 2549.

7.      Suzuki, T., *Time-resolved Photoelectron Spectroscopy of Non-adiabatic Electronic Dynamics in Gas and Liquid Phases.* International Reviews in Physical Chemistry, 2012. **31**(2): p. 265-318.

8.      Men, S., et al., *X-ray Photoelectron Spectroscopy of Pyridinium-Based Ionic Liquids: Comparison to Imidazolium- and Pyrrolidinium-Based Analogues.* Chem. Phys. Chem., 2015. **16**(10): p. 2211-2218.

9.      Winter, B., et al., *Hydrogen Bonds in Liquid Water Studied by Photoelectron Spectroscopy.* The Journal of Chemical Physics, 2007. **126**: p. 124504.

10.     Su, J., et al., *Photoelectron Spectroscopy and Theoretical Studies of Gaseous Uranium Hexachlorides in Different Oxidation States: $UCl_6^{q-}$ (q = 0-2).* The Journal of Chemical Physics, 2015. **142**: p. 134308.

11.     Eland, J.H.D., *Photoelectron Spectroscopy: An Introduction to Ultraviolet Photoelectron Spectroscopy in the Gas Phase, 2nd ed.* 1984, London, UK: Butterworths.

12.     Wilson, K.R., H. Bluhm, and M. Ahmed, *Aerosol Photoemission*, in *Fundamentals and Applications*, J.P. Reid and R. Signorell, Editors. 2011, Taylor and Francis.

13.     Su, C.-C., et al., *VUV Photoelectron Spectroscopy of Cysteine Aqueous Aerosols: A Microscopic View of Its Nucleophilicity at Varying pH Conditions.* Journal of Physical Chemistry Letters, 2015. **6**(5): p. 817-823.

14.     Chylek, P., et al., *Optical properties and mass concentration of carbonaceous smokes.* Applied Optics, 1981. **20**(17): p. 2980-2985.

15.     Jacob, D.J., *Introduction to Atmospheric Chemistry*. 1999, Princeton, NJ: Princeton University Press.

16.     Voiland, A. *Aerosols: Tiny Particles, Big Impact*. 2010  [cited 2015 December 23, 2015]; Available from: http://earthobservatory.nasa.gov/Features/Aerosols/.

17.     Sachdeva, K. and A.K. Attri, *Morphological Characterization of Carbonaceous Aggregates in Soot and Free Fall Aerosol Samples.* Atmospheric Environment, 2007. **42**: p. 1025-1034.

18.     Ramanathan, V., *Atmospheric Brown Clouds: Health, Climate, and Agriculture Impacts*, in *Interactions Between Global Change and Human Health*

2006, The Pontifical Academy of Sciences: Vatican City.

19.     Kroll, J.H. and J.H. Seinfeld, *Chemistry of Secondary Organic Aerosol: Formation and Evolution of Low-Volatility Organics in the Atmosphere.* Atmospheric Environment, 2008. **42**(16): p. 3593-3624.

20.     Keywood, M.D., et al., *Secondary Organic Aerosol Formation from Cyclohexene Ozonolysis: Effect of OH Scavenger and the Role of Radical Chemistry.* Environmental Science and Technology, 2004. **38**: p. 3343-3350.

21.     Smith, A.R., *Furanic Molecules: Multiplexed Synchrotron Photoionization Investigations and Aerosol Studies*, in *Chemistry*. 2015, University of San Francisco: San Francisco.

22.     Ziemann, P.J., *Aerosol Products, Mechanisms, and Kinetics of Heterogeneous Reactions of Ozone with Oleic Acid in Pure and Mixed Particles.* Faray Disscussions, 2005. **130**: p. 469-490.

23.     Gould, N., et al., *Regulation of Protein Function and Signaling by Reversible Cysteine S-Nitrosylation.* J. Biol. Chem., 2013. **288**: p. 26473-26479.

24.     Gronert, S. and R.A.J. Ohair, *Ab Initio Studies of Amino Acid Conformations. 1. The Conformers of Alanine, Serine, and Cysteine.* J. Am. Chem. Soc., 1995. **117**: p. 2071-2081.

25.     Edwards, J.O. and R.G. Pearson, *Factors Determining Nucleophilic Reactivities.* J. Am. Chem. Soc., 1962. **84**: p. 16-24.

26.     *Renewable Alternatives to Fossil Fuels*. 2015   [cited 2015 December 23, 2015]; Available from: http://www.uwsp.edu/wist/Pages/research/biofuels-research.aspx.

27.     Kesselmeier, J. and M. Staudt, *Biogenic Volatile Organic Compounds (VOC): An Overview on Emission, Physiology and Ecology.* J. Atm. Chem., 1999. **33**: p. 23-88.

28.     Wagner, W., M. Nemecek-Marshall, and R. Fall, *Three Distinct Phases of Isoprene Formation During Growth and Sporulation of Bacillus Subtilis.* J. Bacteriology, 1999. **181**(15): p. 4700-4703.

29.     Guenther, A., et al., *Estimates of Global Terrestrial Isoprene Emissions using MEGAN (Model of Emissions of Gases and Aerosols from Nature).* Atmos. Chem. Phys., 2006. **6**: p. 3181-3210.

30.     Carlton, A.G., C. Wiedinmyer, and J.H. Kroll, *A Review of Secondary Organic Aerosol (SOA) Formation from Isoprene.* Atmos. Chem. Phys. , 2009. **9**: p. 4987-5005.

31.     Kamens, R.M., et al., *Ozone-Isoprene Reactions: Product Formation and Aerosol Potential.* International Journal of Chemical Kinetics, 1982. **14**(9): p. 955-975.

32.     Finalyson-Pitts, B.J. and J.N. Pitts, *Chemistry of the Upper and Lower Atmosphere: Theory, Experiments, and Applications*. 2000, San Diego: Academic Press.

33.     Vasconcelos, L.A.d.P., E.S. Macias, and W.H. White, *Aerosol Composition as a Fucntion of Haze and Humidity Levels in the Southwestern US.* Atmospheric Environment, 1994. **28**: p. 3679-3691.

34.     Liggio, J., et al., *Direct Polymerization of Isoprene and α-pinene on Acidic Aerosols.* Geophysical Research Letters, 2007. **34**(5).

35.    Limbeck, A., M. Kulmala, and H. Puxbaum, *Secondary Organic Aerosol Formation in the Atmosphere via Heterogeneous Reaction of Gaseous Isoprene on Acidic Particles.* Geophysical Research Letters, 2003. **30**(19).

36.    Lewandowski, M., et al., *Atmospheric Oxidation of Isoprene and 1,3-butadiene: Influence of Aerosol Acidity and Relative Humidity on Secondary Organic Aerosol.* Atmos. Chem. Phys., 2015. **15**: p. 3773-3783.

37.    Xiao, C., et al., *Conversion of Levulinic Acid to Gamma-Valerolactone Over Few-Layer Graphene-Supported Ruthenium Catalysts.* ACS Catalysis, 2015. **Just Accepted Manuscript**.

38.    Heeres, H., et al., *Combined Dehydration/(transfer)-hydrogenation of $C_6$-sugars (D-glucose and D-fructose) to γ-Valerolactone Using Ruthenium Catalysts.* Green Chemistry, 2009. **11**: p. 1247-1255.

39.    Bond, J.Q., et al., *Integrated Catalytic Conversion of γ-Valerolactone to Liquid Alkenes for Transportation Fuels.* Science, 2011. **327**(5969): p. 1110-1114.

40.    Bond, J.Q., et al., *Interconversion between γ-valerolactone and pentenoic acid combined with decarboxylation to form butene over silica/alumina.* J. Catal., 2011. **281**: p. 290-299.

41.    He, Q., *Investigation of Gamma-Valerolactone + OH and Isobutanol + OH Combustion Systems Using Synchrotron Photoionization Mass Spectrometry*, in *Chemistry*. 2011, University of San Francisco: San Francisco, CA.

42.    Czekner, J., et al., *Absolute photoionization cross-sections of selected furanic and lactonic potential biofuels.* International Journal of Mass Spectrometry, 2013. **348**: p. 39-46.

43.    *Six-Jet Atomizer 9306*. 2015, TSI Inc.: Shoreview, Minnesota.

44.    *R3000 A Compact and Powerful Analysis Tool*. 2015   [cited 2015 December 12, 2015]; Available from: www.scientaomicron.com/en/products/357/1206.

45.    Frisch, M.J., et al., *Gaussian 09*. 2009, Gaussian, Inc.: Wallingford, CT.

46.    Ochterski, J.W., G.A. Petersson, and J.A. Montgomery, *A complete basis set model chemistry. V. Extensions to six or more heavy atoms.* J. Chem. Phys., 1996. **104**: p. 2598-2619.

47.    Montgomery, J.A., et al., *A complete basis set model chemistry. VI. Use of density functional geometries and frequencies.* J. Chem. Phys., 1999. **110**: p. 2822-2827.

48.    Montgomery, J.A., et al., *A complete basis set model chemistry. VII. Use of the minimum population localization method. .* J. Chem. Phys., 2000. **112**: p. 6532-6542.

49.    Martins, G., et al., *Valence Shell Electronic Spectroscopy of Isoprene Studied by Theoretical Calculations and by Electron Scattering, Photoelectron, and Absolute Photoabsorption Measurements.* Phys. Chem. Chem. Phys. , 2009. **11**: p. 11219-11231.

# Chapter 6: Rotamers and Migration: Investigating the Photodissociative Dynamics of the Ethylenediamine Ion

Giel Muller,[†] Krisztina Voronova,[‡] Giovanni Meloni,[†,*] and Bálint Sztáray[‡,*]

[†]University of San Francisco, California USA 94117,

[‡]University of the Pacific, Stockton, California USA 95211,

[*]Corresponding Authors: gmeloni@usfca.edu, bsztaray@pacific.edu

## 6.1 Abstract

The unimolecular dissociation of energy-selected ethylenediamine cations was studied by threshold photoelectron photoion coincidence spectroscopy (TPEPICO) in the photon energy range of 8.60–12.50 eV using a custom-made instrument housed at the University of the Pacific in Stockton, CA. A breakdown diagram and time-of-flight distributions were used to determine 0 K appearance energies for eight channels modeled with RRKM theory: $NH_2CHCH_2^{+\cdot}$ at 9.120 ± 0.010 eV, $CH_3C(NH_2)_2^+$ at 9.200 ± 0.012 eV, $NH_2CHCH_3^+$ at 9.34 ± 0.08 eV, $CH_2NH_2^+$ at 9.449 ± 0.025 eV, $CH_2NH_3^+$ at 9.8 ± 0.1 eV, $c\text{-}C_2H_4NH_2^+$ at 10.1 ± 0.1 eV, $CH_3NHCHCH_2^+$ at 10.2 ± 0.1 eV, and the reappearance of $CH_2NH_2^+$ at 10.2 ± 0.1 eV. The CBS-QB3-calculated pathways highlighted the influence of intramolecular hydrogen attractions on the photodissociation processes, presenting novel isomers and low-energy van der Waals intermediates that lead to dissociative fragments in good agreement with experimental results. While most of the dissociation channels take place through reverse barriers, the 0 K heat of formation of $\cdot CH_2NH_2$ was determined to be 160.6 ± 2.7 kJ mol$^{-1}$, in excellent agreement with literature, and the 0 K heat of formation of $CH_2NH_3^+$ at 860 ± 10 kJ mol$^{-1}$ is the first definitive experimentally measured value available and is in good agreement with theory.

**6.2 Introduction**

The effects of climate change are widely observed and greenhouse gases are a large contributing component. As of 2013, $CO_2$ emissions in the US resulting from liquid fuel combustion for transportation generated 26% of all greenhouse gases.[1, 2] Recent initiatives have focused on reducing emissions by researching novel technologies and alternative energy sources such as electric, hybrid, and biodiesel combustion. Biodiesel has the potential to be a carbon-neutral source of energy, contingent upon both the blend of the fuel and its impact upon the engine in which it is burned.

Many small amine-containing compounds, such as hydrazine and its methyl derivatives, are used extensively in various industrial arenas, including rocket fuel combustion processes.[3, 4] Ethylenediamine, the smallest polyethylene amine, possesses two terminal amino groups that enable the compound to readily form imidazolidines, succinimides, chelates, and polyamides. This versatility accounts for its many uses, ranging from the production of fungicides to biofuels.

The potential roles of ethylenediamine (EN) in fuel combustion are extensive. Tang et al.[5] studied the catalytic activity of EN in the transesterification process of rapeseed oil to generate biofuels, while fuel corporations have been incorporating EN to improve the cetane number in diesel fuels for internal combustion engines.[6] EN has recently been shown to enhance motor performance when coupled with borane to form innovative lubricant and fuel additives.[7] In general, many biodiesel blends with low cetane numbers present longer ignition delays and accelerate the formation of oil sludge. These engine deposits lead to greater release of smoke and exhaust, underlining the importance of effective fuel dispersant-detergents. In an

effort to better understand the combustion processes pertaining to EN polyamides and chelated complexes, it is necessary to realize precise thermochemical data of neutral ethylenediamine and its ionic species in the gas phase.

Threshold photoelectron photoion coincidence spectroscopy (TPEPICO) is an effective technique in determining highly accurate dissociative photoionization onsets, and to explore dissociation dynamics, branching ratios and energy partitioning among the product channels of internal energy-selected cations. Accurate thermochemical parameters of the neutral and ionic species, which are important in combustion and atmospheric models, can be ascertained using the data gathered from TPEPICO measurements.[8-15]

Previous experiments and theoretical computations of EN in the neutral state provide insight to understanding unimolecular dissociation on the cationic potential energy surface. Radom et al.[16] investigated the internal rotation in 1,2-disubstituted C-C bonds, reporting low-energy conformations that are stabilized by intramolecular hydrogen bonding involving the amine moieties. Two gauche rotational isomers (rotamers) were presented and the lowest-energy arrangement aligned with previous electron diffraction studies by Yokozeki et al.,[17, 18] which was calculated to be more than 95% abundance of EN. Over two decades later, Kazerouni et al.[19] conducted an ab initio investigation into the various conformations of ethylenediamine at the HF/6-31G* level using GAUSSIAN 90.[20] Three low-energy configurations were presented, including an anti form of EN with $C_1$ symmetry — still less stable than the two gauche forms. The lowest-energy gauche form was stabilized with hydrogen bonding, while in the other gauche structure the nitrogen pairs were opposite one another. Alsenoy et al.[21] calculated ten conformations of EN using the FORCE method with the 4-21G

basis set, and Lee et al.[22] used molecular orbital theory to explain the structure and conformational energies. Krest'yaninov et al.,[23] guided by Weinhold's[24] view of hydrogen bonding as charge transfer between orbitals, determined the most stable gauche form to have weak intramolecular hydrogen bonding characteristics.

The cationic state of EN is relatively unexplored, however a VUV photoionization experiment was conducted by Wei et al.,[25] where computational analysis at the G3 level was also presented in an attempt to explain the formations of the observed fragments. The experimental and computational results are in rough to good agreement, while some are not. This served as a motivation to revisit the dissociation of the ethylenediamine ion through TPEPICO, using the analysis by Wei et al.[25] as a starting point for the current investigation. With TPEPICO we further characterize the rotation, H-migration, and functional group migration processes involved in EN photodissociation, as these behaviors are of interest to the scientific community[26-29] and can be applied, for example, to combustion diagnostics.[15]

## 6.3 Experimental

The time-of-flight mass spectra of energy-selected EN cations were collected on the custom-built TPEPICO spectrometer located at the University of the Pacific. The apparatus has been described in details and only a brief overview is given here.[14, 30-33] Ethylenediamine was purchased from Sigma Aldrich (≥ 99% purity) and its vapor was effusively introduced into the ionization chamber. The molecules were ionized with vacuum ultraviolet light generated from a hydrogen discharge lamp operating at approximately 1–1.5 Torr $H_2$ pressure and dispersed by a 1 m normal incidence monochromator. The photon energy scale was calibrated using the

hydrogen Lyman-α and Lyman-β resonance lines and the resolution was 8 meV at 10 eV. The photoelectrons were extracted through a 6.75 mm long field of 20 V cm$^{-1}$ and were accelerated into a 13 cm drift tube set to 77 V. A mask at the end of the drift region contained a 1.4 mm aperture for the Channeltron detector (center) and 2 x 8 mm opening for the hot electron detector. The velocity map imaging (VMI), first introduced by the Baer group for TPEPICO,[34] allows electrons to be focused onto small rings contingent upon their velocity perpendicular to extraction. Thus, the hot electrons were eliminated by multiplying the hot electron signal (outer ring) by a well-defined weighted fraction and subtracting from the zero perpendicular velocity signal at the center.[32]

In the linear time-of-flight (LinTOF) setup, the ions were directed with Wiley-McLaren[35] space-focusing geometry and accelerated to 100 eV in the first 5 cm long acceleration region, then rapidly accelerated to 260 eV in a short second acceleration region. Thereafter, ions drifted across a 34 cm field-free region where they were detected. The velocity of the ion is indirectly proportional to its mass and its time-of-flight directly proportional to the square root of the mass of the ion.

Electron detection served as the start signal and its corresponding ion hit served as the stop signal for two time-to-pulse height converters (TPHC); the data acquisition schemes, including accounting for false coincidences, have been previously described.[36] This information was sent to the Ortec multichannel analyzer cards to create TOF spectra that can be used to extract meaningful thermochemical data via computational analysis and modeling.

A weighted factor of 0.18[32, 37] was used to subtract the hot electrons on the ring from the zero-velocity perpendicular electrons in the center to yield TOF spectra

representative of the dissociation reactions. In addition, the TOF spectra is integrated in multiple areas where no peaks are present to establish an effective baseline for noise that is then averaged and subtracted.

The low, 20 V cm$^{-1}$ extraction field is essential to obtain rate information, which is manifested in asymmetric TOF peak shapes. As a side effect, the instrumental peak widths are too wide for baseline separation of fragments with 1 *m/z* difference. In the case of fast dissociations where the peaks are Gaussian-shaped, the deconvolution was achieved using the IGOR[38] multi-peak fitting tools and the center of each peak. Slow dissociations are more complicated due to asymmetric peaks, however if the contribution of one of the ions (either x or x+1) to the total integrated signal is known, it can be subtracted to obtain the other. This process was used once adjacent peaks could be differentiated precisely and one of the peaks was known to be Gaussian-shaped. Relative ion signal was fixed to account for the $^{13}$C and $^{15}$N isotopologues (Figure 6.9).

Asymmetric TOF peaks are symptomatic of slow dissociation processes, where cationic parent molecules with excess energy above the dissociation barrier do not immediately dissociate, leading to a so-called kinetic shift.[39, 40] These non-Gaussian TOF peak shapes are representative of the dissociation rate constants. Therefore, to extract accurate 0 K onset energies and unimolecular dissociation rates, the TOF peak shapes were also modeled by MiniPEPICO[37] using RRKM theory in case of slow processes. Quantum mechanical calculations were conducted at the CBS-QB3 level of theory[41-43] for use in PEPICO analysis with the Gaussian09[44] suite, and in some cases the Gaussian-3 (G3)[45] method was used to compare with previous experimental results. Transition states with one negative

imaginary frequency were visually inspected using GaussView[46] and intrinsic reaction coordinate (IRC)[47, 48] calculations were performed at B3LYP/6-31G(d) level of theory to verify direct relationships between reactants and products. The transitional frequencies were scaled to fit the experimental data in the modeling process.[37]

## 6.4 Theory

PEPICO is widely used in the determination of accurate photoionization onsets, which can then be applied to arrive at valuable thermochemical and kinetic information. The MiniPEPICO program, described in detail by Sztáray, Bodi, and Baer,[37] calculates necessary density and number of states functions, and internal energy distributions to yield a breakdown diagram representing the fractional ion abundances as the function of the photon energy. Breakdown diagrams can be directly compared to the experimental fractional abundances and serve as helpful guides in the determination of parallel and consecutive dissociation pathways. In addition, the MiniPEPICO[37] program enables the experimental dissociation rates to be extracted using Rice, Ramsperger, Kassel, and Marcus's RRKM theory,[49-51] as well as the variational transition state theory (VST)[52] and simplified statistical adiabatic channel model (SSACM).[53] The RRKM rate constant as a function of internal energy (E) is given by

$$k(E) = \frac{\sigma N^{\ddagger}(E - E_0)}{h\rho(E)}, \tag{6.4}$$

where $N^{\ddagger}(E - E_0)$ is the number of states of the TS at excess energy above the dissociation barrier $E_0$, $\rho(E)$ is the density of states of the molecule, $h$ is Planck's constant and $\sigma$ corresponds to the symmetry number of the TS.

Cationic parent species do not always dissociate within the timescale of the experiment, i.e., slowly, and can yield asymmetric daughter ion peaks that are reflective of their dissociation rates. An additional term is utilized by MiniPEPICO[37] to compensate for this process, in which the ion energy distribution function is multiplied by the probability that the ion does not dissociate within the first acceleration region. The rate curves of slow dissociations require the vibrational frequencies of TS modes to be fitted with the appearance energies and the reproduction of the asymmetric TOF distributions as needed to account for kinetic shifts.

Quantum mechanical calculations are invaluable in the PEPICO analysis, as pertinent information is entered into the modeling program to calculate the thermal energy distribution of the neutral and daughter ions, such as rotational constants and frequencies of neutral and cationic ethylenediamine. Estimated transition state structures, with one imaginary frequency each, are determined by constrained optimizations in which either a bond length or a bond angle is scanned, or by using the Synchronous Transit-Guided Quasi-Newton (STQN) method[54, 55] at the B3LYP/6-31G(d) level/basis set and energies with CBS-QB3 optimizations. CBS-QB3 energetic calculations are accompanied by a mean absolute deviation (MAD) from experiments of $\pm$ 0.05 eV.[43, 56-58]

The experimental appearance energies (AE) of the fragments are obtained once the best fit is reached between the experimental and modeled breakdown. In the case of slow dissociations, the TOF spectra are also matched. Combining these appearance energies with known heats of formation of the neutral parents and

fragments, it is possible to arrive at the heats of formation of the daughter ions for those channels, which proceed without reverse activation barriers.

## 6.5 The Resultant Dissociative Photoionization Processes of EN

Time-of-flight spectra of energy-selected ethylenediamine ions were collected in the photon energy range of 8.60–12.50 eV at room temperature. The breakdown diagram (Figure 6.5a) represents the observed fragments at $m/z = 30, 31, 43, 44,$ and 59 as well as their TPEPICO-extracted appearance energies. Raw TOF spectra revealed all peaks to be symmetric, synonymous with fast dissociation processes, aside from that of $m/z = 43$ (Figure 6.5b). TOF peaks corresponding to $m/z = 30, 44,$ and 59 reappear at higher energies, resulting in a total of eight traceable parallel dissociation channels. Each dissociation pathway is outlined below in chronological order with respect to its appearance, along with the experimental reaction rates in Figure 6.5c (for structures of the ions, intermediates and TSs see Figure 6.6.4b).

**1.)** $m/z = 43$, $NH_2CHNH_2^{+\cdot}$. The $m/z = 43$ fragment is the first to appear and does so with a slow dissociation. The asymmetric TOF peak mirrors the dissociation rate and thus the time-of-flight mass spectra needed to be modeled along with the corresponding breakdown diagram as shown in Figure 6.5c. Reaction 1 (**R1**) leads to the resonance-stabilized ethenamine ion [11], resulting from $NH_3$-loss from an H-migration parent ion isomer ([10]):

$$NH_2CH_2CH_2NH_2^{+\cdot} \quad \rightarrow \quad NH_2CHCH_2^{+\cdot} + NH_3 \quad \quad (R1)$$
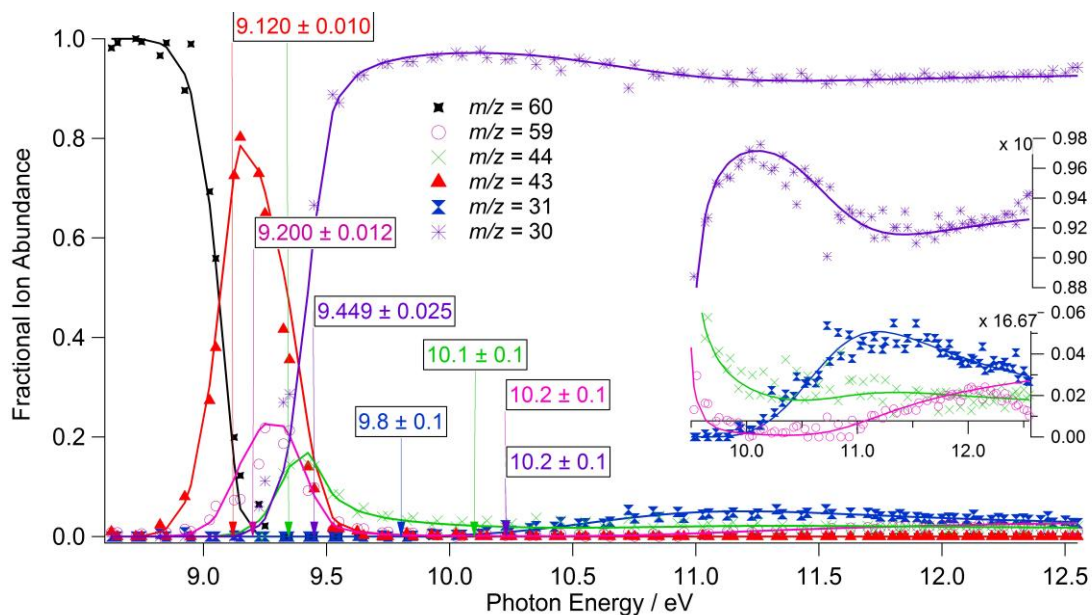
**Figure 6.5a:** Breakdown diagram of internal energy-selected ethylenediamine cations. Experimental data represented by dots and solid lines correspond to the best fit of the RRKM modeling of the data.
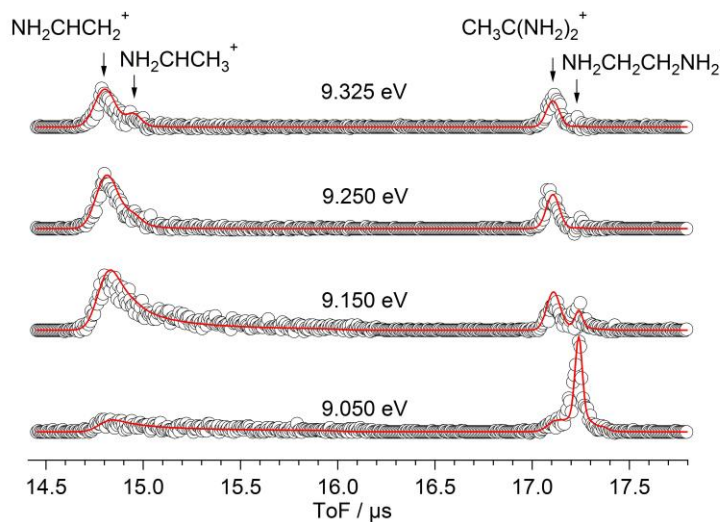


**Figure 6.5b:** Time-of-flight (TOF) mass spectra of ethylenediamine ($NH_2CH_2CH_2NH_2^{+\cdot}$) and the $CH_3C(NH_2)_2^+$, $NH_2CHCH_3^+$, and $NH_2CHCH_2^{+\cdot}$ fragment ions ($m/z = 60$, 59, 44, and 43 respectively).

**2.)** $m/z = 59$, $CH_3C(NH_2)_2^+$. The first hydrogen-loss pathway (**R2**) proceeds via H and $NH_2$-group migration to isomerize and subsequently form the 1-aminoethaniminium ion [18]. In this case the parent and the daughter ion peak shapes are not baseline separated, due to the low field and l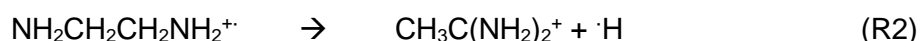ong extraction region, which are essential to obtain unimolecular rate information. However, the kinetic information hidden by the $m/z = 60$ peak, could be extracted from another parallel channel, namely, the formation of the $m/z = 43$, since the first order dissociation rate belongs to the fragmentation of the parent ion.

$$NH_2CH_2CH_2NH_2^{+\cdot} \quad \rightarrow \quad CH_3C(NH_2)_2^+ + \cdot H \qquad (R2)$$

**3.)** $m/z = 44$, $NH_2CHCH_3^+$. The ethylidenimmonium ion, [19], is the proposed cationic structure formed along with the neutral $\cdot NH_2$, from a van der Waals product complex [14]:

$$NH_2CH_2CH_2NH_2^{+\cdot} \quad \rightarrow \quad NH_2CHCH_3^+ + \cdot NH_2 \qquad (R3)$$
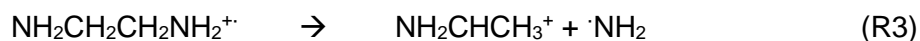
**4.)** $m/z = 30$, $CH_2NH_2^+$. The C-C bond cleavage leading to the methylenimmonium ion [20] is the dominant pathway in EN ion unimolecular dissociation and involves no migration processes:

$$NH_2CH_2CH_2NH_2^{+\cdot} \quad \rightarrow \quad CH_2NH_2^+ + \cdot CH_2NH_2 \qquad (R4)$$
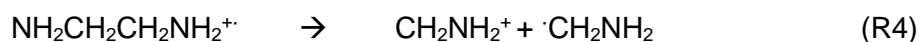
**5.)** $m/z = 31$, $CH_2NH_3^{+\cdot}$. The appearance of this cationic fragment is observable at slightly higher energies than that of $m/z = 30$ in **R4**. The methyleneammonium ion, structure [23], is projected to be the primary contributor through $CH_2NH$-loss and the overall channel is represented by reaction 5:

$$NH_2CH_2CH_2NH_2^{+\cdot} \quad \rightarrow \quad CH_2NH_3^{+\cdot} + CH_2NH \qquad (R5)$$

185
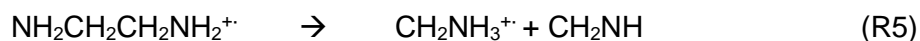
No appearance energy of this ion has been previously reported from EN dissociation.

**6.)** $m/z = 44$, $c$-$C_2H_4NH_2^+$. The reappearance of the $m/z = 44$ corresponds to the formation of cyclic aziridinium ion [28] from $NH_2$-migration and ultimate $NH_2$-loss:

$$NH_2CH_2CH_2NH_2^{+\cdot} \quad \rightarrow \quad c\text{-}C2H4NH_2^+ + {}^{\cdot}NH_2 \quad \quad \quad (R6)$$
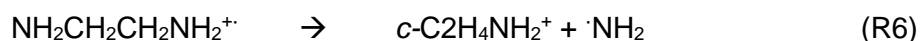
**7.)** $m/z = 59$, $CH_3NHCHCH_2^+$. The reappearance of $m/z = 59$ [36] as shown in the breakdown diagram occurs above 10.2 eV photon energy:

$$NH_2CH_2CH_2NH_2^{+\cdot} \quad \rightarrow \quad CH_3NHCHCH_2^+ + {}^{\cdot}H \quad \quad \quad (R7)$$
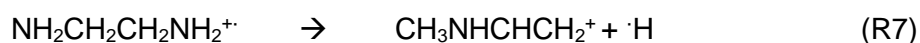
**8.)** $m/z = 30$, $CH_2NH_2^+$. The methylenimmonium ion [37] is formed again as in **R2**, however with a higher energy neutral fragment:

$$NH_2CH_2CH_2NH_2^{+\cdot} \quad \rightarrow \quad CH_2NH_2^+ + CH_3NH^{\cdot} \quad \quad \quad (R8)$$
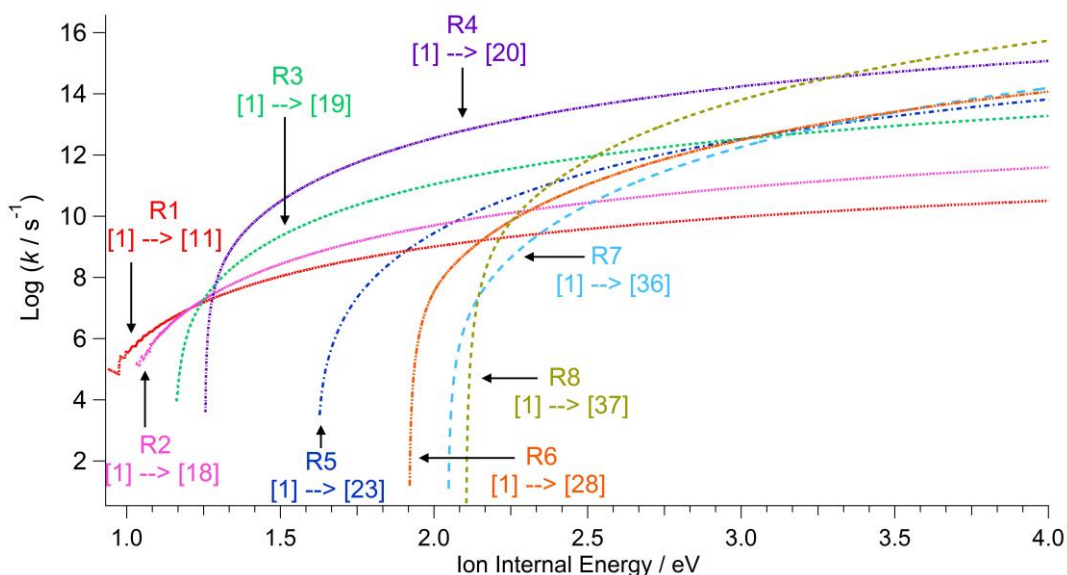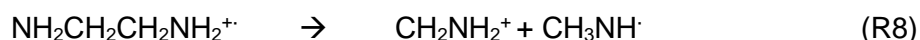


**Figure 6.5c:** RRKM rate constants plotted as a function of EN ion internal energy as determined by modeling of TPEPICO data (for structures of the ions, intermediates and TSs see Figure 6.6.4b).

## 6.6 Computational Analysis and Discussion

### 6.6.1 Neutral EN

Intramolecular hydrogen bonding and stereoelectric effects are known to contribute to the various rotamers of ethylenediamine in the neutral ground state.[16, 23] The lowest-energy neutral conformation was needed to determine accurate relative energies for use in the current TPEPICO analysis, as well as the rotational constants and frequencies necessary for modeling. Potential energy surfaces have been scanned using B3LYP/6-31G(d) where the $NH_2$ moiety rotates around the central carbon bond from cis to trans orientations. Small barriers distinguish multiple configurations. At each minimum observed, the structure was optimized using CBS-QB3 and a following potential energy surface was scanned where the $NH_2$ group rotates on a fixed bond, with the aim to observe the effect of nitrogen-hydrogen positioning in the cis form. The lowest-energy conformation found is geometrically similar to that presented in the previous photodissociation study of ethylenediamine by Wei et al.[25] using G3, however the C-C and C-N bonds are slightly elongated in the current structure. For direct comparison, the current structure found using CBS-QB3 was subsequently optimized with G3, confirming a marginally lower-energy structure of molecular EN than had previously been reported (Figure 6.6.1). The conformation is stabilized by intramolecular hydrogen bonding in the gauche state, in agreement with previous studies.[16-18]
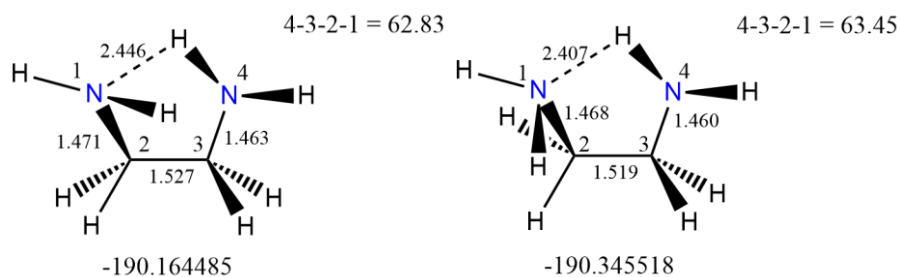
**Figure 6.6.1:** The lowest-energy conformation of neutral ethylenediamine and energy in Hartrees as calculated by CBS-QB3 (left) and G3 (right). The CBS-QB3 neutral total energy is used to determine the relative energies of all stationary points on the potential energy surface and the G3 value can be directly compared with the previous G3 optimization calculations.[25]

## 6.6.2 Cationic EN

Bond lengths, angles, and rotations were scanned in the search for rotamers in the cationic state and minima were again observed with small rotational barriers. Three rotamers play a large role in dissociation processes and are shown as structures [1], [3], and [5] in Figure 6.6.2. Structure [1] was found to be the highest energy cationic rotamer and the orientation is in best agreement with the neutral. The ionization energy (IE) from the neutral structure to cation [1] is calculated at 8.57 eV using CBS-QB3 (8.55 with G3), while the relative energies for conformers [3] and [5] are 8.20 and 8.18 eV, respectively. The calculated ionization energy of EN using rotamer [1] is also in good agreement with 8.54 eV calculated by Wei et al.[25] using G3 and 8.6 eV determined by Kimura et al.[59] through He I photoelectron spectroscopy. Thus, the neutral structure discussed above and the cation [1] served as the molecular EN and corresponding parent ion in the TPEPICO analysis.
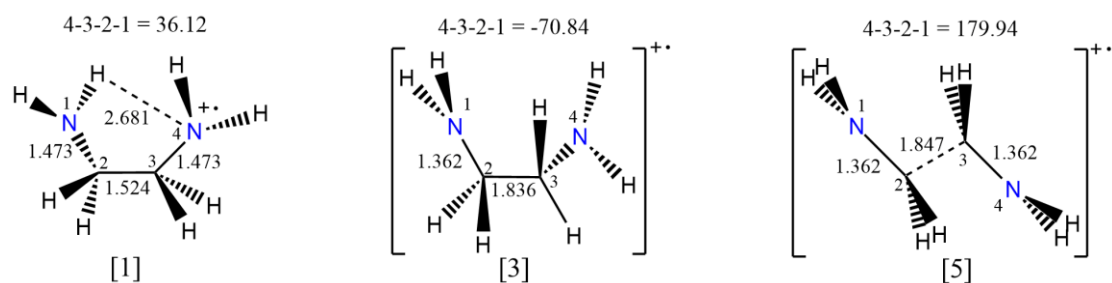
**Figure 6.6.2:** CBS-QB3 calculated geometries of the three cationic ethylenediamine conformers involved in the photodissociative processes.

### 6.6.3 Rotation and Isomerization

As the photon energy increases, if the direct dissociation limit requires great amounts of energy, then rotational and isomerization pathways become more competitive. Previous photodissociation studies have described isomerization pathways prior to dissociation,[28, 29] which was found to be the case for the dissociation of the EN ion, as well.

Figure 6.6.2 represents the potential energy surface of the rotamers and isomers most directly responsible for the fragments we model in our TPEPICO experiment. The first rotational barrier [2]‡ from the lowest-energy cationic configuration [1] is 0.02 eV and leads to rotamer [3] at 0.37 eV lower in energy than the original parent conformation. Rotational barrier [4]‡ lies 0.14 eV above [3] and is the transition to the anti-configuration of EN [5], 0.39 eV lower in energy than the original parent ion. When the EN ion possesses sufficient internal energy to overcome the initial rotational barriers, it can also access H-migration and functional group migration channels leading to lower-energy dissociation pathways than direct abstraction from the original parent molecular ion.

Specifically, the 1,3-hydrogen migration barrier [6]‡ is calculated at 9.13 eV and leads to a low-energy van der Waals product complex [7] that is involved in the **R1**-**R3** unimolecular reactions.
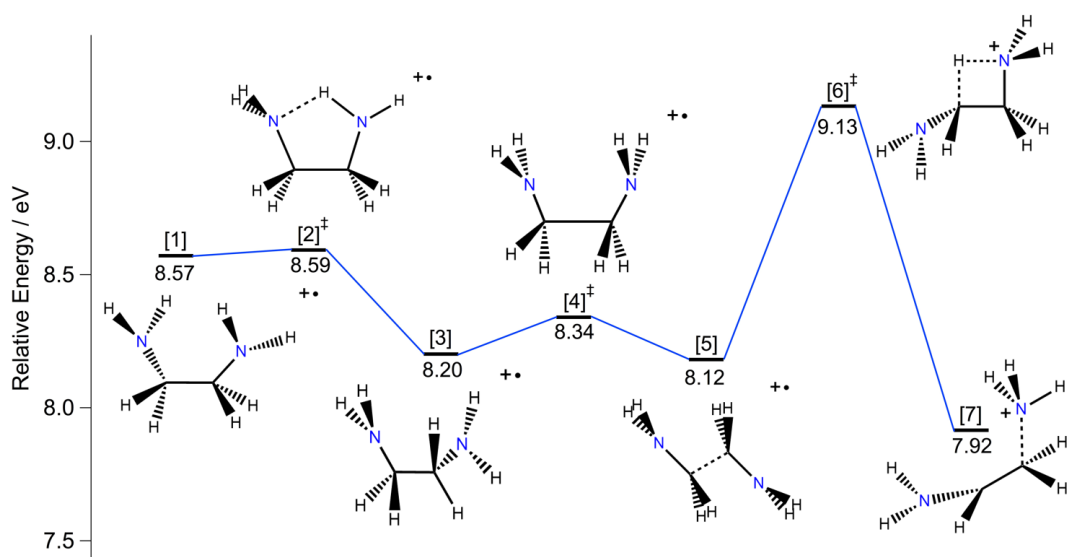


**Figure 6.6.3:** The CBS-QB3 calculated potential energy surface diagram at 0 K of the initial rotations and H-migrations of ethylenediamine ion that yield the parent conformations more directly responsible for dissociation processes. The low-energy configuration [7] leads to the generation of the first three fragments.

### 6.6.4 Dissociation Channels

In the current study, ten dissociation channels are investigated by quantum chemical calculations of which eight channels were traceable and modeled. The computed reaction coordinates are displayed in Figure 6.6.4a with all structures outlined in Figure 6.6.4b along with their energies. The ninth and tenth channels will be outlined in limited detail following the descriptions of the modeled pathways.
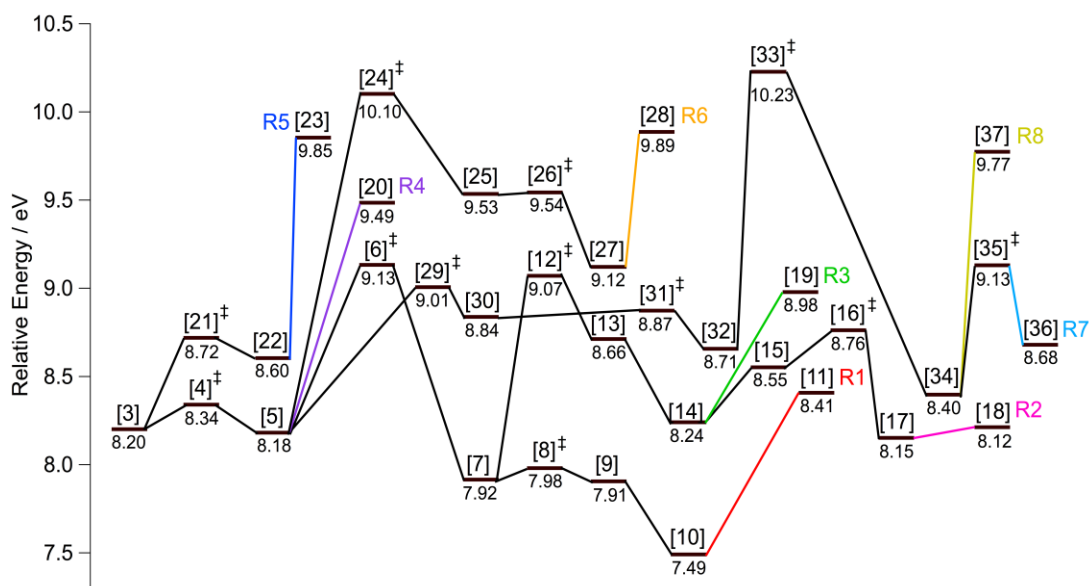
**Figure 6.6.4a:** CBS-QB3 calculated potential energy surfaces for the photodissociation channels **R1–R8** of the ethylenediamine cation with the relative energies at 0 K for the stationary points.

The 1,3-hydrogen migration barrier [6]‡ calculated at 9.13 eV is responsible for the isomerization to lower-energy complex [7]. This intermediate leads to three distinct dissociation pathways ($m/z = 43$, 59, and 44), where the subsequent barriers are all less than the initial 9.13 eV CBS-QB3 barrier. In addition, the relative energies of the products are also lower in energy than the original 9.13 eV CBS-QB3 barrier (8.41 eV, 8.21 eV, and 8.98 eV, respectively). Thus, this transition is the highest-energy saddle point in these unimolecular reactions and has an influential role in the appearance energies of the fragments.

[1]
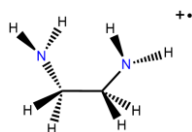


-189.849513

[2]‡
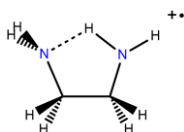


-189.848718

[3]
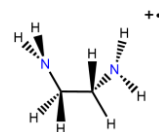


-189.863091

[4]‡
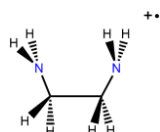


-189.857991

[5]



-189.863825

[6]‡
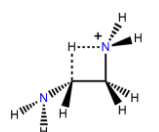


-189.828841

[7]
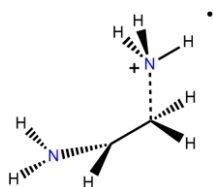


-189.873607

[8]‡
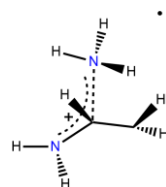


-189.871216

[9]
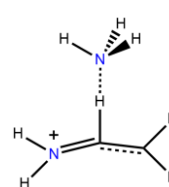


-189.873965

[10]
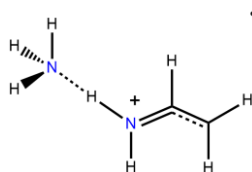


-189.889117

[11]
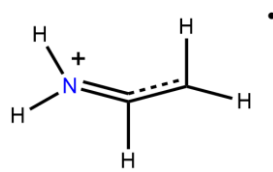


+ NH₃

-133.395330 / -56.460185

[12]‡



-189.831115

192
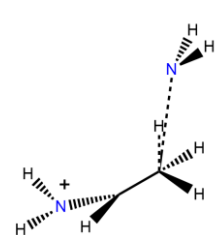
[13]
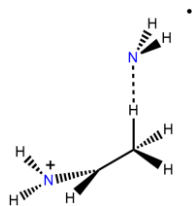


-189.846509

[14]
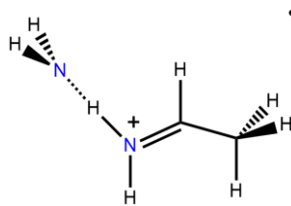


-189.861845

[15]
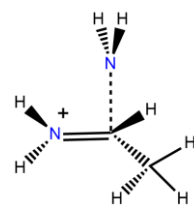


-189.850212

[16] ‡
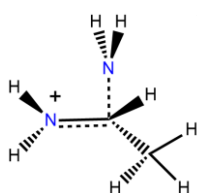


-189.842500

[17]



-189.864917

[18]



+ ·H
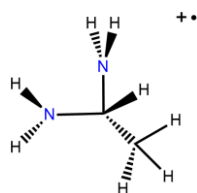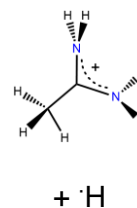
-189.362926 / -0.499818

[19]
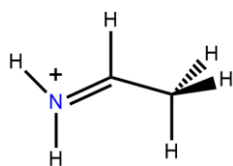


+ ·NH₂

-134.043361 / -

55.791194

[20]



+
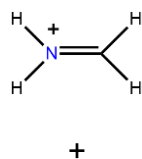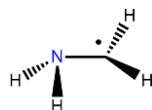


-94.793759 / -95.022133

[21] ‡



-189.844050

193
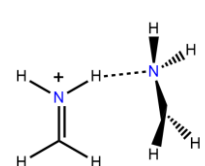
[22]
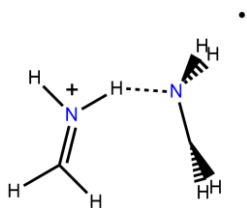


-189.848278

[23]
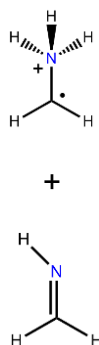


-95.337078 / -94.465271

[24] ‡
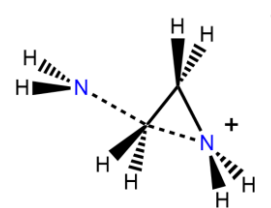


-189.793238

[25]
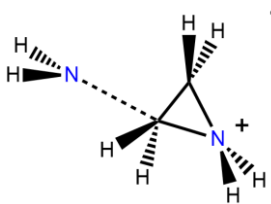


-189.814095

[26] ‡
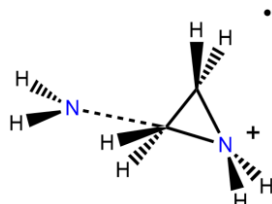


-89.813774

[27]



-189.829306

[28]



+ ·NH$_2$
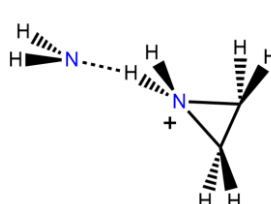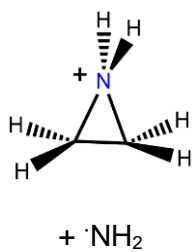
-134.009964 / -55.791194

[29] ‡
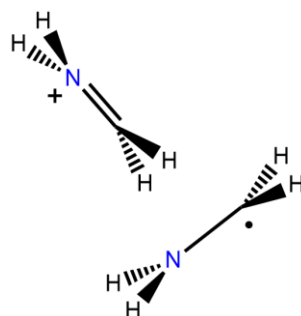


-189.833513

[30]
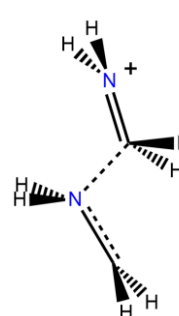


-189.839696

[31] ‡
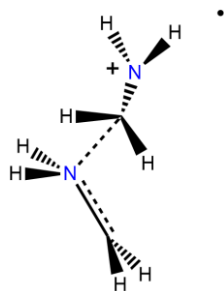


-189.838413

[32]
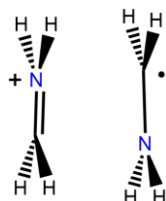


-189.844059

[33] ‡
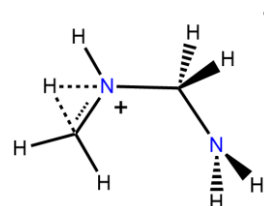


-189.788605

[34]
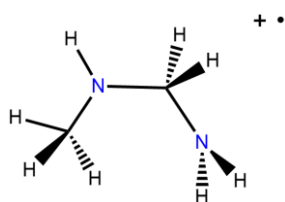


-189.855912

[35]
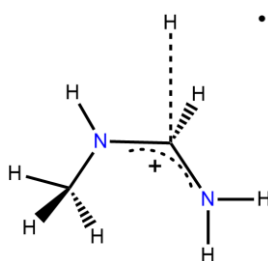


-189.829040

[36]
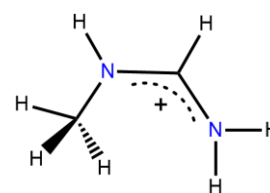


+ ·H

-189.345759 / -0.49982

[37]



+
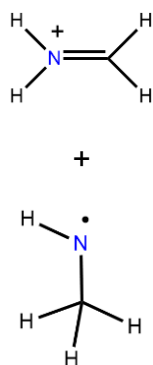


-94.793759 / -

95.011545

**Figure 6.6.4b:** CBS-QB3 calculated geometries and energies at 0 K of stationary points used in this study.

195

**1.)** $m/z = 43$, $NH_2CHNH_2^+$. The low-energy, resonance-stabilized ethenamine cation and neutral ammonia are formed via a series of $NH_3$-migrations, where the functional group "walks" the molecule prior to dissociation as a result of H-interactions with nitrogen. The functional group migration process [7-10] occurs in a low-energy realm relative to the other two processes (**R2** and **R3**) originating from [7]. Overall, this dissociation pathway is the most energetically favorable of channels and is thus the first to occur and the most dominant within the low-energy photon range (Figure 6.5a). This channel is identical to that proposed by Wei et al.[25] and the extracted 0 K appearance energy of 9.120 ± 0.010 eV matches both CBS-QB3 (9.13 eV) and G3 (9.16 eV)[25] theoretical expectations well.

**2.)** $m/z = 59$, $CH_3C(NH_2)_2^+$. There are two parallel channels corresponding to this TOF, evidenced by the increasing fractional abundance, disappearance, and subsequent reappearance at higher energy as shown in the breakdown diagram (Figure 6.5a.). This section outlines the first $m/z = 59$ appearance as it is described by **R2**.

This is the second fragment to form via intermediate [7] and consists of a hydrogen loss after a multi-step process of H and $NH_2$-migrations. The $NH_3$ group in configuration [7] is able to return the hydrogen back to the chain and undergo $NH_2$ functional group migration, [12] – [17]. Structures [13] and [15] are all-real frequency complexes with insignificant barriers calculated to be less than 0.01 eV energy difference and as such, the transition states to and from [14] are not indicated in the potential energy surface diagram. There is very scarce thermochemical data for the EN isomer, 1,1-ethandiamine ion [17], or the hydrogen-loss product 1-

aminoethaniminium ($CH_3C(NH_2)_2^+$, [18]), in which case current results cannot be compared.

The 1,2-hydrogen migration transition of [12] is calculated at 9.07 eV, greater than the product sum energy of **R1** (8.41 eV), and for this reason $m/z = 59$ and 44 are less competitive with $m/z = 43$ at the dissociation limit energy of 9.13 eV and appear at slightly higher energies. In addition, transition state [16]$^{\ddagger}$ at relative energy 8.76 eV is higher in energy still than any stationary point involved in the R1 process to form $m/z = 43$. It follows, then, that the PEPICO photoionization onset of structure [18] at 9.200 ± 0.012 eV is in good agreement with the highest barrier of 9.13 eV calculated using CBS-QB3 and the higher-energy, multistep process helps explain why this fragment appears at energies greater than R1.

This dissociation channel differs from the original $m/z = 59$ formation outlined by Wei et al.,[25] where the experimental onset of $m/z = 59$ was reported at 9.06 eV and the G3 barrier for H-loss from a central carbon was calculated at 0.99 eV above their IE of 8.54 eV. Tunneling was suggested to play a role in their early detection of this fragment. To be thorough, our CBS-QB3 calculations for the same process yielded a barrier at 9.56 eV, in good agreement with Wei et al.'s computational results, however not in experimental agreement with either study. Since the N-H bond is generally known to have greater strength than the C-H bond, it is therefore reasonable that $m/z = 59$ formation from H-loss at the amine site is calculated to require far greater energy regardless of the resulting cationic conformer. It is determined that the **R2** dissociation pathway must involve isomerization and does not arrive from direct H-loss from any of the initial EN ion conformers.

**3.)** $m/z = 44$, $NH_2CHCH_3^+$. The formation of a low-energy fragment ion as a result of $NH_2$-loss begins with H-migration to form complex [7], just as in **R1** and **R2** to form $m/z = 44$ and 59. The H-migration transition [12]‡ at relative energy 9.07 eV is shared with **R2**. Unlike in the **R2** channel where the $NH_2$ migrates and then bonds to form [17], the $NH_2$ group dissociates from the complex to form products with energy sum of 8.98 eV, which is higher than the significant energies involved in both the **R1** and **R2** channels (8.41 eV and 8.76 eV, respectively). This may provide one explanation as to why this fragment is the third to appear in the current study. The TPEPICO experimental appearance energy for this molecular dissociation pathway is found to be 9.34 ± 0.08 eV, as compared to the previous photodissociation study on EN, reporting the AE at 8.90 ± 0.03 eV[25] for the same channel.

Through our study it is also found that methane-loss to form formamidine ($NHCHNH_2^+$) is theoretically energetically possible, however it is 0.36 eV higher in energy than structure [19] and would involve a multistep process of $NH_2$-group and $CH_4$-group migrations. In addition, the breakdown modeling of the $NH_2$-loss pathway matches more agreeably. It is therefore less likely this fragment forms via $CH_4$-loss and is not included in the potential energy surface diagram.

**4.)** $m/z = 30$, $CH_2NH_2^+$. The breakdown diagram in Figure 6.5a shows **R4** is the most dominant channel in EN dissociation within the 8.60–12.50 eV photon energy range, forming the methylenimmonium ion ($CH_2NH_2^+$) and the neutral methylamine fragment ($^.CH_2NH_2$), shown together as structure [20]. These fragments are generated by the bisection of the lowest-energy conformer of the EN ion [5]. Potential energy surfaces involving the C-C stretching of the higher-energy initial conformers [1] and [3] yield small rotational barriers to structure [5] prior to

dissociation. In addition, $m/z = 30$ can also form via C-C bond cleavage of [7] through a roaming process, whereby the $CH_2NH_3^+$ and $CHNH_2$ fragments separate and then rotate to return the H from $CH_2NH_3^+$ prior to molecular dissociation. Though roaming is a relatively new phenomenon in unimolecular dissociation and has been a topic of recent investigation,[27, 60-62] it is not expected to play a role in ethylenediamine dissociation in that the product sum energy (calculated at 9.49 eV) is certainly greater than the barriers witnessed in the various bond-stretching scans.

Using the direct $CH_2NH_2$-loss from EN conformer [5], the experimental 0 K appearance energy of 9.449 ± 0.025 eV is in excellent agreement with CBS-QB3 energy of 9.49 eV. The AE reported by Wei et al.[25] is 9.30 ± 0.03 eV.

**5.)** $m/z = 31$, $CH_2NH_3^+$. Various pathways are investigated for the formation of $m/z = 31$, while only one is believed to be the primary contributor to **R5**. The corresponding neutral ligand of mass 29 from the dissociation of EN can take one of four forms: methylnitrene ($CH_3N$), a zwitterion ($^+NH_2CH^-$), an aminocarbene ($NH_2CH$), or methylenimine ($NHCH_2$). The singlet $CH_3N$ is known to be higher in energy,[63] the zwitterion is calculated with CBS-QB3 to be 1.55 eV higher in energy than $NHCH_2$, and the computational studies of $NH_2CH$ place it at 35–39 kcal mol$^{-1}$ (1.5–1.6 eV) higher in energy than $NHCH_2$.[63-65] The neutral $^.N_2H$ structure was also considered, however, the energy is high and the mechanism to form cationic $CH_3CH_4^+$ at $m/z = 31$ was found to be unlikely. Thus, regardless of the configuration of $m/z = 31$, **R5** must produce the $NHCH_2$ fragment to have energetic agreement with what is observed in the TPEPICO experiment. The pathway leading to the formation of $CH_2NH_3^+$, and $NHCH_2$ [23] is enabled by hydrogen-nitrogen interactions and yields

a relatively low-energy van der Waals complex, [22], as a result of $CH_2NH_2$ group rotation and C-C bond breaking.

Past experiments have contradicted theory[66] to show the distonic methyleneammonium ion ($CH_2NH_3^+$) to be less stable than its conventional isomer, methanimine ($CH_3NH_2$)$^+$. However, additional high-level calculations[67, 68] show that the former to be as much as 8 kJ mol$^{-1}$ (0.08 eV) more stable. In this exploration using CBS-QB3, an intermediate complex involving C-H-N interactions leading to the formation of $CH_3NH_2^+$ is calculated to be 0.09 eV higher in energy than structure [22]. In addition, the resulting energy of $CH_3NH_2^+$ is also nearly 0.04 eV higher in energy than the $CH_2NH_3^+$, consistent with previous theoretical results obtained.[69, 70] Therefore, through EN ion dissociation, the $CH_2NH_3^+$ is preferable to $CH_3NH_2^+$. Consecutive dissociation is not likely as it would require substantially more energy. The RRKM model of $CH_2NH_3^+$ ion from EN is in good agreement with experimental results and the photoionization onset is reported here at 9.8 ± 0.1 eV.

**6.)** *m/z* = 44, *c*-C2H4NH2$^+$. Direct $NH_2$-loss from EN$^+$· rotamer [5] results in a higher-energy cyclic isomer of *m/z* = 44 and is responsible for the reappearance at higher energies (**R6**). The CBS-QB3 dissociation limit is calculated to be 10.10 eV [24] and forms a van der Waals product complex [25] that undergoes $NH_2$-migration to arrive at a lower-energy product complex [27]. This intermediate is strengthened by intramolecular hydrogen bonding between the two amino groups. The second TPEPICO appearance of *m/z* = 44 at 10.1 ± 0.1 eV is in excellent agreement with the CBS-QB3 calculated barrier. The percent abundance of *m/z* = 44 is low at a maximum of 2.5%, due to competition from the two subsequent channels at slightly

higher energies. The appearance energy of this fragment has not been previously reported from EN dissociation.

**7.)** $m/z = 59$, $CH_3NHCHCH_2^+$. The second $m/z = 59$ appearance (**R7**) involves relatively low energy rotational barriers and rotamers, [29]‡ – [32]. A 1,2-hydrogen shift from a terminal $NH_2$-group to an adjacent carbon is calculated at 10.10 eV relative energy [33]‡ to yield the $EN^{+\cdot}$ isomer, methyl-methanediamine ion [34]. This ion in particular is responsible for **R7** and **R8** dissociations. Hydrogen-loss from the central carbon overcomes a small barrier at 9.13 eV to form a resonance-stabilized cationic fragment of $m/z = 59$. The experimental 0 K appearance energy of this channel is 10.2 ± 0.1 eV, again in great accord with the CBS-QB3 calculated barrier at 10.23 eV.

The loss of a hydrogen at any other site of [34] would require additional energy as it would not lead to a resonance-stabilized product or would break stronger N-H interactions. Indeed, a direct hydrogen abstraction from at the amino site of [32] revealed a CBS-QB3 calculated barrier of 10.31 eV and a product sum energy of 9.69 eV, which are the same fragments that would form from the loss of hydrogen at the terminal carbon site of [34]. In addition, the direct loss of a hydrogen from a carbon of either minima [30] or [32] would proceed backward to [5] and yield a CBS-QB3 barrier of 9.56 eV, which was much too high in energy to explain the formation of the first $m/z = 59$ and much too low to be agreeable with the second.

**8.)** $m/z = 30$, $CH_2NH_2^+$. The bulk of the pathway leading to the second appearance of $m/z = 30$ (**R8**) is shared with **R7**. Rotamers [30] and [32] face low-energy barriers to formation and the hydrogen-transfer barrier at 10.23 eV forms the $EN^{+\cdot}$ isomer, methyl-methanediamine, at [34]. The bisection of this isomer is uphill

and does not possess a barrier to dissociation, once again forming the $CH_2NH_2^+$ as in **R4**, but with a higher-energy neutral fragment radical ($CH_3NH^.$) at [37]. Though activation energies and product sum energies do not always accurately predict the relative intensities of ions or their appearance order, it is not surprising in the case of $EN^{+.}$ dissociation that **R8** channel ion appears at slightly higher energy than **R7**. The barrier to formation [35] and the total product energy [36] in **R7** (9.13 and 8.68 eV, respectively) are lower than the total product energy [37] of **R8** (9.77 eV), which offers a potential explanation for the later appearance of $m/z = 30$ despite sharing the same high-energy barrier [33] at 10.23 eV. It is understandable, then, that the TPEPICO appearance energy is reported at 10.2 ± 0.1 eV as compared to the CBS-QB3 barrier of 10.23 eV.

Interestingly, $CH_2NH_2^+$, $^.CH_2NH_2$, and $CH_3NH^.$ are linked in the context of methylamine as a known interstellar molecule.[71] Studies on the photodissociation of methylamine ($CH_3NH_2$) describe $CH_2NH_2^+$ formation and its importance in Titan's ionosphere.[72, 73] It has also been proposed elsewhere[74] that upon exposure to cosmic rays, methylamine can form both $^.CH_2NH_2$ and $CH_3NH^.$ fragments, which are presented in the EN photodissociation channels **R4** and **R8**, respectively, to form $CH_2NH_2^+$. The interconversion barrier between the two isomers was calculated by Knowles et al.[74, 75] at 1.83 eV (from $^.CH_2NH_2$) to ascertain the stability of these radicals as they relate to possible amino acid precursors in space. This 1,2-hydrogen transition loosely resembles the 1,2-hydrogen shift from structure [32] to the $EN^{+.}$ isomer [34], suggesting potential future interest in EN and [34] in astrophysical research.

**9 and 10)** $m/z$ = 43 and 30, $c$-$CHCH_2NH_2^{+\cdot}$ and $CH_2NH_2^+$. Due to the low abundance and technical limitations of the MiniPEPICO program these higher-energy channels were excluded from the modeling.

The ninth channel, involving the reformation of $m/z$ = 43, was observed with a fractional ion abundance of less than 1% and appeared above 10.3 eV. Two pathways of nearly equivalent energetics (10.33 and 10.34 eV) were uncovered using CBS-QB3 leading to the formation of cyclic isomers of $m/z$ = 43, in which it would be difficult to identify and quantify the formation of the isomer(s). However, in theory, the more likely pathway of lower energy and fewer steps involves a 1,2-hydrogen transition from a central carbon to a terminal nitrogen in [5], then losing $NH_3$ molecule to form $c$-$C_2H_4NH_2^+$.

The tenth dissociation channel appears above 12.2 eV in the breakdown diagram, where a discrepancy in the modeling exists as the abundance of $m/z$ = 30 increases and $m/z$ = 59 decreases. Wei et al.[25] presented a mechanism showing the first consecutive dissociation pathway of an isomer of $m/z$ = 59 to form $CH_2NH_2^+$, the zwitterion $^+NH_2CH^-$, and $^\cdot H$ without barrier. The relative CBS-QB3 energy of the formation of these products is calculated to be 12.58 eV. However, as their findings show that calculations for the initial formation of $m/z$ = 59 were in disagreement with the experimental (as was also found with TPEPICO) it is unlikely that the third appearance of $m/z$ = 30 arrives via their proposed isomer.

Alternatively, calculations at the CBS-QB3 level show that at 12.21 eV, structure [34] possesses sufficient internal energy to undergo a 1,3-hydrogen shift to yield a higher-energy $m/z$ = 59 isomer that freely dissociates to $CH_2NH_2^+$ and $NHCH_2$ without barrier. This value is then the highest-energy saddle point in the potential

energy surface for the pathway leading to the third $m/z$ = 30 appearance. The 12.21 eV barrier is in agreement with the approximate experimental appearance of $CH_2NH_2^+$ at 12.2 eV and the disappearance of $m/z$ = 59 within the same photon energy range.

The intramolecular nitrogen-hydrogen attractions play a profound role on the dissociation dynamics of the EN ion. Stable van der Waals complex intermediates are involved in five of the eight modeled channels, and the low energies of these structures incentivize their formations ([10], [14], [22], and [27]). In most cases, these structures dissociate to product fragments without any further barriers, with the exception of **R2** where additional steps are required for H-loss. The functional group migration processes in $NH_2$- and $NH_3$-loss channels are the most emblematic of the influence of hydrogen attractions in EN photodissociation.

### 6.6.5 Thermochemistry

Auxiliary thermochemical data and the results of this work are summarized in Table 6.6.5. The enthalpy of formation of liquid EN was reported in 1900 by Berthelot[76] at –5.82 kcal mol$^{-1}$ (–24.35 kJ mol$^{-1}$). Using the heat of vaporization now averaged from several sources to be 46 kJ mol$^{-1}$, the enthalpy of formation of gas-phase EN using Berthelot's result can be calculated at 21.25 kJ mol$^{-1}$. Seventy years later, however, Good and Moore[77] determined the heat of formation of condensed-phase EN at –15.06 ± 0.13 kcal mol$^{-1}$ (–63.01 ± 0.54 kJ mol$^{-1}$) through oxygen-bomb combustion calorimetry and used enthalpies of vaporization to determine the gas-phase standard enthalpy at –17.03 ± 0.59 kJ mol$^{-1}$. Burkey et al.'s[78] study on the heats of formation of α-aminoalkyl radicals utilized the calculated

heat of formation of EN at $-18.0$ kJ mol$^{-1}$ as prescribed by Benson et al.'s[79] group additivity contributions, however no error bar was provided.

An isodesmic reaction network[14, 72, 80] was used to obtain greater insight to the heat of formation of neutral ethylenediamine, where the heats of formation of ethylene glycol, ammonia, water, methane, and butane are experimentally well-known and shown in Table 6.9a.

$$HOCH_2CH_2OH + 2\ NH_3 \rightarrow NH_2CH_2CH_2NH_2 + 2\ H_2O \qquad (6.6.5a)$$
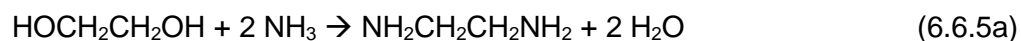
$$\Delta_f H^{\ominus}_{298K}\ [NH_2CH_2CH_2NH_2] = -16.0 \pm 1.6\ \text{kJ mol}^{-1}$$

$$CH_3CH_2CH_2CH_3 + 2\ NH_3 \rightarrow NH_2CH_2CH_2NH_2 + 2\ CH_4 \qquad (6.6.5b)$$
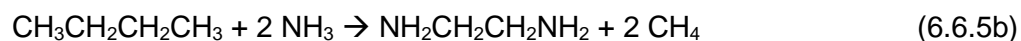
$$\Delta_f H^{\ominus}_{298K}\ [NH_2CH_2CH_2NH_2] = -17.5 \pm 0.8\ \text{kJ mol}^{-1}$$

Using this method the average $\Delta_f H^{\ominus}_{298}$ [NH$_2$CH$_2$CH$_2$NH$_2$] $= -16.8$ kJ mol$^{-1}$ with a standard deviation of $\pm$ 1.0 kJ mol$^{-1}$ was calculated to be in agreement with the experimental value provided by Good and Moore,[77] which was used in conjunction with TPEPICO to determine the heats of formation of photodissociative fragments.

The **R4** channel yields the methylenimmonium ion fragment [20], CH$_2$NH$_2^+$, and the neutral methylamine radical, ·CH$_2$NH$_2$. Previous experiments have been published elsewhere on methylamine (CH$_3$NH$_2$)[72, 73] and ethylamine cation[81] photoionization, where the CH$_2$NH$_2^+$ ion fragment is formed via H-loss and CH$_3$-loss, respectively. Many high-level theoretical and experimental values for the heat of formation of this ion are available in literature[40, 68, 80, 82-85] and a select few are listed in Table 6.6.5. Bodi et al.[72] conducted TPEPICO experiments on primary amines and determined the heat of formation of the CH$_2$NH$_2^+$ ion to be 750.3 $\pm$ 1 kJ mol$^{-1}$, which was used in the determination of the neutral methylamine radical fragment.

**Table 6.6.5:** Auxiliary and derived thermochemical data

| Species | AE / eV | $\Delta_f H^\circ_{0K}$ (kJ mol$^{-1}$) | $\Delta_f H^\circ_{298K}$ (kJ mol$^{-1}$) | | $H^\circ_{298K} - H^\circ_{0K}$ (kJ mol$^{-1}$) |
|---|---|---|---|---|---|
| $NH_2CH_2CH_2NH_2$ | | 11.19 | −17.03 | ± 0.59[a] | 16.42[d] |
| | | | -16.8 | ± 1.0[e] | |
| $NH_2CHCH_2^{+\cdot}$ | 9.120 ± 0.010[b] | | | | |
| | 8.85[c] | | | | |
| | 9.13 ± 0.05[d] | | | | |
| $CH_3C(NH_2)_2^+$ | 9.200 ± 0.012[b] | | | | |
| | 9.06[c] | | | | |
| | 9.13 ± 0.05[d] | | | | |
| $NH_2CHCH_3^+$ | 9.34 ± 0.08[b] | 683.8 | 665.1 | ± 1.4[g] | 13.148[d] |
| | 8.90[c] | | 657[h] | ± 9[h] | |
| | 9.13 ± 0.05[d] | | | | |
| $CH_2NH_2^+$ | 9.449 ± 0.025[b] | 762.3 | 750.3 | ± 1[i] | 10.324[d] |
| | 9.30[c] | 764.0 | 752.1 | ± 1.8[j] | |
| | 9.49[d] | | | | |
| | 10.2 ± 0.1[b] | | | | |
| | 10.23 ± 0.05[d] | | | | |
| $CH_2NH_3^+$ | 9.8 ± 0.1[b] | 860 | 847 | ± 10[b] | 12.813[d] |
| | 9.85 ± 0.05[d] | | 847.9 | ± 1.5[e] | |
| | | | 855[l] | | |
| | | | 832.6[x] | | |

| | | | | | |
|---|---|---|---|---|---|
| $c$-$C_2H_4NH_2^+$ | 10.1 ± 0.1[b] <br> 10.10 ± 0.05[d] | 743 | 724 | ± 9[f] | 11.203[d] |
| $CH_3NHCHCH_2^+$ | 10.2 ± 0.1[b] <br> 10.23 ± 0.05[d] | | | | |
| $NH_3$ | | -38.565 | −45.558 | ± 0.030[j] | 10.045[m] |
| H | | 216.034 | 217.99 | ± 0.000[j] | 6.197[m] |
| $^{\cdot}NH_2$ | | 188.94 | 186.05 | ± 0.15[j] | 9.929[m] |
| $^{\cdot}CH_2NH_2$ | | 160.6 <br><br> 159.63 | 149.7 <br> 149.3 <br> 148.74 | ± 2.7[b] <br> ± 2.5[e] <br> ± 1.01[j] | 11.450[d] |
| $NHCH_2$ | | 96.64 | 88.701 <br> 86.4 | ± 2.09[k] <br> ± 2.9[e] | 10.142[d] |

[a]Good and Moore.[77] [b]This work. [c]Wei et al.[25] [d]CBS-QB3 calculated thermochemical values, [e]Isodemic reaction networks. [f]Solka et al.[86] [g]Traeger et al.[87], [h]Lossing et al.[82], [i]Bodi et al.[80] [j]Active Thermochemical Tables (ATcT)[88-90] [k]Oliveira et al.[83] [l]Sana at al.[68] [m]Chase, M. W.[91] [n]Bouma et al.[70]

The 298 K heat of formation of the $^{\cdot}CH_2NH_2$ fragment is provided in the Active Thermochemical Tables (ATcT)[88] at 148.74 ± 1.01 kJ mol$^{-1}$. Aside from this, current thermochemical data of $^{\cdot}CH_2NH_2$ is believed to be limited to Burkey et al.'s[78] calculated $\Delta_fH^{\ominus}_{298K}$ at 151 kJ mol$^{-1}$ using available experimental values. An isodesmic reaction network is used to calculate the heat of formation of $^{\cdot}CH_2NH_2$ using theoretical calculations and experimental values referenced in Table 6.6.5. The average $\Delta_fH^{\ominus}_{298K}$ [$^{\cdot}CH_2NH_2$] from the isodesmic reactions was calculated to be 149.3

± 2.5 kJ mol$^{-1}$ and the TPEPICO experimental $\Delta_f H^{\ominus}_{298K}$ [˙CH$_2$NH$_2$] = 149.7 ± 2.7 kJ mol$^{-1}$.

$$˙CH_3 + CH_3NH_2 \rightarrow CH_4 + ˙CH_2NH_2 \qquad (6.6.5c)$$

$$\Delta_f H^{\ominus}_{298K} [˙CH_2NH_2] = 150.1 \pm 2.4 \text{ kJ mol}^{-1}$$

$$NH_2 + NH_2CH_3 \rightarrow NH_3 + ˙CH_2NH_2 \qquad (6.6.5d)$$

$$\Delta_f H^{\ominus}_{298K} [˙CH_2NH_2] = 151.3 \pm 4.0 \text{ kJ mol}^{-1}$$

$$NH_3 + ˙CH_2CH_3 \rightarrow CH_4 + ˙CH_2NH_2 \qquad (6.6.5e)$$
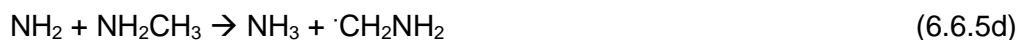
$$\Delta_f H^{\ominus}_{298K} [˙CH_2NH_2] = 146.4 \pm 3.6 \text{ kJ mol}^{-1}$$

The excellent agreement between the isodesmic, experimental and literature values serves as a good calibration for the experimental heat of formation of CH$_2$NH$_3^+$.

The **R5** channel produces the CH$_2$NH$_3^{+˙}$ ion and the neutral CH$_2$NH fragment. A wide range of values are reported in literature[92, 93] for the heat of formation of the neutral fragment, from 69 kJ mol$^{-1}$ by Peerboom et al.[94] to 110.46 kJ mol$^{-1}$ by DeFrees et al.[95] In 2001, Oliveria et al.[83] aimed to reduce the uncertainty by using the W2 thermochemical method, reporting the theoretical standard enthalpy at 21.1 ± 0.5 kcal mol$^{-1}$ (88.7 ± 2.1 kJ mol$^{-1}$). This is the most recent thermochemical value published on CH$_2$NH to-date.

An isodesmic reaction network was explored to determine a CBS-QB3, theoretical-experimental hybrid heat of formation of CH$_2$NH, where the known literature values for pertinent species are provided in Table 6.9a:

$$HNO + CH_2CH_2 \rightarrow CH_2NH + CH_2O \qquad (6.6.5f)$$

$$\Delta_f H^{\ominus}_{298K} [CH_2NH] = 85.7 \pm 4.5 \text{ kJ mol}^{-1}$$

$$CH_2CH_2 + HNNH \rightarrow 2 CH_2NH \qquad (6.6.5g)$$

$$\Delta_f H^{\ominus}_{298K} [CH_2NH] = 87.6 \pm 3.9 \text{ kJ mol}^{-1}$$

$$HNNH + CH_2O \rightarrow CH_2NH + NHO \qquad (6.6.5h)$$

$$\Delta_fH\degree_{298K} [CH_2NH] = 89.5 \pm 1.4 \text{ kJ mol}^{-1}$$

$$NH_3 + CH_2O \rightarrow CH_2NH + H_2O \qquad (6.6.5i)$$

$$\Delta_fH\degree_{298K} [CH_2NH] = 91.5 \pm 4.0 \text{ kJ mol}^{-1}$$

The average heat of formation from the network was found to be 88.6 kJ mol$^{-1}$ with a standard deviation of 2.5 kJ mol$^{-1}$. This is in good agreement with the W2-calculated value by Oliveria et al.[83]

Thermochemical data regarding the $CH_2NH_3^+$ ion is much less available in literature than that of the $CH_2NH$ neutral. In 1983, Bouma et al.[70] revealed results of *ab initio* calculations that placed the heat of formation of $CH_2NH_3^{+\cdot}$ at 199 kcal mol$^{-1}$ (832.6 kJ mol$^{-1}$). Holmes et al.[66] measured the heat of formation of $CH_2NH_3^{+\cdot}$ through collisional ionization mass spectrometry and determined the total $m/z = 31$ signal to be the $^{13}C$ and $^{15}N$ isotopologue of $m/z = 30$ until 10.9 eV, concluding the heat of formation must be higher than 229 kcal mol$^{-1}$ (958 kJ mol$^{-1}$), though no specific value was reported. The most recently provided gas-phase enthalpy of formation (855 kJ mol$^{-1}$)[68] was determined using MO methods at the MP4/6-31+G(2df,p) level.[96]

An isodesmic reaction network was created to establish another baseline for comparison of the enthalpy of formation of $CH_2NH_3^+$ ion, using literature thermochemical data available in Table 6.9a.

$$CH_2CH_2 + NH_3 + H+ \rightarrow CH_2NH_3^+ + CH_3 \qquad (6.6.5j)$$

$$\Delta_fH\degree_{298K} [CH_2NH_3^+] = 848.9 \pm 1.5 \text{ kJ mol}^{-1}$$

$$NH_2NH_2 + CH_3 + H+ \rightarrow CH_2NH_3^+ + NH_3 \qquad (6.6.5k)$$
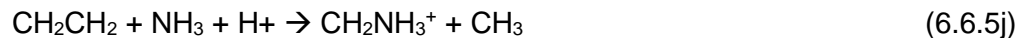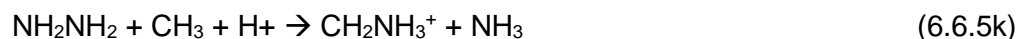
$$\Delta_fH\degree_{298K} [CH_2NH_3^+] = 846.8 \pm 1.6 \text{ kJ mol}^{-1}$$

The resulting $\Delta_f H^\circ_{298K}$ [$CH_2NH_3^+$] were averaged and determined to be 847.9 ± 1.5 kJ mol$^{-1}$, falling between the two previously reported theoretical values.

The experimental activation energy of 9.8 ± 0.1 eV from the current TPEPICO was used along with literature values for the EN parent and the W2-calculated value provided by Oliveira et al.[83] to arrive at the enthalpy of formation of the $CH_2NH_3^+$ ion. We report the experimental $\Delta_f H^\circ_{298K}$ [$CH_2NH_3^+$] at 847 ± 10 kJ mol$^{-1}$ from ethylenediamine photodissociation.

Appearance energies are equivalent to the enthalpy of the unimolecular dissociation reaction at 0 K only in the absence of a reverse barrier. Available gas-phase heats of formation of fragments are presented in Table 6.6.5 and literature $\Delta_f H^\circ_{298K}$ were used, along with that of the parent ethylenediamine, to determine the $\Delta_r H^\circ_{298K}$ for each channel. This value was then converted to $\Delta_r H^\circ_{0K}$ using thermal enthalpy values provided in literature[97] or CBS-QB3 calculated values (thermal correction to enthalpy and the zero-point corrections). While thermochemical data is scarce for several fragments, the heats of formation for both $m/z$ = 44 ($NH_2CHCH_3^+$ and $c$-$C_2H_4NH_2^+$) are available in literature. The reverse barriers for **R3** and **R6** channels were calculated as the difference between the 0 K appearance energies involving barriers and the $\Delta_r H^\circ_{0K}$ using experimental $\Delta_f H^\circ_{298K}$ and are reported as 0.41 eV and 0.55 eV (40 and 53 kJ mol$^{-1}$), respectively.

## 6.7 Conclusions

Threshold photoelectron photoion coincidence spectroscopy experiments were conducted on ethylenediamine in the 8.60–12.50 eV photon energy range, where eight dissociation channels were modeled: $NH_3$-loss, H-loss, $NH_2$-loss,

CH$_2$NH$_2$-loss, CH$_2$NH-loss, a reappearing NH$_2$-loss, a second H-loss, and CH$_3$NH-loss. Two additional pathways were observed: a second NH$_3$-loss and a consecutive dissociation involving H-loss followed by CH$_2$NH-loss. The ninth and tenth dissociations were not modeled due to low fractional ion abundance. All channels involved initial rotational barriers leading to the low-energy anti-conformation of the EN cationic state. The NH$_2$- and NH$_3$-loss pathways involved functional group migrations due to intramolecular hydrogen attractions, highlighting the influence of these interactions on the photodissociation processes. The H-loss pathways involve several rearrangements, including H-migrations and functional group migrations prior to dissociation. CH$_2$NH$_2^+$ is the dominant product of EN dissociation within the scanned photon energy range and forms neutral $\cdot$CH$_2$NH$_2$ via C-C bond cleavage at lower energy, while the ion is again formed at higher energy after H-migration to form the CH$_3$NH neutral radical fragment. The CH$_2$NH-loss pathway yields the CH$_2$NH$_3^+$ ion, where the $\cdot$CH$_2$NH$_2$ fragment rotates to form a hydrogen-bonding stabilized van der Waals complex that facilitates the transfer of an H to form the proposed products. Several of these fragments had not been detected in ethylenediamine dissociation.

Isodesmic reaction networks were used to calculate the heats of formation of ethylenediamine, $\cdot$CH$_2$NH$_2$, CH$_2$NH$_3^{+\cdot}$, and CH$_2$NH to validate the use of literature thermochemical data as anchors in the determination of TPEPICO-derived heats of formation of $\cdot$CH$_2$NH$_2$ and CH$_2$NH$_3^+$. The 0 K and 298 K heats of formation are reported in addition to the reverse barriers for both NH$_2$-loss channels.

## 6.8 Acknowledgements

## 6.9 Supplementary Information
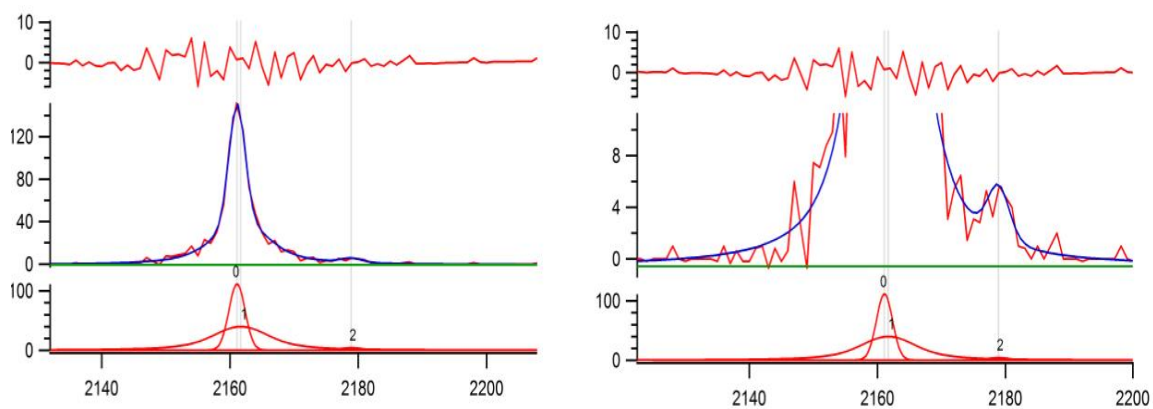


**Figure 6.9:** The IGOR multi-peak fitting in the determination of isotopologue contributions to adjacent peaks. Shown above is parent ion $m/z$ = 60 and the ~ 2.3% $^{13}$C and $^{15}$N isotopologue contribution at 8.8 eV.

**Table 6.9a:** Table of Thermochemical Values Used for Isodesmic Reactions

| Species | $\Delta_f H°_{298}$ / (kJ mol$^{-1}$)[88] | |
|---|---|---|
| H$^+$ | 1530.047 | ± 0.000 |
| CH$_3$ | 146.49 | ± 0.081 |
| H$_2$O | −241.822 | ± 0.027 |
| CH$_4$ | −74.534 | ± 0.057 |
| CH$_2$CH$_2$ | 52.56 | ± 0.15 |
| CH$_2$O | −109.16 | ± 0.11 |
| CH$_3$CH$_2$ | 119.93 | ± 0.37 |
| CH$_3$NH$_2$ | 20.91 | ± 0.53 |
| HOCH$_2$CH$_2$OH | −389.42 | ± 0.49 |
| HNO | 106.92 | ± 0.11 |
| HNNH (trans) | 200.22 | ± 0.56 |

**Table 6.9b:** Geometries for neutral EN and neutral fragments corresponding to stationary points calculated in this work. All calculations were conducted at the CBS-QB3 level.

| **Neutral EN** | N | -1.41260800 | -0.59613000 | 0.13611600 |
|---|---|---|---|---|
| | H | -2.24400000 | -0.73360600 | -0.42780700 |
| | H | -1.72345500 | -0.49105600 | 1.09742300 |
| | C | -0.68186300 | 0.60531300 | -0.29660600 |
| | H | -0.60044300 | 0.57313200 | -1.38665400 |
| | H | -1.18004900 | 1.54906400 | -0.02585400 |
| | C | 0.73030700 | 0.59120800 | 0.28335900 |
| | H | 0.65427900 | 0.61517900 | 1.38638800 |
| | H | 1.24681100 | 1.50952900 | -0.01689900 |
| | N | 1.45942200 | -0.56411600 | -0.24036600 |
| | H | 0.89151300 | -1.39002700 | -0.07046000 |
| | H | 2.33699100 | -0.68962100 | 0.25308900 |

**Stationary Point**

| | | | | |
|---|---|---|---|---|
| **11** | N | -0.62432100 | 0.44152500 | 0.00000500 |
| | H | -0.23819600 | -0.49800400 | -0.00000200 |
| | H | -0.23817800 | 0.91128800 | 0.81365300 |
| | H | -0.23820700 | 0.91128800 | -0.81365600 |
| | | | | |
| **18, 36** | H | 2.53787000 | -0.53254400 | 0.00000000 |
| | | | | |
| **19, 28** | N | -1.82120100 | 0.53353200 | -0.05669500 |
| | H | -1.44720600 | -0.42547500 | 0.00037600 |
| | H | -1.44718900 | 0.96360400 | 0.80236100 |
| | | | | |
| **20** | N | -2.85008700 | 3.15200300 | -0.05304800 |
| | H | -3.25382500 | 3.66908200 | 0.71640100 |
| | H | -2.30138600 | 3.75904800 | -0.64705900 |
| | C | -2.22752800 | 1.95251200 | 0.30268900 |
| | H | -2.74029900 | 1.34620500 | 1.03892800 |
| | H | -1.67828000 | 1.44651400 | -0.48145600 |
| | | | | |
| **23** | C | -1.53727800 | 1.21845600 | 0.19787500 |
| | H | -1.08095000 | 1.95107000 | 0.86709200 |
| | H | -2.55118300 | 1.45320100 | -0.14965000 |
| | N | -0.87680100 | 0.18455500 | -0.11468200 |
| | H | -1.42048900 | -0.41280900 | -0.74347900 |

| **37** | C |  0.62793900 | -0.01192300 |  0.00000000 |
|---|---|---|---|---|
|  | H |  1.12680800 |  0.95943700 | -0.00000100 |
|  | H |  0.97219500 | -0.58171000 | -0.87883500 |
|  | N | -0.80505200 |  0.15291500 |  0.00000000 |
|  | H | -1.20346700 | -0.79488900 |  0.00000000 |
|  | H |  0.97219500 | -0.58170800 |  0.87883600 |

**Table 6.9c:** Geometries for cationic species corresponding to stationary points calculated for this work. All calculations were conducted at the CBS-QB3 level.

| **Stationary Point** | | | | |
|---|---|---|---|---|
| **1** | N |  1.14904400 | -0.65461800 | -0.13466200 |
|  | H |  1.84627700 | -1.12086900 |  0.43736800 |
|  | H |  1.20917200 | -0.89528700 | -1.11871900 |
|  | C |  0.73160800 |  0.71505800 |  0.21019900 |
|  | H |  0.83417400 |  0.83191200 |  1.29026900 |
|  | H |  1.34946900 |  1.47613000 | -0.27472600 |
|  | C | -0.73159800 |  0.71507200 | -0.21015800 |
|  | H | -0.83403200 |  0.83194500 | -1.29024200 |
|  | H | -1.34950800 |  1.47614800 |  0.27469500 |
|  | N | -1.14903800 | -0.65463800 |  0.13460900 |
|  | H | -1.20900500 | -0.89534500 |  1.11867100 |
|  | H | -1.84665000 | -1.12061700 | -0.43719500 |

| 2 | N | -1.23036000 | -0.71346100 | -0.08509500 |
|---|---|---|---|---|
| | H | -1.68909400 | -0.96558800 | -0.95339400 |
| | H | -1.87877500 | -0.89713000 | 0.67235900 |
| | C | -0.74301000 | 0.67003800 | -0.08660400 |
| | H | -0.98651600 | 1.17663200 | -1.02054100 |
| | H | -1.19003100 | 1.25015100 | 0.72069700 |
| | C | 0.81404000 | 0.67342500 | 0.09520900 |
| | H | 1.15260800 | 1.23862400 | 0.98511700 |
| | H | 1.35457300 | 1.17516500 | -0.73037300 |
| | N | 1.27458300 | -0.65203000 | 0.19914800 |
| | H | 0.46266000 | -1.33166600 | 0.13322000 |
| | H | 2.25395500 | -0.90496600 | 0.31986600 |
| | | | | |
| 3 | N | 1.64159000 | -0.48367700 | 0.10521800 |
| | H | 1.68956300 | -1.37431000 | -0.36855600 |
| | H | 2.16546300 | -0.39902100 | 0.96502400 |
| | C | 0.84967000 | 0.52752300 | -0.34774100 |
| | H | 1.15800200 | 1.51198000 | -0.00053800 |
| | H | 0.63876800 | 0.48171400 | -1.41269400 |
| | C | -0.84965200 | 0.52753900 | 0.34772800 |
| | H | -1.15786600 | 1.51203200 | 0.00049500 |
| | H | -0.63885900 | 0.48171900 | 1.41269800 |
| | N | -1.64168600 | -0.48360300 | -0.10515800 |
| | H | -1.68975300 | -1.37417500 | 0.36872400 |
| | H | -2.16475600 | -0.39934700 | -0.96549700 |

| **4** | N | -1.60428800 | 0.61103900 | -0.28734500 |
| | H | -1.65147700 | 1.10149500 | -1.16895700 |
| | H | -1.95456200 | 1.10191200 | 0.52281600 |
| | C | -1.08806000 | -0.61687400 | -0.19454400 |
| | H | -1.30981800 | -1.17300700 | 0.70731500 |
| | H | -0.98283800 | -1.17348300 | -1.11699600 |
| | C | 1.08805800 | -0.61682900 | 0.19468600 |
| | H | 1.30981600 | -1.17317200 | -0.70704400 |
| | H | 0.98283500 | -1.17322300 | 1.11726700 |
| | N | 1.60428700 | 0.61110600 | 0.28720000 |
| | H | 1.95456100 | 1.10178900 | -0.52307500 |
| | H | 1.65147600 | 1.10176600 | 1.16869700 |
| | | | | |
| **5** | N | -1.90226900 | 0.12267300 | 0.00034600 |
| | H | -2.32332900 | 0.44795300 | 0.85972000 |
| | H | -2.32270200 | 0.45153600 | -0.85796900 |
| | C | -0.72807400 | -0.56819400 | -0.00064300 |
| | H | -0.54815100 | -1.13193800 | 0.91047800 |
| | H | -0.54836400 | -1.13022200 | -0.91290200 |
| | C | 0.72790500 | 0.56787500 | -0.00013500 |
| | H | 0.54763400 | 1.13067900 | 0.91150800 |
| | H | 0.54816800 | 1.13081300 | -0.91182400 |
| | N | 1.90261800 | -0.12214500 | 0.00031400 |
| | H | 2.32238800 | -0.45013000 | 0.85931400 |
| | H | 2.32292300 | -0.45048000 | -0.85827700 |

| 6 | N |  1.83021400 | -0.07425200 | -0.15677500 |
|---|---|---|---|---|
|   | H |  1.89852100 |  0.15997400 | -1.13860900 |
|   | H |  2.64374300 | -0.51116700 |  0.25673000 |
|   | C |  0.63850900 | -0.07551000 |  0.49798400 |
|   | H | -0.21982700 | -1.13498000 |  0.30549100 |
|   | H |  0.72564500 | -0.09922900 |  1.58517100 |
|   | C | -0.57034600 |  0.65843700 | -0.07535800 |
|   | H | -0.40532100 |  1.03298800 | -1.08580700 |
|   | H | -0.94424200 |  1.47128700 |  0.54509400 |
|   | N | -1.49976300 | -0.51823000 | -0.09796000 |
|   | H | -2.23168500 | -0.51822000 |  0.60833200 |
|   | H | -1.87735400 | -0.77268200 | -1.00724500 |

| 7 | N | -1.76755300 | -0.52548700 |  0.13341800 |
|---|---|---|---|---|
|   | H | -1.71921100 | -0.81011500 |  1.10352900 |
|   | H | -2.54966700 | -0.87211900 | -0.40505300 |
|   | C | -0.90351800 |  0.34113300 | -0.38932300 |
|   | H | -1.07637400 |  0.60725600 | -1.42630300 |
|   | C |  0.18219500 |  0.87634200 |  0.29984300 |
|   | H |  0.28371400 |  0.72999700 |  1.36746800 |
|   | H |  0.71477700 |  1.70669900 | -0.13813000 |
|   | N |  2.01877500 | -0.44419000 | -0.07397600 |
|   | H |  2.25122300 | -0.43983900 | -1.06319600 |
|   | H |  1.87605400 | -1.40241800 |  0.23229900 |
|   | H |  2.78887100 | -0.03657000 |  0.45017000 |

| 8 | N | -1.56736800 | -0.98658000 | 0.30934800 |
|---|---|---|---|---|
|   | H | -2.36544300 | -0.64641200 | 0.83680600 |
|   | H | -1.48163600 | -1.99184600 | 0.21008300 |
|   | C | -0.67743100 | -0.17269800 | -0.21941500 |
|   | H | 0.18501400 | -0.61002400 | -0.70906700 |
|   | C | -0.77361300 | 1.22150400 | -0.13192300 |
|   | H | -1.61225600 | 1.71095900 | 0.35135100 |
|   | H | 0.00556000 | 1.82936600 | -0.56919000 |
|   | N | 2.33732700 | -0.02915200 | 0.01918200 |
|   | H | 2.56640400 | 0.51575800 | 0.84668000 |
|   | H | 2.84582100 | 0.39146400 | -0.75528700 |
|   | H | 2.74523100 | -0.95029600 | 0.16160800 |
|   |   |   |   |   |
| 9 | N | 1.16233500 | 1.16618400 | 0.00003000 |
|   | H | 2.16703700 | 1.31992300 | 0.00031300 |
|   | H | 0.57404900 | 1.99320400 | -0.00005000 |
|   | C | 0.62638500 | -0.03539200 | -0.00019100 |
|   | H | -0.48078700 | -0.07922100 | -0.00044100 |
|   | C | 1.41533400 | -1.19735700 | -0.00002200 |
|   | H | 2.49996000 | -1.15775200 | 0.00045100 |
|   | H | 0.93706200 | -2.16801300 | 0.00008900 |
|   | N | -2.48971500 | -0.05988600 | 0.00004300 |
|   | H | -2.85403100 | -0.56801800 | -0.80328100 |
|   | H | -2.94650200 | 0.84945600 | -0.01775700 |
|   | H | -2.85544000 | -0.53717400 | 0.82144000 |

| 10 | N | -0.07605400 | 0.53483800 | -0.00026200 |
|----|---|-------------|------------|-------------|
|    | H | -0.32947900 | 1.52013600 | 0.00001100 |
|    | H | 0.98495500 | 0.26826400 | -0.00042800 |
|    | C | -1.02444700 | -0.37107200 | -0.00014400 |
|    | H | -0.69564900 | -1.40640700 | -0.00027900 |
|    | C | -2.39287000 | -0.07419800 | 0.00018300 |
|    | H | -2.74894000 | 0.95027900 | 0.00037900 |
|    | H | -3.12278400 | -0.87284100 | 0.00019500 |
|    | N | 2.58049900 | -0.12864800 | 0.00017100 |
|    | H | 2.84347700 | -0.75378900 | -0.75970300 |
|    | H | 2.88003100 | -0.57951600 | 0.86296700 |
|    | H | 3.16117500 | 0.70216200 | -0.10274100 |
|    |   |             |            |             |
| 11 | C | -2.14684600 | 2.15290200 | -0.23206100 |
|    | H | -1.68160600 | 2.94321000 | -0.80695400 |
|    | H | -3.22308000 | 2.17436600 | -0.09639500 |
|    | C | -1.35665900 | 1.13410600 | 0.31592600 |
|    | H | -0.28114100 | 1.13002800 | 0.16910900 |
|    | N | -1.85423700 | 0.14347900 | 1.02467300 |
|    | H | -2.84999100 | 0.06246400 | 1.21534800 |
|    | H | -1.25558400 | -0.58156100 | 1.40961700 |

| 12 | N |  1.80670500 | -0.33865100 | -0.54389000 |
|----|---|-------------|-------------|-------------|
|    | H |  1.71983600 | -0.05664900 | -1.51452700 |
|    | H |  2.58906900 | -0.93879900 | -0.31141800 |
|    | C |  0.95971100 |  0.05860200 |  0.36564200 |
|    | H |  1.16345200 | -0.29148300 |  1.37470200 |
|    | C | -0.21445100 |  0.82606700 |  0.11227400 |
|    | H | -0.24429000 |  1.36101700 | -0.83584000 |
|    | H | -0.54098100 |  1.42329300 |  0.96007100 |
|    | N | -2.30960200 | -0.76415900 | -0.12931100 |
|    | H | -2.88758700 | -0.67014100 |  0.71393000 |
|    | H | -1.12610500 | -0.08821200 |  0.00009800 |
|    | H | -2.87325900 | -0.39456300 | -0.90353900 |

| 13 | N |  2.01987600 | -0.54358500 | -0.19906500 |
|----|---|-------------|-------------|-------------|
|    | H |  2.17509800 | -0.36128400 | -1.18711300 |
|    | H |  2.65081400 | -1.20097700 |  0.24880100 |
|    | C |  1.06473800 |  0.03311200 |  0.45064500 |
|    | H |  0.98635400 | -0.22508700 |  1.50498300 |
|    | C |  0.09532800 |  0.94656200 | -0.13514300 |
|    | H |  0.32710000 |  1.23440500 | -1.16083400 |
|    | H | -0.01296000 |  1.82979400 |  0.50301100 |
|    | N | -2.78941200 | -0.38481000 | -0.03013000 |
|    | H | -3.27101100 | -0.94212200 | -0.74684600 |
|    | H | -3.52783700 | -0.15477200 |  0.64677000 |
|    | H | -0.90120300 |  0.44076600 | -0.09741500 |

| 14 | C | -0.85118700 | -0.34728800 | 0.00133500 |
|---|---|---|---|---|
| | H | -0.49983500 | -1.37808800 | 0.00490700 |
| | N | 2.77159900 | -0.14401700 | 0.00017700 |
| | H | 3.37983900 | -0.25965600 | 0.81828900 |
| | H | 3.37260900 | -0.28276200 | -0.81969100 |
| | C | -2.30180800 | -0.08832800 | -0.00010800 |
| | H | -2.75069800 | -0.57302900 | 0.87464100 |
| | H | -2.54960200 | 0.97321400 | -0.00258500 |
| | H | -2.74914600 | -0.57661700 | -0.87369600 |
| | N | 0.05970400 | 0.55353100 | -0.00095100 |
| | H | -0.19659300 | 1.53828000 | -0.00394800 |
| | H | 1.09227400 | 0.30575100 | 0.00013700 |

| 15 | C | -0.54821400 | -0.07289500 | -0.41522000 |
|---|---|---|---|---|
| | H | -0.02183200 | -0.16902200 | -1.35645300 |
| | N | 2.11314800 | -0.05110900 | 0.06966700 |
| | H | 2.88700800 | 0.19422700 | -0.56148800 |
| | H | 2.58020300 | -0.29572300 | 0.95231600 |
| | C | -0.84653200 | 1.26530000 | 0.12193100 |
| | H | -1.52618800 | 1.76738400 | -0.57890400 |
| | H | -1.30450800 | 1.23811200 | 1.11103700 |
| | H | 0.07108800 | 1.85569300 | 0.14678500 |
| | N | -0.97628000 | -1.16493600 | 0.12195400 |
| | H | -1.48646300 | -1.16207600 | 1.00013500 |
| | H | -0.78890600 | -2.07070700 | -0.29503600 |

| **16** | C | -0.24207600 | -0.22618400 | -0.41208300 |
| | H | 0.00885100 | -0.16852800 | -1.46475100 |
| | N | 1.42585100 | 0.81350100 | 0.06885400 |
| | H | 2.29823100 | 0.76916200 | -0.47070300 |
| | H | 1.65195900 | 1.01358400 | 1.05011200 |
| | C | -1.29240100 | 0.69740400 | 0.10544500 |
| | H | -2.25606200 | 0.35529900 | -0.28839400 |
| | H | -1.34698800 | 0.68847600 | 1.19599800 |
| | H | -1.12384300 | 1.71416400 | -0.24474700 |
| | N | -0.06220500 | -1.41145700 | 0.14807200 |
| | H | -0.40931900 | -1.61137600 | 1.07787500 |
| | H | 0.47088400 | -2.14027500 | -0.30736800 |
| | | | | |
| **17** | C | 0.04819400 | -0.00069200 | 0.41042100 |
| | H | -0.00814700 | -0.00071700 | 1.49802300 |
| | N | -0.72855000 | 1.11786800 | -0.10002700 |
| | H | -1.59519400 | 1.38893900 | 0.35401000 |
| | H | -0.64393300 | 1.37318700 | -1.07967000 |
| | C | 1.47925300 | 0.00021000 | -0.08336100 |
| | H | 1.99713900 | -0.88556900 | 0.28647700 |
| | H | 1.52481800 | 0.00033800 | -1.17669000 |
| | H | 1.99546900 | 0.88718300 | 0.28630200 |
| | N | -0.72833800 | -1.11735700 | -0.10078300 |
| | H | -0.64380200 | -1.37237000 | -1.08037600 |
| | H | -1.59281000 | -1.39167000 | 0.35523700 |

| 18 | C | -0.05838900 | 0.00012100 | -0.01098500 |
|----|---|-------------|------------|-------------|
|    | N | -0.70476300 | -1.15099900 | -0.00161300 |
|    | H | -1.71416000 | -1.21457200 | 0.02446400 |
|    | H | -0.19406200 | -2.02203700 | -0.01143300 |
|    | C | 1.43735100 | 0.00239700 | 0.00176800 |
|    | H | 1.83224400 | 0.89665300 | -0.47982900 |
|    | H | 1.78412700 | -0.01436600 | 1.03977600 |
|    | H | 1.83393800 | -0.87550400 | -0.50814000 |
|    | N | -0.70892300 | 1.14880400 | -0.00165300 |
|    | H | -1.71857600 | 1.20838000 | 0.02430900 |
|    | H | -0.20147600 | 2.02170000 | -0.01098100 |

| 19 | N | -2.94837800 | 1.38083000 | -0.14826100 |
|----|---|-------------|------------|-------------|
|    | H | -2.52138500 | 2.23040700 | 0.21539000 |
|    | H | -3.94928800 | 1.41434900 | -0.32489900 |
|    | C | -2.25698700 | 0.31933700 | -0.37277900 |
|    | H | -2.80500800 | -0.53717100 | -0.76146300 |
|    | C | -0.81233300 | 0.20662800 | -0.13931100 |
|    | H | -0.63319700 | -0.62766300 | 0.55075300 |
|    | H | -0.32720100 | -0.08344600 | -1.07996200 |
|    | H | -0.35973000 | 1.11841200 | 0.24990900 |

| 20 | N | -2.68021900 | 3.16314000 | 0.06552200 |
|----|---|-------------|------------|-------------|
|    | H | -3.31716500 | 3.63221800 | 0.70959700 |
|    | H | -2.33284900 | 3.72130500 | -0.71444900 |
|    | C | -2.33705100 | 1.94579100 | 0.22656700 |
|    | H | -2.72751600 | 1.38299100 | 1.06926600 |
|    | H | -1.65660500 | 1.47991700 | -0.48004700 |

| 21 | N | 1.41994800 | -0.62138900 | 0.01884500 |
|----|---|------------|-------------|------------|
|    | H | 2.03208400 | -1.28731900 | 0.48210600 |
|    | H | 0.44208700 | -0.91016200 | -0.19928200 |
|    | C | 1.74436200 | 0.61784600 | -0.08349400 |
|    | H | 2.69113000 | 0.97193600 | 0.31028900 |
|    | H | 1.05765000 | 1.30143400 | -0.56691200 |
|    | C | -1.57670000 | 0.75268100 | 0.12581500 |
|    | H | -1.75046000 | 1.39419400 | -0.72504200 |
|    | H | -1.64155600 | 1.12564100 | 1.13635200 |
|    | N | -1.45274100 | -0.61673000 | -0.07976100 |
|    | H | -1.83818400 | -0.95526700 | -0.95655400 |
|    | H | -1.76917600 | -1.19679300 | 0.69152900 |

| 22 | N | 1.36678200 | -0.56062000 | 0.00008100 |
|----|---|------------|-------------|------------|
|    | H | 1.95622600 | -1.39141300 | -0.00076200 |
|    | H | 0.28495300 | -0.68479400 | 0.00064600 |
|    | C | 1.89791900 | 0.59503000 | -0.00000800 |
|    | H | 2.97780800 | 0.71560300 | -0.00094600 |
|    | H | 1.24953600 | 1.46653800 | 0.00081500 |
|    | C | -1.72799900 | 0.74577300 | -0.00015900 |
|    | H | -1.94355300 | 1.22309200 | -0.94343500 |
|    | H | -1.94143200 | 1.22373300 | 0.94328300 |
|    | N | -1.38730700 | -0.63257800 | 0.00010000 |
|    | H | -1.72949900 | -1.12265600 | -0.82380700 |
|    | H | -1.72988300 | -1.12253500 | 0.82394200 |

| **23** | C |  0.01086500 | -0.82670300 |  0.00000000 |
|--------|---|-------------|-------------|-------------|
|        | H | -0.08714600 | -1.30953800 |  0.95960600 |
|        | N |  0.01086500 |  0.64286800 |  0.00000000 |
|        | H |  0.48832500 |  1.02092300 | -0.82774800 |
|        | H | -0.08714600 | -1.30953800 | -0.95960600 |
|        | H | -0.94359800 |  1.03737500 |  0.00000000 |
|        | H |  0.48832500 |  1.02092300 |  0.82774800 |
|        |   |             |             |             |
| **24** | N |  2.18080800 |  0.00772400 | -0.00140400 |
|        | H |  2.76848000 |  0.13920000 | -0.83225400 |
|        | H |  2.75406100 |  0.18853700 |  0.83023800 |
|        | C |  0.13694000 | -0.50486200 | -0.00327200 |
|        | H |  0.26286700 | -1.04013400 | -0.93186000 |
|        | H |  0.26463800 | -1.05170700 |  0.91835600 |
|        | C | -0.65794200 |  0.73647400 |  0.00520700 |
|        | H | -0.61723500 |  1.35159300 | -0.88920000 |
|        | H | -0.61656500 |  1.33956400 |  0.90775000 |
|        | N | -1.74413600 | -0.24333300 | -0.00065600 |
|        | H | -2.27590600 | -0.36866700 |  0.85006500 |
|        | H | -2.27574600 | -0.35823400 | -0.85294600 |

| 25 | N | -2.59057400 | -0.02376900 | 0.00009300 |
| | H | -3.22587900 | 0.05819000 | 0.80502200 |
| | H | -3.22605700 | 0.05783900 | -0.80473100 |
| | C | 0.25130700 | -0.49714800 | 0.00000100 |
| | H | -0.13272900 | -0.91976100 | 0.91617000 |
| | H | -0.13273200 | -0.91989200 | -0.91610700 |
| | C | 0.80713300 | 0.86101900 | -0.00010100 |
| | H | 0.82321900 | 1.43398100 | 0.91767800 |
| | H | 0.82321200 | 1.43384300 | -0.91796500 |
| | N | 1.75788100 | -0.30639800 | -0.00001700 |
| | H | 2.27458800 | -0.50819200 | -0.85123900 |
| | H | 2.27458800 | -0.50806800 | 0.85123500 |
| | | | | |
| 26 | N | 2.36058200 | 0.83576300 | -0.97173400 |
| | H | 3.24088400 | 0.67747200 | -0.46396200 |
| | H | 2.65687000 | 1.39592200 | -1.78208700 |
| | C | -0.50937700 | -0.42256500 | 1.12606500 |
| | H | -0.01137300 | -1.35242900 | 1.36770500 |
| | H | -0.70599900 | 0.24182600 | 1.95741800 |
| | C | -0.41732100 | 0.11749300 | -0.23884600 |
| | H | 0.15884000 | -0.40831100 | -0.98461600 |
| | H | -0.54852100 | 1.17731500 | -0.40533800 |
| | N | -1.68209200 | -0.58927000 | 0.19918800 |
| | H | -2.51648100 | -0.03575100 | 0.37229200 |
| | H | -1.87337300 | -1.51412600 | -0.17564600 |

| 27 | N | -2.39445300 | -0.00003500 | -0.10084100 |
| | H | -3.00080800 | 0.81858200 | -0.22321400 |
| | H | -3.00006800 | -0.81893500 | -0.22496900 |
| | C | 1.25962200 | -0.73854200 | -0.28062600 |
| | H | 0.77171500 | -1.27129600 | -1.08621700 |
| | H | 2.04535700 | -1.27184200 | 0.23781500 |
| | C | 1.25980900 | 0.73817500 | -0.28135500 |
| | H | 0.77206400 | 1.27027600 | -1.08747400 |
| | H | 2.04568500 | 1.27175500 | 0.23658700 |
| | N | 0.31537200 | 0.00038000 | 0.60909600 |
| | H | 0.51772000 | 0.00086000 | 1.60448000 |
| | H | -0.71468000 | 0.00038500 | 0.35709300 |
| | | | | |
| 28 | N | -2.41224000 | 1.26502100 | -0.05162100 |
| | H | -2.56803900 | 1.77457400 | 0.81483200 |
| | H | -2.75776700 | 1.74720500 | -0.87791700 |
| | C | -2.47525500 | -0.23612300 | -0.02029400 |
| | H | -2.75859400 | -0.63976100 | 0.94312500 |
| | H | -2.96335900 | -0.66927600 | -0.88372500 |
| | C | -1.16867200 | 0.43071400 | -0.17751700 |
| | H | -0.50253600 | 0.51166500 | 0.67165300 |
| | H | -0.70728500 | 0.48213600 | -1.15519700 |

| 29 | N | -2.43096800 | 0.09773500 | -0.00173500 |
|----|---|-------------|------------|-------------|
|    | H | -2.94944800 | 0.20700200 | -0.86335800 |
|    | H | -2.95372700 | 0.20710300 | 0.85728800 |
|    | C | -1.14192000 | -0.16929900 | 0.00150400 |
|    | H | -0.63939600 | -0.33747300 | -0.93641800 |
|    | H | -0.64430300 | -0.33700700 | 0.94221500 |
|    | C | 2.00594800 | -0.64206800 | -0.00076000 |
|    | H | 2.16736600 | -1.14648000 | -0.94172800 |
|    | H | 2.16896000 | -1.14850300 | 0.93884100 |
|    | N | 1.62250500 | 0.63491100 | 0.00095300 |
|    | H | 1.63605300 | 1.17700800 | -0.85243100 |
|    | H | 1.63777600 | 1.17521700 | 0.85544500 |
| 30 | N | -2.08571900 | -0.17094100 | 0.00060500 |
|    | H | -2.52016300 | -0.47672300 | 0.86123800 |
|    | H | -2.52118800 | -0.47832600 | -0.85893900 |
|    | C | -1.01109200 | 0.59160300 | -0.00074200 |
|    | H | -0.69018100 | 1.03344100 | -0.93277600 |
|    | H | -0.68905700 | 1.03521000 | 0.93006000 |
|    | C | 2.15286500 | 0.24072700 | 0.00062300 |
|    | H | 2.53693300 | 0.59943700 | 0.94328400 |
|    | H | 2.53806700 | 0.60048600 | -0.94117300 |
|    | N | 1.04530900 | -0.55700700 | -0.00048600 |
|    | H | 0.88941800 | -1.10543600 | -0.83995700 |
|    | H | 0.88840800 | -1.10643400 | 0.83814500 |

| 31 | N | 1.92880100 | -0.39261500 | -0.13568700 |
| | H | 2.52110500 | -0.05844900 | -0.88433300 |
| | H | 1.99831000 | -1.37548100 | 0.09264300 |
| | C | 1.10986600 | 0.40951900 | 0.51234500 |
| | H | 0.62799000 | 0.04535700 | 1.40755000 |
| | H | 1.19063300 | 1.47412100 | 0.34032200 |
| | C | -2.01148700 | -0.44937900 | 0.12648900 |
| | H | -2.58725800 | -0.13021300 | 0.98177600 |
| | H | -2.03988200 | -1.46936800 | -0.22524100 |
| | N | -1.10273400 | 0.41066200 | -0.41429600 |
| | H | -0.80067000 | 0.20664400 | -1.36143300 |
| | H | -1.29284800 | 1.39883000 | -0.28144800 |
| | | | | |
| 32 | N | 1.38346800 | 0.63255900 | -0.00009200 |
| | H | 1.50171500 | 1.15741700 | 0.85568500 |
| | H | 1.49962800 | 1.15724100 | -0.85625400 |
| | C | 1.43073200 | -0.69163700 | 0.00000400 |
| | H | 1.49726600 | -1.22028700 | -0.93910300 |
| | H | 1.50029900 | -1.22008600 | 0.93901400 |
| | C | -1.43126400 | 0.69162500 | 0.00013300 |
| | H | -1.49954600 | 1.22011800 | -0.93893500 |
| | H | -1.49997900 | 1.21994200 | 0.93927100 |
| | N | -1.38307900 | -0.63248600 | 0.00003500 |
| | H | -1.49977000 | -1.15746300 | 0.85594100 |
| | H | -1.49913700 | -1.15732000 | -0.85604400 |

| 33 | N | 0.74622500 | -0.57723100 | 0.09815400 |
|----|---|------------|-------------|------------|
|    | H | 1.27290100 | -1.44569800 | 0.00022900 |
|    | H | 1.14888400 | 0.05807100 | 1.09481700 |
|    | C | 1.51059900 | 0.64488100 | -0.03948800 |
|    | H | 0.92297600 | 1.53721100 | -0.19587600 |
|    | H | 2.55903100 | 0.54736200 | -0.28400900 |
|    | C | -0.77810400 | -0.63602500 | -0.17933200 |
|    | H | -1.13619800 | -1.44717600 | 0.45434300 |
|    | H | -0.83404600 | -0.93597900 | -1.22890900 |
|    | N | -1.37449200 | 0.61116300 | 0.07180000 |
|    | H | -1.77824800 | 1.07497100 | -0.72875100 |
|    | H | -1.98306500 | 0.65560000 | 0.87661500 |
| 34 | N | -1.34997100 | -0.65172000 | -0.00545900 |
|    | H | -1.66314400 | -1.00016100 | 0.88994000 |
|    | C | -0.79872800 | 0.64264400 | -0.00697400 |
|    | H | -1.07944300 | 1.23487600 | -0.88874600 |
|    | H | -1.06371400 | 1.26097900 | 0.86834600 |
|    | C | 1.49814700 | -0.55201100 | -0.02888100 |
|    | H | 0.90547800 | -1.38332300 | -0.40920200 |
|    | H | 1.82494500 | -0.80046100 | 0.99638500 |
|    | N | 0.68535700 | 0.62453200 | 0.00436200 |
|    | H | 2.40099000 | -0.35156400 | -0.61254900 |
|    | H | -2.01966200 | -0.84100200 | -0.73683800 |
|    | H | 1.15033000 | 1.52717000 | 0.11547300 |

| 35 | N | -1.38421300 | -0.61852000 | 0.05532600 |
|---|---|---|---|---|
|  | H | -0.93308300 | -1.49761800 | -0.15471500 |
|  | C | -0.72600100 | 0.54360500 | 0.05766300 |
|  | H | -0.94085800 | 1.09876500 | -1.55223900 |
|  | H | -1.28999100 | 1.42532700 | 0.34875000 |
|  | C | 1.51994900 | -0.49891900 | -0.04680600 |
|  | H | 1.45766400 | -0.90504200 | -1.06101300 |
|  | H | 1.29525700 | -1.28025200 | 0.68354600 |
|  | N | 0.60202200 | 0.62780300 | 0.12297400 |
|  | H | 2.53372400 | -0.14623000 | 0.12622400 |
|  | H | -2.39348500 | -0.62007000 | 0.08628500 |
|  | H | 0.99357200 | 1.55788000 | 0.19035500 |
|  |  |  |  |  |
| 36 | N | -1.42537600 | -0.54131900 | -0.00001200 |
|  | H | -2.43508400 | -0.51025100 | -0.00000400 |
|  | C | -0.73252900 | 0.57853400 | 0.00000100 |
|  | H | -1.28935300 | 1.50930900 | 0.00007000 |
|  | H | 1.33477100 | -1.10659700 | -0.89729900 |
|  | C | 1.48594900 | -0.50227100 | -0.00000600 |
|  | H | 2.50771000 | -0.13144600 | 0.00105800 |
|  | H | 1.33342100 | -1.10771500 | 0.89629500 |
|  | N | 0.57429600 | 0.65087900 | 0.00000800 |
|  | H | 0.97894700 | 1.57775200 | -0.00008700 |
|  | H | -0.99337100 | -1.45555700 | 0.00003100 |

| 37 | N | -2.68021900 | 3.16314000 | 0.06552200 |
|----|---|-------------|------------|------------|
|    | H | -3.31716500 | 3.63221800 | 0.70959700 |
|    | H | -2.33284900 | 3.72130500 | -0.71444900 |
|    | C | -2.33705100 | 1.94579100 | 0.22656700 |
|    | H | -2.72751600 | 1.38299100 | 1.06926600 |
|    | H | -1.65660500 | 1.47991700 | -0.48004700 |

## 6.10 References

1. Energy, U.S.D.o., *Carbon Dioxide Emissions From Energy Consumption by Source*, in *Monthly Energy Review*, U.S.E.I. Administration, Editor. 2014. p. 157-169.
2. Metz, B., et al., *Climate Change 2007: Mitigation. Contribution of Working Group III to the Fourth Assessment Report of the Intergovernmental Panel on Climate Change. Transport and its Infrastructure.* Intergovernmental Panel on Climate Change 2007, 2007.
3. Chen, X.Q., et al., *Catalytic Decomposition of hydrazine over Supported Molybdenum Nitride Catalysts in a Monopropellant Thruster.* Catal. Lett., 2002. **79**(1-4): p. 21-25.
4. Catoire, L., et al., *Visualizations of Gas-Phase NTO/MMH Reactivity.* J. Propul. Power, 2006. **2006**(22): p. 1.
5. Tang, Z., L. Wang, and J. Yang, *Transesterification of rapeseed oil catalyzed by liquid organic amine in supercritical methanol in a continuous tubular-flow reactor.* Eur. J. Lipid Sci. Technol., 2008. **110**: p. 747-753.
6. Company, T.D.C., *Ethyleneamines*, T.D.C. Company, Editor. 2001, The Dow Chemical Company: Midland, Michigan.
7. Pfeil, M.A., et al., *Charaterization of Ethylenediamine Bisborane as a Hypergolic Hybrid Rocket Fuel Additive.* Journal of Propulsion and Power, 2015. **31**(1): p. 365-372.
8. Fischer, K.H., et al., *Bonding in a Borylene Complex Investigated by Photoionization and Dissociative Photoionization.* Chem. Eur. J., 2012. **18**: p. 4533-4540.
9. Sztaray, B. and T. Baer, *Dissociation Dynamics and Thermochemistry of Energy-Selected $CpCO(CO)_2+$ Ions.* J. Am. Chem. Soc., 2000. **122**: p. 9219-9226.
10. Sztaray, B. and T. Baer, *Consecutive and Parallel Dissociation of Energy-Selected $Co(CO)_3NO^+$ Ions.* J. Phys. Chem A, 2002. **106**: p. 8046-8053.
11. Bodi, A., Hemberger, P., *Imaging breakdown diagrams for bromobutyne isomers with photoelectron-photoion coincidence.* Physical Chemistry Chemical Physics, 2014. **16**: p. 505-515.
12. West, B., Joblin, C., Blanchet, V. ,Bodi, A., Sztaray, B., Mayer, P.M., *On the Dissociation of the Napthalene Radical Cation: New iPEPICO and Tandem Mass Spectrometry Results.* Journal of Physical Chemistry, 2012. **116**: p. 10999-11007.
13. Bouwman, J., et al., *Dissociative Photoionization of Quinoline and Isoquinoline.* J. Phys. Chem. A, 2015. **119**: p. 1127-1136.
14. Gengelicski, Z., S.N. Borkar, and B. Sztaray, *Dissociation of Energy-Selected 1,1-Dimethylhydrazine Ions.* J. Phys. Chem. A, 2010. **114**: p. 6103-6110.
15. Voronova, K., et al., *Dissociative Photoionization of Diethyl Ether.* J. Phys. Chem. A, 2015.
16. Radom, L., et al., *Molecular Orbital Theory of the Electronic Structure of Organic Compounds. XVII. Internal Rotation in 1,2-Disubstituted Ethanes.* Journal of the American Chemical Society, 1972. **95**(3): p. 693-698.
17. Yokozeki, A. and K. Kuchitsu, Bull. Chem. Soc. Jap., 1970. **43**: p. 2664.
18. Yokozeki, A. and K. Kuchitsu, ibid., 1971. **44**: p. 2926.
19. Kazerouni, M.R., L. Hedberg, and K. Hedberg, *Conformational Analysis. 16. Ethylenediamine. An Electron-Diffraction and ab Initio Investigation of the Molecular*

*Structure, Conformational Composition, Anti-Gauche Energy and Entropy Differences, and Implications for Internal Hydrogen Bonding.* Journal of the American Chemical Society, 1993. **116**(12): p. 5279-5284.

20.     Frisch, M.J., et al., *Gaussian 90*. 1990, Gaussian, Inc.: Pittsburgh, PA.

21.     Alsenoy, C.V., et al., *THEOCHEM.* J. Mol. Struct., 1986. **136**: p. 77.

22.     Lee, S.J., et al., J. Phys. Chem, 1994. **98**: p. 1129.

23.     Krest'yanimov, M.A., A.G. Titova, and A.M. Zaichikov, *Intra- and Intermolecular Hydrogen Bonds in Ethylene Glycol, Monoethanolamine, and Ethylenediamine.* Russian Journal of Physical Chemistry A, 2014. **88**(12): p. 2114-2120.

24.     Wienhold, F., *THEOCHEM.* J. Mol. Struct., 1997. **181**: p. 398-399.

25.     Wei, L., Yang, B., Wang, J., Huang, C., Sheng, L., Zhang, Y., Qi, F., Lam, C., Li, W., *Vacuum Ultraviolet Photoionization Mass Spectrometric Study of Ethylenediamine.* Journal of Physical Chemistry, 2006. **110**: p. 9089-9098.

26.     Fang, W., et al., *Photoionization and dissociation of the monoterpene limonene: mass spectrometric and computational investigation.* Journal of Mass Spectrometry, 2011. **46**: p. 1152-1159.

27.     Kim, H.-R., *Excursion, Roaming and Migration of Hydrogen Atom during Dissociation of Formaldehyde.* Bull. Korean Chem. Soc., 2014. **35**(5): p. 1285-1293.

28.     Xiao, W., et al., *Unexpected methyl migrations of ethanol dimer under synchrotron VUV radiation.* Journal of Chemical Physics, 2015. **142**(024306): p. 1-7.

29.     Dyakov, Y.A., et al., *Ab initio and RRKM study of photodissociation of azulene cation.* Physical Chemistry Chemical Physics, 2006. **8**: p. 1404-1415.

30.     Baer, T., et al., *Threshold Photoelectron Photoion Coincidence Studies of Parallel and Sequential Dissociation Reactions.* Physical Chemistry Chemical Physics, 2005. **7**: p. 1507-1513.

31.     Kercher, J.P., et al., *Modeling Ionic Unimolecular Dissociations from a Temperature Controlled TPEPICO Study on 1-C4H9I Ions.* Int. J. Mass Spectrom., 2007. **267**: p. 159-166.

32.     Sztaray, B. and T. Baer, *Suppression of Hot Electrons in Threshold Photoelectron Photoion Coincidence Spectroscopy Using Velocity Focusing Optics.* Rev. Sci. Instrum., 2003. **74**(8): p. 3763-3768.

33.     Borkar, S. and B. Sztaray, *Self-Consistent Heats of Formation for the Ethyl Cation, Ethyl Bromide, and Ethyl Iodide from Threshold Photoelectron Photoion Coincidence Spectroscopy.* J. Phys. Chem. A, 2010. **114**(20): p. 6117-6123.

34.     Baer, T. and Y. Li, *Threshold Photoelectron Spectroscopy with Velocity Focusing: An Ideal Match for Coincidence Studies.* Int. J. Mass Spectrom., 2002. **219**: p. 381-389.

35.     Wiley, W.C. and I.H. McLaren, *Time-of-Flight Mass Spectrometer with Improved Resolution.* The Review of Scientific Instruments, 1955. **26**(12): p. 1150-1157.

36.     Bodi, A., et al., *Data acquisition schemes for continuous two-particle time-of-flight coincidence experiments.* Rev. Sci. Instrum., 2007. **78**(8): p. 084102/1- 804102/6.

37.     Sztaray, B., Bodi, A., Baer, T., *Modeling unimolecular reactions in photoelectron photoion coincidence experiments.* Journal of Mass Spectrometry, 2010. **45**: p. 1233-1245.

38.     *IGOR Pro* 2013, Wavemetrics, Inc.: Portland, OR.

39. Lifshitz, C., *Time-resolved appearance energies, breakdown graphs, and mass spectra: The elusive "kinetic shift".* Mass Spectrometry Reviews, 2005. **1**(4): p. 309-348.

40. Chupka, W.A., *Effect of Unimolecular Decay Kinetics on the Interpretation of Appearance Potentials.* The Journal of Chemical Physics, 1959. **30**(1): p. 191-211.

41. Ochterski, J.W., G.A. Petersson, and J.A. Montgomery, *A complete basis set model chemistry. V. Extensions to six or more heavy atoms.* J. Chem. Phys., 1996. **104**: p. 2598-2619.

42. Montgomery, J.A., et al., *A complete basis set model chemistry. VI. Use of density functional geometries and frequencies.* J. Chem. Phys., 1999. **110**: p. 2822-2827.

43. Montgomery, J.A., et al., *A complete basis set model chemistry. VII. Use of the minimum population localization method. .* J. Chem. Phys., 2000. **112**: p. 6532-6542.

44. Frisch, M.J., et al., *Gaussian 09*. 2009, Gaussian, Inc.: Wallingford, CT.

45. Curtiss, L.A., et al., *Gaussian-3 (G3) Theory for Molecules Containing First and Second-Row Atoms.* Journal of Chemical Physics, 1998. **109**: p. 7764-7776.

46. Dennington, R., T. Keith, and J. Millam, *GaussView*. 2009, SemiChem Inc.: Shawnee Mission, KS.

47. Fukui, K., *The path of chemical reactions - the IRC approach.* Acc. Chem. Res., 1981. **14**(12): p. 363-368.

48. Hratchian, H.P. and H.B. Schlegel, *Finding minima, transition states, and following reaction patheways on ab initio potential energy surfaces*, in *Theory and Applications of Computational Chemistry: The First 40 Years*, C.E. Dykstra, et al., Editors. 2005, Elsevier: Amsterdam. p. 195-249.

49. Marcus, R.A. and O.K. Rice, *The kinetics of the recombination of methyl radicals and iodine atoms.* J. Phys. Colloid Chem., 1951. **55**: p. 894.

50. Rice, O.K. and H.C. Ramsperger, *Theories of unimolecular reactions at low pressures.* J. Am. Chem. Soc., 1927. **49**: p. 1617.

51. Rice, O.K. and H.C. Ramsperger, *Theories of unimolecular reactions at low pressures II.* J. Am. Chem. Soc., 1928. **50**: p. 617.

52. Hase, W.L., *Variational unimolecular rate theory.* Acc. Chem. res., 1983. **16**: p. 258.

53. Baer, T. and W.L. Hase, *Unimolecular Reaction Dynamics: Theory and Experiments*. 1996, New York: Oxford University Press.

54. Peng, C. and H.B. Schlegel, *Combining Sychronous Transit and Quasi-Newton Methods to Find Transition States.* Israel J. of Chem., 1993. **33**(449): p. 449-454.

55. Peng, C., et al., *Using redundant internal coordinates to optimize equilibrium geometries and transition states.* Journal of Computational Chemistry, 1998. **17**(1): p. 49-56.

56. Ramakrishna, V. and B.J. Duke, *Extension of complete basis set model chemistries to molecules containing third row atoms Ga-Kr.* Journal of Chemical Physics, 2003. **118**(14): p. 6137-6143.

57. Lewars, E.G., *Computational Chemistry: Introduction to the Theory and Applications of Molecular and Quantum Mechanics, 2nd Edition*. Dordrecht, Heidelberg, London, New York: Springer.

58. Sirjean, B., et al., *Extension of the composite CBS-QB3 method to singlet diradical calculations.* Chemical Physics Letters, 2007. **435**: p. 152-156.

59. Kimura, K., et al., *Ionization energies, Ab initio assignments and valence electronic structure for 200 molecules*, in *Handbook of HeI Photoelectron Spectra of Fundamental Organic Compounds*

1981, Japan Scientific Society Press: Tokyo.

60. Li, H.-K., et al., *Communication: Photodissociation of CH3CHO at 308 nm: Observation of H-roaming, CH3-roaming, and transition state pathways together along the ground state surface.* Journal of Chemical Physics, 2015. **142**: p. 041101-1 - 041101-4.

61. Fernando, R., et al., *Visible/Infrared Dissociation of NO3: Roaming in the Dark of Roaming on the Ground?* The Journal of Physical Chemistry A, 2015. **119**: p. 7163-7168.

62. Heazlewood, B.R., et al., *Roaming is the dominant mechanism for molecular products in acetaldehyde photodissociation.* Proceedings of the National Academy of Sciences, 2008. **105**(35): p. 12719-12724.

63. Zhou, J. and H.B. Schlegel, *Ab Initio Classical Trajectory Study of the Dissociation of Neutral and Positively Charged Methanimine ($CH_2NH^{n+}$ n= 0-2).* J. Phys. Chem. A, 2009. **113**: p. 9958-9964.

64. Pople, J.A., et al., *Comprehensive theoretical study of isomers and rearrangement barriers of even-electron polyatomic molecules HmABHn (A, B = carbon, nitrogen, oxygen, and fluorine).* J. Am. Chem. Soc., 1983. **105**(21): p. 6389-6399.

65. Roithova, J., D. Schroder, and H. Schwarz, *Unimolecular Fragmentation of $CH_3NH_2$: Towards a Mechanistic Description of HCN Formation.* E. J. Org. Chem., 2005(15): p. 3304-3313.

66. Holmes, J.L., et al., *Novel gas-phase ion. The radical cations [CH2XH]+ (X = F, Cl, Br, I, OH, NH2, SH) and [CH2CH2NH3]+.* Can. J. Chem, 1983. **61**(2305): p. 2305-2309.

67. Yates, B.F., R.H. Nobes, and L. Radom, *The methyleneammonium radical cation (CH2NH3+).* Chemical Physics Letters, 1985. **116**(6): p. 474-477.

68. Sana, M., et al., *Heats of formation of isomeric [C, H4, O]+, [C, H3, N]+ and [C, H5, N]+ radical cations.* Chemical Physics Letters, 1992. **190**(6): p. 551-556.

69. Frisch, M.J., et al., *Unusual low-energy isomers for simple radical cations.* Chemical Physics Letters, 1983. **75**(3): p. 323-329.

70. Bouma, W.J., J.M. Dawes, and L. Radom, *The methylamine radical cation [CH3NH2]+· and its stable isomer the methylenammonium radical cation [CH2NH3]+·.* Journal of Mass Spectrometry, 1983. **18**(1): p. 12-15.

71. Wootten, A. *The Cosmic Ice Laboratory - Interstellar Molecules*. [cited 2015; Available from: http://science.gsfc.nasa.gov/691/cosmicice/interstellar.html.

72. Bodi, A., B. Sztaray, and T. Baer, *Dissociative photoionization of mono-, di- and trimethylamine studied by a combined threshold photoelectron photoion coincidence spectroscopy and computational approach.* Physical Chemistry Chemical Physics, 2005. **8**: p. 613-623.

73. Singh, P.C., et al., *Photodissociation Dynamics of Methylamine Cation and its Relevance to Titan's Ionosphere.* The Astrophysical Journal, 2010. **710**: p. 112-116.

74.     Holtom, P.D., et al., *A Combined Experimental and Theoretical Study on the Formation of the Amino Acid Glycine ($NH_2CH_2COOH$) and Its Isomer ($CH_3NHCOOH$) in Extraterrestrial Ices.* The Astrophysical Journal, 2005. **626**(2): p. 940-952.

75.     Knowles, D.J., T. Wang, and J.H. Bowie, *Radical formation of amino acid precursors in interstellar regions? Ser, Cys, and Asp.* Organic and Biomolecular Chemistry, 2010. **8**: p. 4934-4939.

76.     Berthelot, M.P.E., Ann. Chim. Phys. S7, 1900. **20**: p. 163.

77.     Good, W.D. and R.T. Moore, *Enthalpies of Formation of Ethylenediamine, 1,2,-Propanediamine, 1,2,-Butanediamine, 2-Methyl-1,2,-popanediamine, and Isobutylamine.* Journal of Chemical and Engineering Data, 1970. **15**(1): p. 150-154.

78.     Burkey, T.J., et al., *Heats of Formation and Ionization Potentials of Some α-Aminoalkyl Radicals.* J. Am. Chem. Soc., 1982. **105**: p. 4701-4703.

79.     Benson, S.W., et al., *Additivity Rules for the Estimation of Thermodynamics Properties.* Chem. Rev., 1968. **69**: p. 279-324.

80.     Bodi, A., et al., *Photoion Photoelectron Coincidence Spectroscopy of Primary Amines RCH2NH2 (R = H, CH3, C2H5, C3H7, i-C3H7): Alylamine and Alkyl Radical Heats of Formation by Isodesmic Reaction Networks.* J. Phys. Chem. A, 2006. **110**: p. 13425-13433.

81.     Gichuhi, W.K., A.M. Mebel, and A.G. Suits, *UV Photodissociation of Ethylamine Cation: A Combined Experimental and Theoretical Investigation.* J. Phys. Chem. A, 2010. **114**: p. 13296-13302.

82.     Lossing, F.P., Y.-T. Lam, and A. Maccoll, *Gas phase heats of formation of alkyl immonium ions.* Can. J. Chem, 1981. **59**(14): p. 2228-2231.

83.     Oliveira, G.d., et al., *Definitive heat of formation of methylenimine, $CH_2=NH$, and of methylenimmonium, $CH_2NH_2+$ by means of W2 theory.* J. Comput. Chem, 2000. **22**(13): p. 1297-1305.

84.     Atkinson, R., et al., J. Phys. Chem, 2000. **Reference Data**(29): p. 167-266.

85.     Rosenstock, H.M., et al., *Energetics of Gaseous Ions.* Journal of Physical and Chemical Reference Data, 1977. **6**(Supplement No. 1): p. 1-799.

86.     Solka, B.H. and M.E. Russell, *Energetics of Formation of Some Structural Isomers of Gaseous C2H5O+ and C2H6N+ Ions.* The Journal of Physical Chemistry, 1973. **78**(13): p. 1268-1273.

87.     Traeger, J.C. and Z.A. Harvey, *Heat of Formation for the CH3CH=NH2+ Cation by Photoionization Mass Spectrometry.* J. Phys. Chem. A, 2006. **110**: p. 8542-8547.

88.     Ruscic, B. *Active Thermochemical Tables (ATcT) values based on ver. 1.112 of the Thermochemical Network*. 2013.

89.     Ruscic, B., et al., *Introduction to Active Thermochemical Tables: Several "Key" Enthalpies of Formation Revisited.* J. Phys. Chem. A, 2004. **108**: p. 9979-9997.

90.     Ruscic, B., et al., *Active Thermochemical Tables: Thermochemistry for the 21st Century.* J. Phys. Conf. Ser., 2005. **16**: p. 561-570.

91.     Chase, M.W., et al., *JANAF Thermochemical Tables 3rd edition.* J. Phys. Chem, 1985. **Ref. Data**(14): p. Suppl. 1.

92.     Grela, M.A. and A.J. Colussi, *Decomposition of methylamino and aminomethyl radicals. The heats of formation of methyleneimine (CH2[DOUBLE BOND]NH) and*

*hydrazyl (N2H3) radical.* International Journal of Chemical Kinetics, 1988. **20**(9): p. 713-718.

93.    Holmes, J.L., F.P. Lossing, and P.M. Mayer, *Concerning the heats of formation of CH2NH and CH2NH+.* Chemical Physics Letters, 1992. **198**(1-2): p. 211-213.

94.    Peerboom, R.A.L., et al., *Proton affinities and heats of formation of the imines CH2=NH, CH2=NMe and PhCH=NH.* J. Chem. Soc. Perkin Trans. 2, 1990: p. 1825-1828.

95.    DeFrees, D.J. and W.J. Hehre, *Methyleneimine.* J. Phys. Chem, 1978. **82**(4): p. 391-393.

96.    Frisch, M.J., et al. 1984, Carnegie-Mellon Quantum Chemistry Publishing Unit: Pittsburgh, PA.

97.    Chase, M.W., Jr., *NIST-JANAF Thermochemical Tables, Fourth Edition.* Journal of Physical Chemistry, 1998. **Ref. Data**(Monograph 9): p. 1-1951.